

Aminotriazole-Oxalate Based Ultra-microporous Metal Organic Frameworks: Structural Tuning for Gas Adsorption

A Thesis

Submitted in Partial Fulfillment of the Requirements

for the Degree of

Doctor of Philosophy

By

Aparna Banerjee

ID: 20123195



Department of Chemistry

Indian Institute of Science Education and Research, Pune

2017

Dedicated To

Baba-Maa

&

My Supervisor

Prof. K. N. Ganesh



भारतीय विज्ञान शिक्षा एवं अनुसंधान संस्थान, पुणे

INDIAN INSTITUTE OF SCIENCE EDUCATION AND RESEARCH (IISER), PUNE
(An Autonomous Institution, Ministry of Human Resource Development, Govt. of India)
Dr. Homi Bhabha Road, Pune 411008.

CERTIFICATE

Certified that the work incorporated in the thesis entitled "*Aminotriazole-Oxalate Based Ultra-microporous Metal Organic Frameworks: Structural Tuning for Gas Adsorption*" submitted by **Ms. Aparna Banerjee** was carried out by the candidate, under our joint supervision. The work presented here or any part of it has not been included in any other thesis submitted previously for the award of any degree or diploma from any other university or institution.

A handwritten signature in blue ink, appearing to read "K. N. Ganesh".

Prof. K. N. Ganesh
(Supervisor)

Place: Pune

Date: 24-07-2017

A handwritten signature in black ink, appearing to read "R. Vaidhyanathan".

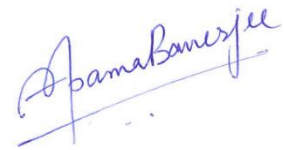
Dr. R. Vaidhyanathan
(Co-supervisor)

DECLARATION

I declare that, this written submission represents my ideas in my own words and where other's ideas have been included; I have adequately cited and referenced the original sources. I also declare that I have adhered to all principles of academic honesty and integrity and have not misrepresented or fabricated or falsified any idea/data/fact/ source in my submission. I understand that violation of the above will be cause for disciplinary action by the Institute and can also evoke penal action from the sources which have thus not been properly cited or from whom proper permission has not been taken when needed.

Place: Pune

Date: 24-07-2017



Ms. Aparna Banerjee

ID: 20123195

Acknowledgement

The past few years of my Ph.D. tenure have been a fascinating journey and will always have a significant impact on my life. I thank to all those who have been a part of this journey.

Fore mostly, I would express my earnest gratitude to my research supervisor Prof. K. N. Ganesh for his unconditional support, valuable suggestions and encouragements during the journey of my Ph.D. which helped in building up a level of confidence to pursue the research even through the tough situations. I also thank my co-guide Dr. R. Vaidhyathan, who has helped me a lot with all the technicalities and construction of this thesis. He has given me opportunities to present my work at various international and national platforms and helped me to develop various scientific skills such as systematic execution & writing of research papers; preparation & delivery of scientific presentations at various platforms.

I am very much grateful to Dr. K. Sreekumar (NCL-Pune) and Dr. V. G. Anand (IISER-Pune), the members of my Research Advisory Committee (RAC), for giving their valuable time, suggestions and expert comments to improve my research work. I would also like to express my sincere regards to Prof. M. Jayakannan (Head of the Department) and the other faculty members of the Chemistry Department IISER-Pune for their support and making a research friendly working atmosphere.

I am thankful to the Ministry of Human Resource Development (MHRD), Government of India, for the construction of such an esteemed institution like IISER Pune. It is my great privilege to have an opportunity to work here as a research scholar since last five years. I sincerely acknowledge Prof. K. N. Ganesh (Director, IISER-Pune) for providing such an outstanding campus with well-equipped research and hostel facilities within the Institute. I am thankful to Department of Science and Technology (DST), Government of India for selecting me as a recipient of the prestigious Prime-Minister doctoral research fellowship-2013 in collaboration with ENOVEX Corp. Further, I am thankful to IISER-Pune for my research scholarships and requisite financial support during the Ph.D. tenure. I am also thankful to IISER-Pune and Infosys Foundation Endowment Fund, for providing generous financial assistance to attend several national and international conferences.

I am grateful to all my lab members. I thank the support and help provided by Shyama, Shalini, Satya, Harpreet and Neha during the initial years of my Ph.D. and to the juniors: Dinesh, Debanjan, Rahul, Sattwick, Rinku, and Kingshuk who made this a memorable and enjoyable journey with their friendly discussions. I thank you all again for the time to time help, discussions, sharing of knowledge and research experience. I also thank all of my IISER colleagues

and friends for their support (especially Shatarupa and Prabhat). I am deeply obliged to all the teachers who have ever taught me since my childhood and all the friends (especially Neha Sareen and Anil from B.H.U), who have been a trustworthy companion and encouraged me to achieve better in life.

I thank all the technical staffs of IISER Pune: Ms. Archana (SCXRD), Mr. Parven Nasa (SCXRD and PXR), Mr. Prashant Kale (PXR), Mr. Nilesh Dumbre (PXR and SEM), Mr. Anil & Mr. Yatish (SEM), Ms. Swati M. Dixit (MALDI-TOF and CHN analysis), Mr. Nitin Dalvi (NMR), Mr. Mahesh Jadhav (TGA), Mr. Suresh Prajapati (UG Chemistry Lab), and Mr. Ganesh Dimbar (IR). Further, I thank Dr. Umeshreddy Kacherki (Librarian) for support through library services and also the whole IT department. I thank the administrative department of IISER-Pune for their support, especially Col. (Retd.) G. Raja Sekhar (Registrar, IISER-Pune), Prof. G. Ambika, Dr. V. S. Rao, Mr. Prabhash and Mr. Mayuresh. I deeply pay my acknowledgement for the support from the office staffs of Dean Doctoral Studies, specially Ms. Dipali Dalvi, Mr. Tushar and Ms. Priyadarshini. I am thankful to whole IISER Pune family for making the campus so lively with the various extracurricular events throughout the year. I also thank the catering services provided by V-square, Shivsagar and MDP. I really appreciate the hard work of house-keeping staffs in keeping the campus neat and tidy. I also thank the Security staffs; it is because of them I can work without worrying much about my belongings either in lab or in my hostel room.

I convey my heartfelt gratitude towards the blessings, endless love and motivation from my parents, Shri Devashish Banerjee & Smt. Bandana Banerjee. This journey wouldn't have been imaginable without their emotional strength, faith, inspiration, serenity and sacrifice. It's so right to mention here that "Behind every successful girl there are wonderful parents." I am also grateful to my elder brother Arunabh Banerjee and sister-in-law Esha Sarswat for their friendly support and always being on my side. Not to forget, the blessings of my maternal and paternal grandparents Shri Sunil Kumar Bose, Smt. Arati Bose, Late Shri M. P. Banerjee and Late. Smt. Anima Banerjee. Apart from them, I wholeheartedly thank all my cousins and uncle-aunts (maternal & paternal) for their love and care.

I would like to thank my dear friend Anant, with whom these long five years felt like a moment. I thank him from the bottom of my heart to be so supportive and caring. It's well said "One best book is equal to hundred friends and one good friend is equal to a library: by Dr. A. P. J. Abdul Kalam"

I even thank to them whose names are missed out unintentionally. Finally, I thank God for giving me such a wonderful life.

Aparna Banerjee

Contents

| | |
|---|--------------|
| Contents | i-iii |
| Synopsis | iv-ix |
| Abbreviations | x-xi |
| Rights and Permissions | xii |
| List of Publications | xiii |
| | |
| 1. Introduction | 1-41 |
| 1.1 Carbon dioxide: a global greenhouse gas | 2 |
| 1.2 Carbon capture technologies | 4 |
| 1.2.1 Oxy-fuel combustion | 5 |
| 1.2.2 Pre-combustion CO ₂ capture | 6 |
| 1.2.3 Post-combustion CO ₂ capture | 6 |
| 1.3 Significant parameters for CCS from flue gas | 7 |
| 1.3.1 Enthalpy of adsorption | 7 |
| 1.3.2 CO ₂ selectivity | 7 |
| 1.3.3 Humid stability and recyclability of the material | 8 |
| 1.4 Traditional techniques used for post-combustion CO ₂ capture | 8 |
| 1.5 Solid sorbents for post-combustion CO ₂ capture | 10 |
| 1.5.1 Zeolites | 11 |
| 1.5.2 Activated carbons | 11 |
| 1.6 Metal organic frameworks (MOFs) | 12 |
| 1.6.1 MOFs with open metal sites | 16 |
| 1.6.2 MOFs with Lewis basic sites | 19 |
| 1.6.3 Flexible frameworks | 23 |
| 1.7 Ultra-microporous MOFs and CO ₂ capture from flue gas | 27 |
| 1.8 Outline and thesis objective | 32 |
| 1.9 References | 34 |
| | |
| 2. Ultra-microporous metal organic frameworks built from rigid linkers showing solvent and temperature induced structural transformation | 42-64 |
| 2.1 Introduction | 43 |
| 2.2 Experimental section | 44 |
| 2.2.1 Materials | 44 |
| 2.2.2 Physical measurements | 44 |
| 2.2.3 Synthesis | 46 |

Contents

| | | |
|-----------|---|---------------|
| 2.3 | Results and discussions | 47 |
| 2.3.1 | Synthesis | 47 |
| 2.3.2 | Crystal structures | 47 |
| 2.3.3 | Bulk characterizations for compound 1 | 51 |
| 2.3.4 | Gas adsorption studies for compound 1 | 56 |
| 2.3.5 | Bulk characterizations for compound 2 | 57 |
| 2.3.6 | Gas adsorption studies for compound 2 | 59 |
| 2.4 | Conclusion | 62 |
| 2.5 | References | 63 |
| 3. | Bimetallic ultra-microporous aminotriazole-oxalate frameworks showing selective CO₂ capture and stability under humid conditions | 65-80 |
| 3.1 | Introduction | 66 |
| 3.2 | Experimental section | 67 |
| 3.2.1 | Materials | 67 |
| 3.2.2 | Physical measurements | 67 |
| 3.2.3 | Synthesis | 68 |
| 3.3 | Results and discussions | 69 |
| 3.3.1 | Synthesis | 69 |
| 3.3.2 | Crystal structure | 70 |
| 3.3.3 | Bulk characterizations | 72 |
| 3.3.4 | Gas adsorption studies | 74 |
| 3.4 | Conclusion | 78 |
| 3.5 | References | 79 |
| 4. | Enhancing carbon capture capacities of a rigid ultra-microporous MOF through gate-opening assisted by low CO₂ pressures and swiveling oxalate pillars | 81-101 |
| 4.1 | Introduction | 82 |
| 4.2 | Experimental section | 84 |
| 4.2.1 | Materials | 84 |
| 4.2.2 | Physical measurements | 84 |
| 4.2.3 | Synthesis | 85 |
| 4.3 | Results and discussions | 87 |
| 4.3.1 | Synthesis | 87 |
| 4.3.2 | Crystal structures | 88 |
| 4.3.3 | Bulk characterizations | 89 |
| 4.3.4 | Gas adsorption studies | 90 |
| 4.4 | Conclusion | 98 |
| 4.5 | References | 100 |

Contents

| | |
|---|----------------|
| 5. Stabilization of an unstable Zinc-aminotriazolate framework via in-situ Schiff bond formation: transformation from 1st generation to 2nd generation MOF | 102-125 |
| 5.1 Introduction | 103 |
| 5.2 Experimental section | 105 |
| 5.2.1 Materials | 105 |
| 5.2.2 Physical measurements | 105 |
| 5.2.3 Synthesis | 106 |
| 5.3 Results and discussions | 108 |
| 5.3.1 Synthesis | 108 |
| 5.3.2 Crystal structure | 109 |
| 5.3.3 Bulk characterizations | 110 |
| 5.3.4 Gas adsorption studies | 119 |
| 5.4 Conclusion | 122 |
| 5.5 References | 123 |
| 6. Thesis summary | 126 |
| 7. Appendix | 127-181 |

Synopsis

The thesis entitled “**Aminotriazole-Oxalate Based Ultra-microporous Metal Organic Frameworks: Structural Tuning for Gas Adsorption**” describes the synthesis and characterization of a series of ultra-microporous metal organic frameworks (UMMOFs). These UMMOFs based on oxalic acid and aminotriazole linkers have been investigated for their CO₂ adsorbing capabilities under the post-combustion conditions. In this thesis, all three generations of MOFs (**1st, 2nd and 3rd**) have been demonstrated based upon their structure-property relationships. In the first three working chapters, the UMMOFs have been tuned via different synthetic parameters, such as solvent, temperature and metal cations for the enhancement of their CO₂ adsorption capacity and framework stability (adsorption-desorption cycling and hydrolytic). Finally, the last chapter demonstrates the structural stabilization of an unstable large pore MOF via pore modulation approach, which results into a significant increase of the CO₂ uptake capacity.

Chapter 1: Introduction

Chapter 1 briefly demonstrates the devastating effects of the global warming due to the ever-rising concentration of CO₂ in the atmosphere. Anthropogenic emissions from power plants and other energy production units contribute significantly to the global warming. Carbon-dioxide (CO₂) present in these flue gases needs to be sequestered. Traditional techniques involve the use of alkanol amines as CO₂ scrubbers. This capture occurs by chemisorption via formation of carbamates. Due to chemical bond formation, the regenerative process becomes expensive in terms of energy and economy. Porous materials with physisorptive type of interaction, which includes zeolitic materials, activated porous carbon etc., are investigated for CO₂ capture and storage, due to their easy regeneration. Noticeably, Metal organic frameworks (MOFs), another class of porous material, has drawn considerable interest for CO₂ adsorption owing to their periodic structures, tunable pore size, and high surface areas. However, the selective CO₂ capture from flue gas creates a big challenge since CO₂ is present in very low partial pressures as compared to N₂. Thus, emphasis is given to the factors important for CO₂ adsorption from flue gas, which includes high CO₂ selectivity and appropriate pore dimensions that can facilitate both thermodynamic and kinetic separation of CO₂ from flue gas. Solid

Synopsis

sorbent with optimal interaction and pore dimensions will be a suitable candidate for CO₂ capture from flue gas. The Ultra-microporous MOFs (UMMOFs) with pore dimension less than 6 Å are vastly explored for their application in selective separation of gasses. Further, emphasis is on the stability factors (adsorption-desorption cycling and hydrolytic), which are crucial for a solid sorbent to be employed for pressure/vacuum swing type post-combustive CO₂ separation from the industrial effluents.

Chapter 2: Ultra-microporous metal organic frameworks built from rigid linkers showing solvent and temperature induced structural transformation

Chapter 2 demonstrates two Co-aminotriazole-oxalate based UMMOFs, which have been investigated for CO₂ adsorbing properties (*Figure 1*). Interestingly, despite being built from short and rigid linkers these MOFs show stimuli responsive flexible behaviour, which makes them 3rd generation MOFs.

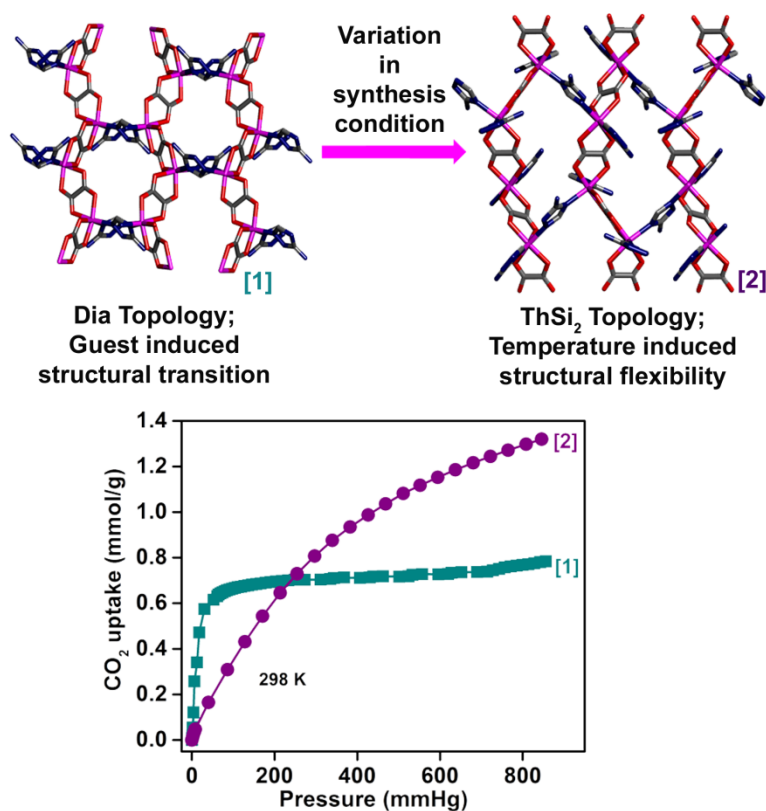


Figure 1 The two Co-Hatz-Ox UMMOFs, 1 and 2, obtained via synthetic variation and their respective CO₂ adsorption isotherms at 298 K.

Synopsis

Focus has been given to the subtle structural transitions arising from the framework-guest interactions, which leads to a marked change in CO₂ uptakes of the UMMOFs. The negatively contributing solvent triggered structural flexibility results in significant lowering of the CO₂ capacity in **1**, while framework **2** obtained via variation in the synthesis condition, results in a framework which shows 40% more CO₂ uptake than **1** (*Figure 1*). However, when it comes to the hydrolytic stability, framework **2** shows structural degradation when exposed to steam.

Chapter 3: Bimetallic ultra-microporous aminotriazole-oxalate frameworks showing selective CO₂ capture and stability under humid conditions

Chapter 3 focuses on a metal driven partial deprotonation of the aminotriazole linkers. This is achieved by partial replacement of the Cobalt/Nickel centres by Zinc, which is supplied in a more basic form leading to the deprotonation of the aminotriazole. This leads to the formation of more stable bimetallic UMMOFs (*Figure 2*).

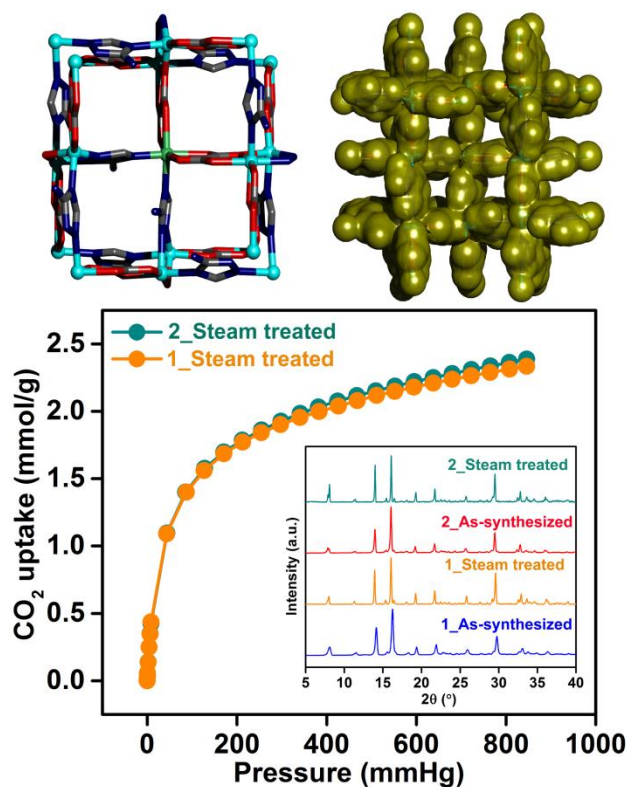


Figure 2 The structure of the bimetallic MOF and their respective CO₂ adsorption profiles after steam treatment (inset: shows the PXRD comparison of the as-synthesized sample with the steam treated one).

Synopsis

Further, we demonstrate that this inclusion of the μ -3 bridging aminotriazoles brings inherent stability to the framework. The importance of the presence of hydroxide species in the reaction medium in generating the desired aminotriazolate anions is also revealed. These frameworks with aminotriazoles in its construction show improved stability under humid conditions and exhibit higher CO₂ uptakes compared to the Co-Hatz-Ox presented in the earlier chapter (Figure 2).

Chapter 4: Enhancing carbon capture capacities of a rigid ultra-microporous MOF through gate-opening assisted by low CO₂ pressures and swivelling oxalate pillars

Chapter 4 reveals the crucial role of solvents in deciding the higher dimensional structure of the MOFs. The solvent variation approach has been exploited for tuning CO₂ uptake capacity of a family of rigid ZnAtzOx UMMOFs (Figure 3).

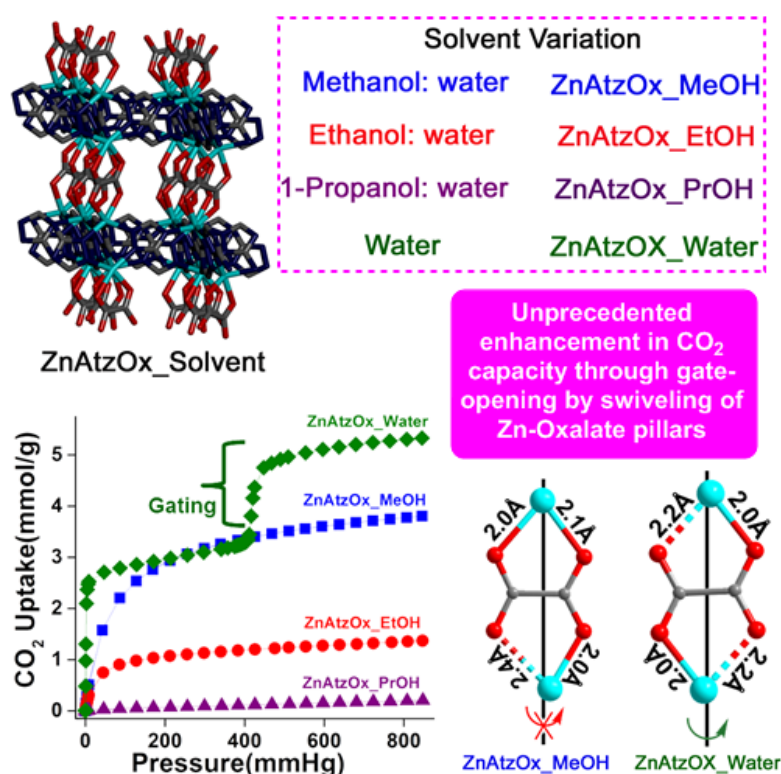


Figure 3 A representative of polymorphic ZnAtzOx framework obtained by employing solvent variations. A comparison of the CO₂ adsorption isotherms observed for this family of polymorphs. Swivelling of the Zn-Oxalate pillars leads to gating and increased CO₂ uptake in ZnAtzOX_Water phase.

Synopsis

A structure-property relationship has been presented which explains an unprecedented enhancement of CO₂ capacities via gate opening phenomena in this otherwise rigid framework. A systematic crystallographic investigation has been pursued to explain the enhanced uptake in this family of UMMOFs. Effectively, this gas induced structural changes result in a 42% enhancement in the CO₂ uptake capacity of this flexible UMMOF (ZnAtzOx_Water) as compared to its rigid counterpart (ZnAtzOx_MeOH). This happens without compromising the CO₂/N₂ selectivity, originating from its inherent molecular-sieving capability (*Figure 3*). The CO₂ uptake shown by this flexible UMMOF is among the highest reported uptakes till date, and is the highest reported for an oxalate-triazolate MOF, which makes it a potential candidate for “*Vacuum Swing Adsorption (VSA)*”.

Chapter 5: Stabilization of an unstable Zn-aminotriazolate framework via in-situ Schiff bond formation: transformation from “1st generation to 2nd generation MOF”

Chapter 5 presents an all aminotriazolate Zn-MOF, which collapses upon solvent removal. Importantly, a designed approach for the stabilization of this rather unstable Zn-aminotriazolate framework via in-situ Schiff bond formation reaction is demonstrated (*Figure 4*). A benzene templated Zn-aminotriazolate framework undergoes an irreversible framework collapse upon solvent removal and thus represents a 1st generation MOF (*Figure 4*). It has been revealed that how the pore modulation approach has led to the partition of the large pores responsible for framework collapse into smaller compartments. This has been done by introduction of the aromatic diimine struts into the structure via a Schiff bond formation between the free -NH₂ groups of the aminotriazolates and pillaring terephthalaldehyde units (*Figure 4*). This brings stability to the framework, and improves the CO₂ uptake. This Schiff bond stabilized MOF exhibits good post-adsorption stability as compared to its parent framework. Thus the findings present a generalizable and easy approach to transforming a “1st generation MOF to a 2nd generation one”.

Synopsis

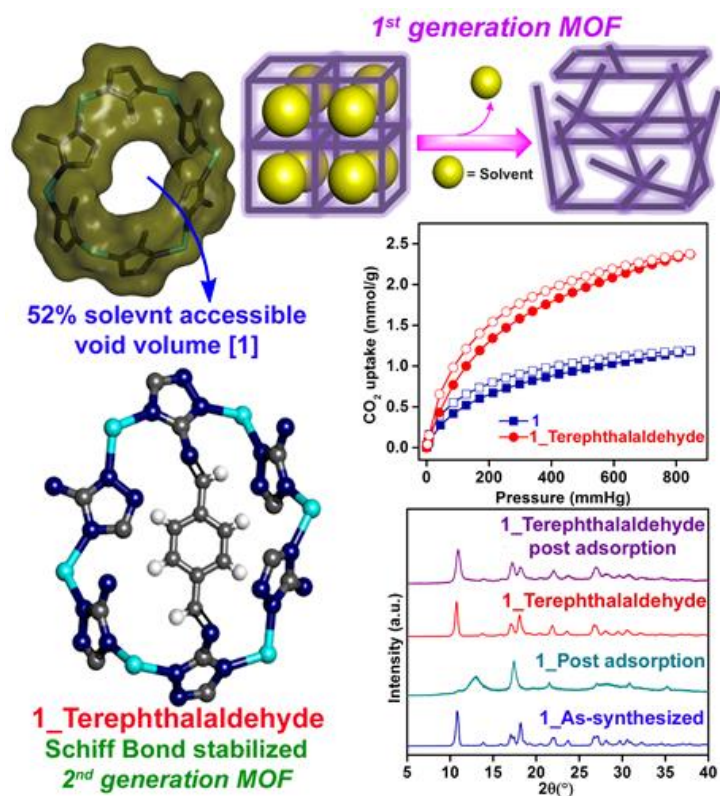
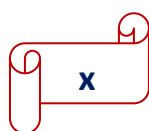


Figure 4 An unstable Zn-Atz MOF [1] which collapses upon solvent removal and its framework stabilization via in-situ Schiff bond formation. The Schiff-bond stabilized MOF representing the class of 2nd generation framework shows an enhancement of the CO₂ uptake as compared to the parent MOF 1 and also improved stability, as evident from the post-adsorption PXRD patterns.

Symbols & Abbreviations

| | |
|-----------------------|---|
| SCXRD | Single crystal X-ray diffraction |
| PXRD | Powder X-ray diffraction |
| VT-PXRD | Variable temperature powder X-ray diffraction |
| TGA | Thermo-gravimetric analysis |
| DSC | Differential Scanning Calorimetry |
| FT-IR | Fourier Transform Infrared Spectroscopy |
| NLDFT | Non-Linear Density Functional Theory |
| BET | Brunauer–Emmett–Teller |
| SADABS | Siemens Area-Detector ABSorption correction program |
| SAINT | Siemens Area-Detector Integration Software |
| GCMC | Grand Canonical Monte Carlo Simulation |
| MOF | Metal-organic framework |
| UMMOF | Ultra-microporous metal organic framework |
| CCS | Carbon Capture and Sequestration |
| LLGHGs | Long-lived greenhouse gases |
| IPCC | Intergovernmental Panel on Climate Change |
| TSA | Temperature swing adsorption |
| PSA | Pressure swing adsorption |
| VSA | Vacuum swing adsorption |
| MeOH | Methanol |
| EtOH | Ethanol |
| PrOH | 1-Propanol |
| BuOH | 1-Butanol |
| MeCN | Acetonitrile |
| DMF | N, N-dimethylformamide |
| DEF | N, N-diethylformamide |
| DMA | N,N-dimethylacetamide |
| DEE | N,N-diethylacetamide |
| DEP | N,N-diethylpropionamide |
| DPE | N,N-dipropylacetamide |
| DPP | N,N-dipropylpropionamide |
| DMSO | Dimethylsulfoxide |
| MEA | Monoethanolamine |
| DEA | Diethanolamine |
| MDEA | Methyldiethanolamine |
| TEA | Trisethanolamine |
| EN | Ethylenediamine |
| MMEN | N,N'-dimethyleneamine |
| DMEN | N,N-dimethylethylenediamine |
| H ₂ DOBDC | 2,5-Dioxido-1,4-benzenedicarboxylic acid |
| H ₂ DOBPCD | 4,4'-Dioxido-3,3'-biphenyldicarboxylic acid |
| H ₃ BTC | 1,3,5-Benzenetricarboxylic acid |
| H ₂ BPDC | 4,4'-Biphenyldicarboxylic acid |
| BPEE | 1,2-Bis(4-pyridyl)ethylene |
| BPTC | 3,3',5,5'-Biphenyltetracarboxylic acid |
| H ₃ BTTri | 1,3,5-Tri(1H-1,2,3-triazol-4-yl)benzene |
| 4,4'-BPE | Trans-1,2-bis(4-pyridyl)ethylene |



Symbols & Abbreviations

| | |
|-----------------------|--|
| AZDC | 4,4'-(Diazene-1,2-diyl)dibenzoic acid |
| SiF ₆ | Hexafluorosilicate |
| DPA | 4,4'-Dipyridylacetylene |
| 4PyC | 4-Pyridinecarboxylic acid |
| Hatz | 3-Aminotriazole/ 3-Amino-1,2,4-triazole |
| Atz | 3-Aminotriazolate/ 3-Amino-1,2,4-triazolate |
| Ox | Oxalate |
| TEPA | Tetraethylenepentamine |
| NDC | Naphthalene dicarboxylic acid |
| TPT | 2,4,6-Tri(4-pyridyl)-1,3,5-triazine |
| TPBTM | N,N',N''-tris(isophthalyl)-1,3,5-benzenetricarboxamide |
| H ₂ TP | Terephthalic acid |
| H ₂ PZDC | Pyrazine-2,3-dicarboxylic acid |
| AZPY | 4,4'-Azopyridine |
| H ₂ BTCA | Benzotriazole-5-carboxylic acid |
| 4,4'-bipy | 4,4'-Bipyridyl |
| H ₂ PYDC | Pyridine-2,5-dicarboxylic acid |
| INA | Isonicotinate |
| IUPAC | International Union of Pure and Applied Chemistry |
| HOA/ ΔH_{ads} | Heat of adsorption |
| SBU | Secondary building unit |
| scCO ₂ | Supercritical CO ₂ |
| mg | Milligram |
| g | Gram |
| °C | Degree Celsius |
| Å | Angstrom |
| min | Minutes |
| µl | Microliter |
| ml | Milliliter |
| m | Meter |
| cc/cm ³ | Cubic-centimeter |
| mmol | Millimoles |
| ppm | Parts per million |
| K | Kelvin |
| RT | Room Temperature |
| kWh | kilowatt-hour |
| 1° | Primary |
| 2° | Secondary |
| 3° | Tertiary |
| kJ/mol | Kilo-joule/mole |

Chapter 2

Reprinted (adapted) with permission from “*Eur. J. Inorg. Chem.* **2017**, 2464-2468; DOI: 10.1002/ejic.201700107” © 2017 Wiley-VCH Verlag GmbH & Co. KGaA, Weinheim.

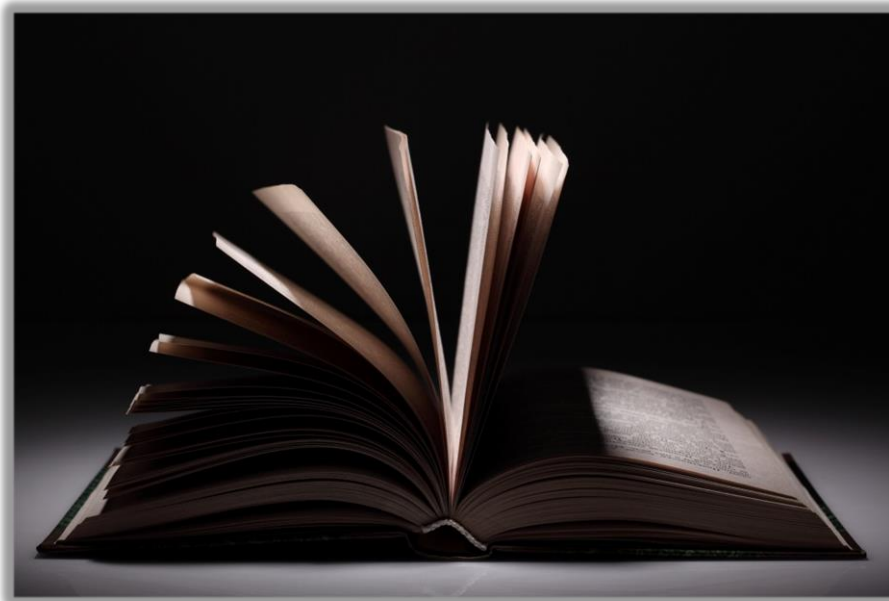
Chapter 4

Reprinted (adapted) with permission from “*Chem. Commun.* **2016**, 52, 1851-1854; DOI: 10.1039/c5cc08172f” © The Royal Society of Chemistry 2016.

Publications

- 1) Enhancing the carbon capture capacities of a rigid ultra-microporous MOF through gate-opening at low CO₂ pressures assisted by swiveling oxalate pillars
Aparna Banerjee, Shyamapada Nandi, Parveen Nasa, and Ramanathan Vaidhyanathan
Chem. Commun. **2016**, 52,1851-1854.
- 2) Ultra-microporous Metal–Organic Framework Built from Rigid Linkers Showing Structural Flexibility Resulting in a Marked Change in Carbon Dioxide Capacity
Aparna Banerjee, Debanjan Chakraborty, and Ramanathan Vaidhyanathan
Eur. J. Inorg. Chem. **2017**, 2464–2468.
- 3) Stabilization of an unstable Zinc-aminotriazolate framework via in-situ Schiff bond formation: transformation from 1st generation to 2nd generation MOF
Aparna Banerjee, and Ramanathan Vaidhyanathan
(Manuscript under preparation)
- 4) Bimetallic ultra-microporous aminotriazole-oxalate frameworks showing selective CO₂ capture and stability under humid conditions
Aparna Banerjee, and Ramanathan Vaidhyanathan
(Manuscript under preparation)

Chapter 1



Introduction

Introduction

1.1 Carbon dioxide: a global greenhouse gas

The ever-increasing level of CO₂ concentration in the atmosphere is well known major threat to the environment.¹⁻⁴ These emissions which shoot out mainly from the burning of fossil fuels (coal, natural gas and oil) will continue to progress in the coming years due to the rapid industrialization making it an intractable problem for the mankind.¹⁻⁵ Ideally use of alternative cleaner energy sources, instead of depending upon the existing carbon based sources would be an efficient way of living for the coming generations.⁶⁻⁸ But all such attempts are still in its infancy and some important modifications are to be done to make it possible at the industrial scale. Thus the Carbon Capture and Sequestration (CCS) technique plays a pivotal role in controlling the CO₂ concentration by capturing it from the emission sources.⁹

During the pre-industrialization time, the atmospheric carbon sink was considered to be enough to control the amount of carbon-dioxide produced in the atmosphere. However after industrial revolution, there is an escalation in the atmospheric CO₂ level, posing a major concern to the environment.¹⁰ More than three times increase in the CO₂ level has been reported since the past two decades. The volumetric CO₂ concentration in atmosphere during 2000, 2010 and 2011 was 368 ppm, 388 ppm and 390 ppm respectively (*Figure 1.1*).^{10,11} As per the report in the Global greenhouse bulletin, the earth's CO₂ concentration reached as high as 400 ppm in 2015 (*Figure 1.1*), accounting for a 2 ppm rise every year and at least 144% increase in the CO₂ level as compared to the pre-industrialization time (between 1750 to 2015).¹² It has also been stated that 2016 is the first year in which the CO₂ concentration remained 400 ppm throughout the year.¹² Further, the annual greenhouse gas index showed that in the past decade the radiative emission instigated by the long-lived greenhouse gases (LLGHGs) has increased by 37% in which 80% is only accounted from CO₂.¹⁰⁻¹² The Intergovernmental Panel on Climate Change (IPCC)⁴ report states that the carbon dioxide concentration in 2100 may reach up to 570 ppm, which will result in an average increase in the mean global temperature by 1.9°C (274.9 K).¹³⁻¹⁵

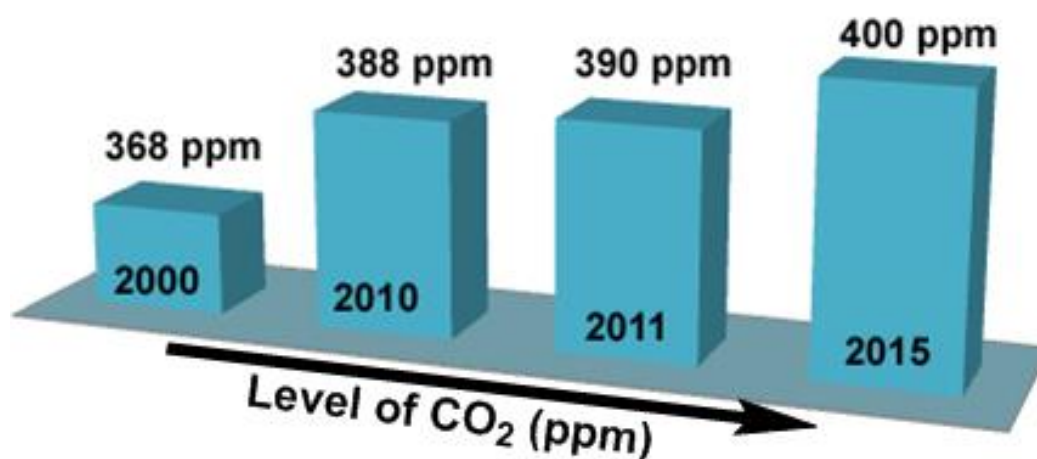


Figure 1.1 Pictorial representation of the continuously increasing CO₂ level in atmosphere.

Production of electricity is one of the major man-made activities adding up to the atmospheric CO₂ level. The electricity generation from the combustion of coal causes 30-40% of the total anthropogenic CO₂ emissions.^{16,17} Further, at the global scale it is foreseen that, the electricity generation from coal and gas will upsurge from 11.8 trillion kWh in 2007 to 21.9 trillion kWh in 2035.^{18,19} Establishment of the CO₂ capture materials within the coal and gas fired power plants will be a vital step in efficient and selective capture of CO₂ from the industrial effluents, also known as flue gas. This can significantly help in mitigating the global greenhouse gas concentration.⁹

Carbon capture and sequestration (CCS) process involves the selective capture of CO₂ from fuel combustion or industrial process, followed by which the pure CO₂ is compressed to a supercritical fluid and is transported and injected into the geological formations such as salt water aquifers or depleted oil reservoirs.²⁰⁻²² This sequestered CO₂ is further used in enhanced oil recovery.^{21,22} As an alternative measure, this recovered CO₂, could be used as a reactant in different types of chemical conversion and also in food industries.²³⁻²⁸ Although these provide alternative paths for the removal of the excess atmospheric CO₂, they are not very long lasting owing to the rising growth rate of CO₂ emission.¹⁰⁻¹⁵ A more favourable scenario would be the conversion of these captured CO₂ into a fuel for transportation, provided some energy efficient conversion method based on the renewable sources of energy could be developed in the near future.²⁹⁻³⁴

The most significant challenge associated with the CCS is the carbon capture from the post-combustion sources due to the large cost of energy associated with the regeneration of the traditional sorbents.³⁵⁻³⁸ The traditionally employed technologies, the use of alcoholamines for CO₂ sequestration from flue gas streams, causes an energy penalty of approximately 30% of the total power generated.³⁹

This is mainly needed for the heating of a large amount of water for the dissolution of the amine sorbents. Another challenging feature to be kept in mind for the selective CO₂ capture from flue gas is the relatively lower concentration of CO₂ (15-16%) as compared to N₂ (73-77%), which originates due to the combustion of the coal in the air.³⁵⁻³⁹ The typical concentration of CO₂ and N₂ along with the other constituents of flue gas is tabulated below (*Table 1.1*).³⁵⁻³⁹ Hence, there is an urgent need for exploration of novel materials for the selective capture of CO₂ from flue gas, which must have high affinity for the CO₂ and at the same time low energy penalty for regeneration.

Table 1.1 Typical composition for post-combustion flue gas generated from a coal-fired power plant.³⁵

| Molecule | Concentration by volume |
|------------------|-------------------------|
| N ₂ | 73-77% |
| CO ₂ | 15-16% |
| H ₂ O | 5-7% |
| O ₂ | 3-4% |
| SO ₂ | 800 ppm |
| SO ₃ | 10 ppm |
| NO _x | 500 ppm |
| HCl | 100 ppm |
| CO | 20 ppm |
| Hydrocarbons | 10 ppm |
| Hg | 1 ppm |

1.2 Carbon capture technologies

The three major technologies employed for the CO₂ capture from the coal and gas-fired power plants are oxy-fuel combustion, pre-combustion and post-combustion CO₂ capture (*Figure 1.2*).^{9,35} The choice of a particular capture system depends

upon the CO_2 concentration in the gas stream, pressure of the gas stream and the type of the fuel used.^{9,35}

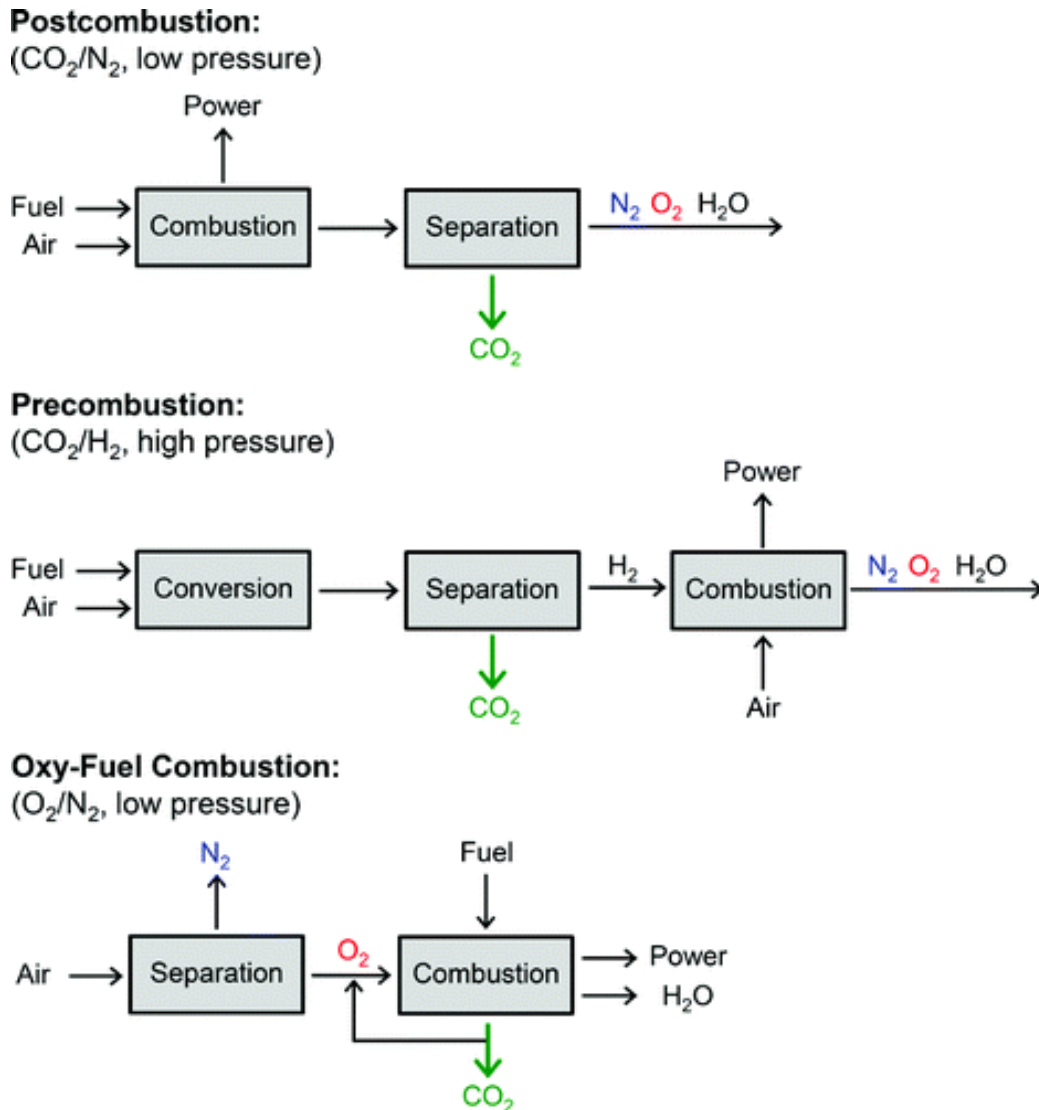


Figure 1.2 Schematic of the various types of CO₂ capture technologies. The processes for post-combustion capture, pre-combustion capture, and oxy-fuel combustion, which are described in detailed in the following sections. The main separation required for each type of process is indicated next to each of the headings in parentheses. (Adapted with permission from “Sumida et al. *Chem. Rev.* **2012**, 112, 724” © 2011 American Chemical Society.)

1.2.1 Oxy-fuel combustion

In oxy-fuel combustion, the carbon based fuel is combusted in a clean O₂ environment and almost pure CO₂ is generated as the combustion product. This process is almost similar to that of post-combustion technique with a difference that in this case flue gas generated has more CO₂ concentration and no N₂

concentration. The most significant advantage of this process is that the major combustion product is CO_2 , thus makes carbon capture process much easier.^{35,40-43}

1.2.2 Pre-combustion CO_2 capture

Pre-combustion CO_2 capture refers to the removal of the CO_2 from the fossil fuel sources by gasification prior to the combustion.⁴⁴⁻⁴⁵ This results in zero CO_2 production during the combustion process. In this regard, the gasification of coal takes place at high temperature and pressure to produce syn-gas (a mixture of H_2 , CO , CO_2 and H_2O).⁴⁴⁻⁴⁷ Consequently, a mixture of H_2 and CO_2 is produced at high pressure (5-40 bar) and temperature ($\sim 40^\circ\text{C}$; 313 K) via water gas shift reaction.⁴⁸ Thus pre-combustion CO_2 capture refers to selective capture of CO_2 from CO_2/H_2 mixture at high pressures, followed by which the H_2 is combusted in power plants for electricity generation.⁴⁴⁻⁴⁸

1.2.3 Post-combustion CO_2 capture

Post combustion CO_2 capture involves the selective CO_2 capture from flue gas streams. Flue gas is produced by the burning of fossil fuels in the air. Due to the combustion in air, it majorly consists of N_2 (~ 0.75 bar), whereas CO_2 is present at comparatively low partial pressures (~ 0.15 bar).^{9,35-37,49} Other minor constituents of flue gas are H_2O , CO , O_2 , NO_x and SO_x (*Table 1.1*). The total pressure for the release of flue gas stream is ~ 1 bar. Importantly, the material used for CO_2 separation from flue gas must have high affinity for CO_2 over the other flue gas components, fast regeneration of the capture material with less energy penalty, long term stability under working conditions and high diffusion rates for CO_2 .

The selective CO_2 capture in post-combustion process is more challenging as compared to oxy-fuel combustion and pre-combustion process owing to dilute CO_2 concentrations ($\sim 5-15\%$) present in the flue gas streams.⁵⁰ Many materials are known which show higher uptake at high CO_2 pressures due to their high surface areas. But not all these materials are best suited for post-combustion CO_2 capture as in this case the partial pressure of CO_2 is considerably less as compared to N_2 .^{9,35} Hence, to find relevant materials for post-combustion CO_2 capture, one should see the low pressure CO_2 uptake, preferably near 0.15 bar. Further, the CO_2/N_2 isotherm

comparisons at the initial low pressure region could give a more real outlook from the performance point of view of the material.

1.3 Significant parameters for CCS from flue gas

1.3.1 Enthalpy of adsorption

Enthalpy of adsorption is one of the most significant parameters and is crucial for effective mapping of the adsorbent materials for practical use as CO₂ adsorbents.³⁵ This parameter defines the affinity of CO₂ molecules with the framework sites. If the value is too high, it refers to a very strong interaction between the adsorbate-adsorbent and at the same time the regeneration cost of the material is considerably increased.^{35,51} On the other hand, a low value for enthalpy of adsorption puts a question on the purity of the regenerated CO₂. Hence an optimum value of this parameter is very decisive in attaining both selectivity and cost effective regeneration of the material.⁵¹⁻⁵⁴ This is termed as isosteric heat of adsorption (HOA/ ΔH_{ads}) and is expressed with respect to CO₂ loadings. The value obtained at the zero loading states the interaction of the CO₂ molecules with the most favorable sites of the bare framework.

1.3.2 CO₂ Selectivity

High CO₂ selectivity is desirable for carbon capture application. The selective separation of molecules depends upon two factors: a) kinetic separation and b) thermodynamic separation.^{35,55-57} The kinetic separation is based on size exclusion or molecular sieving effect. For CO₂/N₂ separation the kinetic diameters are almost similar (*Table 1.2*).⁵⁵⁻⁵⁷ Thus the sorbent should have appropriate pore dimension such that it can allow the diffusion of a particular component while blocking the others of the flue gas streams. While the difference in the affinity of various components of flue gas to be adsorbed at the active sites of the sorbent give rise to adsorptive or thermodynamic separation.^{58,59} For physisorption, various parameters are responsible such as polarizability or quadrupole moment of the gaseous molecules (*Table 1.2*). The CO₂ having high polarizability as well as high quadrupole moment as compared to N₂, and thus has more affinity to get adsorbed at the polarized surfaces.^{58,59}

Table 1.2 The physical parameters of different gases important to carbon-dioxide capture processes.³⁵

| Molecule | Kinetic Diameter (Å) | Polarizability (10^{-25} cm^3) | Dipole moment ($10^{-19} \text{ esu}^{-1} \text{ cm}^{-1}$) | Quadrupole moment ($10^{-27} \text{ esu}^{-1} \text{ cm}^{-1}$) |
|------------------|----------------------|--|---|---|
| H ₂ | 2.89 | 8.04 | 0 | 6.62 |
| N ₂ | 3.64 | 17.4 | 0 | 15.2 |
| O ₂ | 3.46 | 15.8 | 0 | 3.9 |
| CO | 3.76 | 19.5 | 1.10 | 25.0 |
| NO | 3.49 | 17.0 | 1.59 | |
| H ₂ O | 2.65 | 14.5 | 18.5 | |
| H ₂ S | 3.60 | 37.8 | 9.78 | |
| CO ₂ | 3.30 | 29.1 | 0 | 43.0 |
| NO ₂ | | 30.2 | 0 | |

1.3.3 Humid stability and recyclability of the material

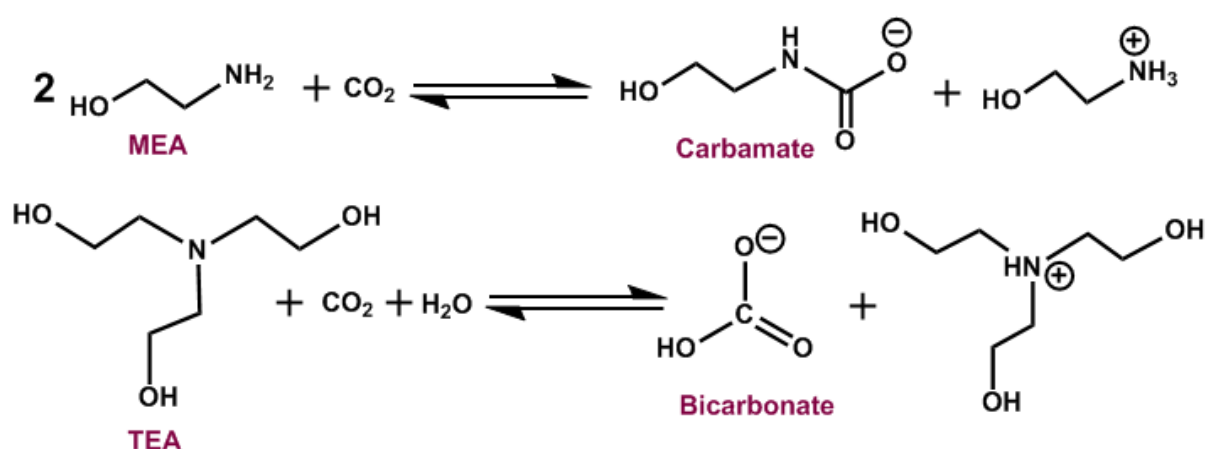
Apart from the initial screening of the CO₂ selective sites in the framework, another factor which should be taken into account is the moisture stability of the sorbent materials. Flue gas streams consist of considerable amount of water vapour (5-7% by volume).⁶⁰⁻⁶³ Although, there might be a possibility of partial dehumidification of the flue gas but the complete dehydration is costly and is generally not likely to be done before CO₂ adsorption. Hence the humid stability of the sorbents is a crucial factor to be considered.^{60,61}

1.4 Traditional techniques used for post-combustion CO₂ capture

Current technologies involve the use of aqueous amines as CO₂ scrubbers. This includes the aqueous solutions of monoethanolamine (MEA), diethanolamine (DEA), or methyldiethanolamine (MDEA) as the adsorbents for selective CO₂ capture.^{35,39,64-66} Although these have a high efficiency for CO₂ capture as high as 98%, but the commercial development of this technique is less certain. The high energy penalty arises from two factors: a) the energy needed for heating the large amount of water for dissolution of amines and b) the energy required for the breaking of the C-N chemical bond of the carbamate or bicarbonate species formed due to the interaction

between amines and CO₂.⁶⁶ This process carries an overall energy penalty of ~30% of the total energy production at the power plant units.⁶⁴⁻⁶⁶

The interaction between the amines and CO₂ results in an acid-base reaction and causes the formation of carbamate or bicarbonate species depending upon the type of amine used (*Scheme 1.1*).^{35,66} Reaction of CO₂ with MEA generates carbamate species whereas the reaction of CO₂ with triethanolamine (TEA) generates unstable bicarbonate species, which makes the reversible reaction in the latter case more favourable and so the regeneration of the adsorbed CO₂ (*Scheme 1.1*).



Scheme 1.1 The reaction schemes showing the formation of Carbamate (Top) and Bicarbonate (Bottom) products from the reaction between CO₂ with MEA and TEA respectively. (Adapted with permission from “Sumida et al. *Chem. Rev.* **2012**, *112*, 724” © 2011 American Chemical Society.)

However, in general the energy requirement for the regeneration of the adsorbed CO₂ falls in the decreasing order of 1° > 2° > 3° amines.³⁹ Although with the actual capture systems there could be some exceptions depending upon the concentration of the amines.³⁵ Certainly the interaction between the aqueous amines and CO₂ fall under the chemisorption regime with the enthalpy of absorption falling in the range of 50 to 100 kJ/mol at 298 K⁶⁷ and further this class of materials also show low CO₂ loadings. Apart from this there are few other major disadvantages associated with the use of aqueous alkanolamines as CO₂ adsorbents at large scale.⁶⁸ These are unstable to heat, hence limiting the regeneration temperature and 100% regeneration of the capture material. Further, over time, these liquid amines

decompose affecting their overall performance and finally, their corrosive nature affects the walls of the container vessels.⁶⁸

Due to these limitations for the use of amine scrubbing technologies as an efficient way for CO₂ capture from flue gas, the development of new generation CO₂ capture technologies are in demand.⁶⁹⁻⁷¹ There are two major goals to be taken care of for constituting an efficient CO₂ capture material from flue gas: a) efficient CO₂ interaction at low pressure region and b) reduction of the cost for the regeneration of the adsorbent. There are several solid materials such as zeolites, activated carbon and metal organic frameworks (MOFs) which fall under the class of physical adsorbents, has come into considerable attention from the researchers since the past few decades as efficient CO₂ capture materials.

1.5 Solid sorbents for post-combustion CO₂ capture

Solid Sorbents are a class of materials that have been extensively studied for CO₂ capture application.⁷²⁻⁷⁶ The regeneration of this class of materials takes place via three different procedures (*Figure 1.3*): a) temperature swing adsorption (TSA), b) pressure swing adsorption (PSA) and c) vacuum swing adsorption (VSA).^{5,9,35,39,51}

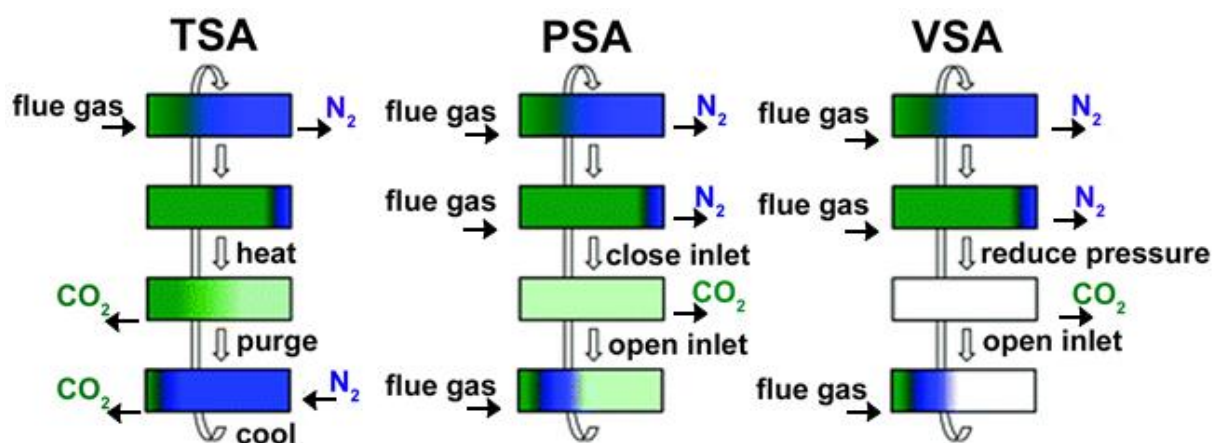


Figure 1.3 Schematic diagrams of idealized temperature swing adsorption (TSA), pressure swing adsorption (PSA), and vacuum swing adsorption (VSA) processes for regenerating solid adsorbent in a fixed-bed column. (Adapted with permission from “Sumida et al. *Chem. Rev.* **2012**, *112*, 724” © 2011 American Chemical Society.)

Instead of applying these processes separately, sometimes these are combined and are used for regeneration of the adsorptive material. In pilot plants the solid sorbents are packed into a large fixed bed column. For the regeneration of the

adsorbed gas the column undergoes the following processes. In TSA the adsorbed gas is released by increasing the temperature of the bed,^{9,51,77} whereas in PSA and VSA the adsorbed gas is released by lowering the pressure of the bed.^{77,78-85} The difference between PSA and VSA is that in the former the pressure is reduced to ambient level whereas in the latter one the pressure is reduced to sub-atmospheric level by applying vacuum.^{84,85}

1.5.1 Zeolites

Under the class of solid sorbents for the aspect post combustion CO₂ capture, aluminosilicates, more commonly known as zeolites, have been thoroughly explored.⁸⁶⁻⁹³ For example Zeolite-13X showed a relatively higher BET surface area of 726 m²/g and micropore volume of 0.25 cm³/g at room temperature, suggesting a promising candidate for CO₂ capture at room temperature.⁹⁴⁻⁹⁷ Due to the lack of any sort of chemical interaction between the adsorbate-adsorbent, it could be anticipated that the regeneration cost of this class of adsorbent material will not be as high as in the case of alcoholamines.^{35,98} Further, it has been perceived that on varying the Si/Al ratio in zeolites, their CO₂ adsorptive properties could be tuned and which in turn has a crucial role in deciding the selectivity and cost of regeneration for the adsorptive material.^{35,98-101} It has been observed that using zeolites instead of alcoholamines for the post-combustion CO₂ capture in small scale pilot plants is more feasible in terms of the rapidness of the CO₂ adsorption and also much reduced energy penalty for the process to take place.¹⁰² However, there are some practical limitations to the use of zeolites as the adsorbent in the post-combustion CO₂ capture.^{103,104} The water vapour present in the flue gas stream along with CO₂ and N₂ saturates the zeolitic pores, resulting in lowering of the actual CO₂ uptake capacity over the time.^{103,104}

1.5.2 Activated carbons

Another class of porous solid sorbents comprises of activated carbons.^{9,35,39,105-107} These are amorphous in nature and are prepared by pyrolysis of different carbon containing materials like polymers, fly ash, biomolecules etc.¹⁰⁸ A huge advantage with this class of material lies to the fact that the cost of preparation is very low. The production of this class of material consists of two consecutive steps, i.e.

carbonization followed by activation.¹⁰⁵⁻¹⁰⁸ Activated porous carbons are used in several industrial applications such as water treatment, monitoring air pollution and gas purification. These materials show high CO₂ uptake at high pressures owing to their large surface areas.³⁵ However, at the same time due to lack of molecular sieving, they prove to be of less utility as compared to zeolites for the selective CO₂ capture from the flue gas streams. Due to which the activated porous carbons are more suitable candidates for CO₂ sequestration from pre-combustion process than the post-combustion process.^{35,39}

1.6 Metal organic frameworks (MOFs)

Since past two decades the area of metal organic framework has attracted considerable amount of interest from researchers.¹⁰⁹⁻¹¹⁴ Their modular structure combined of metal nodes (ions or clusters) and organic struts and presence of potential voids makes them applicable for various fields like gas storage, molecular separation, heterogeneous catalysis, drug delivery, proton conductivity and magnetism etc. (Figure 1.4).¹¹⁵⁻¹¹⁷

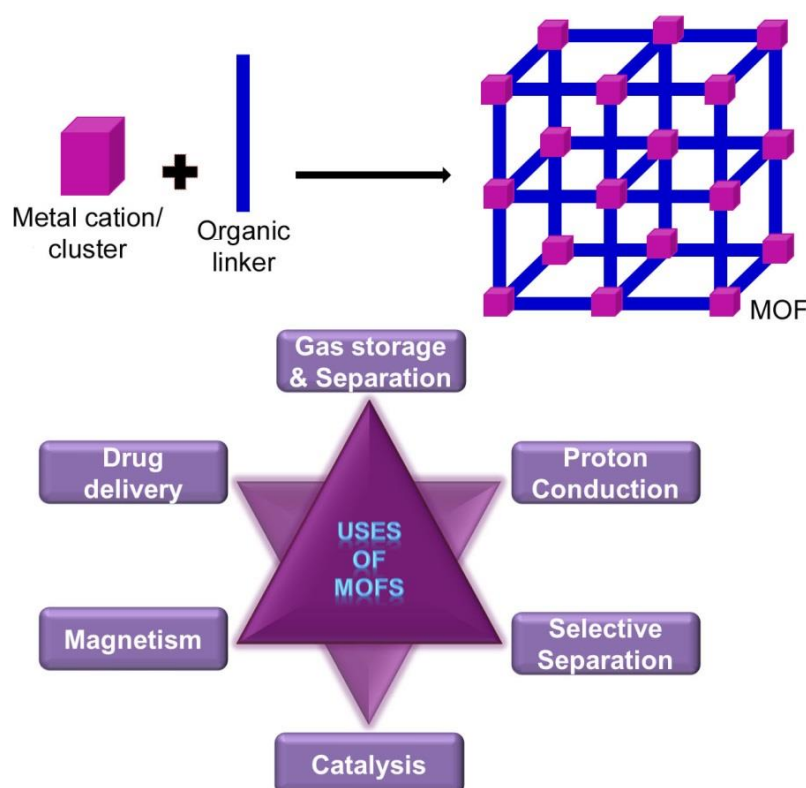


Figure 1.4 Pictorial representation of the periodic structure of MOFs constructed from the smart choice of metal ions/clusters with organic linkers and the some of the potential uses of MOFs.

Interestingly, owing to their ultra-high porosity with free volume ~90%, high surface area and potential scalability, MOFs become immensely attractive from the industrial point of view.^{115,117,118} The uniqueness of these materials lies in the possibility of tailor made synthesis by a smart choice of metal ion and ligands, making them more versatile than other periodic solid sorbents like zeolites.¹¹⁹⁻¹²⁴

A systematic design and construction of a family of dicarboxylate based IRMOFs (Iso-Reticular MOFs) have been reported by Yaghi and co-workers.¹²⁵ They have shown that pore dimensions for the MOFs could be altered by varying the linker's length and functionalities, without any variation in the overall MOF morphology. The pore size of the IRMOF series falls within the range of 3.8 to 28.8 Å (*Figure 1.5*).¹²⁵ Depending upon the pore dimensions, the porous materials are classified by IUPAC. According to this, for microporous material, $d < 20$ Å; for mesoporous $20 \text{ Å} < d < 500 \text{ Å}$; and for macroporous $d > 500 \text{ Å}$ (where, d is the pore dimension).¹²⁶⁻¹²⁹ Recently, the nanoporous materials are referred to be the one having pore dimensions in the range of $10 \text{ Å} < d < 100 \text{ Å}$ and ultra-microporous frameworks are treated as a sub-class of microporous frameworks having pore dimensions below 6 Å.¹²⁶⁻¹²⁹

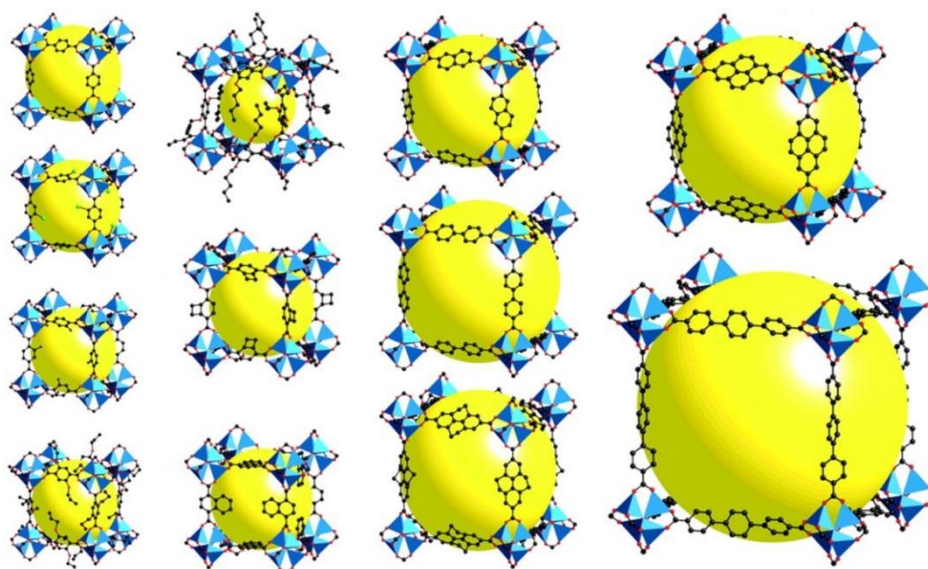


Figure 1.5 Single crystal x-ray structures of IRMOF-series. Colour code: Zn (blue polyhedra), O (red spheres), C (black spheres), Br (green spheres), amino-groups (blue spheres). The large yellow spheres represent the largest van der Waals spheres that would fit in the cavities without touching the frameworks. All Hydrogen atoms have been omitted, and only one orientation of disordered atoms is shown for clarity ("From Eddaoudi et al. *Science* **2002**, 295, 469. Reprinted with permission from AAAS.").

MOFs are synthesized by a wide range of method,¹³⁰⁻¹³³ out of which solvothermal method is the most commonly used (*Figure 1.6*).¹³¹ Solvent plays a crucial role in deciding the structure of the MOF in addition to their purity and scalability. Solvent modifications can produce MOFs of same chemical compositions but with altered structure, ligand orientation, pore size etc.^{130,134-142} Although MOFs with different pore sizes has different utilizations, but in the context of CO₂ capture from flue gas, ultra-microporous MOFs are considered to be the best ones.^{120,143-149} This is due to the fact that with such a confined pore dimensions these frameworks would show effective molecular sieving effect, which is highly beneficial for CO₂/N₂ separation under the post combustion working conditions.¹⁴⁶⁻¹⁴⁸

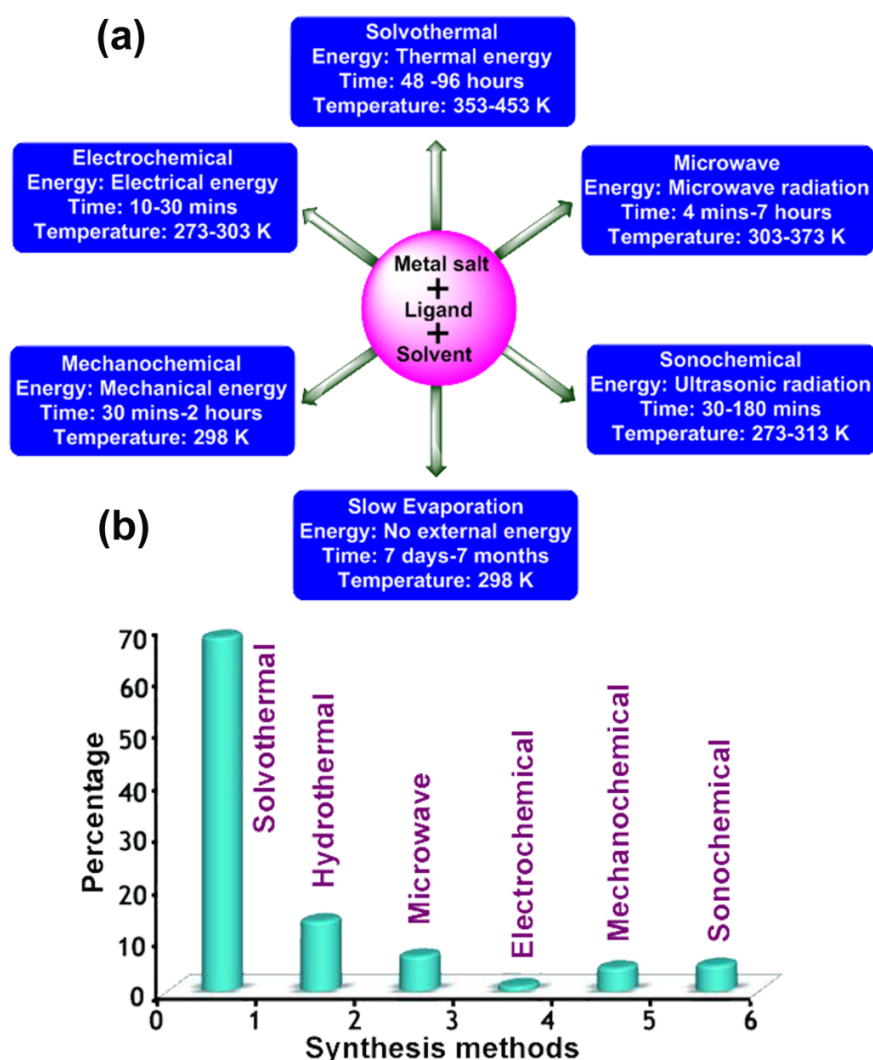


Figure 1.6 (a) Synthesis conditions commonly used for MOF preparation; (b) indicative summary of the percentage of MOFs synthesized using the various preparation routes (Adapted with permission from “Dey et al. *Acta Cryst.* **2014**, *B70*, 3” © 2014 International Union of Crystallography.)

Apart from the classification based on pore size, MOFs are further classified as 1st, 2nd and 3rd generations subjecting to their framework behaviour (Figure 1.7).¹⁵⁰ As mentioned above MOFs consists of voids filled by guest solvent molecules. The 1st generation MOFs shows irreversible framework rupture upon guest removal with no permanent porosity which makes them practically of no use in the context of gas adsorption. Second generation MOFs, considered analogous to zeolites are the one with the most stable and robust framework, which undergoes no change in the structural integrity upon solvent removal. Lastly, the third generation frameworks are the dynamic frameworks which show a reversible response to external stimuli like temperature, pressure and solvent etc.¹⁵⁰ A detailed description of this type of frameworks and their role in CO₂ capture from flue gas has been provided in the later part of the text.

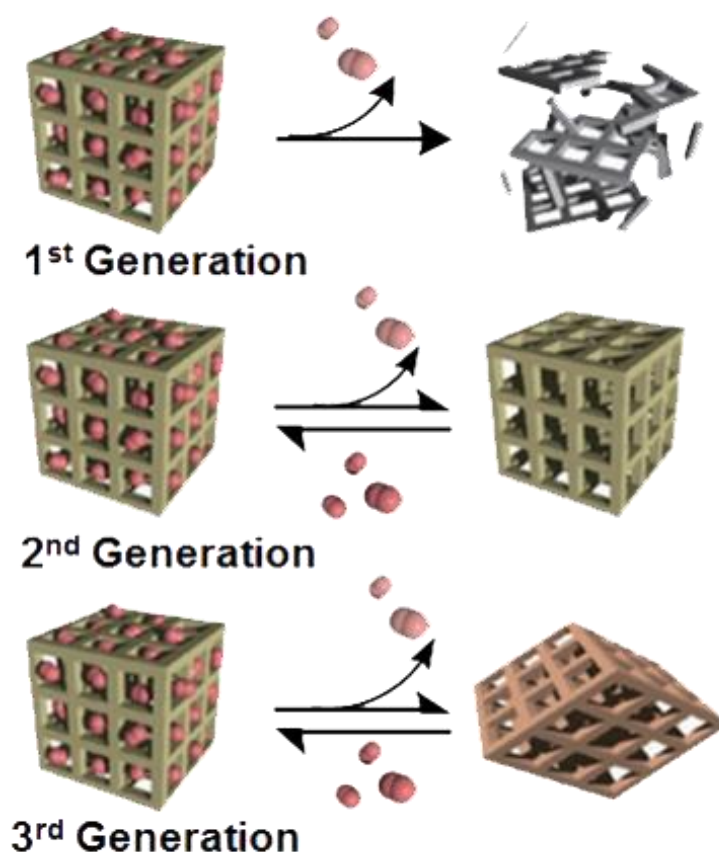


Figure 1.7 Classification of porous coordination polymers into three categories. The first-generation materials collapse on guest removal. The second-generation materials have robust and rigid frameworks, and retain their crystallinity when the guests are not present in the pores. The third-generation materials are transformable accompanied by structural transformation. (Adapted with permission from “Horike et al. *Nat. Chem.* **2009**, *1*, 695” © 2009 Macmillan Publishers Limited.)

A literature review for some already reported MOFs is presented here with their utility as CO₂ adsorbing material from flue gas. These materials have been subdivided into three major sections: a) MOFs with open metal sites, b) MOFs with Lewis basic site, c) Flexible frameworks.

1.6.1 MOFs with open metal sites

During MOF synthesis, the metal center can coordinate with the organic ligand or solvent molecules.¹⁵¹⁻¹⁵³ A careful removal of these coordinated solvent molecules generates unsaturated metal centers which are highly advantageous for CO₂ adsorption (*Figure 1.8*).^{151,154} These open metal centers act as Lewis acidic sites causing strong polarization of the adsorbent gas molecules and hence favoring high CO₂ capture abilities.¹⁵⁴ The presence of such bare metal sites lends the opportunity for the further functionalization of the MOFs.¹⁴⁷

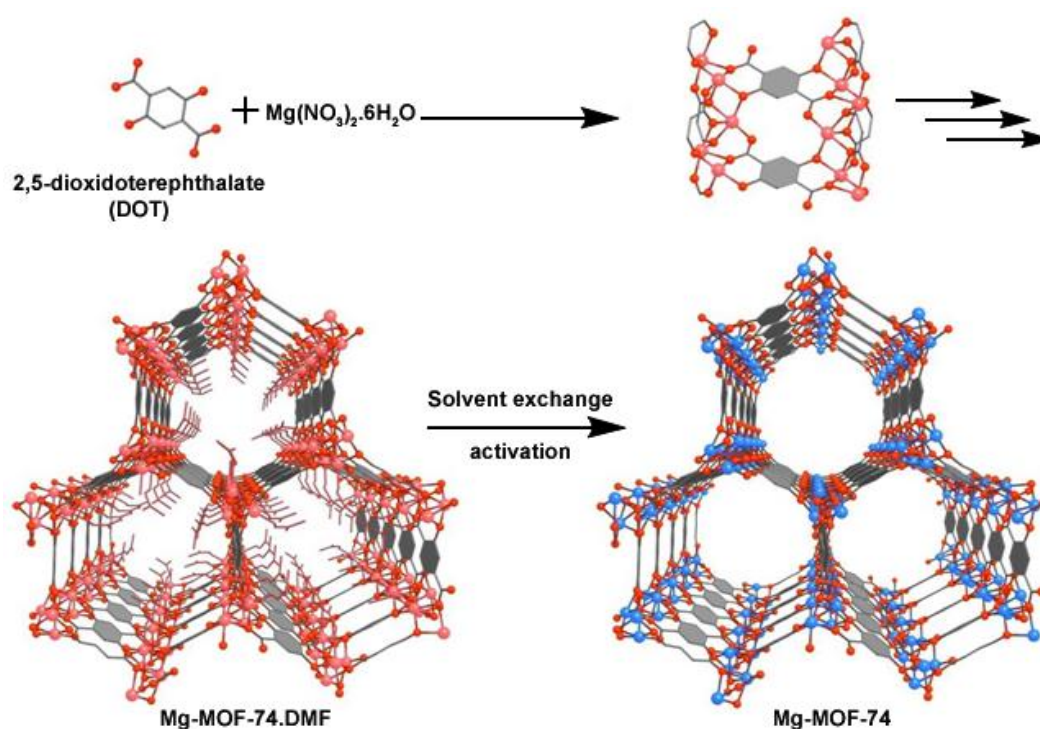


Figure 1.8 Single crystal structure of Mg-MOF-74, formed by reaction of the DOT linker with Mg(NO₃)₂·6H₂O. The structure consists of 1D inorganic rods linked by DOT to form linear hexagonal channels. C atoms are shown in grey, O atoms in red, 6-coordinate Mg atoms and terminal ligands in pink and 5-coordinate Mg atoms in blue. H atoms and terminal ligands on the fragment at top right are omitted for clarity (Adapted with permission from "Britt et al. *Proc. Natl. Acad. Sci. U. S. A.* **2009**, *106*, 20637").

The M-MOF-74 series (also known as M/dobdc, $M = \text{Mg}^{2+}$, Ni^{2+} , Co^{2+} and Zn^{2+} ; dobdc: 2,5-dioxido-1,4-benzenedicarboxylate) provides an excellent example of frameworks containing open metal sites.^{151,155-157} Due to the favorable CO_2 interaction with the open metal sites of the framework, these M-MOF-74 proves to be highly efficient in performing selective CO_2 capture from flue gas and shows high CO_2 capacity at low to moderate pressure regimes.¹⁵⁵⁻¹⁶² However, role of the open metal centers could be understood from the fact that despite being isostructural, difference in the CO_2 uptake capacities have been noticed for different metal centers.^{147,163} Among the whole series, Mg-MOF-74 showed the highest CO_2 uptake, with capacity as high as 5.87 mmol/g at 0.15 bar at 303 K (Figure 1.9) and is still treated as benchmark material for CO_2 capture from flue gas.^{51,164}

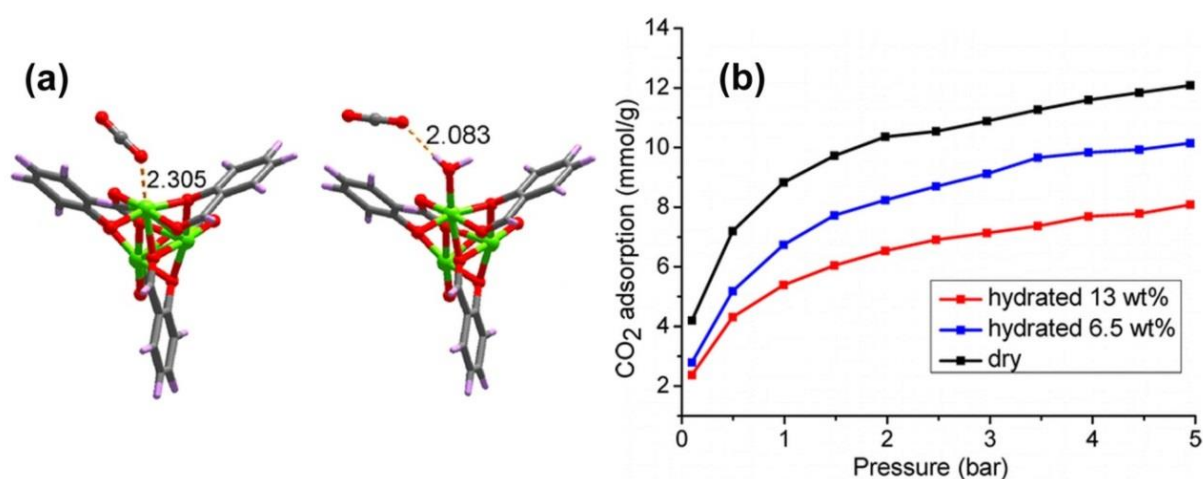


Figure 1.9 (a) Optimized structures of the Mg-MOF-74 cluster with (right) and without (left) water coordination interacting with CO_2 (Color scheme: Mg atoms, green; O atoms, red; C atoms, gray; and H atoms, lavender.) and (b) GCMC simulated adsorption isotherms for CO_2 in dry and hydrated Mg-MOF-74 at 298 K (Adapted with permission from “Yu et al. *J. Phys. Chem. C* **2013**, *117*, 3383” © 2013 American Chemical Society.)

The higher CO_2 uptake for Mg-MOF-74 has been attributed to the more ionic character of the Mg-O bond which facilitates a greater degree of polarization of the adsorbate molecules, i.e. CO_2 .^{147,165,166} Further, $\text{Mg}_2(\text{dobpdc})$ (dobpdc: 4,4'-dioxido-3,3'-biphenyldicarboxylate) has also been constructed by ligand expansion technique. This material with wider porous channel as compared to its “bdc” analogue also proved to be very efficient CO_2 capture material at low partial pressures (~ 0.15 bar, 298 K) with a 4.85 mmol/g of CO_2 uptake.¹⁶⁷ In spite of looking like a very promising candidate for CO_2 separation from flue gas, M-MOF-74

frameworks gets affected from the trace amount of contaminants present in the flue gas streams such as SO_2 , SO_3 and hydrates, due to their strong affinity for the adsorption sites triggering a binding competition for the CO_2 (Figure 1.9).^{168,169}

One of the interesting feature noticed in some of the open metal frameworks is that in the presence of water, sometimes, their CO_2 adsorbing capacity gets noticeably enhanced.¹⁷⁰ This could be seen in the case of one of the mostly studied open metal framework HKUST-1, made up of paddlewheel $\text{Cu}_2(\text{COO})$ units connected through btc^{3-} linkers.¹⁷⁰ Interestingly, in the presence of one molecule of water per two Cu atom sites accounting for $\sim 4\%$ of relative humidity, the CO_2 capacity shoots up to 8 mmol/g at 1 bar, 298 K as compared to 5 mmol/g for the dry framework under similar conditions (Figure 1.10).¹⁷⁰

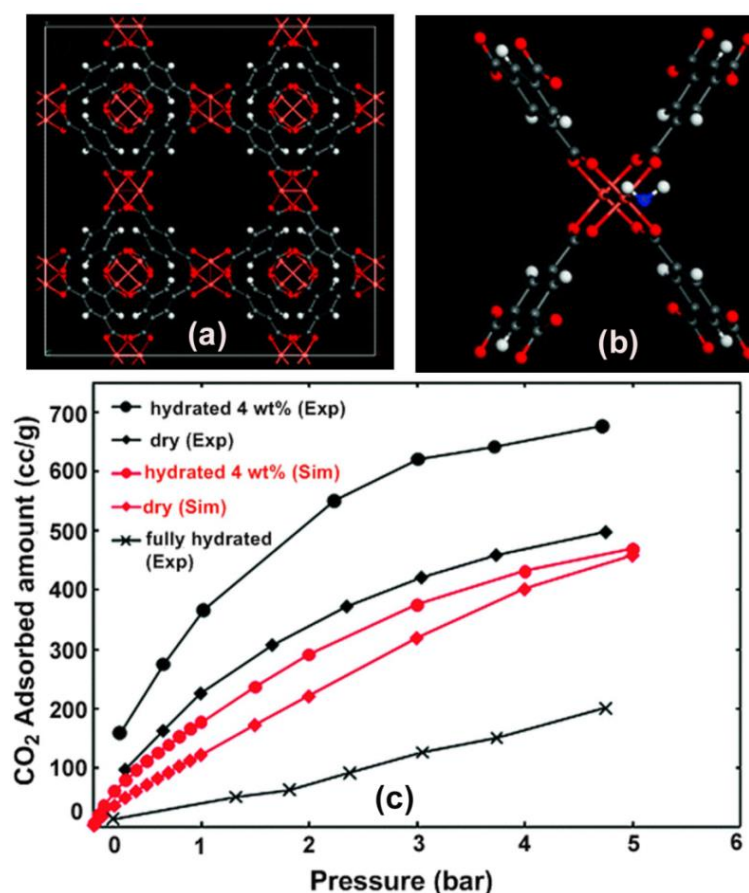


Figure 1.10 (a) Dry Cu-BTC unit cell and (b) hydrated Cu-BTC (4 wt %) with coordinated water molecule from DFT (Colour Code: Copper: orange, Oxygen: red, carbon: grey and hydrogen: white. The oxygen atom of the coordinated water molecule is shown in blue.) (c) Simulated and experimental adsorption isotherms for CO_2 at 298 K in Cu-BTC with different water contents (Adapted with permission from from "Yazaydin et al. *Chem. Mater.* **2009**, 21, 1425" © 2009 American Chemical Society.)

This uptake was four times more than that of the capacity shown by Zeolite 13X.^{147,170} This increase in uptake has been attributed to the electrostatic interaction between the CO₂ molecules and bound water molecules. However, with 30% relative humidity accounts for a 75% decrease of the CO₂ uptake followed by only 1 mmol/g of CO₂ uptake remaining in case of fully hydrated form.^{35,170-172}

Interestingly, this phenomenon has been observed to be case sensitive and response distinctly to different unsaturated metal centers. Yu et al. studied the effect of water on the CO₂ adsorption abilities of M-HKUST-1 series (M= Zn, Co, Ni and Mg).¹⁷³ It was observed that for metal centers Zn, Ni and Co, both CO₂ capture capacity and selectivity enhances with increase in water content relative to their dry frameworks. The reason for this is the increase in columbic nature of interaction taking place between the electric field created by the water molecules and the quadrupole moment of CO₂ and this was consistent with the effect of water on the CO₂ adsorption for the parent framework HKUST-1 (with Cu metal center). However, at high pressure regime, the water content showed a dramatic decrease in the CO₂ uptake for Mg-HKUST-1, although the low pressure CO₂ capture for the hydrated form remains higher than its corresponding dry framework. This has been attributed to the increase of both columbic and non-columbic interactions in case of Mg-HKUST-1 in the low pressure region, whereas in the high pressure region the increase in both columbic and non-columbic interaction drops significantly resulting in less CO₂ loading as compared to its dry framework.¹⁷³

1.6.2 MOFs with Lewis basic sites

MOFs with surface functionalization fall under this category. It is already well recognized that the presence of Lewis basic sites like –NH₂, alkylamine, and arylamine groups improves the CO₂ selectivity.¹⁴⁷ However, it is important to mention here that introduction of functional groups could also affect the saturation capacity of the framework, owing to the blocking of the pore accessibility.¹⁴⁷ A superior CO₂ uptake has been observed for amino-MIL-53 as compared to its parent framework (*Figure 1.11*).¹⁷⁴ Similar improvements have also been witnessed for the amine functionalized USO-2-Ni and USO-3-In-A,¹⁷⁵ comparative to their non-functionalized parent frameworks. Yaghi and co-workers^{176,177} have reported a series of pore functionalized IRMOFs and their applicability in selective CO₂ capture in presence of

water. It has been clearly demonstrated, that the presence of Lewis basic sites enhances both the selectivity and capacity for CO₂.¹⁷⁸ These Lewis basic sites can be introduced in the framework in pre- or post-synthetic manner.¹⁷⁴⁻¹⁷⁹

In this regard, the dialkylamine grafted Cu-BTTri and Mg₂(dobpdc) (H₃BTTri: 1,3,5-tri(1H-1,2,3-triazol-4-yl)benzene and dobpdc: 4,4'-dioxido-3,3'-biphenyldicarboxylic acid) proves to be one of the best suited MOFs for CO₂ separation under post combustion conditions.^{180,167} Here one of the amine gets coordinated to the bare metal sites whereas the second amine acts as Lewis basic site for preferential CO₂ adsorption.^{147,180,167}

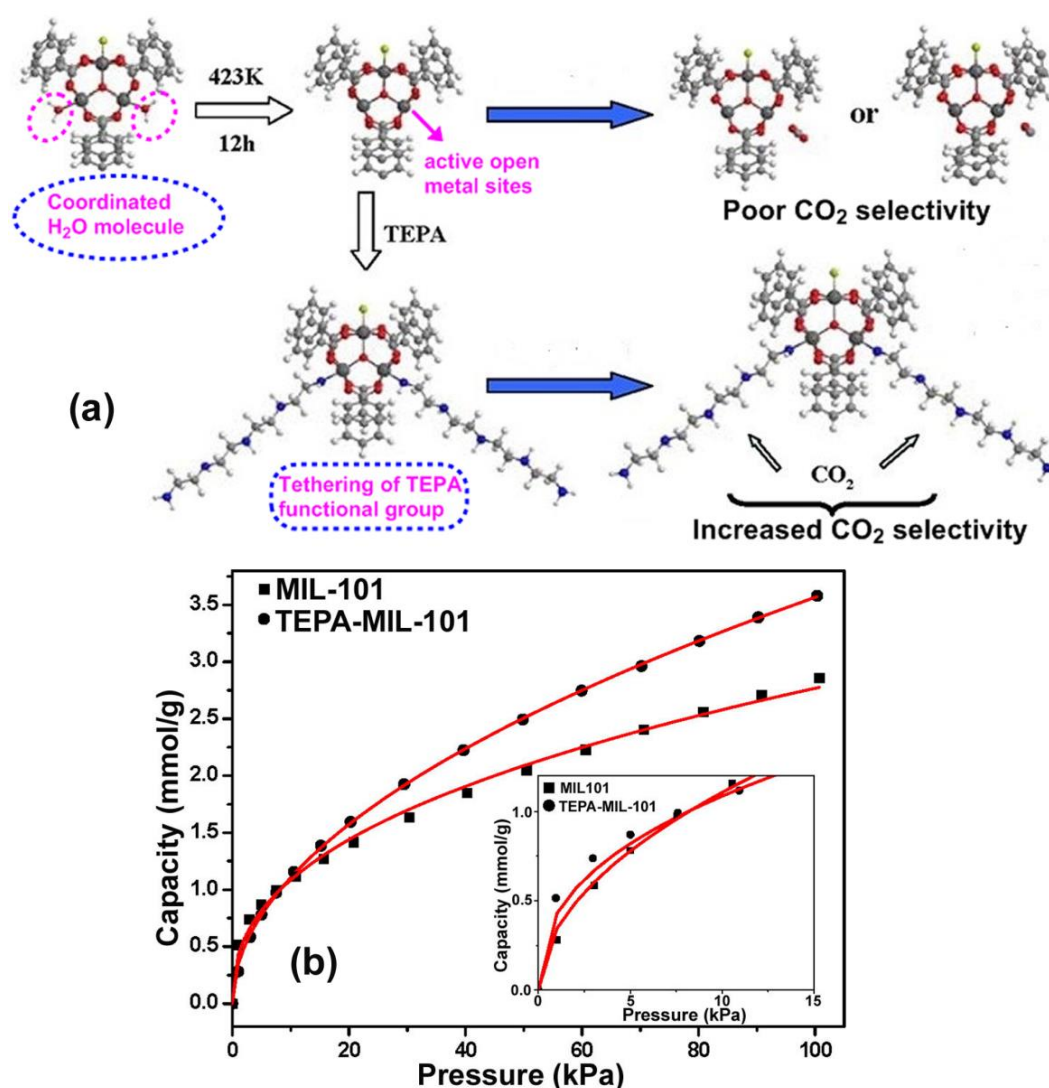


Figure 1.11 (a) Schematic representation of the MIL-53 and amino-MIL-53 and (b) CO₂ adsorption isotherms on MIL-101 and TEPA-MIL-101 at 298 K; (TEPA = tetraethylenepentamine), (Adapted with permission from “Wang et al. *J. Phys. Chem. C* **2012**, 116, 19814” © 2012 American Chemical Society.)

Long and co-workers^{180,167} have tuned the CO₂ adsorbing property for the CuBTTri framework by binding different types of amines to the unsaturated metal center. It has been observed for en-CuBTTri (en: ethylenediamine, 1° amine and H₃BTTri: 1,3,5-tri(1H-1,2,3-triazol-4-yl)benzene), at pressures below 0.06 bar it showed a greater attraction for CO₂ than CuBTTri, whereas the overall capacity at 1 bar is less for en-CuBTTri as compared to its parent framework. This has been attributed to the clogging of the pores due to “en” grafting. On the other hand the binding of “mmen” (mmen: N,N'-dimethylethylenediamine, 2° amine) results to a 4.7 times enhancement in the CO₂ uptake at 298 K and 0.15 bar in comparison to the non-functionalized CuBTTri framework (Figure 1.12).¹⁸⁰

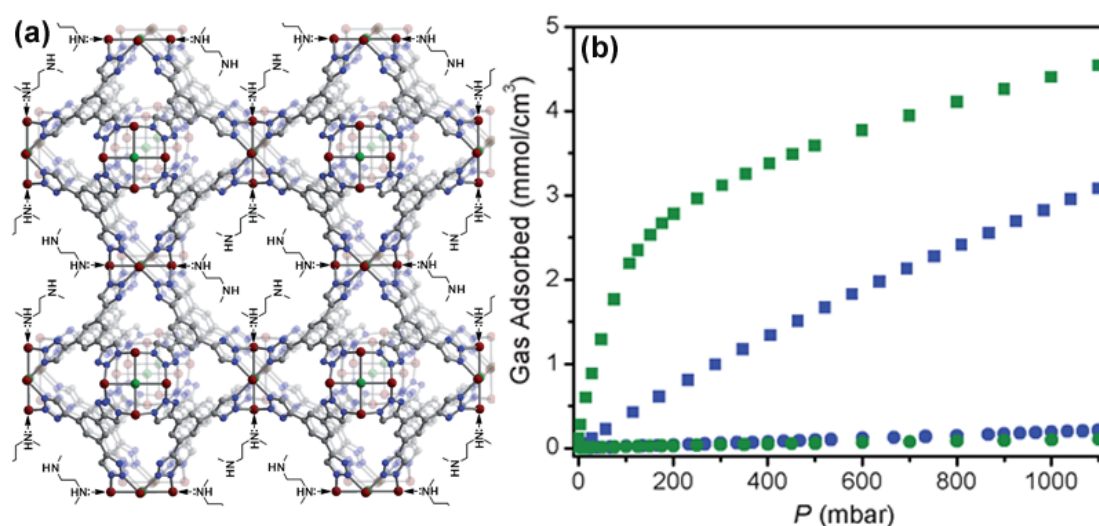


Figure 1.12 (a) A portion of the structure of the amine functionalized metal–organic framework mmen-CuBTTri, with red, green, blue and gray spheres representing Cu, Cl, N and C atoms, respectively. Stoichiometric incorporation of the diamine N,N'-dimethylethylenediamine onto open metal sites within the pores begets a framework with excellent capacity and selectivity for CO₂ capture at low pressures and (b) Isotherms for CO₂ (squares) and N₂ (circles) adsorption at 25 °C for mmen-CuBTTri (green) and CuBTTri (blue) (Adapted with permission from “McDonald et al. *Chem. Sci.* **2011**, 2, 2022” © The Royal Society of Chemistry 2011.)

In particular, grafting of Mg₂(dobpdc) with “en” (1° amine) / mmen (2° amine) ligands showed a higher CO₂ capacity with enhanced water stability as compared to the non-functionalized parent framework under the same working conditions (Figure 1.13).¹⁶⁷ However, it has been perceived that in case of 1° and 2° amines, the interaction with the CO₂ is chemisorptive, suggesting a low working capacity for the material unless a high regeneration temperature is applied.^{147,181} Apart from the amine functionalization, other functional groups like hydroxyl, amides, and halides

are also shown to be effectively increasing the CO₂ capture capability of the MOFs.¹⁸²⁻¹⁸⁶ An acylamide decorated MOF has been synthesized, exhibiting high CO₂ capacity and CO₂/N₂ selectivity. The framework based on N,N',N''-tris(isophthyl)-1,3,5-benzenetricarboxamide (TPBTM) linker containing amide linkages exhibit enhanced CO₂ binding capability as compared to its structural analogue PCN-61 whose framework is based on C-C triple bonds links.¹⁸³

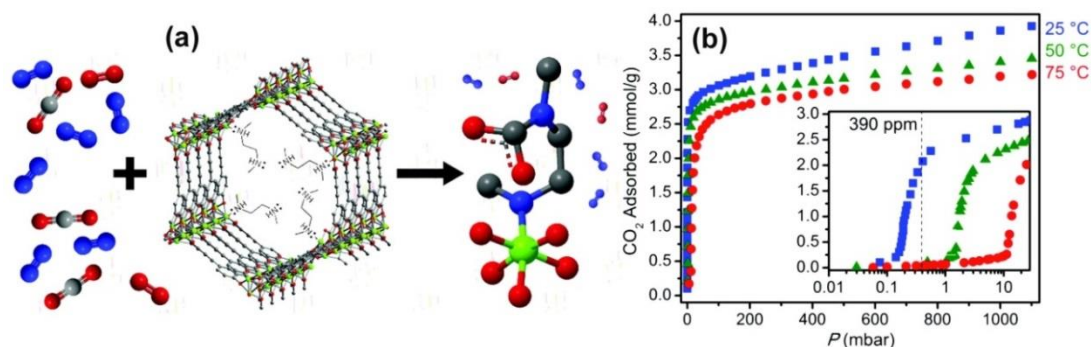


Figure 1.13. (a) The framework structure of $\text{mmem-Mg}_2(\text{dobpdc})$ and (b) Adsorption of CO₂ in mmen-2 at 25 °C (blue squares), 50 °C (green triangles), and 75 °C (red circles). Inset: The isotherms at very low pressures exhibit a step that shifts to higher pressures at higher temperatures. The dashed, vertical line marks the current partial pressure of CO₂ in air (390 ppm) (Adapted with permission from “McDonald et al. *J. Am. Chem. Soc.* **2012**, *134*, 7056” © 2012 American Chemical Society.)

In this regard, Chen and co-workers¹⁸⁴ have recently shown two highly CO₂ selective MOFs consisting of monodentate hydroxide functional groups. Interestingly, these hydroxide MOFs showed an exorbitant increase of ~410% and 540% in the volumetric CO₂ capacity at 0.15 bar and 298 K as compared to their non-functionalized parent structures. The interaction between CO₂ and hydroxides results in the formation of an unstable bicarbonate species with a mechanism similar to the binding of CO₂ with carbonic anhydrase. Owing to the formation of the bicarbonate species their regenerative cost is considerably low as compared to the 1°/2° amine grafted MOFs (amine grafted Mg-MOF-74). However, the heat of adsorption calculation by Virial model suggested ΔH_{ads} value ranging between 99-110 kJ/mol at zero coverage which clearly points towards a chemisorptive type of interaction between CO₂ and the hydroxide functional groups.

To overcome this, recently, heterodiamine-grafted MOFs¹⁸⁵ have been pursued to ensure both selectivity and fast regeneration process of the adsorbent material. In this approach, $\text{dmen-Mg}_2(\text{dobpdc})$ framework (dmen: N,N-

dimethylethylenediamine and dobpdcc: 4,4'-dioxido-3,3'-biphenyldicarboxylate) have been post-synthetically prepared by Lee et al. containing both primary and tertiary amine, which gives a CO₂ uptake of 4.34 mmol/g at 40°C (313 K) and 1 bar. Remarkably, it has been observed that almost no CO₂ gets adsorbed at or above 75°C (348 K) at 1 bar, whereas in case of en-Mg₂(dobdc) and mmen-Mg₂(dobdc) this temperature is as high as 120° C (393 K), suggesting that dmen-Mg₂(dobpdcc) could be regenerated at much lower temperature as compared to “en” and “mmen” functionalized frameworks.

Further, another alternative measure would be the use of aromatic amine based frameworks for efficient capture of CO₂ under post-combustive conditions. Due to their less basic character as compared to the aliphatic amines the regeneration cost of the material will be highly reduced. For example, Rosi and co-workers¹⁸⁶ synthesized an adenine based CO₂ selective MOF known as bio-MOF-100 (Figure 1.14). A dense lining of amino and pyrimidine groups were present throughout the porous channel of the framework, with each individual cavity having a direct exposure of four amino and four pyrimidine groups making it highly efficient for selective CO₂ capture with a maximum CO₂ uptake of 4.1 mmol/g and N₂ uptake of 0.13 mmol/g at 298 K, with a moderate enthalpy of adsorption of about 45 kJ/mol at zero coverage.¹⁸⁶

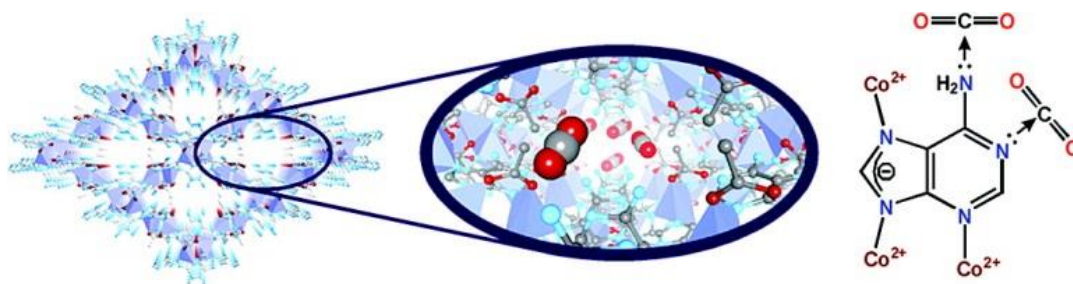


Figure 1.14. Structural view of Co₂(ad)₂(CO₂CH₃)₂·2DMF·0.5H₂O (bio-MOF-100). Pyrimidine and amino groups of adeninate (ad) decorate the pores of the framework; zoomed picture shows the framework pore embedded with Lewis basic groups, used for highly efficient selective CO₂ adsorption (Adapted with permission from “ An et al. *J. Am. Chem. Soc.* **2010**, 132, 38” © 2010 American Chemical Society.)

1.6.3 Flexible frameworks

The reversible structural dynamism shown by 3rd generation MOFs in response to external stimuli such as temperature, pressure, solvent or guest inclusion etc.¹⁵⁰

makes this class of framework distinct and more attractive as compared to the classical frameworks. In microporous frameworks it would be highly beneficial if this framework flexibility could be tuned, as it gives control to a new dimension such as kinetic regulation over pore expansion and contraction. For the guest dependent structural dynamicity, the guest removal or inclusion could either lead to expansion or contraction of the pore apertures, depending upon the nature of the framework.¹⁸⁷ This type of solvent dependent flexibility has been evidenced in frameworks of MIL-series, which shows a H₂O dependent expansion and contraction of the pore openings (*Figure 1.15*).¹⁸⁷

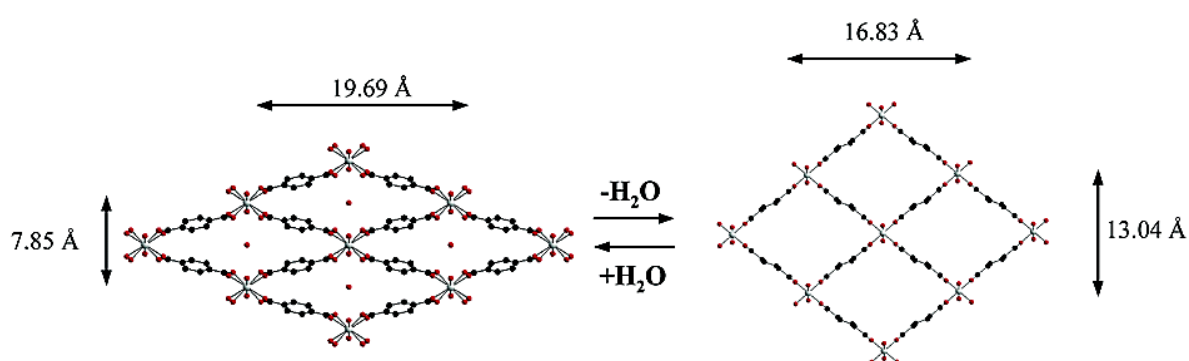


Figure 1.15. Schematic representation of the reversible hydration-dehydration of MIL-53t and MIL-53ht (Adapted with permission from “Serre et al. *J. Am. Chem. Soc.* **2002**, *124*, 13519” © 2002 American Chemical Society.)

Importantly, the pressure dependent framework dynamicity could be gas specific and can be witnessed by their respective adsorption isotherm profiles.¹⁸⁸⁻¹⁹¹ However, the structural changes could accompany a substantial variation in the unit cell parameter and these are referred as breathing effects, whereas in some cases only small orientation change of the linker take place giving rise to a gating phenomenon. In the case of breathing a hysteretic adsorption isotherm is observed, on the contrary in case of gating only a step isotherm is noticed with the desorption profile completely tracing back the adsorption branch.¹⁹⁰

A sudden increase in the CO₂ capacity resulted for the ZIF-7 (with Zn metal) framework constructed from benzimidazolate linkers.¹⁸⁸ The increase in the CO₂ capacity accompanies by a large breathing effect and a reversible hysteretic adsorption isotherm. On the contrary another member of the same family based on methyl-imidazolate (ZIF-8) showed a hysteretic adsorption isotherm for N₂, which has been attributed to the swing effect of the methyl-imidazolate linkers.¹⁹⁰ Some

temperature dependent flexible frameworks are also known in ZIF series for example upon heating ZIF-4 undergoes a reversible transition between the crystalline and amorphous stage.^{190,192}

Remarkably, a Zn-based MOF¹⁹³ [$\text{Zn}_2(\text{bpdc})_2(\text{bpee})$; bpdc = 4,4'-biphenyldicarboxylate, bpee = 1,2-bis(4-pyridyl)ethylene] showed a CO_2 stepped isotherm at ~ 0.1 atm pressure, with no noticeable hysteresis, and the desorption branch exactly traces back the adsorption profile (*Figure 1.16*). This has been attributed to the interaction of CO_2 with the framework, resulting into the twisting of the “bpee” ligand owing to the type of connectivity of the carboxylate groups to the metal center. This twist in the framework causes a substantial increase of the CO_2 capacity as compared to other gas such as N_2 , H_2 and CH_4 .

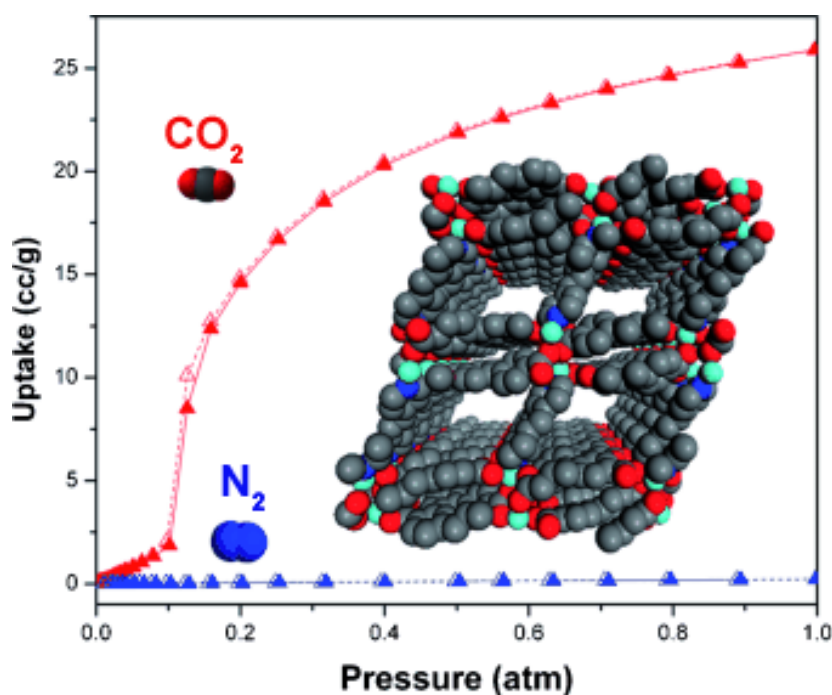


Figure 1.16 The CO_2 induced structural flexibility in $\text{Zn}_2(\text{bpdc})_2(\text{bpee})$ framework leading to high selective uptake of CO_2 at 25°C and up to 1 atm (post-combustive working conditions); CO_2 (triangles) and N_2 (circles) adsorption-desorption. Filled symbols denote the adsorption branch and open symbols denote the desorption branch. (Adapted with permission from “Wu et al. *Chem. Eur. J.* **2010**, *16*, 13951” © 2010 Wiley-VCH Verlag GmbH & Co. KGaA, Weinheim.)

In the case of PCN-200¹⁹⁴ also known as “elastic single molecule trap”, the unit cell volume reduction occurs from 2489 \AA^3 to 2226 \AA^3 upon desolvation and simultaneously the kinetic diameter increases from 2.9 \AA to 4.4 \AA (*Figure 1.17*). Upon saturating the framework with CO_2 the unit cell volume become identical to the

parent framework, except the β angle which showed a considerable difference in pore shape and size for the CO₂ loaded form as compared to its parent structure.

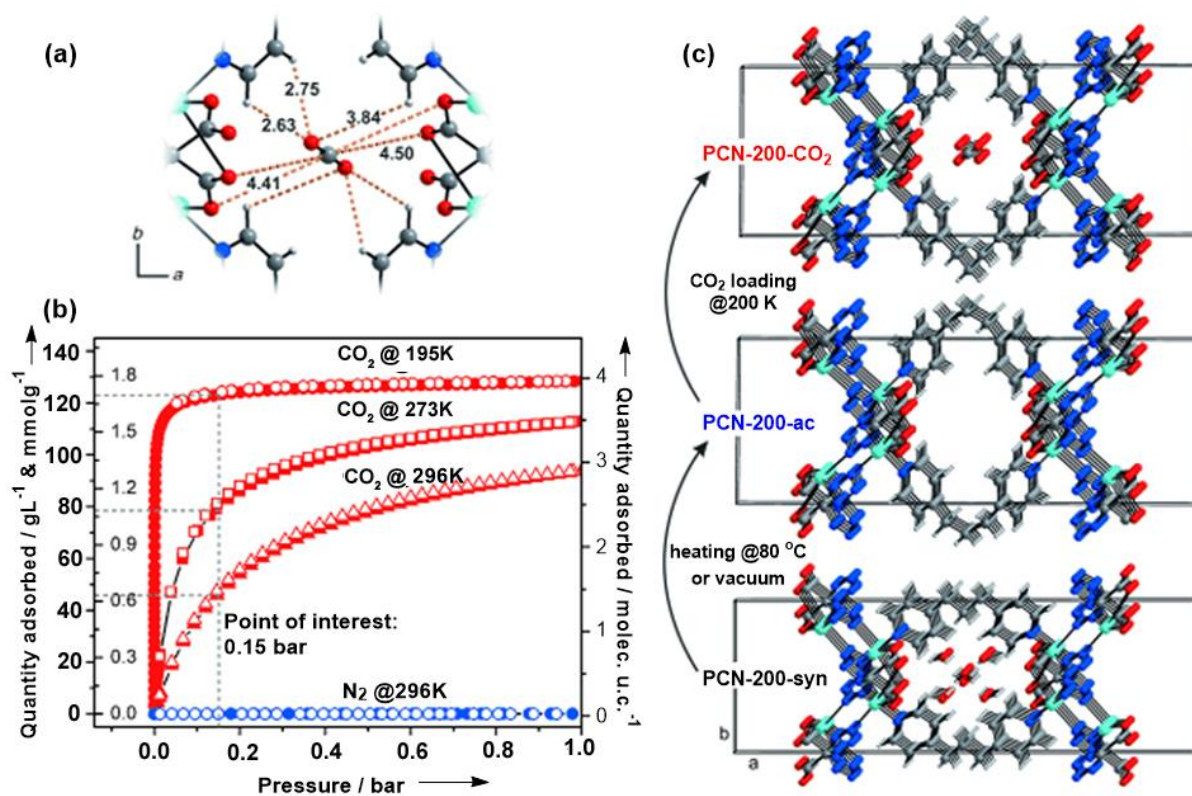


Figure 1.17 a) close-up view of the multipoint bonded CO₂ molecule in the pore (distances are given in Å), (b) Gas adsorption isotherms for CO₂ and N₂ of PCN-200-ac. CO₂ at 195 K (red circles), 273 K (rectangles), 296 K (triangles) and N₂ at 296 K (blue circles). The filled and open symbols represent adsorption and desorption, respectively, and the gray dashed lines indicate the adsorption values at 0.15 bar (partial pressure of CO₂ in flue gas with typical composition of 14–16 % CO₂ and 75 % N₂) and (c) Structural changes of PCN-200 upon activation and CO₂ adsorption obtained by in situ SPD data: perspective view of a single pore in its unit cell along the c axis of the as-synthesized (PCN-200-syn, bottom), activated (PCN-200-ac, middle), and CO₂-loaded phase (PCN-200-CO₂, top) (Adapted with permission from “Wriedt et al. *Angew. Chem. Int. Ed.* **2012**, 51, 9804” © 2012 Wiley-VCH Verlag GmbH & Co. KGaA, Weinheim.)

Two Nickel based flexible MOFs, SNU-M10 [(Ni₂L²)(bptc)] and SNU-M11 [(Ni₂L⁴)(bptc)] (bptc: 3,3',5,5'-biphenyltetracarboxylic acid) have been designed by Choi et al.¹⁹⁵ that showed flexible behavior. These frameworks having ethyl and butyl pillars show high CO₂ selectivity and hysteretic CO₂ adsorption isotherms (Figure 1.18). Further, it has been noted that the gate opening pressure for SNU-M11 (based on butyl pillar) is at a higher value as compared to SNU-M10 (based on ethyl pillar), suggesting ethyl pillars to be more flexible than the butyl ones.

Lyndon and co-workers¹⁹⁶ have reported a triply interpenetrated Zn-MOF based on flexible 4,4'-bpe and azdc (4,4'-bpe: Trans-1,2-bis(4-pyridyl)ethylene and azdc: 4,4'-(diazene-1,2-diyl)dibenzoic acid) linker which showed light induced dynamic behavior resulting in large changes in CO₂ uptake capacity. A thorough study has been reported by Fisher and co-workers¹⁹⁷⁻¹⁹⁹ on the flexibility of the dangling side groups. They noticed that the chain length of the dangling groups has a significant impact on the structural flexibility and CO₂ selectivity over N₂ and CH₄.

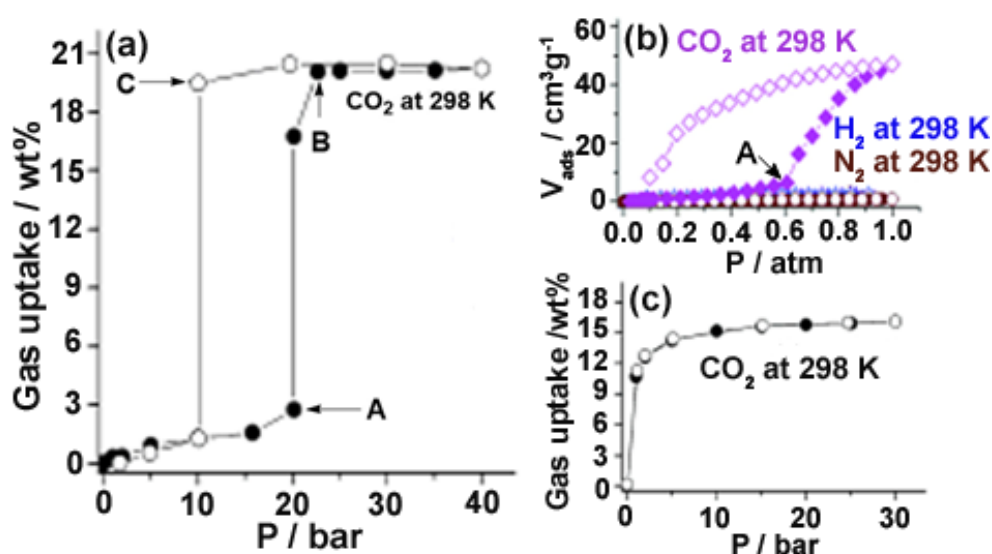


Figure 1.18 (a) Excess CO₂ sorption measured at 298 K up to 40 bar for SNU-M11; Filled shapes: adsorption. Open shapes: desorption. The CO₂ sorption isotherms of SNU-M10 (b) Measured at 298 K (pink) up to 1 atm compared to the sorption isotherms of N₂ (brown) and H₂ (blue). c) Excess CO₂ sorption measured at 298 K up to 30 bar. Filled shapes: adsorption. Open shapes: desorption (Adapted with permission from “Choi et al. *Angew. Chem. Int. Ed.* **2009**, *48*, 6865” © 2009 Wiley-VCH Verlag GmbH & Co. KGaA, Weinheim.)

1.7 Ultra-microporous MOFs and CO₂ capture from flue gas

Materials showing optimal interaction with CO₂, along with minimum energy penalty and less cost of regeneration will be an ideal candidate for CO₂ sequestration from flue gas.¹⁴⁷ Ultra-microporous MOFs with appropriate pore dimensions are efficient physical adsorbents for selective CO₂ capture from flue gas, owing to their effective molecular sieving capabilities. Due to the physical nature of interaction with the adsorbed CO₂ molecules, the regeneration cost is also highly reduced. The size exclusion technique has been shown to be truly beneficial for selective CO₂ removal from the flue gas streams. Given the nearly similar kinetic diameters for CO₂ (3.3 Å)

and N₂ (3.6 Å), ultra-microporous MOFs having pore dimensions slightly greater than 3.3 Å and less than 3.6 Å would be highly effective for CO₂ capture from flue gas. Further, into their confined space, it will be beneficial if the flexibility could be imparted in these frameworks which will create additional space for CO₂ to fill up, but at the same time retain the selectivity.

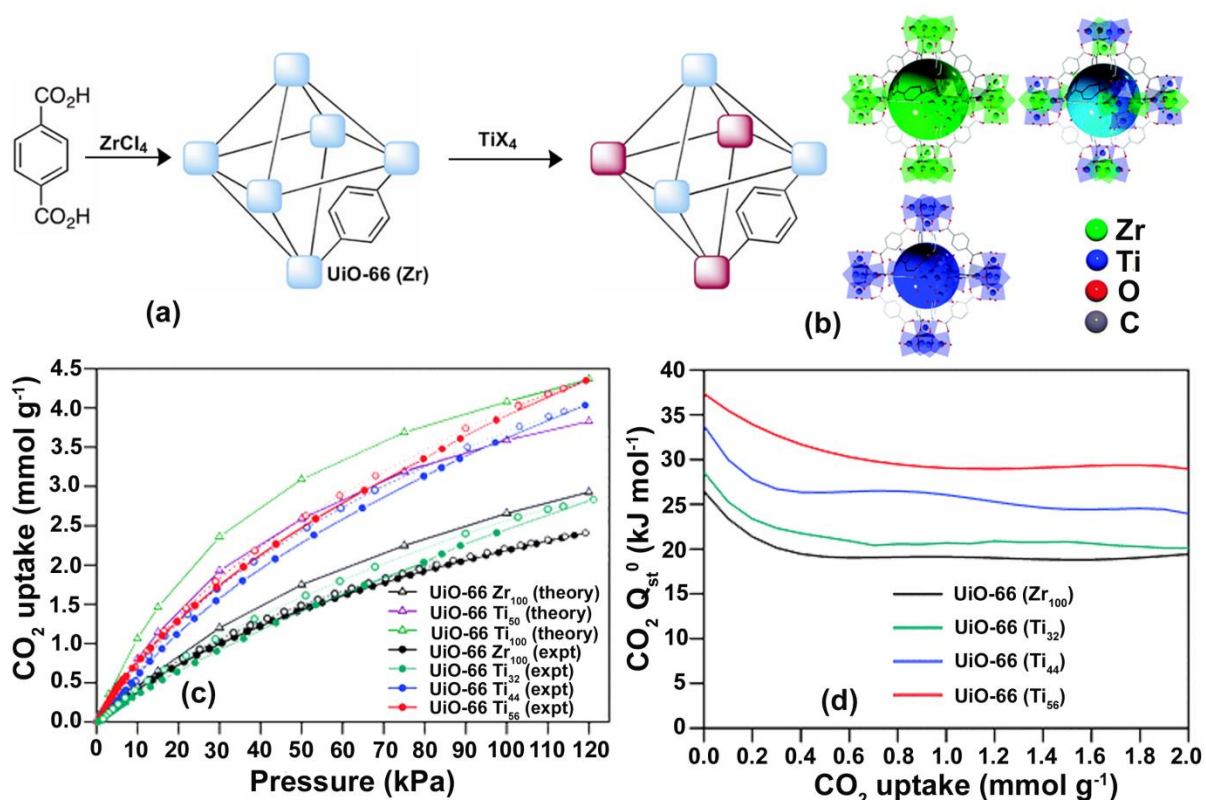


Figure 1.19 (a) Post-synthetic cation Exchange of UiO-66 (adapted with permission from “Kim et al. *J. Am. Chem. Soc.* **2012**, *134*, 18082” © 2012 American Chemical Society.) (b) The Zr-based metal organic framework UiO-66 can undergo post-synthetic exchange with Ti(IV) to deliver heterometallic MOFs, with decreased octahedral cages sizes, (c) CO₂ uptake can be increased by up to 81% through substitution of Zr atoms with Ti at 273 K. Simulations show that Ti loading increases above that synthetic attainable does not deliver further CO₂ uptake. The empty circles represent desorption data, while the solid circles represent adsorption data and (d) Isosteric heat of adsorption as a function of CO₂ uptake increases significantly with Ti loading level (Adapted with permission from “Lau et al. *Chem. Commun.* **2013**, *49*, 3634” © The Royal Society of Chemistry 2013.)

Kim et al.²⁰⁰ reported a hetero-metallic MOF, in which the post-synthetic exchange of Zr with Ti cations resulted in a significant decrease of the pore size, owing to the smaller size of the Ti ions. It has been predicted that the Ti doped MOF having ideal pore dimensions for CO₂ adsorption, could show dramatic enhancement

in the CO₂ capacity as compared to the parent structure (*Figure 1.19*).²⁰⁰ By the similar technique improvement in the CO₂ capacities have been achieved in Ti-exchanged UiO-66 MOFs (*Figure 1.19*).^{201,202}

It has also been observed that for the enhancement of the molecular sieving effect, the interpenetrated structures having proper pore apertures are more beneficial as compared to their non-interpenetrated reticular MOFs. Han et al.²⁰³ conducted a (Grand Canonical Monte-Carlo) GCMC simulation study on 14 prototypical MOFs and delivered that the interpenetrating structures result in a higher binding affinity for CO₂, approximately twice as compared to their non-interpenetrated structures. This results in higher uptake at low pressure regime, although the CO₂ saturation value at high pressure region remains high for the non-interpenetrated structures.^{147,203} Similar results have been perceived in two ultra-microporous iso-reticular frameworks: NJU-Bai7 and NJU-Bai8 (*Figure 1.20*).²⁰⁴ Due to pore apertures falling in the exact range (3.4 X 3.4 for NJU-Bai7 and 4 X 3.3 Å² for NJU-Bai8) these MOFs showed better CO₂ adsorbing capacity at post-combustion working conditions (~0.15 bar) as compared to SYSU framework, which has a similar structure with comparatively larger pores (6.3 X 6.3 Å²).

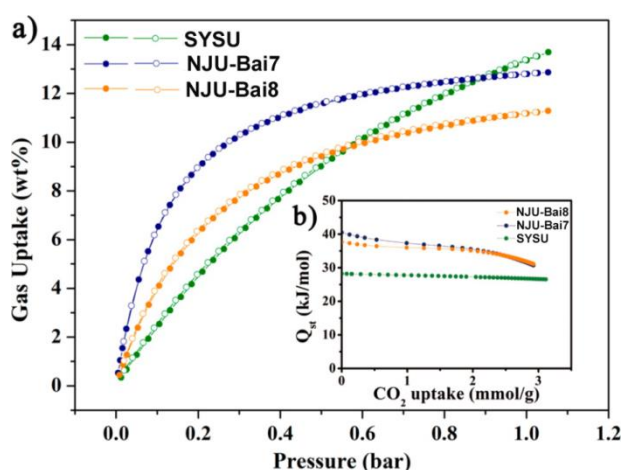


Figure 1.20 (a) CO₂ adsorption isotherms for SYSU, NJU-Bai7, and NJU-Bai8 at 298 K. (b) CO₂ adsorption enthalpy of SYSU, NJU-Bai7, and NJU-Bai8 (Adapted with permission from “Du et al. *J. Am. Chem. Soc.* **2013**, 135, 562” © 2013 American Chemical Society.)

On the other hand Zaworotko and co-workers have tuned the CO₂ adsorbing capacity of SIFSIX series of MOFs.²⁰⁵⁻²⁰⁸ The framework is based on 4,4'-bipyridine and hexafluorosilicate anions has been showed as a promising candidate in CO₂

capture applications (Figure 1.21).²⁰⁵⁻²⁰⁸ It has been observed that the doubly interpenetrated framework of SIFSIX-2-Cu-i comprising of smaller pores has much higher CO₂ capacity as compared to SIFSIX-2-Cu ([Cu(dpa)₂(SiF₆)_n]; dpa: 4,4'-dipyridylacetylene), having similar non-interpenetrated framework.²⁰⁹ Importantly, these materials also exhibit an outstanding CO₂ selectivity over N₂, H₂ and CH₄.

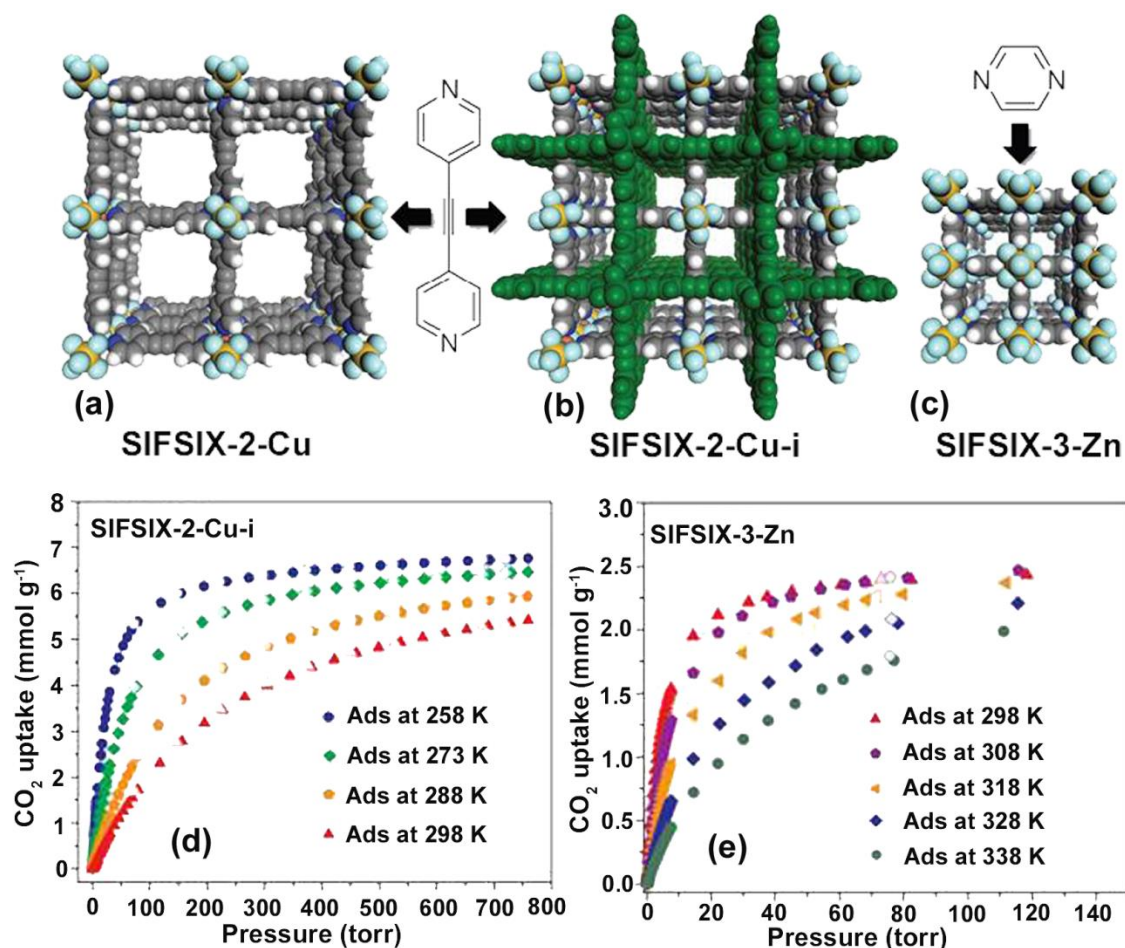


Figure 1.21 The variable pore size channel structures of SIFSIX-2-Cu, SIF-SIX-2-Cu-i and SIFSIX-3-Zn. (a) SIFSIX-2-Cu; pore size 13.05 Å, BET apparent surface area (N₂ absorption) 3140 m²/g, (b) SIFSIX-2-Cu-i, pore size 5.15 Å, BET apparent surface area (N₂ absorption) 735 m²/g (c) SIFSIX-3-Zn, pore size 3.84 Å, apparent surface area (determined from CO₂ absorption isotherm) 250 m²/g. Colour code; C:grey, N:blue, Si:yellow, F:light blue. All hydrogen atoms and guest molecules are omitted for clarity. Note that the green net represents the interpenetrated net in SIFSIX-2-Cu-i. Variable temperature CO₂ sorption isotherms for (d) SIFSIX-2-Cu-i and (e) SIFSIX-3-Zn (Adapted with permission from “Nugent et al. *Nature* **2013**, 495,80–84” ©2013 Macmillan Publishers Limited.)

In a recent study by Nandi et al.,²¹⁰ reported a Ni-(4PyC)₂•DMF (4PyC: 4-pyridinecarboxylic acid) ultra-microporous MOF for an excellent selective CO₂ adsorption capacity under humid post-combustion condition. This material shows an

optimal interaction with CO₂ ($\Delta H_{\text{ads}} = 33$ kJ/mol), which makes the CO₂ regeneration step cost effective. Interestingly, the CO₂ selectivity observed for this material is comparable to that of the few benchmark materials specifically quoted for post-combustion CO₂ capture.²¹⁰

Another remarkable feature of MOFs originates with the feasibility of introducing different functional groups (polar functional groups which will show high interactions with CO₂) inside the pores, which in turn helps in increasing the CO₂ affinity of the framework.¹⁸²⁻¹⁸⁶ These results in conjunctive effects. As mentioned earlier, the presence of four free 1° amine groups and four pyrimidine groups as functional sites in the adenine based bio-MOF-100 enhances its CO₂ capture capacity.¹⁸⁶

A similar trend has been realized for Zn₂(Atz)₂(Ox) (Atz: 3-aminotriazolate and Ox: oxalate) ultra-microporous MOF, reported by Shimizu and co-workers.^{211,212} This framework selectively adsorbed high amount of CO₂ owing to the amine functionalized triazole linkers but at the same time shows a moderate enthalpy of adsorption arising from the interaction of CO₂ with the aromatic amines. Interestingly, the increased CO₂ uptake takes place via cooperative type of interaction between the protruding free amines and the adsorbed CO₂-CO₂ molecules (*Figure 1.22*). On the other hand the Zn₃(Atz)₃(PO₄)²¹³ framework reported by the same group showed lesser CO₂ capacity as compared to Zn₂(Atz)₂(Ox) framework. This has been attributed to the improper orientations of the free amine groups, and also the densely grouped amines interfere with each other's ability to bind with CO₂ which results in to a lower CO₂ uptake in Zn₃(Atz)₃(PO₄) as compared to Zn₂(Atz)₂(Ox).²¹³ Extensive efforts have to be made to come up with the optimum pore apertures along with the functional group grafting and orientation, which could help in enhancing the CO₂ selectivity as well as capacity. Although an elaborate research have been persuaded to identify the correct material for CO₂ sequestration from flue gas, very few traditional ultra-microporous MOFs have emerged to exhibit pore size tunability for CO₂ capture from flue gas.

Thus, as a modification to the existing power plants, the post combustion CO₂ capture from industrial effluents will be an efficient step to mitigate the ever rising global CO₂ concentration. For this the synthesis and characterization of novel ultra-

microporous frameworks seem to be an important measure. As mentioned earlier, the appropriate pore dimensions will facilitate the kinetic separation and at the same time the possibility of grafting polar functional groups inside the pores of the framework would enhance the thermodynamic separation of CO₂. Hence, for synthesis of suitable UMMOFs, both these parameters have to be considered.

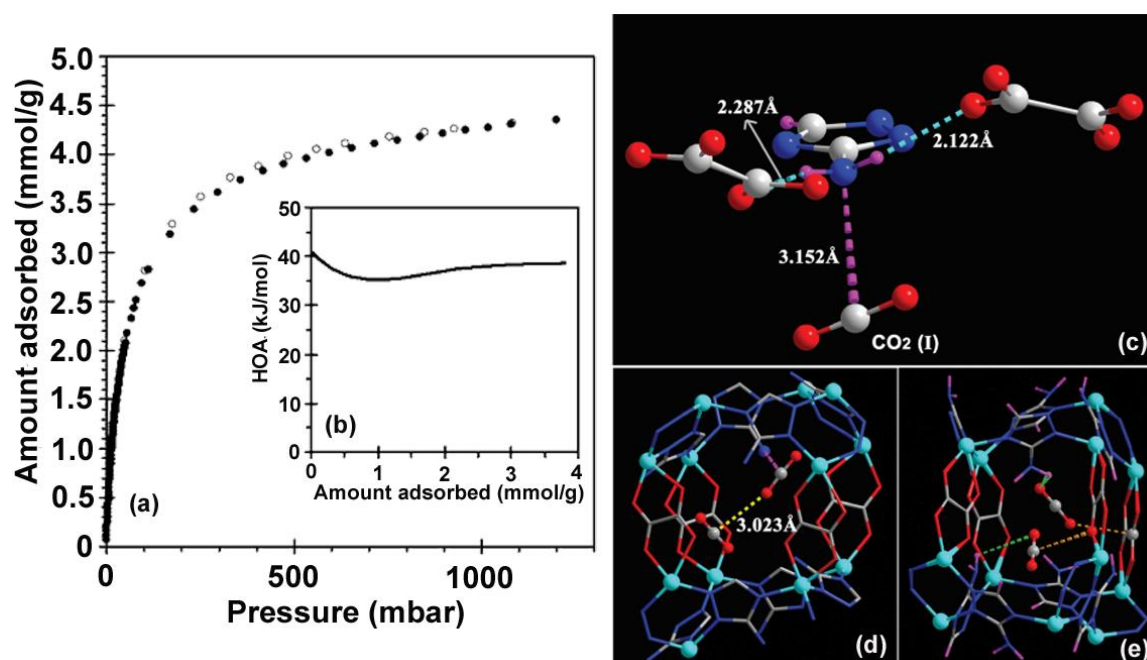


Figure 1.22 (a) CO₂ sorption isotherm of 1 carried out at 273 K, closed circles adsorption, open circles desorption and (b) Inset shows the enthalpy of adsorption as a function of CO₂ loading (Adapted with permission from "Vaidhyanathan et al. *Chem. Commun.* **2009**, 5230" © The Royal Society of Chemistry 2009.) X-ray structure of CO₂ binding in 1·(CO₂)_{1.3} at 173 K. (c) The role of the amine group of Atz in binding CO₂-I is depicted. The hydrogen atoms of the amine group (located crystallographically) H-bond to oxalate oxygen atoms, directing the nitrogen lone pair toward the Carbon atom of the CO₂ molecule. H-bond distances shown are for H-acceptor interactions. (d) Both crystallographically independent CO₂ molecules are shown trapped in a pore, showing the cooperative interaction between CO₂-I and CO₂-II molecules. The CO₂...NH₂ interaction is represented as a dotted purple bond, and the CO₂...CO₂ interaction is indicated as a dotted yellow bond. (e) This panel shows the other interactions present. The CO₂-I...Ox interactions are shown in orange, and the CO₂...NH₂ hydrogen bond interactions are shown in green. For clarity, H atoms are shown in purple ("From Vaidhyanathan et al. *Science* **2010**, 330, 650. Reprinted with permission from AAAS.").

1.8 Outline and thesis objective

The previous sections highlighted the progress made in the synthesis and characterization of different materials, especially MOFs, for carbon capture and

sequestration (CCS) from industrial effluents. Special emphasis has been given to ultra-microporous MOFs as an emerging class of solid sorbent for CO₂ capture under post combustion working conditions. UMMOF bring advantage as gas separation sorbent due to their intrinsic molecular sieving effect. It has been discussed that tethering of polar functional groups into these frameworks would help in enhancing their CO₂ capacity. In this regard, as discussed earlier, the Zn₂(Atz)₂(Ox) MOF seems to be an interesting example. The high CO₂ selectivity and capacity arises from the basic triazolate groups and polarizing oxalates ligands. Additionally, due to the presence of aromatic amines the enthalpy of adsorption was also not very high.

This thesis demonstrates the systematic synthetic approach for obtaining a series of ultra-microporous MOFs (UMMOFs) using transition metal ions with small and rigid linkers: 3-aminotriazole (Hatz) and oxalic acid (H₂Ox) and tuning their CO₂ adsorption properties. In this respect, chapters 2, 3 and 4 describe the synthesis, characterizations and sorption characteristics of few ultra-microporous MOFs. The CO₂ capacity for these UMMOFs has been tuned based upon different synthetic parameters such as temperature, metal ion, and solvent. Whereas the last chapter demonstrates the stabilization of an unstable MOF via pore modulation approach and studies its CO₂ uptake capacity.

Two major objectives of this thesis are as follows:

- 1) Synthesis of ultra-microporous MOFs based on oxalic acid and 3-aminotriazole linker.
- 2) Tuning their CO₂ adsorption properties and stability.

1.9 References

1. Inventory of U.S. *Greenhouse Gas Emissions and Sinks 1990–2015*.
2. Shakun, J. D.; Clark, P. U.; He, F.; Marcott, S. A.; Mix, A. C.; Liu, Z.; Otto-Bliesner, B.; Schmittner, A.; Bard, E. *Nature* **2012**, *484*, 49.
3. Goeppert, A.; Czaun, M.; May, R. B.; Surya Prakash, G. K.; Olah, G. A.; Narayanan, S. R. *J. Am. Chem. Soc.* **2011**, *133*, 20164.
4. Quadrelli, R.; Peterson, S. *Energy Policy* **2007**, *35*, 5938.
5. Rao, A. B.; Rubin, E. S. *Environ. Sci. Technol.* **2002**, *36*, 4467.
6. Hadjipaschalis, I.; Poullikkas, A.; Efthimiou, V. *Renew. Sustainable Energy Rev.* **2009**, *13*, 1513.
7. Graves, C.; Ebbesen, S. D.; Mogensen, M.; Lackner, K. S.; *Renew. Sustainable Energy Rev.* **2011**, *15*, 1.
8. Akorede, M. F.; Hizam, H.; Pouresmaeil, E. *Renew. Sustainable Energy Rev.* **2010**, *14*, 724.
9. Olajire, A. A.; *Energy* **2010**, *35*, 2610.
10. Rackley S. *Carbon capture and storage*. Burlington, MA: Butterworth-Heinemann/Elsevier **2010**.
11. WMO, *Greenhouse gas Bulletin (GHG Bulletin)* **2012**, No. 8.
12. WMO, *Greenhouse Gas Bulletin (GHG Bulletin)* **2015**, No. 12.
13. IPCC. *Climate Change 2001 Impacts, Adaptation and Vulnerability 2001*
14. Pachauri, R. K.; Reisinger, A. *IPCC Fourth Assessment Report, Intergovernmental Panel on Climate Change* **2007**.
15. Stewart, C.; Hessami, M. *Energy Convers. Manage.* **2005**, *46*, 403.
16. Demirbas, A. *Energy Sources-Part A* **2008**, *30*, 70.
17. Petron, G.; Tans, P.; Frost, G.; Chao, D.; Trainer, M.J. *Geophys. Res.* **2008**, *13*, 1.
18. *International Energy Outlook: DOE/EIA-0484, U.S. Energy Information Administration* 2010 <http://www.eia.gov/forecasts/ieo/index.cfm> (Accessed March **2010**).
19. Botzen, W. J. W.; Gowdy, J. M.; van den Bergh, J. C. J. M. *Climate Policy* **2008**, *8*, 569.
20. *Carbon Capture and Storage, Full-Scale Demonstration Progress Update* www.iea.org/G8/docs/ccs_g8_july09.pdf, OECD/IEA, **2009**.
21. Godec, M.; Kuuskraa, V.; Van Leeuwen, T.; Melzer, S.; Wildgust, N. *Energy Procedia* **2011**, *4*, 2162.
22. Stevens, S. H.; Kuuskraa, V. A.; Gale, J.; Beecy, D. *Environ Geosci.* **2001**, *8*, 200.
23. Xiaoding, X.; Moulijn, J. A. *Energy & Fuels* **1996**, *10*, 305.
24. Raventós, M.; Duarte, S.; Alarcón, R. *Food Sci. Tech. Int.* **2002**, *8*, 269.
25. Kai Man, K. Y.; Curcic, I.; Gabriel, J.; Shik Chi, E. T. *ChemSusChem* **2008**, *1*, 893.
26. Rau, G. H. *Environ. Sci. Technol.* **2011**, *45*, 1088.
27. Jhong, H.-R.; Ma, S.; Kenis, P. J. A. *Curr. Opin. Chem. Eng.* **2013**, *2*, 191.
28. He, L.-N.; Yang, Z.-Z.; Liu, A.-H.; Gao, J. *Advances in CO₂ Conversion and Utilization (ACS Symp. Ser.)* **2010**, Chapter 6, 77.
29. Centi, G.; Perathoner, S. *Catal. Today* **2009**, *148*, 191.
30. Jiang, Z.; Xiao, T.; Kuznetsov, V. L.; Edwards, P. P. *Phil. Trans. R. Soc. A* **2010**, *368*, 3343.

31. Benson, E. E.; Kubiak, C. P.; Sathrum, A. J.; Smieja, J. M. *Chem. Soc. Rev.* **2009**, *38*, 89.
32. Roy, S. C.; Varghese, O. K.; Paulose, M.; Grimes, C. A. *ACS Nano* **2010**, *4*, 1259.
33. Varghese, O. K.; Paulose, M.; LaTempa, T. J.; Grimes, C. A. *Nano Lett.* **2009**, *9*, 731.
34. Ganesh, I. *Renew. Sustainable Energy Rev.* **2014**, *31*, 221.
35. Sumida, K.; Rogow, D. L.; Mason, J. A.; McDonald, T. M.; Bloch, E. D.; Herm, Z. R.; Bae, T.-H.; Long, J. R. *Chem. Rev.* **2012**, *112*, 724.
36. Samanta, A. K.; Zhao, A.; Shimizu, G. K. H.; Sarkar, P.; Gupta, R.; *Ind. Eng. Chem. Res.* **2012**, *51*, 1438.
37. Bhowan, A. S.; Freeman, B. C. *Environ. Sci. Technol.* **2011**, *45*, 8624.
38. Drage, T. C.; Snape, C. E.; Stevens, L. A.; Wood, J.; Wang, J.; Cooper, A. I.; Dawson, R.; Guo, X.; Satterley, C.; Irons, R. *J. Mater. Chem.* **2012**, *22*, 2815.
39. Rochelle, G. T. *Science* **2009**, *325*, 1652.
40. Buhre, B.J.P.; Elliott, L.K.; Sheng, C.D.; Gupta, R.P.; Wall, T.F. *Prog. Energy Combust. Sci.* **2005**, *31*, 283.
41. Toftegaard, M. B.; Brix, J.; Jensen, P. A.; Glarborg, P.; Jensen, A. D. *Prog. Energy Combust. Sci.* **2010**, *36*, 581.
42. Scheffknecht, G.; Al-Makhadmeh, L.; Schnell, U.; Maier, J. *Int. J. Greenh. Gas Control* **2011**, *5*, S16.
43. Wall, T.; Liu, Y.; Spero, C.; Elliott, L.; Khare, S.; Rathnam, R.; Zeenathal, F.; Moghtaderi, B.; Buhre, B.; Sheng, C.; Gupta, R.; Yamada, T.; Keiji, *Chem. Eng. Res. Des.* **2009**, *87*, 1003.
44. Nandi, S.; Luna, P. D.; Daff, T. D.; Rother, J.; Liu, M.; Buchanan, W.; Hawari, A. I.; Woo, T. K.; Vaidhyanathan, R. *Sci. Adv.* **2015**, *1*, e1500421, DOI: 10.1126/sciadv.1500421.
45. Herm, Z. R.; Swisher, J. A.; Smit, B.; Krishna, R.; Long, J. R. *J. Am. Chem. Soc.* **2011**, *133*, 5664.
46. Martin, C. F.; Stöckel, E.; Clowes, R.; Adams, D. J.; Cooper, A. I.; Pis, J. J.; Rubiera, F.; Pevida, C. *J. Mater. Chem.* **2011**, *21*, 5475.
47. Drage, T.C.; Kozynchenko, O.; Pevida, C.; Plaza, M.G.; Rubiera, F.; Pis, J.J.; Snape, C.E.; Tennison, S. *Energy Procedia* **2009**, *1*, 599.
48. Van Selow, E.R.; Cobden, P.D.; Van den Brink, R.W.; Hufton, J.R.; Wright, A. *Energy Procedia* **2009**, *1*, 689.
49. Wang, M.; Lawal, A.; Stephenson, P.; Sidders, J.; Ramshaw, C. *Chem. Eng. Res. Des.* **2011**, *89*, 1609.
50. Leung, D. Y.C.; Caramanna, G.; Maroto-Valer, M. M. *Renew. Sustainable Energy Rev.* **2014**, *39*, 426.
51. Mason, J. A.; Sumida, K.; Herm, Z. R.; Krishna, R.; Long, J. R. *Energy Environ. Sci.* **2011**, *4*, 3030.
52. Merel, J.; Clause, M.; Meunier, F.; *Ind. Eng. Chem. Res.* **2008**, *47*, 209.
53. Zhang, W.; Liu, H.; Sun, Y.; Cakstins, J.; Sun, C.; Snape, C. E. *Appl. Energy* **2016**, *168*, 394.
54. Li, X.; Wang, S.; Chen, C. *Energy Procedia* **2013**, *37*, 836.
55. Bae, Y.-S.; Lee, C.-H. *Carbon* **2005**, *43*, 95.
56. Ma, Y.; Balbuena, P. B. *Chem. Phys. Lett.* **2012**, *552*, 136.
57. Dickey, A. N.; Yazaydin, A. O.; Willis, R. R.; Snurr, R. Q. *Can. J. Chem. Eng.* **2012**, *90*, 825.

58. Bae, Y.-S.; Farha, O. K.; Hupp, J. T.; Snurr, R. Q. *J. Mater. Chem.* **2009**, *19*, 2131.
59. Williams, J. J.; Wiersum, A. D.; Seaton, N. A.; Duren, T. *J. Phys. Chem. C* **2010**, *114*, 18538.
60. Mason, J. A.; McDonald, T. M.; Bae, T.-H.; Bachman, J. E.; Sumida, K.; Dutton, J. J.; Kaye, S. S.; Long, J. R. *J. Am. Chem. Soc.* **2015**, *137*, 4787.
61. Lasseguettea, E.; Carta, M.; Brandani, S.; Ferrari, M.-C. *Int. J. Greenh. Gas Control* **2016**, *50*, 93.
62. Granite, E. J.; Pennline, H. W. *Ind. Eng. Chem. Res.* **2002**, *41*, 5470.
63. Lee, K. B.; Sircar, S. *AIChE J.* **2008**, *54*, 2293.
64. Abu-Zahra, M. R. M.; Schneiders, L. H. J.; Niederer, J. P.M.; Feron, P. H. M.; Versteeg, G. F. *Int. J. Greenh. Gas Control* **2007**, *1*, 37.
65. Zhang, Y.; Chen, H.; Chen, C.-C.; Plaza, J. M.; Dugas, R.; Rochelle, G. T. *Ind. Eng. Chem. Res.* **2009**, *48*, 9233.
66. da Silva, E. F.; Svendsen, H. F. *Int. J. Greenh. Gas Control* **2007**, *1*, 151.
67. le Bouhelec, E. B.; Mougine, P.; Barreau, A.; Solimando, R. *Energy & Fuels* **2007**, *21*, 2044.
68. Strazisar, B. R.; Anderson, R. R.; White, C. M. *Energy & Fuels* **2003**, *17*, 1034.
69. Li, Y.; Paul Wang, H.; Liao, C.-Y.; Zhao, X.; Hsiung, T.-L.; Liu, S.-H.; Ted Chang, S.-G. *Environ. Sci. Technol.* **2017**, (DOI: 10.1021/acs.est.7b00006).
70. Kozak, F.; Petig, A.; Morris, E.; Rhudy, R.; Thimsen, D. *Energy Procedia* **2009**, *1*, 1419.
71. Vericella, J. J.; Baker, S. E.; Stolaroff, J. K.; Duoss, E. B.; Hardin IV, J. O.; Lewicki, J.; Glogowski, E.; Floyd, W. C.; Valdez, C. A.; Smith, W. L.; Satcher Jr., J. H.; Bourcier, W. L.; Spadaccini, C. M.; Lewis, J. A.; Aines, R. D. *Nat. Commun.* **2015**, *6*, (doi:10.1038/ncomms7124).
72. Berger, A. H.; Bhowan, A. S. *Energy Procedia* **2013**, *37*, 25.
73. Abunowara, M.; Elgarni, M. *Energy Procedia* **2013**, *37*, 16.
74. Glier, J. C.; Rubin, E. S. *Energy Procedia* **2013**, *37*, 65.
75. Ünverena, E. E.; Monkula, B. Ö.; Sarioğlana, Ş.; Karademira, N.; Alper, E. *Petroleum* **2017**, *3*, 37.
76. Wang, Q.; Luo, J.; Zhong, Z.; Borgna, A. *Energy Environ. Sci.* **2011**, *4*, 42.
77. Hedin, N.; Andersson, L.; Bergström, L.; Yan, J. *Appl. Energy* **2013**, *104*, 418.
78. Andersen, A.; Divekar, S.; Dasgupta, S.; Cavka, J. H.; Aarti, Nanoti, A.; Spjelkavik, A.; Goswami, A. N.; Garg, M. O.; Blom, R. *Energy Procedia* **2013**, *37*, 33.
79. Zhang, J.; Webley, P. A.; Xiao, P. *Energy Convers. Manage.* **2008**, *49*, 346.
80. Schell, J.; Casas, N.; Marx, D.; Blom, R.; Mazzotti, M. *Energy Procedia* **2013**, *37*, 167.
81. Ho, M. T.; Allinson, G. W.; Wiley, D. E. *Ind. Eng. Chem. Res.* **2008**, *47*, 4883.
82. Xiao, P.; Zhang, J.; Webley, P.; Li, G.; Singh, R.; Todd, R. *Adsorption* **2008**, *14*, 575.
83. Zhang, J.; Webley, P. A. *Environ. Sci. Technol.* **2008**, *42*, 563.
84. Aaron, D.; Tsouris, C. *Sep. Sci. Technol.* **2005**, *40*, 321.
85. Liu, Z.; Grande, C. A.; Li, P.; Yu, J.; Rodrigues, A. E. *Sep. Purif. Technol.* **2011**, *81*, 307.
86. Cejka, J.; Corma, A.; Zones, I. S. *Zeolites and Catalysis: Synthesis, Reactions and Applications*, Wiley-VCH: Weinheim, Germany, **2010**.
87. Kusakabe, K.; Kuroda, T.; Murata, A.; Morooka, S. *Ind. Eng. Chem. Res.* **1997**, *36*, 649.

88. Cavenati, S.; Grande, C. A.; Rodrigues, A. E. *J. Chem. Eng. Data* **2004**, *49*, 1095.
89. Cavenati, S.; Grande, C. A.; Rodrigues, A. E. *Chem. Eng. Sci.* **2006**, *61*, 3893.
90. Himeno, S.; Tomita, T.; Suzuki, K.; Yoshida, S. *Microporous Mesoporous Mater.* **2007**, *98*, 62.
91. Ghoufi, A.; Gaberova, L.; Rouquerol, J.; Vincent, D.; Llewellyn, P. L.; Maurin, G. *Microporous Mesoporous Mater.* **2009**, *119*, 117.
92. Liang, Z.; Marshall, M.; Chaffee, A. L. *Energy Procedia* **2009**, *1*, 1265.
93. García, E. J.; Perez-Pellitero, J.; Pirngruber, G. D.; Jallut, C.; Palomino, M.; Rey, F.; Valencia, S. *Ind. Eng. Chem. Res.* **2014**, *53*, 9860.
94. Lee, J.-S.; Kim, J.-H.; Kim, J.-T.; Suh, J.-K.; Lee, J.-M.; Lee, C.-H. *J. Chem. Eng. Data* **2002**, *47*, 1237.
95. Wang, Y.; LeVan, M. D. *J. Chem. Eng. Data* **2009**, *54*, 2839.
96. O'Keefe, M.; Peskov, M. A.; Ramsden, S. J.; Yaghi, O. M. *Acc. Chem. Res.* **2008**, *41*, 1782.
97. Jiang, J.; Yu, J.; Corma, A. *Angew. Chem. Int. Ed.* **2010**, *49*, 3120.
98. Palomino, M.; Corma, A.; Rey, F.; Valencia, S. *Langmuir* **2010**, *26*, 1910.
99. Remy, T.; Peter, S. A.; Tendeloo, L. V.; Van der Perre, S.; Lorgouilloux, Y.; Kirschhock, C. E. A.; Baron, G. V.; Denayer, J. F. M. *Langmuir* **2013**, *29*, 4998.
100. Hudson, M. R.; Queen, W. L.; Mason, J. A.; Fickel, D. W.; Lobo, R. F.; Brown, C.M. *J. Am. Chem. Soc.* **2012**, *134*, 1970.
101. Cheung, O.; Hedin, N. *RSC Adv.* **2014**, *4*, 14480.
102. Zhang, J.; Webley, P. A.; Xiao, P. *Energy Convers. Manage.* **2008**, *49*, 346.
103. Li, G.; Xiao, P.; Webley, P.; Zhang, J.; Singh, R.; Marshall, M. *Adsorption* **2008**, *14*, 415.
104. Li, G.; Xiao, P.; Webley, P.; Zhang, J.; Singh, R. *Energy Procedia* **2009**, *1*, 1123.
105. Wickramaratne, N. P.; Jaroniec, M. *ACS Appl. Mater. Interfaces* **2013**, *5*, 1849.
106. Drage, T. C.; Blackman, J. M.; Pevida, C.; Snape, C. E. *Energy & Fuels* **2009**, *23*, 2790.
107. Creamer, A. E.; Gao, B. *Environ. Sci. Technol.* **2016**, *50*, 7276.
108. Choi, S.; Drese, J. H.; Jones, C. W. *ChemSusChem* **2009**, *2*, 796.
109. Furukawa, H.; Cordova, K. E.; O'Keefe, M.; Yaghi, O. M. *Science* **2013**, *341*, 974.
110. James, S. L. *Chem. Soc. Rev.* **2003**, *32*, 276.
111. Long, J. R.; Yaghi, O. M. *Chem. Soc. Rev.* **2009**, *38*, 1213.
112. Zhou, H.-C.; Long, J. R.; Yaghi, O. M. *Chem. Rev.* **2012**, *112*, 673.
113. Zhou, H.-C.; Kitagawa, S. *Chem. Soc. Rev.* **2014**, *43*, 5415.
114. Yaghi, O. M.; Li, H.; Davis, C.; Richardson, D.; Groy, T. L. *Acc. Chem. Res.* **1998**, *31*, 474.
115. Czaja, A. U.; Trukhan, N.; Müller, U. *Chem. Soc. Rev.* **2009**, *38*, 1284.
116. Kuppler, R. J.; Timmons, D. J.; Fang, Q.-R.; Li, J.-R.; Makal, T. A.; Young, M. D.; Yuan, D.; Zhao, D.; Zhuang, W.; Zhou, H.-C. *Coord. Chem. Rev.* **2009**, *253*, 3042.
117. Mueller, U.; Schubert, M.; Teich, F.; Puetter, H.; Schierle-Arndt, K.; Pastre, J. *J. Mater. Chem.* **2006**, *16*, 626.
118. Furukawa, H.; Ko, N.; Go, Y. B.; Aratani, N.; Choi, S. B.; Choi, E.; Yazaydin, A. Ö.; Snurr, R. Q.; O'Keefe, M.; Kim, J.; Yaghi, O. M. *Science* **2010**, *329*, 424.

119. Eddaoudi, M.; Moler, D. B.; Li, H.; Chen, B.; Reineke, T. M.; O'Keeffe, M.; Yaghi, O. M. *Acc. Chem. Res.* **2001**, *34*, 319.
120. Phan, A.; Doonan, C. J.; Uribe-Romo, F. J.; Knobler, C. B.; O'Keeffe, M.; Yaghi, O. M. *Acc. Chem. Res.* **2010**, *43*, 58.
121. O'Keeffe, M.; Yaghi, O. M. *Chem. Rev.* **2012**, *112*, 675.
122. Furukawa, H.; Go, Y. B.; Ko, N.; Park, Y. K.; Uribe-Romo, F. J.; Kim, J.; O'Keeffe, M.; Yaghi, O. M. *Inorg. Chem.* **2011**, *50*, 9147.
123. Furukawa, H.; Müller, U.; Yaghi, O. M. *Angew. Chem. Int. Ed.* **2015**, *54*, 3417.
124. Wang, L. J.; Deng, H.; Furukawa, H.; Gándara, F.; Cordova, K. E.; Peri, D.; Yaghi, O. M. *Inorg. Chem.* **2014**, *53*, 5881.
125. Eddaoudi, M.; Kim, J.; Rosi, N.; Vodak, D.; Wachter, J.; O'Keeffe, M.; Yaghi, O. M. *Science* **2002**, *295*, 469.
126. Thommes, M.; Kaneko, K.; Neimark, A. V.; Olivier, J. P.; Rodriguez-Reinoso, F.; Rouquerol, J.; Sing, K. S. W. *Pure Appl. Chem* **2015**, *87*, 1051.
127. Sing, K. S. W.; Everett, D. H.; Haul, R. A. W.; Moscou, L.; Pierotti, R. A.; Rouquerol, J.; Siemieniowska, T. *Pure Appl. Chem* **1985**, *57*, 603.
128. Forster, S.; Plantenberg, T. *Angew. Chem. Int. Ed.* **2002**, *41*, 688.
129. Qiu, L.-G.; Xu, T.; Li, Z.-Q.; Wang, W.; Wu, Y.; Jiang, X.; Tian, X.-Y.; Zhang, L.-D. *Angew. Chem. Int. Ed.* **2008**, *47*, 9487.
130. Stock, N.; Biswas, S. *Chem. Rev.* **2012**, *112*, 933.
131. Dey, C.; Kundu, T.; Biswal, B. P.; Mallick, A.; Banerjee, R. *Acta Cryst.* **2014**, *B70*, 3.
132. Bosch, M.; Yuan, S.; Rutledge, W.; Zhou, H.-C. *Acc. Chem. Res.* **2017**, *50*, 857.
133. Da Silva, G. G.; Silva, C. S.; Ribeiro, R. T.; Ronconi, C. M.; Barros, B. S.; Neves, J. L.; Júnior, S. A. *Synth. Met.*, **2016**, *220*, 369.
134. Bauer, S.; Serre, C.; Devic, T.; Horcajada, P.; Marrot, J.; Férey, G.; Stock, N. *Inorg. Chem.* **2008**, *47*, 7868.
135. Ahnfeldt, T.; Guillou, N.; Gunzelmann, D.; Margiolaki, I.; Loiseau, T.; Férey, G.; Senker, J.; Stock, N. *Angew. Chem. Int. Ed.* **2009**, *48*, 5163.
136. Long, P.; Wu, H.; Zhao, Q.; Yang, Y.; Dong, J.; Li, J. *Microporous Mesoporous Mater.* **2011**, *142*, 489.
137. Loiseau, T.; Mellot-Draznieks, C.; Muguerra, H.; Férey, G.; Haouas, M.; Taulelle, F. *C. R. Chim.* **2005**, *8*, 765.
138. Senkowska, I.; Hoffmann, F.; Froba, M.; Getzschmann, J.; Bohlmann, W.; Kaskel, S. *Microporous Mesoporous Mater.* **2009**, *122*, 93.
139. Senkowska, I.; Kaskel, S. *Eur. J. Inorg. Chem.* **2006**, 4564 (DOI: 10.1002/ejic.200600635).
140. Hao, X.-R.; Wang, X.-L.; Shao, K.-Z.; Yang, G.-S.; Su, Z.-M.; Yuan, G. *CrystEngComm.* **2012**, *14*, 5596.
141. Peng, L.; Zhang, J.; Xue, Z.; Han, B.; Sang, X.; Liu, C.; Yang, G. *Nat. Commun.* **2014**, *5*, 4465.
142. Ding, R.; Huang, C.; Lu, J.; Wang, J.; Song, C.; Wu, J.; Hou, H.; Fan, Y. *Inorg. Chem.* **2015**, *54*, 1405.
143. Banerjee, R.; Furukawa, H.; Britt, D.; Knobler, C.; O'Keeffe, M.; Yaghi, O. M. *J. Am. Chem. Soc.* **2009**, *131*, 3875.
144. Sekizkardes, A. K.; Culp, J. T.; Islamoglu, T.; Marti, A.; Hopkinson, D.; Myers, C.; Elkaderic, H. M.; Nulwala, H. B. *Chem. Commun.* **2015**, *51*, 13393.
145. Bloch, W. M.; Babarao, R.; Hill, M. R.; Doonan, C. J.; Sumbly, C. J. *J. Am. Chem. Soc.* **2013**, *135*, 10441.

146. Nandi, S.; Haldar, S.; Chakraborty, D.; Vaidhyathan, R. *J. Mater. Chem. A* **2017**, *5*, 535.
147. Zhang, Z.; Yao, Z.-Z.; Xiang, S.; Chen, B. *Energy Environ. Sci.* **2014**, *7*, 2868.
148. Kang, Z.; Xue, M.; Fan, L.; Huang, L.; Guo, L.; Wei, G.; Chen, B.; Qiu, S. *Energy Environ. Sci.* **2014**, *7*, 4053.
149. Xiang, S.; He, Y.; Zhang, Z.; Wu, H.; Zhou, W.; Krishna, R.; Chen, B. *Nat. Commun.* **2012**, *954*, 1.
150. Horike, S.; Shimomura, S.; Kitagawa, S. *Nat. Chem.* **2009**, *1*, 695.
151. Britt, D.; Furukawa, H.; Wang, B.; Glover, T. G.; Yaghi, O. M. *Proc. Natl. Acad. Sci. U. S. A.* **2009**, *106*, 20637.
152. Pentylala, V.; Davydovskaya, P.; Ade, M.; Pohle, R.; Urban, G. *Sens. Actuator B-Chem.* **2016**, *225*, 363.
153. He, Y.; Chen, B. *Encyclopedia of Inorganic and Bioinorganic Chemistry* **2014**, (DOI: 10.1002/9781119951438.eibc2213).
154. Park, J.; Kim, H.; Han, S. S.; Jung, Y. *J. Phys. Chem. Lett.* **2012**, *3*, 826.
155. Hou, X.-J.; He, P.; Li, H.; Wang, X. *J. Phys. Chem. C* **2013**, *117*, 2824.
156. Dietzel, P. D. C.; Johnsen, R. E.; Fjellvag, H.; Bordiga, S.; Groppo, E.; Chavanc, S.; Blom, R. *Chem. Commun.* **2008**, 5125.
157. Queen, W. L.; Brown, C. M.; Britt, D. K.; Zajdel, P.; Hudson, M. R.; Yaghi, O. M. *J. Phys. Chem. C* **2011**, *115*, 24915.
158. Lin, L. C.; Kim, J.; Kong, X.; Scott, E.; McDonald, T. M.; Long, J. R.; Reimer, J. A.; Smit, B. *Angew. Chem. Int. Ed.* **2013**, *52*, 4410.
159. Kong, X.; Scott, E.; Ding, W.; Mason, J. A.; Long, J. R.; Reimer, J. A. *J. Am. Chem. Soc.* **2012**, *134*, 14341.
160. Poloni, R.; Smit, B.; Neaton, J. B. *J. Phys. Chem. A* **2012**, *116*, 4957.
161. Dzubak, A. L.; Lin, L.-C.; Kim, J.; Swisher, J. A.; Poloni, R.; Maximoff, S. N.; Smit, B.; Gagliardi, L. *Nat. Chem.* **2012**, *4*, 810.
162. Becker, T. M.; Heinen, J.; Dubbeldam, D.; Lin, L.-C.; Vlugt, T. J. H. *J. Phys. Chem. C* **2017**, *121*, 4659.
163. Glover, T. G.; Peterson, G. W.; Schindler, B. J.; Britt, D.; Yaghi, O. *Chem. Eng. Sci.* **2011**, *66*, 163.
164. Bae, T.-H.; Long, J. R. *Energy Environ. Sci.* **2013**, *6*, 3565.
165. Bao, Z.; Yu, L.; Ren, Q.; Lu, X.; Deng, S. J. *Colloid Interface Sci.* **2011**, *353*, 549.
166. Yazaydin, A. O.; Snurr, R. Q.; Park, T. H.; Koh, K.; Liu, J.; LeVan, M. D.; Benin, A. I.; Jakubczak, P.; Lanuza, M.; Galloway, D. B.; Low, J. L.; Willis, R. R. *J. Am. Chem. Soc.* **2009**, *131*, 18198.
167. McDonald, T. M.; Lee, W. R.; Mason, J. A.; Wiers, B. M.; Seop Hong, C.; Long, J. R. *J. Am. Chem. Soc.* **2012**, *134*, 7056.
168. Yu, J.; Balbuena, P. B. *J. Phys. Chem. C* **2013**, *117*, 3383.
169. Yu, K.; Kiesling, K.; Schmidt, J. R. *J. Phys. Chem. C* **2012**, *116*, 20480.
170. Yazaydin, A. O.; Benin, A. I.; Faheem, S. A.; Jakubczak, P.; Low, J. J.; Willis, R. R.; Snurr, R. Q. *Chem. Mater.* **2009**, *21*, 1425.
171. Liu, J.; Wang, Y.; Benin, A. I.; Jakubczak, P.; Willis, R. R.; LeVan, M. D. *Langmuir* **2010**, *26*, 14301.
172. Yu, K.; Schmidt, J.R. *J. Phys. Chem. C* **2013**, *117*, 3192.
173. Yu, J.; Wu, Y.; Balbuena, P. B. *ACS Sustainable Chem. Eng.* **2016**, *4*, 2387.
174. Wang, X.; Li, H.; Hou, X.-J. *J. Phys. Chem. C* **2012**, *116*, 19814.
175. Arstad, B.; Fjellvåg, H.; Kongshaug, K. O.; Swang, O.; Blom, R. *Adsorption* **2008**, *14*, 755.

176. Millward, A. R.; Yaghi, O. M. *J. Am. Chem. Soc.* **2005**, *127*, 17998.
177. Fracaroli, A. M.; Furukawa, H.; Suzuki, M.; Dodd, M.; Okajima, S.; Gándara, F.; Reimer, J. A.; Yaghi, O. M. *J. Am. Chem. Soc.* **2014**, *136*, 8863.
178. Chen, C.; Kim, J.; Park, D.-W.; Ahn, W.-S. *Mater. Lett.* **2013**, *106*, 344.
179. Wang, X.; Li, H.; Hou, X.-J. *J. Phys. Chem. C* **2012**, *116*, 19814.
180. McDonald, T. M.; D'Alessandro, D. M.; Krishna, R.; Long, J. R. *Chem. Sci.* **2011**, *2*, 2022.
181. Demessence, A.; D'Alessandro, D. M.; Foo, M. L.; Long, J. R. *J. Am. Chem. Soc.* **2009**, *131*, 8784.
182. Zhang, Z.; Zhao, Y.; Gong, Q.; Li, Z.; Li, J. *Chem. Commun.* **2013**, *49*, 653.
183. Zheng, B.; Bai, J.; Duan, J.; Wojtas, L.; Zaworotko, M. J. *J. Am. Chem. Soc.* **2011**, *133*, 748.
184. Liao, P.-Q.; Chen, H.; Zhou, D.-D.; Liu, S.-Y.; He, C.-T.; Rui, Z.; Ji, H.; Zhang, J.-P.; Chen, X.-M. *Energy Environ. Sci.* **2015**, *8*, 1011.
185. Lee, W. R.; Jo, H.; Yang, L.-M.; Lee, H.; Ryu, D. W.; Lim, K. S.; Song, J. H.; Min, D. Y.; Han, S. S.; Seo, J. G.; Park, Y. K.; Moon, D.; Hong, C. S. *Chem. Sci.* **2015**, *6*, 3697.
186. An, J.; Geib, S. J.; Rosi, N. L. *J. Am. Chem. Soc.* **2010**, *132*, 38.
187. Serre, C.; Millange, F.; Thouvenot, C.; Nogues, M.; Marsolier, G.; Louer, D.; Férey, G. *J. Am. Chem. Soc.* **2002**, *124*, 13519.
188. Aguado, S.; Bergeret, G.; Titus, M. P.; Moizan, V.; Nieto-Draghi, C.; Bats, N.; Farrusseng, D. *New J. Chem.* **2011**, *35*, 546.
189. Fairen-Jimenez, D.; Moggach, S. A.; Wharmby, M. T.; Wright, P. A.; Parsons, S.; Duren, T. *J. Am. Chem. Soc.* **2011**, *133*, 8900.
190. Chokbunpiam, T.; Chanajaree, R.; Remsungnen, T.; Saengsawang, O.; Fritzsche, S.; Chmelik, C.; Caro, J.; Janke, W.; Hannongbua, S. *Microporous Mesoporous Mater.* **2014**, *187*, 1.
191. Moggach, S. A.; Bennett, T. D.; Cheetham, A. K. *Angew. Chem. Int. Ed.* **2009**, *48*, 7087.
192. Bennett, T. D.; Goodwin, A. L.; Dove, M. T.; Keen, D. A.; Tucker, M. G.; Barney, E. R.; Soper, A. K.; Bithell, E. G.; Tan, J.-C.; Cheetham, A. K. *Phys. Rev. Lett.* **2010**, *104*, 115503.
193. Wu, H.; Reali, R. S.; Smith, D. A.; Trachtenberg, M. C.; Li, J. *Chem. Eur. J.* **2010**, *16*, 13951.
194. Wriedt, M.; Sculley, J. P.; Yakovenko, A. A.; Ma, Y.; Halder, G. J.; Balbuena, P. B.; Zhou, H.-C. *Angew. Chem. Int. Ed.* **2012**, *51*, 9804.
195. Choi, H.-S.; Suh, M. P. *Angew. Chem. Int. Ed.* **2009**, *48*, 6865.
196. Lyndon, R.; Konstas, K.; Ladewig, B. P.; Southon, P. D.; Kepert, C. J.; Hill, M. R. *Angew. Chem. Int. Ed.* **2013**, *52*, 3695.
197. Henke, S.; Schmid, R.; Grunwaldt, J.-D.; Fischer, R. A. *Chem. Eur. J.* **2010**, *16*, 14296.
198. Henke, S.; Schneemann, A.; Wutscher, A.; Fischer, R. A. *J. Am. Chem. Soc.* **2012**, *134*, 9464.
199. Henke, S.; Fischer, R. A. *J. Am. Chem. Soc.* **2011**, *133*, 2064.
200. Kim, M.; Cahill, J. F.; Fei, H.; Prather, K. A.; Cohen, S. M. *J. Am. Chem. Soc.* **2012**, *134*, 18082.
201. Lau, C. H.; Babarao, R.; Hill, M. R. *Chem. Commun.* **2013**, *49*, 3634.
202. Smith, S. J. D.; Ladewig, B. P.; Hill, A. J.; Lau, C. H.; Hill, M. R. *Sci. Rep.* **2015**, *5*, 7823.
203. Han, S. S.; Jung, D.-H.; Heo, J. *J. Phys. Chem. C* **2013**, *117*, 71.

204. Du, L.; Lu, Z.; Zheng, K.; Wang, J.; Zheng, X.; Pan, Y.; You, X.; Bai, J. *J. Am. Chem. Soc.* **2013**, *135*, 562.
205. Subramanian, S.; Zaworotko, M. J. *Angew. Chem. Int. Ed.* **1995**, *34*, 2559.
206. Lin, M. J.; Jouaiti, A.; Kyritsakas, N.; Hosseini, M. W. *CrystEngComm.* **2009**, *11*, 189.
207. Uemura, K.; Maeda, A.; Maji, T. K.; Kanoo, P.; Kita, H. *Eur. J. Inorg. Chem.* **2009**, 2329.
208. Burd, S. D.; Ma, S.; Perman, J. A.; Sikora, B. J.; Snurr, R. Q.; Thallapally, P. K.; Tian, J.; Wojtas, L.; Zaworotko, M. J. *J. Am. Chem. Soc.* **2012**, *134*, 3663.
209. Nugent, P.; Belmabkhout, Y.; Burd, S. D.; Cairns, A. J.; Luebke, R.; Forrest, K.; Pham, T.; Ma, S.; Space, B.; Wojtas, L.; Eddaoudi, M.; Zaworotko, M. J. *Nature* **2013**, *495*, 80.
210. Nandi, S.; Collins, S. P.; Chakraborty, D.; Banerjee, D.; Thallapally, P. K.; Woo, T. K.; Vaidhyanathan, R. *J. Am. Chem. Soc.* **2017**, *139*, 1734.
211. Vaidhyanathan, R.; Iremonger, S. S.; Dawson, K. W.; Shimizu, G. K. H. *Chem. Commun.* **2009**, 5230.
212. Vaidhyanathan, R.; Iremonger, S. S.; Shimizu, G. K. H.; Boyd, P. G.; Alavi, S.; Woo, T. K. *Science* **2010**, *330*, 650.
213. Vaidhyanathan, R.; Iremonger, S. S.; Shimizu, G. K. H.; Boyd, P. G.; Alavi, S.; Woo, T. K. *Angew. Chem. Int. Ed.* **2012**, *51*, 1826.

Chapter 2



Ultra-microporous metal organic frameworks built from rigid linkers showing solvent and temperature induced structural transformation

2.1 Introduction

Metal organic frameworks (MOFs) are highly crystalline compounds and have demonstrated promise in several applications, among which gas adsorption is the most prominent.¹⁻⁸ Their periodic structures formed with the combination of metal ions/clusters and organic struts, contain regular voids filled with a variety of guests such as solvent molecules, counter anions and cations, this modular construct makes them pertinent candidates for different applications.¹⁻⁶ MOFs with their microporous/micro-mesoporous structure can be chemically tuned to be sorbents selective to Carbon-dioxide (CO₂). Thus can actually help mitigate the adverse effects of the increasing levels of this green-house gas in the atmosphere.^{1,9-20} The architecture of these periodic materials can be tuned by the choice of the metal ions and organic linkers.^{3,21-27} Depending on the pore dimensions, microporous MOFs are further sub-classified into ultra-microporous MOFs (UMMOFs, pore size less than 6 Å). UMMOFs can be potential candidates for selective sequestration of CO₂ from flue gas, the industrial effluent typically occurring as black smoke at the outlet of a chimney, where the partial pressure of CO₂ is considerably less as compared to N₂.³ Another interesting feature of the MOFs is their framework dynamicity, which can be triggered by external stimuli like temperature, solvent, pressure etc. Such dynamic MOFs are termed as **3rd generation MOFs**.^{16,28-31} Framework dynamicity generally arises from the flexibility of the metal-ligand coordination or the presence of long, flexible linkers. Such dynamic frameworks are typically associated with large pore structures constructed from relatively long linkers.³²⁻³⁴ Sometimes MOFs with small linkers but large pores are also known to show dynamic behaviour.³⁵⁻³⁷ Lack of such framework flexibility in ultra-microporous MOFs is expected as they are built from short and rigid chelating linkers.³⁸⁻⁴¹

Though the structure of MOFs can be regulated easily, it is still a challenge to construct UMMOFs with desired sorption and separation properties, since their performances depend on various other factors like temperature, solvent, counter anions etc.³²⁻³⁴ Further, their porosities can be strongly impacted by subtle geometrical (bond angles and bond lengths) and orientational changes in the framework components. For practical applications these UMMOFs need to have significantly large surface area for good capacity and small pores to obtain high

selectivity.¹⁻¹⁰ High selectivity arises generally from molecular sieving, strong framework-gas and gas-gas interactions within their pore confinement. Typically such ultra-micropores are achieved by combining short linkers with metal ions or metal clusters.³⁸⁻⁴¹ One of the best suited designs would be to construct an UMMOF with the pores lined up with polarizing functionalities such as oxalates, hydroxyl, amine groups, to impart good CO₂ adsorption characteristics.³⁸⁻⁴¹

Considering these CO₂ interactive-design aspects, oxalic acid (H₂Ox) and aminotriazoles (Hatz) linkers were employed to obtain two novel Cobalt based ultra-microporous frameworks [Co(C₂O₄)(C₂N₄H₄)](H₂O)₄ (**1**) and [Co₂(C₂O₄)₂(C₂N₄H₄)₃](CH₃OH) (**2**). While **1** adopts a 4-Connected Diamondoid (*Dia*) topology, **2** (obtained by a variation in the synthetic procedure) adopts a more open 3-connected Thorium Silicide (*ThSi*₂) topology, due to the different binding modes of aminotriazoles. Interestingly, despite their strong and rigid linkers, both these frameworks show structural flexibility: **1** shows a guest dependent structural flexibility arising from the unbuckling of the Co-oxalate (Co-Ox) and Co-aminotriazole (Co-Hatz) chains and **2** shows a temperature dependent structural transition arising due to the rotation of the μ-2 bridging aminotriazole units resulting into sliding of the Co-Ox chains. Although the MOFs presented in this chapter are not sufficiently high-reaching in the aspects of CO₂ adsorption capacity, still they provide some new insights. Importantly, they demonstrate that the ultra-microporous frameworks built up of rigid struts can show stimuli dependent structural flexibility, representing a member of the class of **3rd generation MOFs**. Here, a detailed investigation to point out the key structural features responsible for the flexibility and the loss of porosity in this rather rigid ultra-microporous MOFs are presented.

2.2 Experimental section

2.2.1 Materials: All chemicals used were from the commercially available sources without any further purification.

2.2.2 Physical measurements:

2.2.2.1 Powder X-ray diffraction: Powder XRDs were carried out using a Rigaku Miniflex-600 instrument and processed using PDXL software.

2.2.2.2 Variable temperature powder X-ray diffraction: VT-PXRD patterns were measured on Bruker D8 Advanced X-Ray diffractometer at different temperatures using Cu-K α radiation ($\lambda = 1.5406 \text{ \AA}$) with a scan speed of $0.5^\circ \text{ min}^{-1}$ and a step size of 0.01° in 2 theta.

2.2.2.3 Thermo-gravimetric analysis: Thermo-gravimetric analysis was carried out on NETSZCH TGA-DSC system. The TGAs were done under N₂ gas flow (50ml/min) and samples were heated from RT to 550°C at 2°C/min.

2.2.2.4 Single crystal X-ray diffraction: Single Crystal data was collected using Bruker Single crystal X-ray diffractometer, at wavelength: 1.5418 Å. Single-crystal data was collected on a Bruker SMART APEX four-circle diffractometer equipped with a CMOS photon 100 detector (Bruker Systems Inc.) and with a Cu K α radiation (1.5418 Å). The incident X-ray beam was focused and monochromated using Microfocus (I μ S). Crystal of **1**, **1*** and **2** was mounted on nylon Cryo loops with Paratone-N oil. Data were collected at 100 K and integrated using Bruker SAINT Software and corrected for absorption using SADABS. Structures were solved by Intrinsic Phasing module of the direct methods and refined using the SHELXTL 2014 software suite. All non-hydrogen atoms were located from iterative examination of difference F-maps following which the structure was refined using least-squares method. Hydrogen atoms were placed geometrically and placed in a riding model.

2.2.2.5 Infra-red spectrophotometry: IR was recorded in attenuated total reflectance (ATR) mode on neat samples on a Bruker Alpha spectrophotometer.

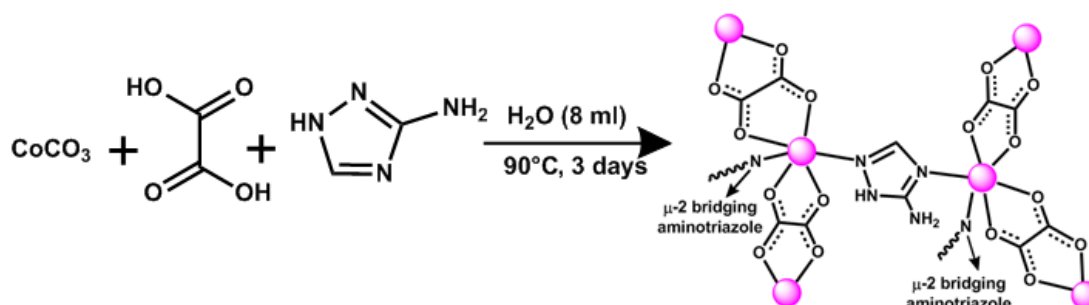
2.2.2.6 Adsorption: Adsorption studies were done on 3-Flex sorption and Quantachrome IQ adsorption analyser. All of the gases used were of 99.999% purity. For fitting the isotherms, BET and Langmuir methods were employed. For pore size distribution calculation NLDFT was used. Heat of adsorption calculation was done by Virial method.

2.2.2.7 Elemental analysis: Elemental analyses were performed on a Vario-EL cube elemental analyser.

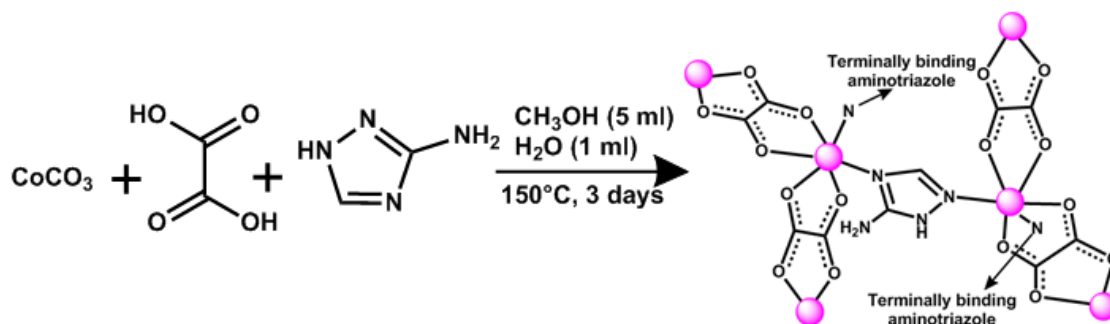
2.2.3 Synthesis

2.2.3.1 Synthesis of $[\text{Co}(\text{C}_2\text{O}_4)(\text{C}_2\text{N}_4\text{H}_4)](\text{H}_2\text{O})_4$ (1): In a typical synthesis of **1**, 0.1 g of CoCO_3 , 0.0736 g of oxalic acid and 0.3563 g of 3-aminotriazole (Hatz) were added in 8 ml of H_2O solvent, in a 23 ml autoclave, which was stirred for 30 minutes at room temperature and then made to react hydrothermally at 90°C for 3 days (*Scheme 2.1*). On cooling, pink square shaped crystals, suitable for single crystal X-ray diffraction analysis were obtained. Bulk sample was then washed with copious amount of H_2O : CH_3OH (1:1, 5 ml each) to remove any unreacted organics and then dried in air, FT-IR (cm^{-1}): 3930, 3875, 3737, 3618, 3559, 3505, 3398, 3367, 3347, 3104, 3083, 2993, 2771, 2310, 1619, 1523, 1316, 1212, 1055, 984, 879, 792, 680. Analytical data observed (%): C (15.47), H (3.65), N (18.86); calculated (%): C (15.85), H (3.99), N (18.49).

2.2.3.2 Synthesis of $[\text{Co}_2(\text{C}_2\text{O}_4)_2(\text{C}_2\text{N}_4\text{H}_4)_3](\text{CH}_3\text{OH})$ (2): In a typical synthesis of **2**, 0.1 g of CoCO_3 , 0.0736 g of oxalic acid and 0.3563 g of 3-aminotriazole (Hatz) were added in a mixture of 1 ml H_2O + 5 ml CH_3OH , in a 23 ml autoclave. The reaction was stirred for 30 minutes at room temperature and then made to react solvothermally at 150°C for 3 days (*Scheme 2.2*). On cooling, red octahedral shaped crystals, suitable for single crystal X-ray diffraction were obtained. Bulk sample was then washed with copious amount of H_2O : CH_3OH (1:1, 5 ml each) to remove any unreacted organics and then dried in air, FT-IR (cm^{-1}): 3934, 3872, 3731, 3605, 3383, 3192, 3117, 2981, 2860, 2785, 2320, 2120, 2071, 1613, 1523, 1344, 1297, 1211, 1064, 969, 868, 783, 704. Analytical data observed (%): C (22.52), H (2.32), N (29.39); calculated (%): C (22.85), H (2.79), N (29.07).



Scheme 2.1 Synthesis scheme of $[\text{Co}(\text{C}_2\text{O}_4)(\text{C}_2\text{N}_4\text{H}_4)](\text{H}_2\text{O})_4$ (**1**); the pink spheres represents the Co^{2+} ions.



Scheme 2.2 Synthesis scheme of $[\text{Co}(\text{C}_2\text{O}_4)_2(\text{C}_2\text{N}_4\text{H}_4)_3](\text{CH}_3\text{OH})$ (**2**); the pink spheres represents the Co^{2+} ions.

2.3 Results and discussions

2.3.1 Synthesis

Compound **1** was obtained under hydrothermal condition by reacting CoCO_3 , oxalic acid and Hatz in the stoichiometric ratio of 1:1:5 with water as solvent at temperature 90°C for 3 days (*Scheme 2.1*). Whereas, compound **2** was obtained under solvothermal condition by reacting CoCO_3 , oxalic acid and 3-aminotriazole in a stoichiometric ratio 1:1:5 with methanol (5 ml)-water (1 ml) as solvent system at 150°C for 3 days (*Scheme 2.2*). Synthesis of **2** was attempted also using other solvent mixtures like ethanol-water and propanol-water etc. From the single crystal analysis as well as the bulk analysis from PXRD it was observed that all combinations of alcohol-water solvent mixtures produced the same MOF irrespective of the alcohols used as the synthesis solvent. In the crystals grown from the methanol and ethanol, they could be located in the pores using SCXRD, but in the case of higher alcohols only the occluded water molecules were found in the framework pores.

2.3.2 Crystal structures

Compound **1** crystallizes in monoclinic $\text{P}2_1/\text{c}$ space group (*Appendix A2.1*). The asymmetric unit consists of one Co^{2+} metal ion, one oxalate and one neutral aminotriazole linker and four solvent water molecules. The metal centres have octahedral coordination environment.

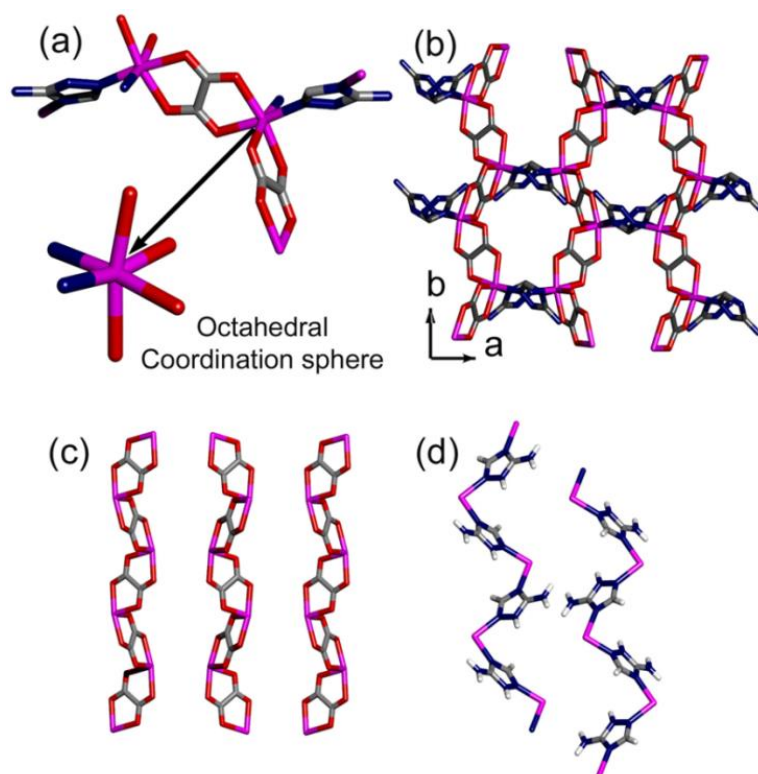


Figure 2.1 (a) The molecular unit of **1** and the octahedral coordination environment of Co^{2+} , (b) crystal structure view along c-axis (solvents have been removed for clarity). The oxalate lining and the basic free primary amine groups protruding inside the pores can be seen, (c) Co-Ox chains running along the b-axis, and (d) Co-Hatz chains which are running through the plane of the paper (c-axis). Colour Code: Cobalt: magenta, Nitrogen: blue, Oxygen: red, Carbon: grey.

Four of the coordination sites are satisfied by two bidentate chelating oxalates and the other two are from singly binding neutral aminotriazole units (Hatz). Importantly, the Hatz units adopt a μ -2 bridging mode (*Appendix A2.2*). Figure 2.1 shows the view along the c-axis. The structure is made up of Co-Ox and Co-Hatz chains linked together. It is interesting to note that the porous channels along c-axis are lined with the polarizing oxalate groups and the basic free amines protruding inside the pores (*Figure 2.1*). The porous channels are filled with solvent water molecules (*Appendix A2.5*). Importantly, set side by side with $\text{Zn}(\text{Atz})_2$ MOF,⁴² (Atz: aminotriazolate) which was built entirely from μ -2 bridging aminotriazolate units, in the present case, μ -2 bridging Atz units have been replaced by two rigidly chelating oxalate units. Hence a more rigid framework could be anticipated. A PLATON-squeeze analysis of the crystal structure of **1** revealed the presence of 35% solvent accessible void. There is an underlying higher symmetry to the framework. When the oxalates and aminotriazoles are reduced to linear linkers, the coordination around

the Co metal centre is tetrahedral, i.e. it bears a 4-connected net. Such tetrahedra are linked by oxalate and aminotriazole ligands into adamantane type units. Topological analysis reveal that it forms a Diamondoid (Dia) topology with uni-nodal {6, 6} connected network, with vertex symbol as $[6_2.6_2.6_2.6_2.6_2.6_2]$ as derived from TOPOS (Figure 2.2).

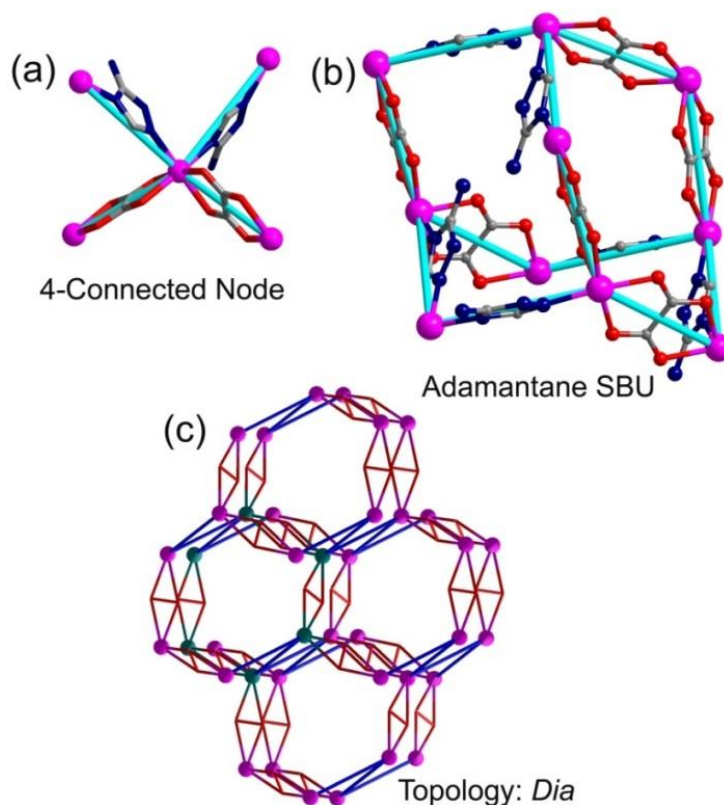


Figure 2.2 (a) Representation of the 4-connected Co^{2+} node, (b) pictorial representation of the adamantane secondary building unit (SBU), and (c) 6-membered ring forming *Dia* topology for framework 1.

Compound **2** crystallizes in monoclinic $P2_1/n$ space group (*Appendix A2.1*). SCXRD analysis revealed that the asymmetric unit consists of two distinct Cobalt metal centres, two oxalate and three aminotriazole moieties and a solvent methanol molecule. Each metal centre has octahedral coordination environment around it, out of which four are satisfied by two bidentately chelating oxalates and the other two from the singly binding neutral Hatz units. Different from the previous structure of **1**, in compound **2**, one of the μ -2 bridging Hatz is terminally coordinated, whereas the second Hatz still retains the μ -2 bridging mode (*Figure 2.3*). This reduces the connectivity around metal centre from four to three and yields a more open framework.

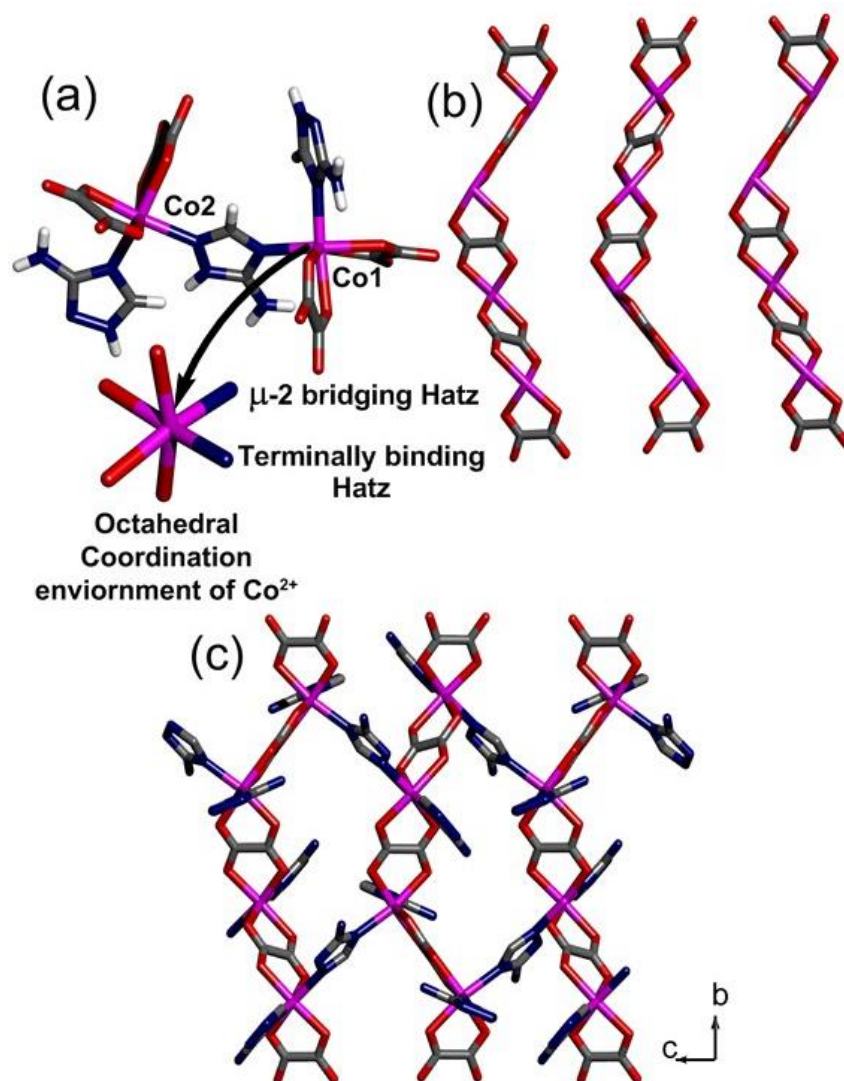


Figure 2.3 (a) Building unit of **2**, shows two distinct Co^{2+} centres and their octahedral coordination environment, (b) Co-Ox chains along a-axis representing a herringbone type of arrangement, and (c) crystal structural view along a-axis showing the μ -2 bridging Hatz units linking the Co-Ox chains in **2**.

Figure 2.3 shows the crystal structure view along a-axis, representing the framework with inundated Co-Ox chains that looks like herringbone arrangement. These oxalate chains are further bridged by the μ -2 bridging Hatz and the terminal Hatz are shown to be pointing in and out across the chains. A PLATON-squeeze analysis of the crystal structure of **2** revealed the presence of 16% solvent accessible void. When the oxalate and Hatz units are reduced to linear linker the metal centre becomes a 3-connected node. Topological analysis reveal that it attends to a rare uni-nodal $\{10, 3\}$ connected Thorium Silicide (ThSi_2) topology with vertex symbol as $[10_2.10_4.10_4]$ (Figure 2.4).

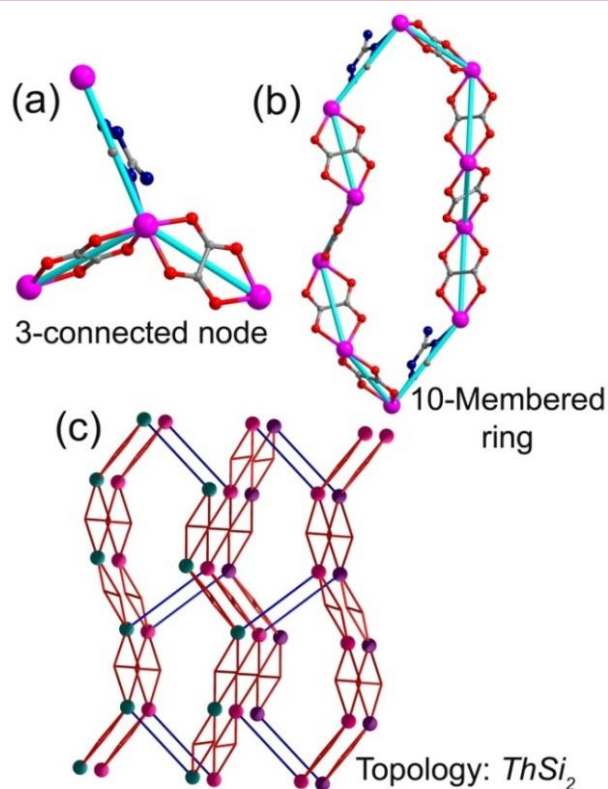


Figure 2.4 (a) Representation of the 3-connected node for Co^{2+} , (b) pictorial representation of the 10-membered ring, and (c) 10-membered ring forming $ThSi_2$ topology for framework **2**, green and violet balls are guide to the eye for locating the 10-membered ring in the $ThSi_2$ network.

2.3.3 Bulk characterizations for compound 1

The bulk purity of the sample **1** was confirmed from the match between the synthesized and simulated powder X-ray diffraction pattern (Figure 2.5a).

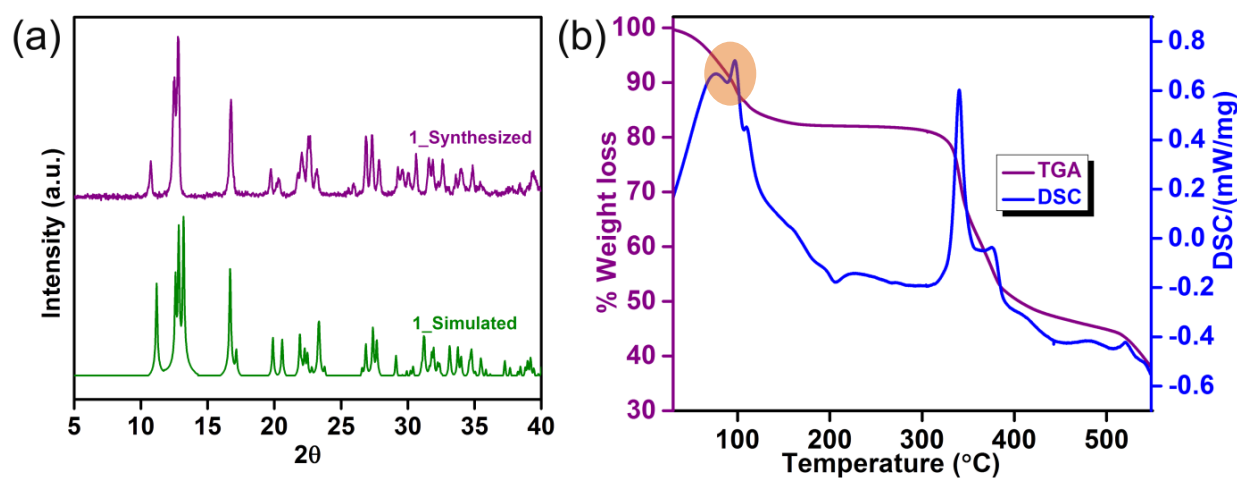


Figure 2.5 (a) Comparison of the simulated and as-synthesized PXRD patterns for **1**, and (b) TGA-DSC profile of **1**, signifying the solvent dependent structural transformation.

TGA showed a significant solvent loss followed by good thermal stability up to 100°C (373 K) and 300°C (573 K) respectively (Figure 2.5b). Further, it was observed from the DSC trace of the TGA, that there are two peaks around 100°C (373 K) (Figure 2.5b; DSC), which could be attributed to the solvent loss, capable of inducing a structural transformation. To gain further insights, **1** was examined using a variable temperature PXRD (VT-PXRD), from which a noticeable structural transformation at 100°C (373 K) (Figure 2.6) could be observed. This is the temperature at which the material is expected to desolvate completely. Low-temperature evacuations followed by solvent exchanges were carried out, but the solvent loss seems to trigger this structural transformation irrespective of the solvent or heating rate or the order of vacuum.

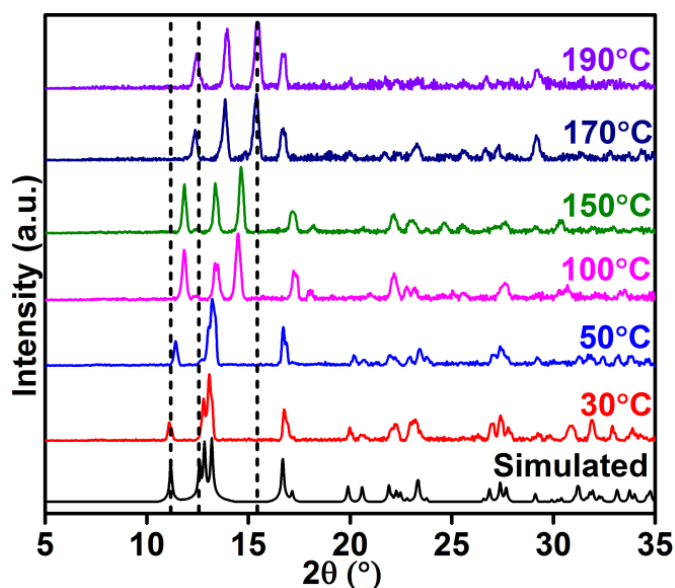


Figure 2.6 VT-PXRD patterns for **1**, showing structural transformation at 100°C (373 K). The dotted lines are guide for the eye.

Now, considering that the framework is significantly rigid with only small ultramicropores, the noticeable solvent-triggered structural transformation is quite intriguing. This structural transformation was characterized by both shrinkage in the lattice length and significant changes in the bond angles. But the peak shifts happen in an asymmetric manner suggesting it is not a mere temperature driven lattice contraction or expansion (Figure 2.6). The structural change causes some of the peaks (100, 110) to shift toward higher 2θ and some new peaks (at $2\theta=14, 28.5^\circ$) start to appear (Figure 2.6).

The structural transition was correlated with the unit cell changes determined by carrying out the variable temperature measurements on a single crystal (*Appendix A2.9*). When **1** is desolvated, a structural change with decrease in a- and c- axes and increase in b-axis was observed (*Figure 2.7*). The beta angle drops from 117° to 111°. [It should be noted that in a single crystal, weight loss seems to occur at much lower temperature as compared to the bulk phase (VT-PXRD). This is explained by the fact that the solvent could easily be removed from the single crystal owing to small volume of the sample involved compared to the bulk sample (thermocouple used in VT-PXRD was calibrated before the experiment)].

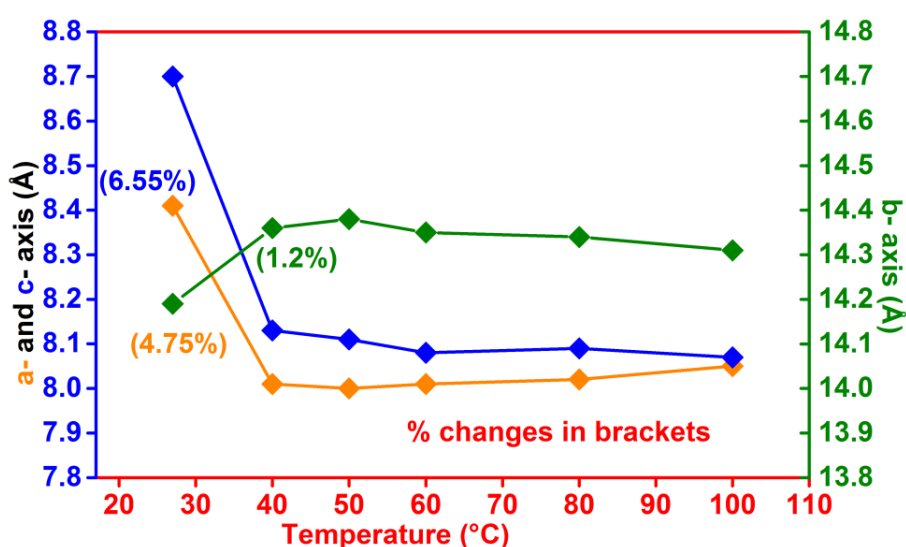


Figure 2.7 Changes in the unit cell parameters with temperature/desolvation measured from SCXRD.

Obtaining direct crystallographic evidence on how the framework of such rigid ultra-microporous MOFs can deform creating substantial changes in the CO₂ uptakes is critical. To investigate this, **1** was evacuated and the structure of the desolvated phase, **1***, was obtained. For this purpose, the single crystal was desolvated on the cryo loop at 373 K and equilibrated for 4 hours. It was then cooled again at 100 K and the data was obtained (due to the rigid nature of the **1***, lattice parameters do not change much upon cooling to 100 K (*Figure 2.8 and Appendix A2.1*)). The coordination environment of the metal centre and the asymmetric unit of **1*** still remains same as that of the as-made framework **1** (*Figure 2.8*). A careful comparison of the desolvated structure **1***, with the as-made framework **1** provided some valuable information, particularly, as to what extent does the structure had to

deform to considerably change the pore accessibility. The Co-Ox and Co-Hatz chains showed significant buckling upon desolvation ($\angle\text{Co-Hatz-Co} = 91.5^\circ$ to 79.4°) and ($\angle\text{Co-Ox-Co} = 118.95^\circ$ to 112.27°) and this explains the decrease in a- and c-axes (*Figure 2.9, Appendix A2. 12*). Meanwhile, it can be seen that the same buckling contributes to expansion of the b-axis (*Appendix A2. 12*). These changes in unit cell dimensions overall reflect the 16% decrease in the unit cell volume. On the whole, these structural changes result in the decrease of the pore size of the largest channel along the c-axis (*Figure 2.9c*).

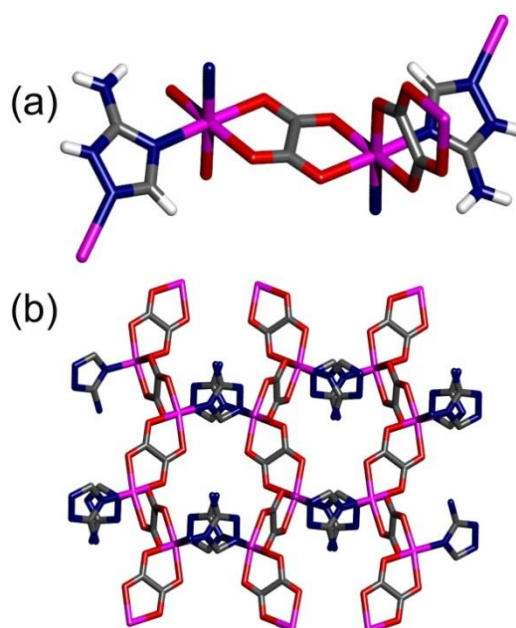


Figure 2.8 (a) Building unit of **1*** and (b) view along crystallographic c-axis, shows that the octahedral coordination environment of Co²⁺ ions and the overall morphology of the framework remain same after desolvation.

Importantly, the PLATON analysis also suggests that there is only 7.7% solvent accessible voids left in the **1***, which is just 1/5th of the void volume estimated for the solvent-free crystal structure of **1**. So in effect, it was observed that even in this ultra-microporous MOFs constructed from short bridging linkers, such framework flexibility occurs giving rise to marked impact on the framework openness. Also framework **1** can be brought back if **1*** is soaked in mother liquor for some time, signifying the solvent dependent structural transformation of the framework (*Figure 2.10*). Importantly it was also noticed that this framework has such strong solvent dependence that even a little exposure of the **1*** sample to the ambient atmosphere changes the PXRD pattern of the sample (*Appendix A2. 13*).

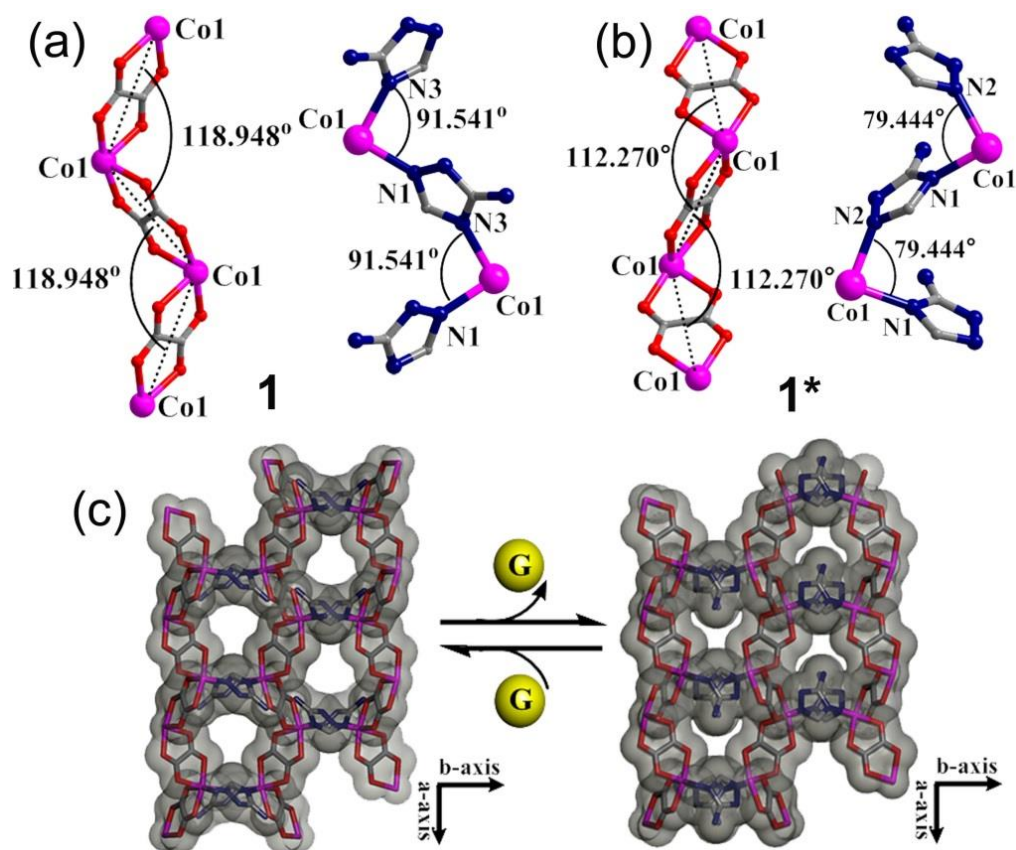


Figure 2.9 (a) Co-Ox and Co-Hatz chains in **1**, (b) and Co-Ox and Co-Hatz chains in **1*** representing the sharp change in angles resulting from the buckling of the chains. (c) Connolly surface representation for **1** and **1***, signifying the resultant decrease in pore volume.

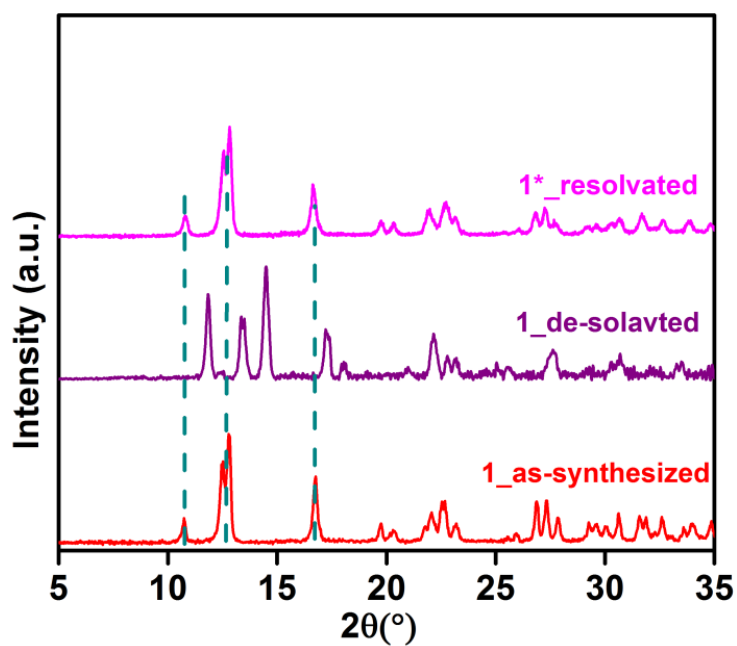


Figure 2.10 PXRD plots signifying the guest dependent reversible behavior of **1**.

2.3.4 Gas adsorption studies for compound 1

To investigate the CO₂ adsorbing property of **1**, the sample was activated by heating at 70°C (343 K) under vacuum (10⁻³ Torr). From PXRD it was confirmed that this activation causes the same structural transformation and generates **1***. Further the sample exposed to pure CO₂ stream at 298 K resulted in an uptake of 0.78 mmol/g at 1 bar pressure (*Figure 2.11*). This lowering uptake of CO₂ can be correlated with the observed decrease in the void volume of **1*** as compared **1**.

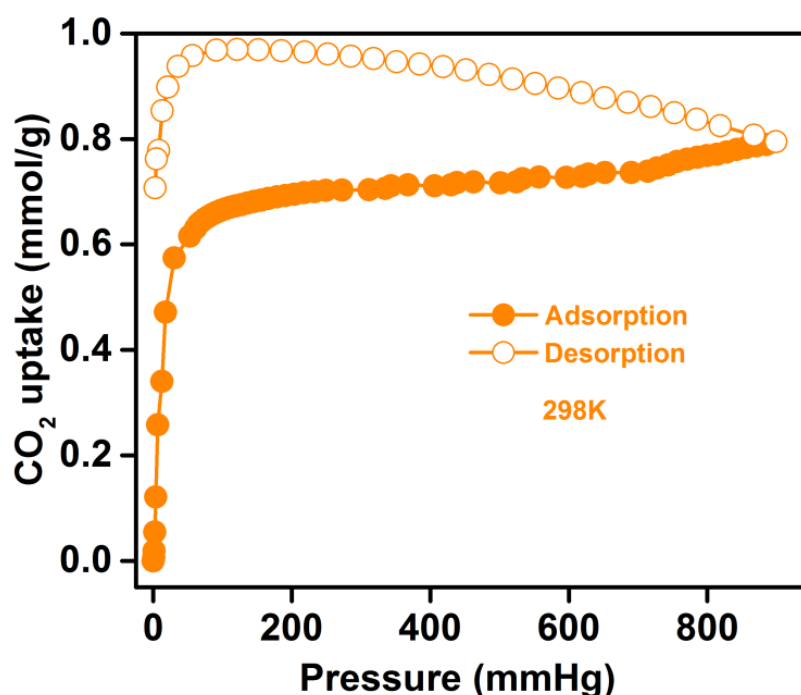


Figure 2.11 CO₂ adsorption isotherm at 298 K for **1**. Please note that the filled symbols show the adsorption branch whereas the open symbols shows desorption branch at 298 K.

The sharp uptake at low partial pressures can be explained by the presence of basic groups in the framework.^{38,39} The hysteresis in the isotherm can be explained by the presence of highly constricted pores in the desolvated structure, which has very small window opening into relatively larger ultra-microporous spaces (Please see *Figure 2.9c*). The hysteresis could not close completely even after prolonged equilibration times, which might be due to some gas entrapment in these constricted pores.

Thus an ultra-microporous MOF has been synthesized; whose pores are lined by the oxalate and basic free 1° amine groups. Due to the negatively contributing

solvent dependent structural transformation the gas uptake is largely compromised. From SCXRD, it was attributed that this distortion is due to the inefficiency of a μ -2 bridging aminotriazoles to prevent the buckling of the oxalate chains. However, this is in contrast with the report by Chen et.al.,⁴² where a framework (MAF-66) built entirely by μ -2 bridging aminotriazoles shows permanent porosity. By comparing present framework with the MAF-66's it was found that the major difference arises from the fact that in the current case, framework has "neutral" μ -2 bridging aminotriazoles, whereas MAF-66 has an anionic aminotriazolate framework. This relatively weaker binding of neutral μ -2 bridging aminotriazoles allows the Co-Hatz chains and the Co-Ox chains to buckle. Notably, in the as-synthesized MOF, the solvent trapped in the ultra-micropore is able to prevent such distortions, suggesting that these solvents have significantly strong interactions with the framework. In order to bring out the impact of the structural changes on the porosity in the present ultra-microporous MOF, **1**, it was compared with other reported MOFs, in terms of unit cell volume change and the associated void volume change in these MOFs (*Appendix A2.15*). From the comparisons it can be seen that in present case 16% change in unit cell volume brings a 78% change in void-volume. This observation indicates that the substantial change in adsorption characteristics can be brought about by structural changes in case of rigid ultra-microporous MOFs. This becomes critical when it comes to enhancing guest selectivity via molecular-sieving and in increasing framework-guest and guest-guest interactions.

2.3.5 Bulk characterizations for compound **2**

Bulk purity of the sample was confirmed by the match between the simulated and experimental powder pattern. TGA showed a weight loss of 2-3% up to 200°C (473 K) with a thermal stability up to 300°C (573 K)(*Figure 2.12*). A hump in the DSC profile in the temperature region of 190°C (463 K)-200°C (473 K) was evident, and could be attributed to some sort of structural transformation at this temperature (*Figure 2.12*). This was further verified through a VT-PXRD experiment. In agreement with the TGA plot, VT-PXRD also indicated that sample is well crystalline even at high temperatures and thus possess high thermal stability.

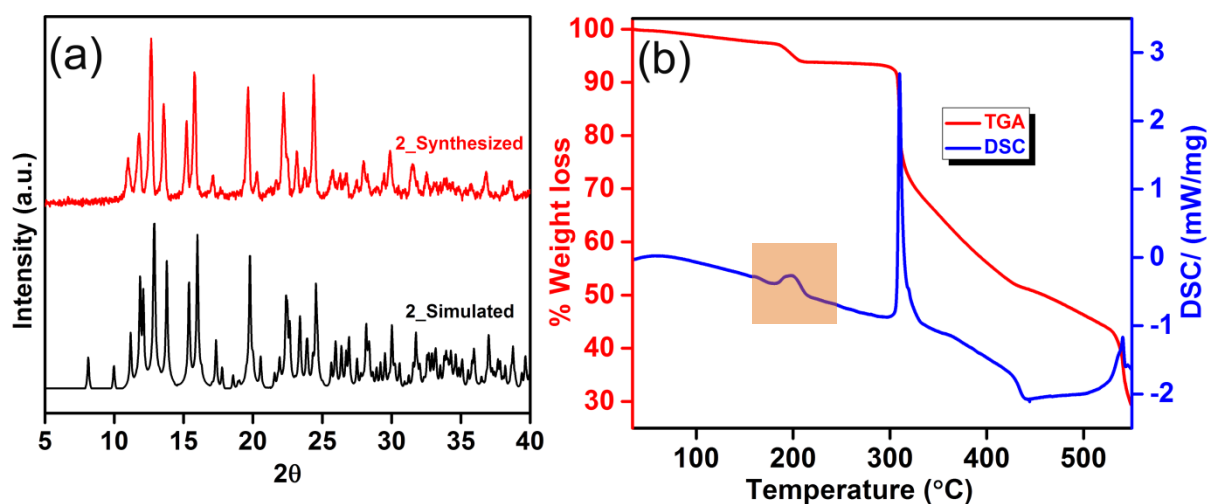


Figure 2.12 (a) Comparison of the simulated and as-synthesized PXRD patterns for **2** and (b) TGA-DSC profile of **2**, the DSC branch shows the hump at 200°C (473 K) signifying the temperature dependent structural transformation.

Importantly it can be seen that some new peaks especially in the low 2θ region arises at and above 190°C (463 K) but disappears on re-cooling of the sample (Figure 2.13). These observations from the DSC profile and the VT-PXRD experiment suggested that the framework undergoes a temperature dependent structural transition (Figure 2.12b: DSC profile and Figure 2.13).

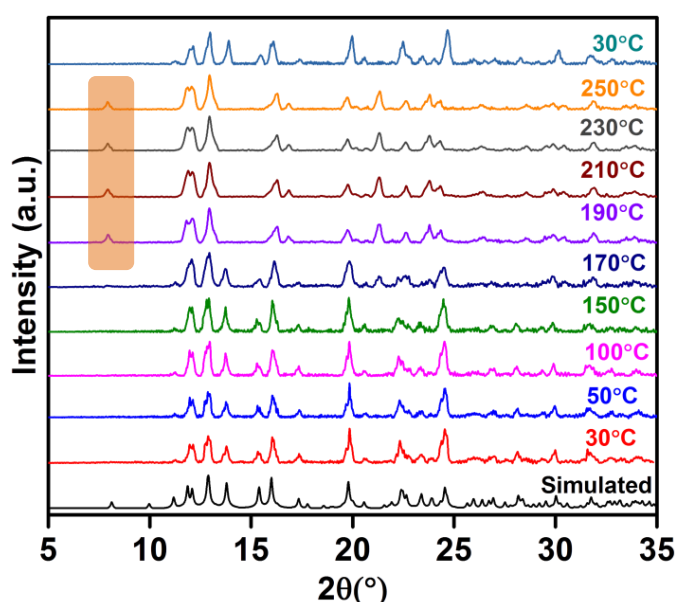


Figure 2.13 The VT-PXRD pattern of **2**, showing temperature dependent structural transformation for **2** (the highlighted area is a guide for the eye).

To further support this observation, unit cell parameters using SCXRD were collected at regular intervals starting from 100 K to 463 K (190°C). It was seen that at

190°C (463 K), the lattice parameters showed considerable difference with those obtained at lower temperatures (*Appendix A2.21*). Additionally the powder pattern obtained at 190°C (463 K) was indexed. The unit cell parameters obtained experimentally matched well with the indexed unit cell, confirming the purity of the transformed phase at higher temperature (*Appendix A2.21 and Appendix A2.22*). This structural transition could be accounted from the rotation of the μ -2 bridging Hatz linkers causing sliding of the Co-Ox chains (*Appendix A2.22*). [A data collection for a crystal of **2** at 190°C (463 K) was attempted but a good refinable data could not be obtained; since at such a high temperature the thermals were unacceptably high].

2.3.6 Gas adsorption studies for compound **2**

Gas adsorption measurements were performed on sample **2**. Sample **2** was initially soaked in methanol for 24 hours. After that it was evacuated at 150°C (423 K) for 12 hour at the degassing unit of Quantachrome adsorption analyzer, followed by direct exposure to pure CO₂ stream.

The CO₂ uptake at temperatures 195, 273, and 298 K under 1.1 bar pressure were 1.97, 1.64 and 1.3 mmol/g respectively (*Figure 2.14a*). N₂ isotherm obtained at 298 K and 1.1 bar pressure showed negligible uptake, suggesting the CO₂ selective behavior of **2** at room temperature (*Figure 2.14b*).

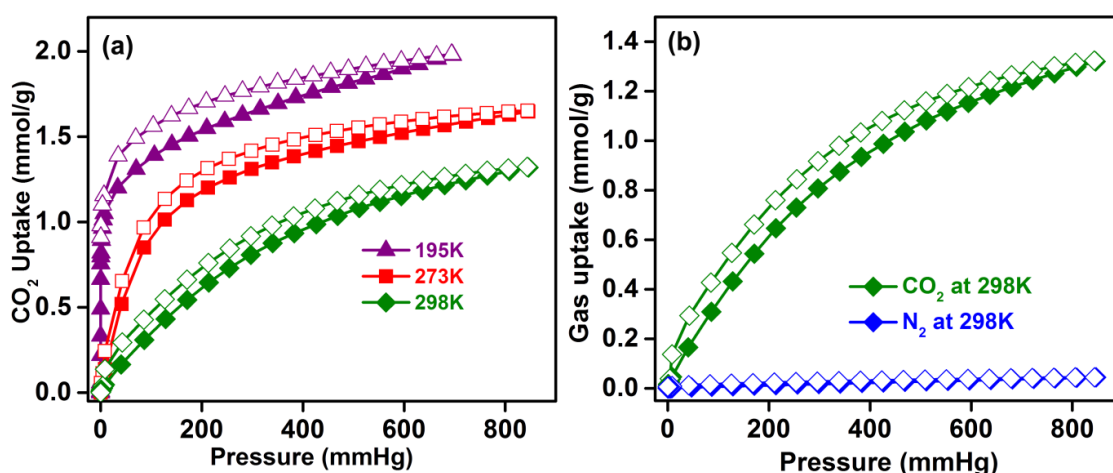


Figure 2.14 (a) CO₂ adsorption isotherm for **2** measured at different temperatures and (b) compound **2** shows a good CO₂/N₂ apparent selectivity as evident from the comparative adsorption isotherms of CO₂ and N₂ 298 K, 1 bar pressure. Please note that the filled symbols show the adsorption branch whereas the open symbols show desorption branch at a particular temperature.

Compound **2**, obtained via a different synthetic procedure showed nearly 40% increase in the CO₂ uptake as compared to **1**. Although the gas uptake capacity was increased, it still it did not reach to that of the high impact materials. A careful structural investigation of framework **2** provides the reason for this behavior, where one can see that the major channel along [110] plane gets blocked due to the dangling terminal Hatz ligands (*Figure 2.15*). Repeated attempts were made to remove these neutral Hatz (like activation at higher temperatures followed by thorough washing by methanol) but were not successful in doing so and after a certain point the framework itself started to collapse. This indicates that though these dangling aminotriazoles are not the part of the network, still provide sufficient stability to the structure by filling up the massive pore along [110] direction.

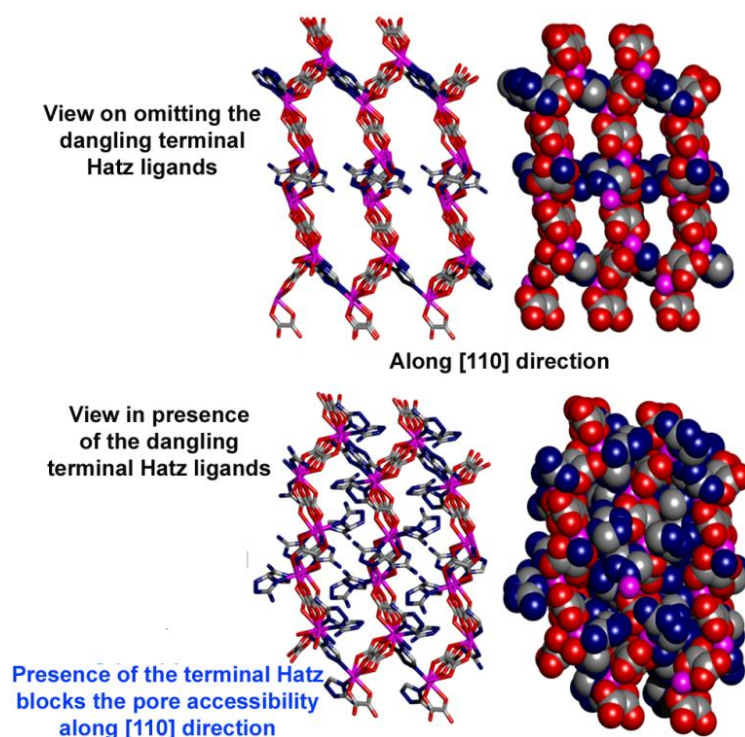


Figure 2.15 Crystallographic representation of the dangling terminal Hatz blocking the large pores along [110] direction in framework **2**.

BET, Langmuir and NLDFT fits were obtained using the 273 K CO₂ isotherm of **2**. A BET and Langmuir calculation from 273 K CO₂ isotherm indicated a surface area of 217 and 219 m²/g with corresponding correlation co-efficient as 0.9988 and 1, respectively (*Appendix A2.23 and Appendix A2.24*). DFT analysis isotherm fitting gave a pore volume of 0.096 cc/g with a fitting error of 1.014 %. The half pore width of 2.39 Å obtained by DFT fit reflects the ultra-microporous nature of the framework

(Appendix A2.25 and Appendix A2.26). A shallow rise in the CO₂ uptake profile shows a moderate interaction of CO₂ with the framework. A quantification of the CO₂ adsorptive interaction with the framework was evaluated by calculating the enthalpy of adsorption (Heat of adsorption, HOA) using a virial model. At zero loading, HOA was determined to be 36 kJ mol⁻¹, indicative of the interaction of CO₂ with the most energetically favored sites in the framework (Appendix A2.27-Appendix A2.30), whereas at high loading the HOA decreases to a value 22 kJ mol⁻¹ suggesting the presence of adsorption sites of moderate strength.

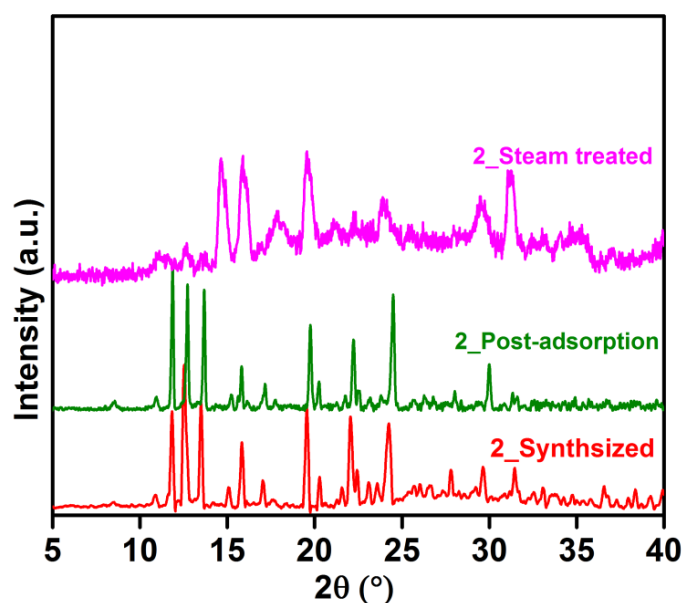


Figure 2.16 Comparison of the PXR D patterns of the post-adsorption sample and steam treated sample with as-synthesized PXR D pattern of **2**, which shows that the sample is stable to the activation procedure but is unstable to steam treatment.

The stability of the sample was evaluated by comparing the PXR D of the post-adsorption sample with the as-synthesized one. It was observed that there was almost no substantial loss in crystallinity of the sample after undergoing four adsorption-desorption cycles (Figure 2.16). Further, to look for hydrolytic stability, 100 mg of the sample was exposed to steam, but it was observed that the sample started to lose its crystallinity upon undergoing this treatment (Figure 2.16). As reported in the literature,^{43,44} MOFs which generally show hydrolytic instability comprise of the ligands which are easily replaceable by water molecules.^{43,44} Accordingly, since framework **2** consists of weakly binding terminal neutral Hatz, which are easily replaced by water molecules under the exposure of steam, results in the degradation of the framework.

2.4 Conclusion

The present chapter demonstrates the synthesis of two novel ultra-microporous MOFs. Both the materials have been investigated for their gas adsorption properties and were shown to be CO₂ selective but with substantially low uptakes than what were expected from SCXRD structures. **1** showed a significant loss in the CO₂ capacity owing to the negatively contributing solvent triggered structural flexibility. While **2** with a more open framework, obtained by a variation in the synthetic procedure shows a temperature dependent structural flexibility arising from the rotation of the μ -2 bridging Hatz linkers. It has about 40% higher CO₂ uptake as compared to **1** at 298 K, 1 bar. Interestingly, these ultra-microporous MOFs constructed from rigid chelating linkers showed substantial structural flexibility and thus representing the class of **3rd generation MOFs**. Further, the loss of porosity in case of **1** could be attributed to the relatively weaker binding modes of neutral μ -2 bridging triazoles which are unable to prevent the buckling of the Co-Hatz and Co-Ox chains upon desolvation. Notably, in the as-synthesized form of **1**, the solvent trapped in the ultra-micropore are able to prevent such distortions suggesting that solvents have significantly strong interactions with the framework. On the other hand, **2** showed a moderate room temperature CO₂ uptake and good apparent CO₂/N₂ selectivity. However, this material shows instability under humid conditions, which could be attributed to the relatively weaker binding mode of the terminal neutral triazoles, which makes them easier to get replaced by water molecules and hence facilitates the structural degradation.

2.5 References

1. Li, J.-R.; Kupplera, R. J.; Zhou, H.-C. *Chem. Soc. Rev.* **2009**, *38*, 1477.
2. Sumida, K.; Rogow, D. L.; Mason, J. A.; McDonald, T. M.; Bloch, E. D.; Herm, Z. R.; Bae, T.-H.; Long, J. R. *Chem. Rev.* **2012**, *112*, 724.
3. Zhang, Z.; Yao, Z.-Z.; Xiang, S.; Chen, B. *Energy Environ. Sci.* **2014**, *7*, 2868.
4. Li, B.; Wen, H.-M.; Zhou, W.; Chen, B. *J. Phys. Chem. Lett.* **2014**, *5*, 3468.
5. Kang, Z.; Xue, M.; Fan, L.; Huang, L.; Guo, L.; Wei, G.; Chen, B.; Qiu, S. *Energy Environ. Sci.* **2014**, *7*, 4053.
6. Xiang, S.; He, Y.; Zhang, Z.; Wu, H.; Zhou, W.; Krishna, R.; Chen, B. *Nat. Commun.* **2012**, *3*, 954.
7. Britt, D.; Tranchemontagne, D.; Yaghi, O. M. *Proc. Natl. Acad. Sci.* **2008**, *105*, 11623.
8. Nandi, S.; Luna, P. D.; Daff, T. D.; Rother, J.; Liu, M.; Buchanan, W.; Hawari, A. I.; Woo, T. K.; Vaidhyathan, R. *Sci. Adv.* **2015**, *1*:e1500421, 1.
9. Quadrelli, R.; Peterson, S. *Energy Policy* **2007**, *35*, 5938.
10. Pachauri, R. K.; Reisinger, A. *IPCC Fourth Assessment Report, Intergovernmental Panel on Climate Change* **2007**.
11. Choi, S.; Drese, J. H.; Jones, C. W. *ChemSusChem.* **2009**, *2*, 796.
12. Keskin, S.; van Heest, T. M.; Sholl, D. S. *ChemSusChem.* **2010**, *3*, 879.
13. Li, J.-R.; Ma, Y.; McCarthy, M. C.; Sculley, J.; Yu, J.; Jeong, H.-K.; Balbuena, P. B.; Zhou, H.-C. *Coord. Chem. Rev.* **2011**, *255*, 1791.
14. Ma, S.; Zhou, H.-C. *Chem. Commun.* **2010**, *46*, 44.
15. D'Alessandro, D. M.; Smit, B.; Long, J. R. *Angew. Chem. Int. Ed.* **2010**, *49*, 6058.
16. Kitagawa, S.; Kitaura, R.; Noro, S. *Angew. Chem. Int. Ed.* **2004**, *43*, 2334.
17. Lin, J. B.; Zhang, J. P.; Chen, X. M. *J. Am. Chem. Soc.* **2010**, *132*, 6654.
18. Morris, W.; Leung, B.; Furukawa, H.; Yaghi, O. K.; He, N.; Hayashi, H.; Houndonougbo, Y.; Asta, M.; Laird, B. B.; Yaghi, O.M. *J. Am. Chem. Soc.* **2010**, *132*, 11006.
19. Tan, Y. X.; Wang, F.; Kangand, Y.; Zhang, J. *Chem. Commun.* **2011**, *47*, 770.
20. Zhang, J.; Wu, H.; Emge, T. J.; Li, J. *Chem. Commun.* **2010**, *46*, 9152.
21. Park, H. J.; Lim, D. W.; Yang, W. S.; Ohand, T. R.; Suh, M. P. *Chem. Eur. J.* **2011**, *17*, 7251.
22. Wang, F.; Tan, Y. X.; Yang, H.; Zhang, H. X.; Kang, Y.; Zhang, J. *Chem. Commun.* **2011**, *47*, 5828.
23. Li, B.; Wang, H.; Chen, B. *Chem. Asian J.* **2014**, *9*, 1474.
24. Alawisi, H.; Li, B.; He, Y.; Arman, H. D.; Asiri, A. M.; Wang, H.; Chen, B. *Cryst. Growth Des.* **2014**, *14*, 2522.
25. Zhang, Z.; Xiang, S.; Chen, B. *CrystEngComm* **2011**, *13*, 5983.
26. Liu, J.; Thallapally, P. K.; McGrail, B. P.; Brown, D. R.; and Liu, J. *Chem.Soc.Rev.* **2012**, *41*, 2308.
27. Kimand, T. K.; Suh, M. P. *Chem. Commun.* **2011**, *47*, 4258.
28. Schneemann, A.; Bon, V.; Schwedler, I.; Senkovska, I.; Kaskel, S.; and Fischer, R. A. *Chem. Soc. Rev.* **2014**, *43*, 6062.

29. Horike, S.; Shimomura, S.; Kitagawa, S. *Nat. Chem.* **2009**, *1*, 695.
30. Kitaura, R.; Seki, K.; Akiyama, G.; Kitagawa, S. *Angew. Chem. Int. Ed.* **2003**, *42*, 428.
31. Li, L.; Wang, Y.; Yang, J.; Wang, X.; Li, J. *J. Mater. Chem. A* **2015**, *3*, 22574.
32. Alhamami, M.; Doan, H.; Cheng, C.-H. *Materials* **2014**, *7*, 3198.
33. Yang, W.; Davies, A. J.; Lin, X.; Suyetin, M.; Matsuda, R.; Blake, A. J.; Wilson, C.; Lewis, W.; Parker, J. E.; Tang, C. C.; George, M. W.; Hubberstey, P.; Kitagawa, S.; Sakamoto, H.; Bichoutskaia, E.; Champness, N. R.; Yang, S.; Schroder, M. *Chem. Sci.* **2012**, *3*, 2993.
34. Serre, C.; Millange, F.; Thouvenot, C.; Nogues, M.; Marsolier, G.; Louer, D.; Ferey, G. *J. Am. Chem. Soc.* **2002**, *124*, 13519.
35. Tan, N. Y.; Ruggiero, M. T.; Orellana-Tavra, C.; Tian, T.; Bond, A. D.; Korter, T. M.; Fairen-Jimenez, D.; Zeitler, J. A. *Chem. Commun.* **2015**, *51*, 16037.
36. Zheng, B.; Pan, Y.; Lai, Z.; Huang, K.-W. *Langmuir* **2013**, *29*, 8865.
37. Fairen-Jimenez, D.; Moggach, S. A.; Wharmby, M. T.; Wright, P. A.; Parsons, S.; and Duren, T. *J. Am. Chem. Soc.* **2011**, *133*, 8900.
38. Vaidhyanathan, R.; Iremonger, S. S.; Dawson, K. W.; Shimizu, G. K. H. *Chem. Commun.* **2009**, 5230.
39. Vaidhyanathan, R.; Iremonger, S. S.; Shimizu, G. K. H.; Boyd, P. G.; Alavi, S.; Woo, T. K. *Science* **2010**, *330*, 650.
40. Vaidhyanathan, R.; Iremonger, S. S.; Shimizu, G. K. H.; Boyd, P. G.; Alavi, S.; Woo, T. K. *Angew. Chem. Int. Ed.* **2012**, *51*, 1826.
41. Nugent, P.; Belmabkhout, Y.; Burd, S. D.; Cairns, A. J.; Luebke, R.; Forrest, K.; Pham, T.; Ma, S.; Space, B.; Wojtas, L.; Eddaoudi, M.; Zaworotko, M. J. *Nature* **2013**, *495*, 80.
42. Lin, R.-B.; Chen, D.; Lin, Y.-Y.; Zhang, J.-P.; Chen, X.-M. *Inorg. Chem.* **2012**, *51*, 9950.
43. Tan, K.; Nijem, N.; Gao, Y.; Zuluaga, S.; Li, J.; Thonhauser, T.; Chabal, Y. J. *CrystEngComm.* **2015**, *17*, 247.
44. Lasseuguette, E.; Carta, M.; Brandani, S.; Ferrari, M.-C. *Int. J. Greenh. Gas Control* **2016**, *50*, 93.
45. Seo, J.; Bonneau, C.; Matsuda, R.; Takata, M.; Kitagawa, S. *J. Am. Chem. Soc.* **2011**, *133*, 9005.
46. Maji, T. K.; Uemura, K.; Chang, H.-C.; Matsuda, R.; Kitagawa, S. *Angew. Chem. Int. Ed.* **2004**, *43*, 3269.; *Angew. Chem.* **2004**, *116*, 3331.
47. Xiao, J.; Wu, Y.; Li, M.; Liu, B.-Y.; Huang, X.-C.; Li, D. *Chem. Eur. J.* **2013**, *19*, 1891.
48. Zeng, M.-H.; Fenga, X.-L.; Chen, X.-M. *Dalton Trans.* **2004**, 2217.
49. Yang, S.; Lin, X.; Lewis, W.; Suyetin, M.; Bichoutskaia, E.; Parker, J. E.; Tang, C. C.; Allan, D. R.; Rizkallah, P. J.; Hubberstey, P.; Champness, N. R.; Thomas, K. M.; Blake, A. J.; Schröder, M. *Nat. Mater.* **2012**, *11*, 710.

Chapter 3



**Bimetallic ultra-microporous
aminotriazole-oxalate frameworks
showing selective CO₂ capture and
stability under humid conditions**

3.1 Introduction

The selective carbon-dioxide capture from the post-combustive sources is an efficient way to mitigate the escalation in the global greenhouse effect.^{1,2} However, the presence of CO₂ at considerable low partial pressures as compared to N₂, makes the overall process challenging.^{3,4} Ultra-microporous MOFs with appropriate pore dimensions, capable of showing molecular sieving effect, has emerged as efficient candidate for this purpose.⁵⁻⁸ However, another major challenge which is mostly encountered in this process is the presence of ~5-7 % of water vapour in the flue gas stream.^{3,9,10} The presence of water vapour affects the framework integrity. Also at the same time water could compete with CO₂ for the active adsorbing sites, resulting into the decrease of the overall CO₂ capacity.¹¹⁻¹⁴ Therefore, for practical application the material should be water stable and tethered with such functional groups which could effectively enhance the CO₂ affinity of the framework.¹⁵⁻²⁵ Among numerous porous MOFs reported, many of them could not withstand the humid conditions.²⁶⁻²⁹ Several attempts have been made to understand the relative stability of these frameworks under humid conditions. It has been noted that in general the water molecules attacks the metal-ligand (M-L) coordination bond and causes a displacement type of reaction resulting into phase change, loss in crystallinity, reduction or destruction of the porosity in these materials.^{5,30-32} Other factors which account for the MOFs stability are the basicity of the organic linker and also the shielding provided by the functional groups to the metal-ligand coordination sites.³³⁻³⁸ It has been reported that in general azolate based MOFs are more stable as compared to the dicarboxylate based MOFs owing to the greater basicity of the azolate linkers, which would cause stronger M-N bonds imparting more stability to the framework.³⁹⁻⁴⁷

However, it has been noticed that the neutral aminotriazole based framework [Co₂(C₂O₄)₂(C₂N₄H₄)₃](CH₃OH) reported in the chapter 2, does not show the stability under humid conditions. This most likely is due to the relatively weaker binding of the dangling neutral aminotriazole linkers, which could easily be replaced by water molecules and result in framework degradation.^{5,48} Further, it is well known that greater the basicity of the ligand, stronger will be the M-L bond³⁹⁻⁴⁷ and this points at

the need for deprotonation of the aminotriazole linkers, for construction of an aminotriazolate based framework which will be stable under humid condition.

This chapter demonstrates the synthesis, structural characterization, thermal analysis and gas adsorption studies for two isostructural bimetallic ultra-microporous MOFs $[\text{Zn}_6\text{Co}_1(\text{C}_2\text{O}_4)_6(\text{C}_2\text{H}_4\text{N}_4)_4(\text{C}_2\text{H}_3\text{N}_4)_2]$ [1] and $[\text{Zn}_6\text{Ni}_1(\text{C}_2\text{O}_4)_6(\text{C}_2\text{H}_4\text{N}_4)_4(\text{C}_2\text{H}_3\text{N}_4)_2]$ [2]. These two bimetallic MOFs based upon oxalic acid and 3-aminotriazole linkers have been observed to be completely stable under humid conditions with no loss in their CO_2 uptake capacity. Importantly, it has been discussed that how the use of basic Zn-salt in the reaction facilitates the deprotonation of the aminotriazole linkers and results in the formation of moisture stable ultra-microporous MOFs.

3.2 Experimental section

3.2.1 Materials: All chemicals were used from the commercially available sources without further purification.

3.2.2 Physical measurements:

3.2.2.1 Powder X-ray diffraction: PXRD analyses were carried out using a Rigaku Miniflex-600 instrument and processed using PDXL software.

3.2.2.2 Variable temperature powder X-ray diffraction: VT-PXRD patterns were measured on Bruker D8 Advanced X-Ray diffractometer at different temperatures using $\text{Cu-K}\alpha$ radiation ($\lambda = 1.5406 \text{ \AA}$) with a scan speed of $0.5^\circ \text{ min}^{-1}$ and a step size of 0.01° in 2 theta.

3.2.2.3 Thermo-gravimetric analysis: Thermo-gravimetric analysis was carried out on NETSZCH TGA-DSC system. The routine TGAs were done under N_2 gas flow (50 ml/min) and samples were heated from RT to 950°C at $5^\circ\text{C}/\text{min}$.

3.2.2.4 Single crystal X-ray diffraction: Single crystal data was collected using Bruker Single crystal X-ray diffractometer, at wavelength: 1.5418 \AA . Single-crystal data was collected on a Bruker SMART APEX four-circle diffractometer equipped with a CMOS photon 100 detector (Bruker Systems Inc.) and with a $\text{Cu K}\alpha$ radiation (1.5418 \AA). The incident X-ray beam was focused and monochromated using Microfocus (μS) source. Crystal of **2** was mounted on nylon Cryo loops with

Paratone-N oil. Data were collected at 100 K and integrated using Bruker SAINT software and corrected for absorption using SADABS. Structures were solved by Intrinsic Phasing module of the direct methods and refined using the SHELXTL 2014 software suite. All non-hydrogen atoms were located from iterative examination of difference F-maps following which the structure was refined using least-squares method. Hydrogen atoms were placed geometrically and placed in a riding model. Due to the weak diffraction through the crystal and diffuse nature of the solvent molecules, it was difficult to locate them, hence a squeeze model using PLATON has been provided.

3.2.2.5 Infra-red spectrophotometry: IR was recorded in attenuated total reflectance (ATR) mode on neat samples on a Bruker Alpha spectrophotometer.

3.2.2.6 Adsorption: Adsorption studies were done on Quantachrome IQ adsorption analyser. All of the gases used were of 99.999% purity. For fitting the isotherms BET and Langmuir methods were employed. For pore size distribution calculation NLDFT was used. Heat of adsorption calculations were done by Virial method.

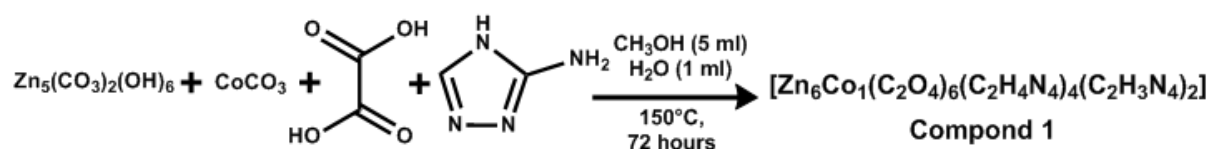
3.2.2.7 Elemental analysis: Elemental analyses were performed on a Vario-EL cube elemental analyser.

3.2.2.8 Elemental mapping: Ultra Plus Field Emission Scanning Electron Microscope with integral charge compensator and embedded EsB and AsB detectors. Oxford X-max instruments 80mm². (Carl Zeiss NTS, GmbH), Imaging conditions: 2kV, WD=2mm, 200kX, Inlens detector.

3.2.3 Synthesis

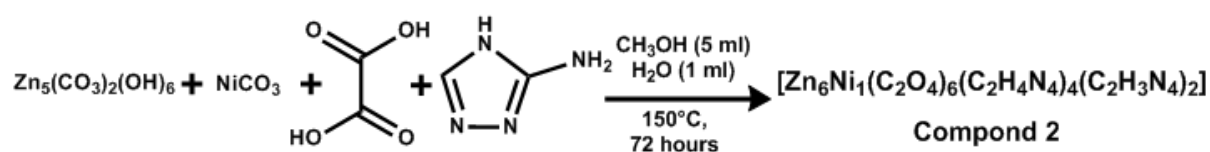
3.2.3.1 Synthesis of compound 1: In a typical synthesis for compound **1**, the metal salts 0.05 g of CoCO₃, 0.05 g of Zn₅(CO₃)₂(OH)₆, 0.0791 g of oxalic acid and 0.3563 g of 3-aminotriazole (Hatz) were added in 5 ml of CH₃OH and 1 ml of H₂O in a 23 ml autoclave. The reaction mixture was stirred for 30 minutes at room temperature and reacted solvothermally at 150°C for 3 days (*Scheme 3.1*). On cooling, pink coloured micro-crystalline sample was obtained (*Appendix A3.1*). The bulk sample was then washed with copious amount of H₂O: CH₃OH solvent mixture to remove any unreacted organics present, followed by which the sample was dried in air, FT-IR

(cm^{-1}): 3947, 3876, 3839, 3621, 3491, 3321, 3200, 3111, 2874, 2621, 2483, 2038, 1656, 1550, 1311, 1226, 1059, 864, 789, 701, 660. Analytical data for the solvent-free framework; observed (%): C (19.44), H (1.89), N (22.26); calculated (%): C (19.45), H (1.50), N (22.69). Note: Large-sized single crystals suitable for X-ray diffraction could not be obtained for this phase.



Scheme 3.1 Synthesis scheme for compound 1.

3.2.3.2 Synthesis of compound 2: In a typical synthesis for compound 2, the metal salts 0.05 g of NiCO_3 , 0.05 g of $\text{Zn}_5(\text{CO}_3)_2(\text{OH})_6$, 0.0791 g of oxalic acid and 0.3563 g of 3-aminotriazole (Hatz) were added in 5 ml of CH_3OH and 1 ml of H_2O in a 23 ml autoclave. The reaction mixture was stirred for 30 minutes at room temperature and reacted solvothermally at 150°C for 3 days (Scheme 3.2). On cooling, blue crystalline powder was obtained with few bluish plate shaped crystals, (Appendix A3.1). The bulk sample was washed with copious amount of H_2O : CH_3OH solvent mixture to remove any unreacted organics present, followed by which the sample was dried in air, FT-IR (cm^{-1}): 3937, 3873, 3792, 3598, 3495, 3355, 3284, 3108, 2914, 2452, 2081, 1640, 1538, 1311, 1212, 1061, 990, 858, 790, 675. Analytical data for the solvent-free framework; observed (%): C (19.33), H (1.82), N (22.41); calculated (%): C (19.45), H (1.50), N (22.69).



Scheme 3.2 Synthesis scheme for compound 2.

3.3 Results and discussions

3.3.1 Synthesis

Two bimetallic MOFs have been synthesized under similar solvothermal conditions, with methanol-water solvent mixture at 150°C for 3 days. In the synthesis of compound 1, Zinc and Cobalt were used along with stoichiometric amount of oxalic

acid and aminotriazole organic ligands. While in the synthesis of compound **2**, Nickel has been used in place of Cobalt under exact same reaction conditions. The solvothermal reaction yielded compounds **1** and **2** as pink and blue crystalline powders which suggests the presence of Co(II) and Ni(II) ions in them, respectively (*Appendix A3.1*).

It is important to mention here that the solvent mixture, temperature and ligand stoichiometry are same as that used for the synthesis of $[\text{Co}_2(\text{C}_2\text{O}_4)_2(\text{C}_2\text{N}_4\text{H}_4)_3](\text{CH}_3\text{OH})$ phase (Chapter 2, MOF **2**). In the present case "basic" Zn-salt has been introduced into the reaction condition for the synthesis of compound **1**.

3.3.2 Crystal structure

A micro-crystalline powder was obtained for compound **1**; however single crystals of suitable size for a single crystal X-ray diffraction analysis could not be obtained. On the other hand for compound **2**, few very small bluish plate shaped crystals were observed. Such a crystal has been mounted and data collection was done. The single crystal diffraction data for **2** revealed that it crystallizes in orthorhombic crystal system with $Fdd2$ space group (*Appendix A3.2*). The asymmetric unit of **2** consists of four distinct metal centres, three oxalate linkers and three aminotriazole linkers (*Figure 3.1a*). Out of the four metal centres, three are Zn(II) ions with full occupancies and the fourth one is Ni(II) ion with half occupancy. The framework has three oxalate ($\{\text{C}_2\text{O}_4\}^{2-}$) motifs and one aminotriazolate ($\{\text{C}_2\text{H}_3\text{N}_4\}^-$) which provide the charge balance to the overall neutral framework **2**, while the rest two aminotriazoles ($\text{C}_2\text{H}_4\text{N}_4$) bind with the metal centres in their neutral form in a μ -2 bridging mode. The oxalates offer a wide angle chelation to metal centres in an end-to-end manner. Interestingly, the molecular packing shows that the oxygen atom O3A provides an additional μ -2 bridging coordination between Zn1 and Zn3, which results into the formation of a five membered ring formed of O3A, N3, N4, Zn1 and Zn3. (*Figure 3.1b and Figure 3.1d*). The neutral aminotriazole linkers provide μ -2 bridging coordination while the aminotriazolate showed a μ -3 bridging coordination, with two Zn centres (Zn1 and Zn3) and the Ni1 centre. The metal centres Zn1, Zn2 and Ni1 are having octahedral coordination spheres. For Zn2 and Ni1 four of the coordination sites are satisfied by four oxygen atoms from two different oxalate linkers. While the rest two

are satisfied by the two different μ -2 bridging neutral aminotriazole linkers for Zn2, and two nitrogen atoms of two different μ -3 bridging aminotriazolate linkers for Ni1, respectively (Figure 3.1c and Figure 3.1d).

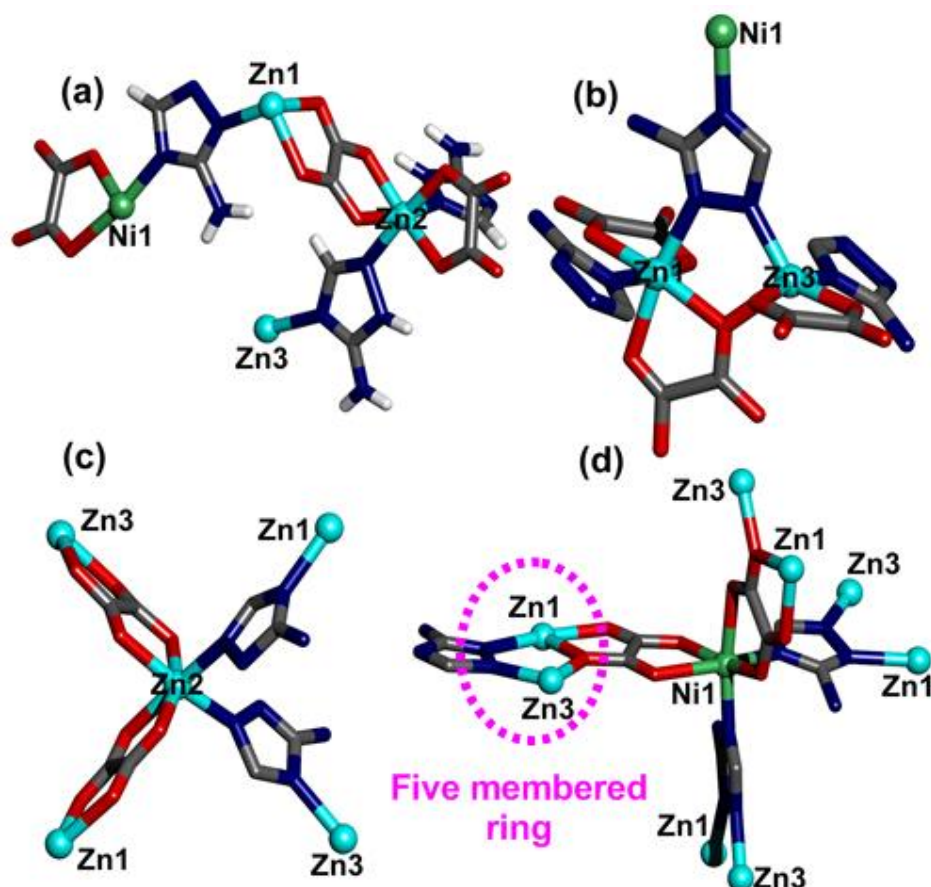


Figure 3.1 (a) Asymmetric unit of framework 2, (b) structural fragment showing the octahedral coordination sphere of Zn1 and distorted square pyramidal coordination sphere of Zn3 metal centers (c) structural fragment showing the octahedral Zn2 center and (d) the octahedral Ni2 center with the five membered ring formed of N3, N4, Zn1, Zn3 and O, colour code: Zinc: cyan, Nickel: green, Oxygen: red, Carbon: grey and Nitrogen: blue, Hydrogen: white.

Octahedral coordination for Zn1 are satisfied by four oxygen atoms, out of which three are from bis-chelating oxalates and remaining one from the μ -2 bridging oxygen O3A. The rest of the two coordination sites are satisfied by two nitrogen atoms each from one μ -2 bridging neutral aminotriazole and one from μ -3 bridging aminotriazolate linker (Figure 3.1b). Similarly, the Zn3 metal centre is having a distorted square pyramidal geometry with coordinations satisfied with three oxygen atoms, out of which two are from a bis-chelating oxalate and the rest one is from the μ -2 bridging oxygen atom O3A. The rest two coordination sites are satisfied by

nitrogen atoms, one from each μ -2 bridging aminotriazole and μ -3 bridging aminotriazolate linkers (Figure 3.1b). Now, on colliding the five membered rings mentioned above to a single node, formation of an interesting square grid has been observed, and this gives an overall 4-connected network considering Ni1 as the point of origin. This particular crystallographic arrangement gives rise to a framework with 1D-porous channel along the b-axis (Figure 3.2), while the rest of the two crystallographic axes (a and c) are not accessible.

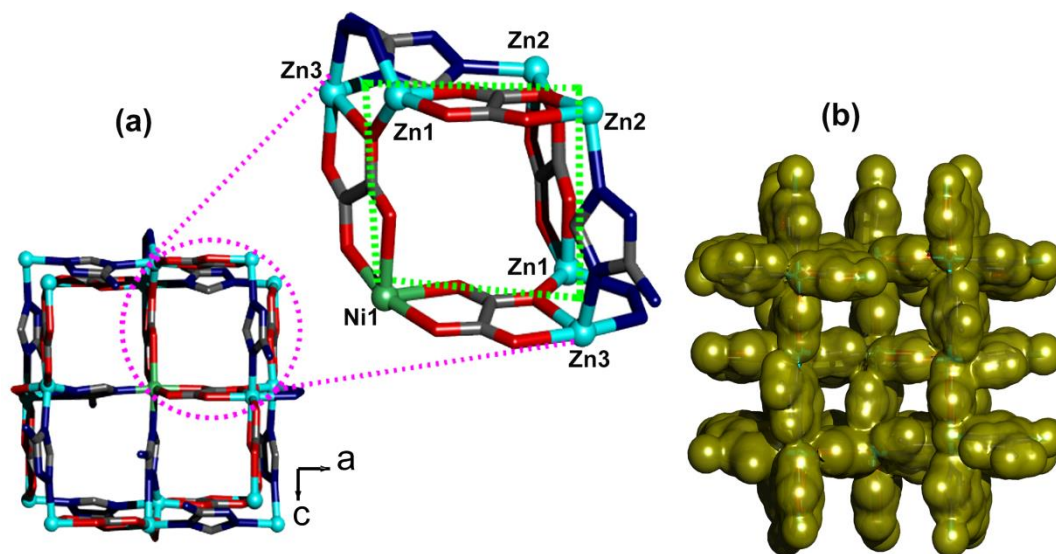


Figure 3.2 (a) View of the square grid formed due to the particular arrangement of metal ions and ligands (the dotted green lines are guide to eye to show the grid) and (b) Connolly surface representation showing the porous channel running along the b-axis, colour code: Zinc: cyan, Nickel: green, Oxygen: red, Carbon: grey and Nitrogen: blue, Hydrogens are removed for clarity.

3.3.3 Bulk characterizations

It was observed that the powder x-ray diffraction patterns for both compound **1** and compound **2** matched exactly with each other, suggesting the frameworks are isostructural (Figure 3.3a).

The bulk phase purity was further confirmed by the match between the as-synthesized and simulated PXRD patterns (Figure 3.3b). Further, to affirm the presence of both the metals, elemental mapping and EDAX analysis were performed. These qualitative analyses confirmed the presence of Zn and Co metal ions in compound **1**, and Zn and Ni metal ions in compound **2** (Appendix A3.7 and Appendix A3.8).

The thermal stability of these isostructural bimetallic frameworks were analysed by performing TGA experiment under nitrogen atmosphere within a temperature range of 30 (303 K)-950°C (1223 K). For the as-synthesized samples of **1** and **2**, an initial weight loss of ~6% was observed, which can be attributed to the loss of the entrapped solvent molecules from the framework pores, followed by a high thermal stability up to 310°C (583 K) (*Figure 3.4*).

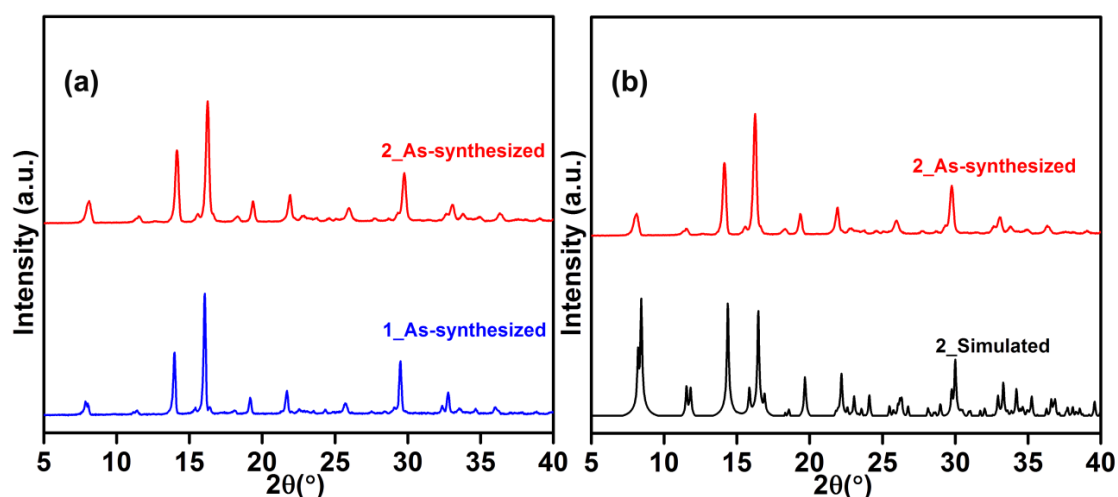


Figure 3.3 (a) The exact match between PXRD patterns for as-synthesized compound **1** and **2**, suggesting the formation of isostructural frameworks. (b) Comparison between the simulated and as-synthesized PXRD patterns of **2**, confirming the bulk phase purity of these samples.

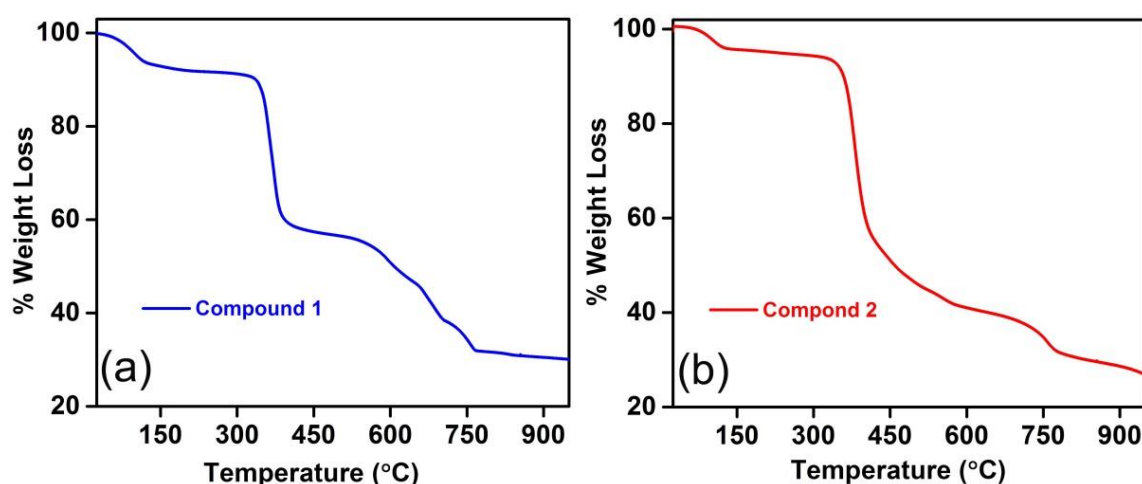


Figure 3.4 TGA plots for (a) compound **1** and (b) compound **2**, showing the high thermal stability up to 310°C (583 K).

However, due to the diffused nature of the solvent, it was difficult to locate the solvent molecules in the crystal structure of **2**. Further, the squeeze model for **2**

suggested a solvent accessible void volume of 2956 \AA^3 which accounts for the initial weight loss in the TGA profile. The thermal stability shown by these MOFs have been found to be in accordance with the results obtained from variable temperature PXRD experiment. The VT-PXRD profiles for **1** and **2** showed no peak shifts till 300°C (573 K), which suggests that the frameworks are stable and does not undergoes any sort of solvent or temperature dependent phase transformations (*Appendix A3.9 and Appendix A3.10*).

3.3.4 Gas adsorption studies

The gas adsorption experiments were performed on these frameworks. Activation of the samples involved pre-soaking in methanol for one day followed by an evacuation at 150°C (423 K) for 12 hours. The activated samples were then subjected to the pure CO_2 gas streams. The CO_2 adsorption isotherms for compound **1** and **2** were measured at different temperatures, till 1.1 bar CO_2 pressure. Both the MOFs showed type 1 adsorption isotherm profiles, with similar CO_2 uptakes. The CO_2 uptakes for these isostructural frameworks were found to be 2.4, 2, 1.80 and 1.62 mmol/g at 273, 293, 303 and 313 K respectively (*Figure 3.5*).

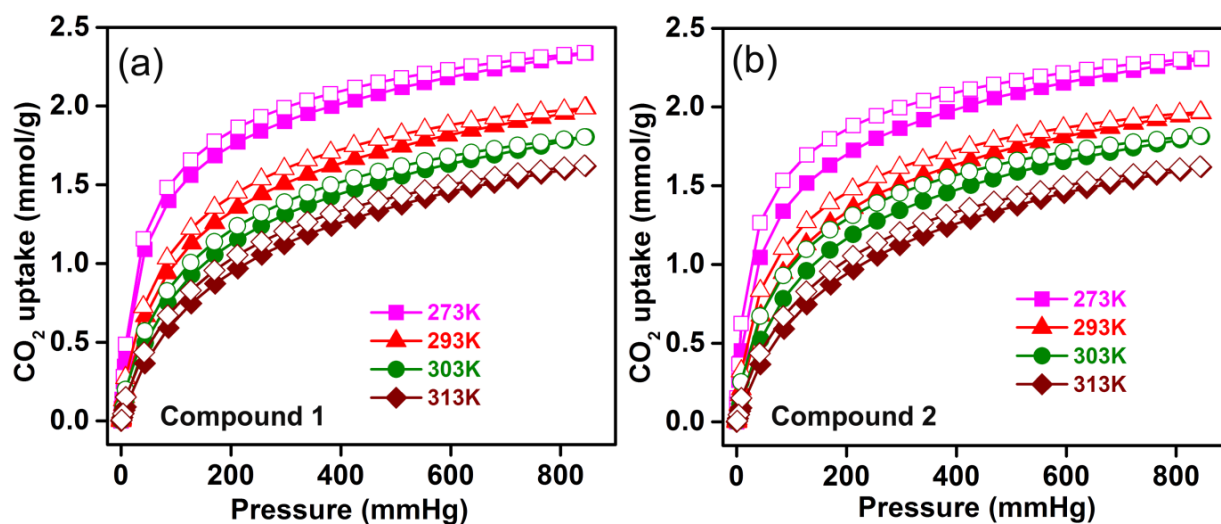


Figure 3.5 CO_2 adsorption plots at various temperatures for (a) compound **1** and (b) compound **2**. Please note that the filled symbols shows the adsorption branch whereas the open symbols shows the desorption branch at a particular temperature.

The same CO_2 uptake shown by these frameworks pointed towards the fact that the change of metal nodes did not affect the overall framework structure and porosity. Further, to know the maximum CO_2 capacity at 1.1 bar, a 195 K CO_2

adsorption isotherm was measured for compound **1**, which showed an uptake of 3.67 mmol/g (*Appendix A3.11*). However, it was perceived that the slope of the CO₂ adsorption isotherm at 195 K and 1.1 bar pressure was not zero, indicating that the framework might be able to accommodate more CO₂ gas at higher pressure ranges.

Importantly, the CO₂ uptake for these isostructural frameworks has been compared with the already reported oxalate-aminotriazolate MOF by Shimizu and co-workers.^{44,45} It was observed that the Zn₂(Atz)₂Ox ultra-microporous MOF^{44,45} reported by them had more CO₂ capacity as compared to the present bimetallic MOFs. This could be attributed to the occurrence of protruding free primary amine groups in the pores of Zn₂(Atz)₂Ox MOF, which facilitates CO₂-amine interactions, and give rise to cooperative effect responsible for the enhanced CO₂ uptake in the Zn₂(Atz)₂Ox framework. Whereas, in the present case the free primary amine of the aminotriazole and aminotriazolate groups does not point directly towards the framework pores, resulting into a comparatively lower CO₂ capacity than Zn₂(Atz)₂Ox MOF. Similar phenomena have been observed for the Zn-based aminotriazolate-phosphate⁴³ framework reported by the same group, in which due to lack of proper orientation of the primary amines, the CO₂ uptake was not as high as anticipated. Also, these bimetallic frameworks reported in the present chapter, have pore accessibility only along the b-axis while the access along the other two orthogonal directions are blocked. Interestingly, in comparison to the ultra-microporous MOFs reported in the chapter 2, the CO₂ capacities shown by these bimetallic MOFs were indeed higher.

BET and Langmuir surface areas for framework **1** and **2** were estimated from their 273 K CO₂ adsorption isotherm branch. For framework **1**, the BET and Langmuir surface area were calculated to be 284 m²/g and 290 m²/g respectively (*Appendix A3.12 and Appendix A3.13*), whereas for **2**, the BET surface area came around 295 m²/g and Langmuir surface area was calculated to be 297 m²/g (*Appendix A3.14 and A3.15*). The pore size distribution was estimated by DFT analysis which showed a half pore width of 2.28 Å for both **1** and **2**, signifying the ultra-microporous nature of these bimetallic frameworks (*Appendix A3.16-A3.19*).

To estimate the interaction of CO₂ with these frameworks, heat of adsorption calculations were done by virial method. For this Virial equation has been fitted to the

273 K and 293 K CO₂ adsorption isotherm branches of frameworks **1** and **2**. The heat of adsorption (HOA) value of 35 and 33 kJ/mol were obtained for **1** and **2** respectively at zero loadings (*Figure 3.6 and Appendix A3.20-A3.25*). These HOA values obtained signify a moderate interaction of CO₂ with the framework. Further, the HOA profile showed a gradual decrease with the increase in CO₂ loadings and reaches a minimum value of ~25 kJ/mol at high loadings (*Figure 3.6*), indicating the presence of only one type of adsorptive sites in the framework. The apparent CO₂/N₂ selectivity could be observed from comparison of the CO₂ and N₂ adsorption isotherms at 303 K for both framework **1** and **2** (*Figure 3.7*).

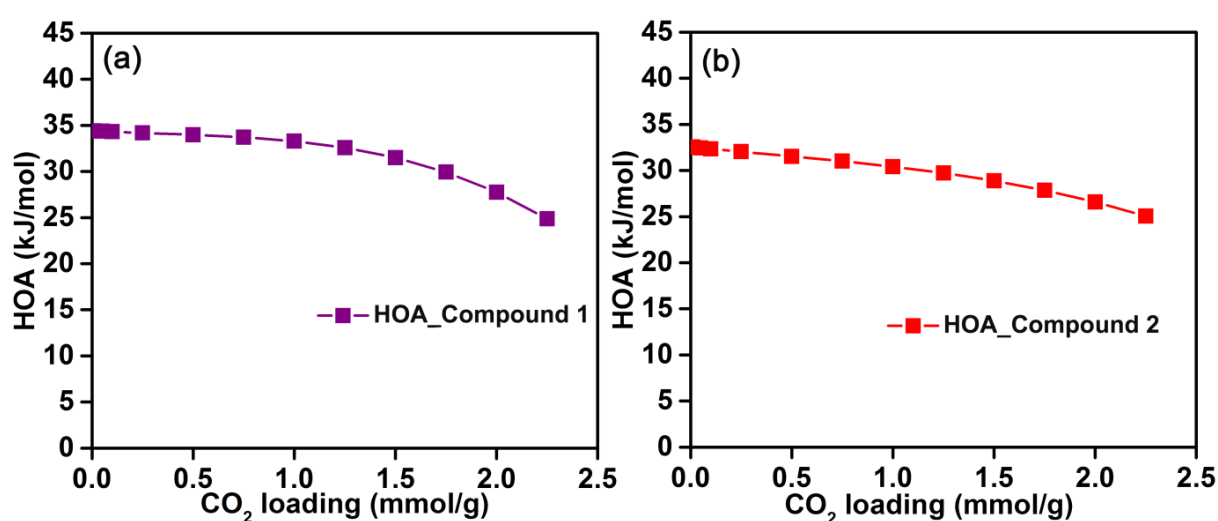


Figure 3.6 HOA plots obtained from virial fitting at temperatures 273 K and 298 K for MOFs **1** and **2**.

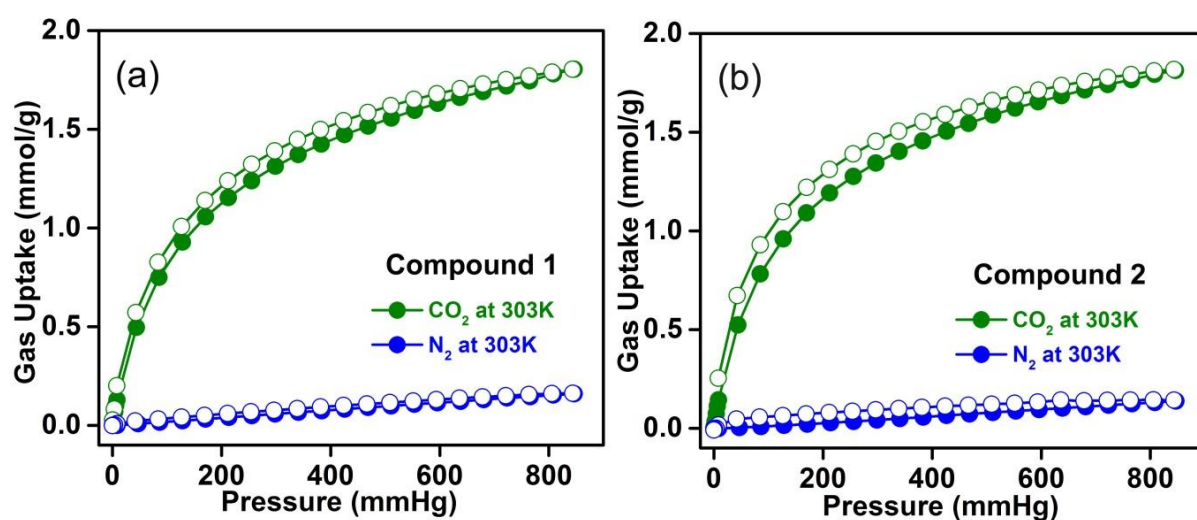


Figure 3.7 The comparison between the CO₂ and N₂ adsorption isotherms at 303 K for compound **1** and **2** showing the high apparent CO₂/N₂ selectivity.

One of the major goals of this study was to introduce hydrolytic stability. To see this, the bulk samples of compound **1** and **2** were exposed to steam for a period of 72 hours. The PXRD of these steam treated samples showed no substantial loss in the crystallinity (*Appendix A3.26*). Followed by this, the steam treated samples were exposed to CO₂ at 273 K. It was observed that upon steam treatment no loss in CO₂ capacity took place, which signifies the stability of these MOFs under hydrolytic conditions (*Figure 3.8*). If these bimetallic frameworks are compared with the only cobalt based framework, ([Co₂(C₂O₄)₂(C₂N₄H₄)₃](CH₃OH)) obtained in chapter 2, one can understand the reason for the steam stability incorporated into these bimetallic frameworks.

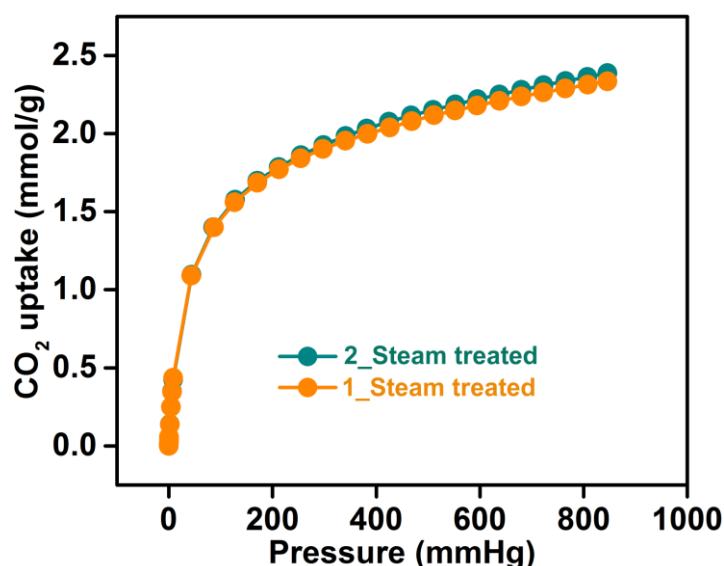


Figure 3.8 CO₂ adsorption isotherms at 273 K for the steam treated samples of **1** and **2**.

The [Co₂(C₂O₄)₂(C₂N₄H₄)₃](CH₃OH) (Chapter 2) framework having neutral dangling aminotriazoles, made it easier to be replaced by water molecules causing the overall structural degradation under humid conditions. However, in the present case the framework consists of μ -2 bridging neutral aminotriazoles and relatively stronger μ -3 bridging aminotriazolate linkers, which makes it comparatively difficult to get replaced with water under humid conditions. Now, under the similar reaction conditions the [Co₂(C₂O₄)₂(C₂N₄H₄)₃](CH₃OH) framework obtained in the chapter 2 was completely based on neutral aminotriazole linkers. Whereas in the present case the introduction of the hydroxide containing basic Zn-salt assists a partial deprotonation of the aminotriazole linkers and results into μ -3 bridging aminotriazolate form, which improves the steam stability of the frameworks. This has

been further affirmed based on some of the already reported literature, which suggests that the M-N bonds in the azolate based frameworks are much stronger to be affected under different type of chemical and hydrolytic conditions, owing to their more basic character.³⁹⁻⁴⁷ The post adsorption stability for these bimetallic MOFs were confirmed by comparing the PXRD patterns of the post adsorption and as-synthesized samples, which suggested that the samples were completely intact after undergoing several adsorption-desorption cycles (*Figure 3.9*).

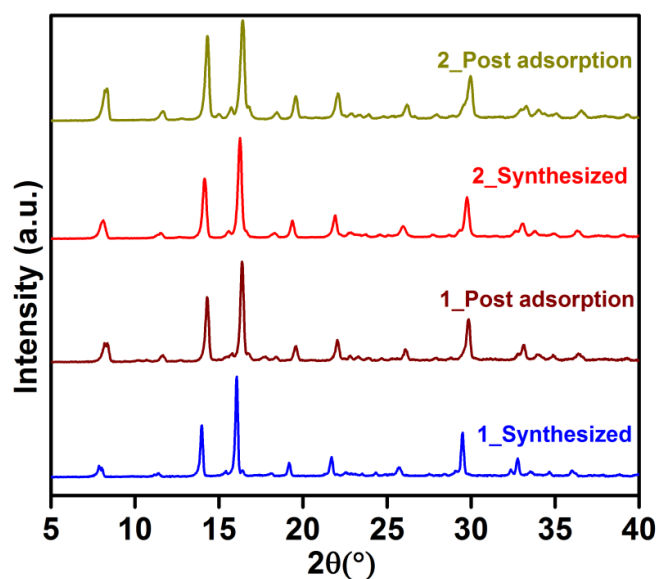


Figure 3.9 Post adsorption PXRD comparisons for the bimetallic MOFs after several adsorption-desorption cycles.

3.4 Conclusion

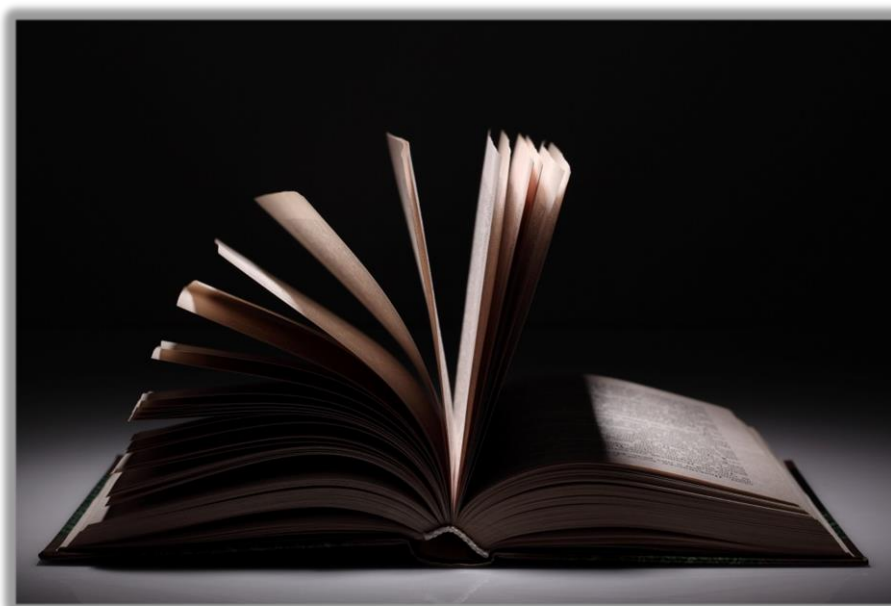
The present chapter demonstrates the synthesis and characterizations of two isostructural bimetallic MOFs. The single crystal structure reveals the presence of ultra-micropores in them. Both these MOFs have shown good selective CO₂ adsorption. Further, it has been observed that these MOFs show good thermal and hydrolytic stability. The hydrolytic stability and the permanent porosity of these MOFs have been ascribed to the rigid μ -3 binding mode of the anionic aminotriazolate linker. It has been shown that the presence of hydroxide species in the reaction medium facilitates the partial deprotonation of the aminotriazole linkers and thus favoring the formation of frameworks that are stable under humid conditions.

3.5 References

1. Quadrelli, R.; Peterson, S. *Energy Policy* **2007**, *35*, 5938.
2. CO₂ Emissions from Fuel Combustion Highlights (2015 Edition) © OECD/IEA, **2015**.
3. Sumida, K.; Rogow, D. L.; Mason, J. A.; McDonald, T. M.; Bloch, E. D.; Herm, Z. R.; Bae, T.-H.; Long, J. R. *Chem. Rev.* **2012**, *112*, 724.
4. Ciferno, J. P.; Fout, T. E.; Jones, A. P.; Murphy, J. T. *Chem. Eng. Prog.* **2009**, *105*, 33.
5. Zhang, Z.; Yao, Z.-Z.; Xiang, S.; Chen, B. *Energy Environ. Sci.* **2014**, *7*, 2868.
6. Nandi, S.; Collins, S.; Chakraborty, D.; Banerjee, D.; Thallapally, P. K.; Woo, T.K.; Vaidhyanathan, R. *J. Am. Chem. Soc.* **2017**, *139*, 1734.
7. Nugent, P.; Belmabkhout, Y.; Burd, S. D.; Cairns, A. J.; Luebke, R.; Forrest, K.; Pham, T.; Ma, S.; Space, B.; Wojtas, L.; Eddaoudi, M.; Zaworotko, M. J. *Nature* **2013**, *495*, 80.
8. Du, L.; Lu, Z.; Zheng, K.; Wang, J.; Zheng, X.; Pan, Y.; You, X.; Bai, J. *J. Am. Chem. Soc.* **2013**, *135*, 562.
9. Keskin, S.; Heest, T. M. V.; Sholl, D. S. *ChemSusChem* **2010**, *3*, 879.
10. Granite, E. J.; Pennline, H. W. *Ind. Eng. Chem. Res.* **2002**, *41*, 5470.
11. Li, G.; Xiao, P.; Webley, P.; Zhang, J.; Singh, R.; Marshall, M. *Adsorption* **2008**, *14*, 415.
12. Li, G.; Xiao, P.; Webley, P. A.; Zhang, J.; Singh, R. *Energy Procedia* **2009**, *1*, 1123.
13. Liang, Z.; Marshall, M.; Chaffee, A. L. *Energy Procedia* **2009**, *1*, 1265.
14. Zhang, J.; Xiao, P.; Li, G.; Webley, P. A. *Energy Procedia* **2009**, *1*, 1115.
15. Nandi, S.; Chakraborty, D.; Vaidhyanathan, R. *Chem. Commun.* **2016**, *52*, 7249.
16. Iremonger, S. S.; Liang, J.; Vaidhyanathan, R.; Shimizu, G. K. H. *Chem. Commun.* **2011**, *47*, 4430.
17. McDonald, T. M.; Lee, W. R.; Mason, J. A.; Wiers, B. M.; Hong, C. S.; Long, J. R. *J. Am. Chem. Soc.* **2012**, *134*, 7056.
18. McDonald, T. M.; D'Alessandro, D. M.; Krishna, R.; Long, J. R. *Chem. Sci.* **2011**, *2*, 2022.
19. Qiao, Z.; Wang, N.; Jiang, J.; Zhou, J. *Chem. Commun.* **2016**, *52*, 974.
20. Lin, Y.; Kong, C.; Chen, L. *RSC Adv.* **2016**, *6*, 32598.
21. Maity, D. K.; Halder, A.; Bhattacharya, B.; Das, A.; Ghoshal, D. *Cryst. Growth Des.* **2016**, *16*, 1162.
22. Zheng, B.; Bai, J.; Duan, J.; Wojtas, L.; Zaworotko, M. J. *J. Am. Chem. Soc.* **2011**, *133*, 748.
23. Fracaroli, A. M.; Furukawa, H.; Suzuki, M.; Dodd, M.; Okajima, S.; Gá ndara, F.; Reimer, J. A.; Yaghi, O. M. *J. Am. Chem. Soc.* **2014**, *136*, 8863.
24. Liao, P.-Q.; Chen, H.; Zhou, D.-D.; Liu, S.-Y.; He, C.-T.; Rui, Z.; Ji, H.; Zhang, J.-P.; Chen, X.-M.; *Energy Environ. Sci.* **2015**, *8*, 1011.
25. Zhang, Z.; Zhao, Y.; Gong, Q.; Li, Z.; Li, J. *Chem. Commun.* **2013**, *49*, 653.

26. Low, J. J.; Benin, A. I.; Jakubczak, P.; Abrahamian, J. F.; Faheem, S. A.; Willis, R. R. *J. Am. Chem. Soc.* **2009**, *131*, 15834.
27. Yu, J.; Wu, Y.; Balbuena, P. B. *ACS Sustainable Chem. Eng.* **2016**, *4*, 2387.
28. Liu, J.; Wang, Y.; Benin, A. I.; Jakubczak, P.; Willis, R. R.; LeVan, M. D. *Langmuir* **2010**, *26*, 14301.
29. Yu, K.; Kiesling, K.; Schmidt, J. R. *J. Phys. Chem. C* **2012**, *116*, 20480.
30. Greathouse J. A.; Allendorf M. D. *J. Am. Chem. Soc.* **2006**, *128*, 10678.
31. Cychoz, K. A.; Matzger, A. J. *Langmuir* **2010**, *26*, 17198.
32. Li, Y.; Yang, R. T. *Langmuir* **2007**, *23*, 12937.
33. Ma, D.; Li, Y.; Li, Z. *Chem. Commun.* **2011**, *47*, 7377.
34. Jasuja, H.; Zang, J.; Sholl, D. S.; Walton, K. S. *J. Phys. Chem. C* **2012**, *116*, 23526.
35. Zhang, W.; Hu, Y.; Ge, J.; Jiang, H.-L.; Yu, S.-H. *J. Am. Chem. Soc.* **2014**, *136*, 16978.
36. Drache, F.; Bon, V.; Senkovska, I.; Marschelke, C.; Synytska, A.; Kaskel, S. *Inorg. Chem.* **2016**, *55*, 7206.
37. Wu, T.; Shen, L.; Luebbbers, M.; Hu, C.; Chen, Q.; Ni, Z.; Masel, R. I. *Chem. Commun.* **2010**, *46*, 6120.
38. Nguyen J. G.; Cohen S. M. *J. Am. Chem. Soc.* **2010**, *132*, 4560.
39. Huang, X.-C.; Lin, Y.-Y.; Zhang, J.-P.; Chen, X.-M. *Angew. Chem. Int. Ed.* **2006**, *45*, 1557.
40. Gu, J.-Z.; Lu, W.-G.; Jiang, L.; Zhou, H.-C.; Lu, T.-B. *Inorg. Chem.* **2007**, *46*, 5835.
41. Choi, H. J.; Dinca, M.; Dailly, A.; Long, J. R. *Energy Environ. Sci.* **2010**, *3*, 117.
42. Galli, S.; Masciocchi, N.; Colombo, V.; Maspero, A.; Palmisano, G.; Lopez-Garzon, F. J.; Domingo-Garcia, M.; Fernandez-Morales, I.; Barea, E.; Navarro, J. A. R. *Chem. Mater.* **2010**, *22*, 1664.
43. Vaidhyanathan, R.; Iremonger, S. S.; Shimizu, G. K. H.; Boyd, P. G.; Alavi, S.; Woo, T. K. *Angew. Chem. Int. Ed.* **2012**, *51*, 1826.
44. Vaidhyanathan, R.; Iremonger, S. S.; Dawson, K. W.; Shimizu, G. K. H.; *Chem. Commun.* **2009**, 5230.
45. Vaidhyanathan, R.; Iremonger, S. S.; Shimizu, G. K. H.; Boyd, P. G.; Alavi, S.; Woo, T. K. *Science* **2010**, *330*, 650.
46. Gelfand, B. S.; Lin, J.-B.; Shimizu, G. K. H. *Inorg. Chem.* **2015**, *54*, 1185.
47. Lin, R.-B.; Chen, D.; Lin, Y.-Y.; Zhang, J.-P.; Chen, X.-M. *Inorg. Chem.* **2012**, *51*, 9950.
48. Tan, K.; Nijem, N.; Gao, Y.; Zuluaga, S.; Li, J.; Thonhauser, T.; Chabal, Y. J. *CrystEngComm.* **2015**, *17*, 247.

Chapter 4



**Enhancing carbon capture capacities
of a rigid ultra-microporous MOF
through gate-opening assisted by low
CO₂ pressures and swiveling oxalate
pillars**

4.1 Introduction

The area of porous coordination polymers, also known as metal organic frameworks (MOFs), has gained tremendous interest since last few decades due to its various applications.¹⁻⁹ Modular structures of these co-ordination polymers combined with appropriate choice of ligands and metal ions enables construction of rigid or dynamic frameworks.¹⁰⁻¹⁴ The length and symmetry of the organic linker, generally decides the amount of void space that can be introduced into these materials, and in addition it could promote flexibility of the framework. It can be very advantageous, if the flexibility can be manipulated.¹⁰⁻¹⁴ MOFs with stable and robust frameworks that maintain their porous structure before and after guest-sorption, are regarded as '2nd generation MOFs' which are good adsorbents analogous to zeolites.¹⁰ The '3rd generation' MOFs exhibit dynamic structure where the flexibility of framework induces reversible response to the external stimuli such as pressure or temperature and can be gas specific.¹¹⁻¹⁶ Some of them exhibit hysteretic isotherms, which originate from a molecular gate opening mechanism.¹¹⁻²⁰ In some cases, hysteresis can be manipulated by carefully controlling the external parameters such as heat and pressure.¹⁷⁻²⁰ In general, this property is associated with MOFs that are built from relatively longer struts and sometimes in large pore frameworks built from short linkers.¹⁷⁻²² In chapter 2, it was demonstrated that ultra-microporous MOFs also show this type of stimuli responsive framework dynamicity, but is rare.²³ Maximum benefit of a gate-opening can be realized when a subtle molecular motion produces big change in porosity of the material and thereby its gas uptake capacity.^{21,22} Generally, MOFs are synthesized solvothermally and the solvents play a crucial role in deciding their structure, texture and phase purity. The dynamic role of solvents in deciding the structure of MOFs has been investigated using both theoretical and experimental methods.²⁴⁻³⁰ The activation energetics and the reaction thermodynamics in many cases are determined by the solvents and hence can account for the changes of potential energy barrier and overall free energy via solute-solvent interactions.²⁶

The pore size of the MOFs could be controlled by the appropriate choice of solvent. Senkovska et al.,³¹ in a systematic study demonstrate the effect of solvent size on the frameworks of naphthalene dicarboxylic acid (NDC) based MOFs, where

the two MOFs $[\text{Mg}_3(\text{NDC})_3(\text{DEF})_4]$ and $[\text{Mg}_3(\text{NDC})_3(\text{DMF})_4]$ reported, showed that the use of DMF instead of DEF causes a significant reduction in the pore dimensions. Further, when 5% H_2O -DMF solvent mixture was used, a completely new discrete molecule was obtained. Similar results have been realized for MOFs constructed from $\text{Zn}(\text{NO}_3)_2 \cdot 6\text{H}_2\text{O}$ and H_2BDC in dry DEF and normal DEF (with moisture content).²⁵ This slight variation of the moisture content of the solvent yielded two different frameworks $[\text{Zn}_4(\mu_4\text{-O})(\mu\text{-BDC})_3] \cdot 3\text{DEF}$ and $[\text{NH}_2\text{Et}_2]_2[\text{Zn}_3(\mu\text{-BDC})_4] \cdot (2.5\text{DEF})$.²⁵ To see the templating effect caused by solvents, Hao et al.³² employed a Zn based 1,3,5-benzenetricarboxylate (BTC) MOF and carried out solvent variation with solvents of varying size (DMF, DMA, DEF, DEP, DPE and DPP). It was observed that by increasing the size of the solvent, the pore size of MOFs correspondingly increases from 9 Å to 23 Å.³² Hence, from these observations it was clear that in MOF synthesis, solvents in general plays two crucial roles: (i) they can be '*structure directing agents*' interacting strongly with the framework's components right from their construction of smaller building units to the final higher dimensional structure or (ii) they could form weaker interactions with the framework's components which co-operatively provide sufficient strength to act as a 'template' by filling up the voids and allowing the framework to grow around them.^{32,33,34} Interestingly, Chen et al.,³⁵ constructed a MOF by solvothermally reacting $\text{Zn}(\text{NO}_3)_2$, oxalic acid (Ox) and 3-aminotriazole (Hatz) at 130°C with solvent as water-DMF mixture and obtained $[\text{Zn}_4(\text{Atz})_4(\text{CO}_3)(\text{Ox})(\text{H}_2\text{O})_2] \cdot \text{H}_2\text{O}$.³⁵ In an another report, Shimizu and co-workers,^{36,37} synthesized an ultra-microporous MOF with the similar framework component in methanol-water mixture to obtain $\text{Zn}_2(\text{C}_2\text{O}_4)(\text{C}_2\text{N}_4\text{H}_3)_2 \cdot (\text{H}_2\text{O})_{0.5}$, (ZnAtzOx_MeOH) (1) framework, which was demonstrated to be highly porous and CO_2 selective at the low pressure region. Selectivity arises both due to its appropriate pore dimensions as well as the chemical functionality of the pores, which favored the CO_2 -amine host-guest interactions.³⁶ This material, though it had remarkable CO_2 selectivity, showed a capacity of only 3.8 mmol/g at 293 K, 1 bar, which is not sufficient for gaining practical utility. This requirement motivated present work to improve CO_2 capacity of this material to make it a good Vacuum Swing Adsorption (VSA) candidate.³⁶⁻³⁸ Considering, the key role played by solvent in deciding the final structure and porosity of resulting MOF^{28,30-34} and realizing that the formation of the porous ZnAtzOx phase in methanol, the present

work set out to investigate methods to improving the capacity for CO₂ adsorption in ZnAtzOx phases, by tuning the framework structure via varying the solvent.

This chapter reports the synthesis, structural characterization, thermal analysis and adsorption studies of a family of topologically related ZnAtzOx frameworks obtained under solvothermal conditions. Importantly, through choice of solvent it is shown how a 3rd generation porous material with topology similar to its rigid 2nd generation counterparts can be obtained. And, this 3rd generation MOF exhibits higher CO₂ capacities arising from exceptionally subtle '*molecular swiveling*' assisted gate opening.

4.2 Experimental section

4.2.1 Materials: All chemicals were used from the commercially available sources without further purification.

4.2.2 Physical measurements:

4.2.2.1 Powder X-ray diffraction: Powder XRDs were carried out using a Rigaku Miniflex-600 instrument and processed using PDXL software.

4.2.2.2 Variable temperature powder X-ray diffraction: VT-PXRD patterns were measured on Bruker D8 Advanced X-Ray diffractometer at different temperatures using Cu-K α radiation ($\lambda = 1.5406 \text{ \AA}$) with a scan speed of $0.5^\circ \text{ min}^{-1}$ and a step size of 0.01° in 2 theta.

4.2.2.3 Variable temperature powder X-ray diffraction under CO₂: Sample was loaded on to a 0.5 mm glass capillary and then evacuated by heating at 150°C for 12 hours, then was backfilled with CO₂ at ~ 900 mbar pressures. The capillary, while mounted in the measurement position in the X-ray diffractometer, was heated using a constant flow of hot air stream, temperature of which was continuously monitored using a K-type thermocouple and fed back to the electronic heater controller, which controlled the heater power to reach the set-point temperature. The thermocouple was placed in close to the capillary, without interfering with the path of the X-ray, to ensure that the actual temperature of the capillary was measured with good accuracy.

4.2.2.4 Thermo-gravimetric analysis: Thermo-gravimetric analysis was carried out on NETSZCH TGA-DSC system. The routine TGAs were done under N₂ gas flow (50ml/min) and samples were heated from RT to 550°C at 2°C/min.

4.2.2.5 Single crystal X-ray diffraction: Single-crystal data was collected on a Bruker SMART APEX four-circle diffractometer equipped with a CMOS photon 100 detector (Bruker Systems Inc.) and with a Cu K α radiation (1.5418 Å). Single crystal data was collected using Bruker Single crystal X-ray diffractometer at wavelength of 1.5418 Å. The incident X-ray beam was focused and monochromated using Microfocus (1 μ S). Crystal of **2***, **3** and **4** was mounted on nylon Cryo loops with Paratone-N oil. Data were collected at 100 K and was integrated using Bruker SAINT Software, corrected for absorption using SADABS. Structures were solved by Intrinsic Phasing module of the direct methods and refined using the SHELXTL 2014 software suite. All non-hydrogen atoms were located from iterative examination of difference F-maps following which the structure was refined using least-squares method. Hydrogen atoms were placed geometrically and placed in a riding model.

4.2.2.6 Infra-red spectrophotometry: IR spectra were obtained by making KBr pellets using a Nicolet ID5 attenuated total reflectance IR spectrometer operating at ambient temperature.

4.2.2.7 Adsorption: Adsorption studies were done on Quantachrome IQ adsorption analyser using gases used were of 99.999% purity. Further for fitting the isotherms, BET and Langmuir methods were employed. For pore size distribution calculation NLDFT was used. Heat of adsorption calculation was done by virial method. Simultaneously, heat of adsorption (HOA) calculations has also been done by fitting the adsorption isotherm in to Langmuir-Freundlich dual site model.

4.2.2.8 Elemental analysis: Elemental analyses were performed on a Vario-EL cube elemental analyser.

4.2.3 Synthesis

All synthesis employed Zn₅(CO₃)₂(OH)₆, Oxalic acid and 3-aminotriazole in the ratio 1:1:5 and the solvothermal reactions were carried out at 180°C for 2 days.

4.2.3.1 Synthesis of $[\text{Zn}_2(\text{C}_2\text{O}_4)(\text{C}_2\text{N}_4\text{H}_3)_2](\text{H}_2\text{O})_x$ (2): In a typical synthesis of Compound **2**, 0.1 g of $\text{Zn}_5(\text{CO}_3)_2(\text{OH})_6$, 0.0819 g of oxalic acid and 0.3824 g of 3-amino-1,2,4-triazole were added in 5 ml of H_2O , in a 23 ml autoclave, which was stirred for 30 minutes at room temperature and then reacted hydrothermally at 180°C for 2 days. On cooling, colorless microcrystalline product was obtained, which was washed with copious amounts of H_2O and methanol to remove any unreacted organics, followed by which the product was dried in air, FT-IR (cm^{-1}): 3855, 3737, 3683, 3641, 3435, 3349, 2364, 2323, 1736, 1637, 1544, 1517, 1409, 1310, 1226, 1065, 1003, 891, 801, 651. Analytical data for the solvent-free framework; observed (%): C (18.42), H (1.65), N (29.16); calculated (%): C (18.72), H (1.57), N (29.11).

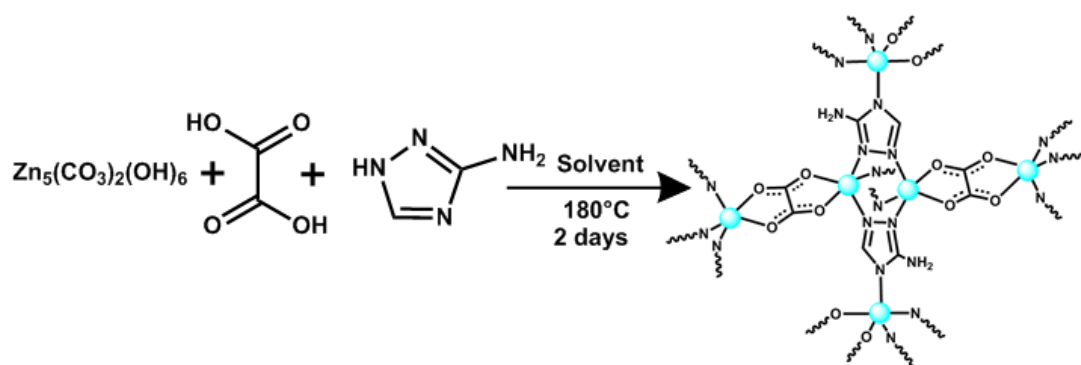
4.2.3.2 Synthesis of $[\text{Zn}_2(\text{C}_2\text{O}_4)(\text{C}_2\text{N}_4\text{H}_3)_2](\text{C}_2\text{H}_5\text{OH})$ (3): Compound **3** was synthesized in a mixed solvent medium. In a typical synthesis, 0.1 g of $\text{Zn}_5(\text{CO}_3)_2(\text{OH})_6$, 0.0819 g of oxalic acid and 0.3824 g of 3-amino-1,2,4-triazole were added in a solvent mixture of 1 ml H_2O + 5 ml ethanol, in a 23 ml autoclave, which was stirred for 30 minutes at room temperature followed by solvothermal reaction at 180°C for 2 days. On cooling, colorless crystals suitable for single crystal x-ray diffraction were obtained. The bulk product was washed with copious amounts of H_2O and methanol to remove any unreacted organics and dried in air, FT-IR (cm^{-1}): 3850, 3736, 3669, 3653, 3400, 1746, 1677, 1627, 1609, 1541, 1510, 1351, 1321, 1215, 1208, 1049, 986, 784, 658. Analytical data observed (%): C (22.42), H (2.65), N (26.1); calculated (%): C (22.29), H (2.81), N (26.00).

4.2.3.3 Synthesis of $[\text{Zn}_2(\text{C}_2\text{O}_4)(\text{C}_2\text{N}_4\text{H}_3)_2](\text{C}_3\text{H}_7\text{OH})$ (4): Compound **4** was synthesized in a mixed solvent medium. In a typical synthesis, 0.1 g of $\text{Zn}_5(\text{CO}_3)_2(\text{OH})_6$, 0.0819 g of oxalic acid and 0.3824 g of 3-amino-1,2,4-triazole were added in a solvent mixture of 1 ml H_2O + 5 ml 1-propanol, in a 23 ml autoclave, which was stirred for 30 minutes at room temperature followed by solvothermal reaction at 180°C for 2 days. On cooling, colorless crystals suitable for single crystal x-ray diffraction were obtained. The bulk product was then washed with copious amounts of H_2O and methanol to remove any unreacted organics and dried in air, FT-IR (cm^{-1}): 3849, 3731, 3636, 3418, 3354, 3231, 1640, 1547, 1520, 1423, 1310, 1218, 1066, 1004, 874, 801, 640. Analytical data framework; observed (%): C (24.42), H (3.65), N (25.6); calculated (%): C (24.29), H (3.17), N (25.18).

4.2.3.4 Synthesis of $[\text{Zn}_2(\text{C}_2\text{O}_4)(\text{C}_2\text{N}_4\text{H}_3)_2]$ (solvent)(2^*): Compound 2^* was synthesized in a mixed solvent medium. In a typical synthesis, 0.1 g of $\text{Zn}_5(\text{CO}_3)_2(\text{OH})_6$, 0.0819 g of oxalic acid and 0.3824 g of 3-amino-1,2,4-triazole were added in a solvent mixture of 3 ml H_2O + 3 ml 1-butanol, in a 23 ml autoclave, which was stirred for 30 minutes at room temperature followed by solvothermal reaction at 180°C for 2 days. On cooling, colorless crystals suitable for single crystal x-ray diffraction were obtained. The bulk product was then washed with copious amounts of H_2O and methanol to remove any unreacted organics and dried in air. Analytical data for the solvent-free framework; observed (%): C (18.35), H (1.32), N (29.47); calculated (%): C (18.72), H (1.57), N (29.11).

It is to be noted here that Phase $2/2^*$ could be synthesized using single solvent reactions involving BuOH, however, this does not yield large enough single crystals for x-ray diffraction. Use of H_2O + Solvent (Solvent = pentanol, hexanol, heptanol) in a 1:5 ratio during synthesis yielded $2/2^*$ as microcrystalline solids. This suggests all aliphatic alcohols bulkier than butanol could act as templates for synthesis of 2 .

A general synthetic scheme for the synthesis of the polymorphic phases is shown below (Scheme 4.1)



Scheme 4.1 A general solvothermal reaction scheme for the synthesis of ZnAtzOx polymorphic phases. The cyan spheres represent the Zn^{2+} cations.

4.3 Results and discussions

4.3.1 Synthesis

Metal organic frameworks with composition $[\text{Zn}_2(\text{C}_2\text{O}_4)(\text{C}_2\text{N}_4\text{H}_3)_2](\text{H}_2\text{O})_x$ (2), $[\text{Zn}_2(\text{C}_2\text{O}_4)(\text{C}_2\text{N}_4\text{H}_3)_2](\text{Solvent})_x$ (2^*), $[\text{Zn}_2(\text{C}_2\text{O}_4)(\text{C}_2\text{N}_4\text{H}_3)_2](\text{C}_2\text{H}_5\text{OH})$ (3) and

$[\text{Zn}_2(\text{C}_2\text{O}_4)(\text{C}_2\text{N}_4\text{H}_3)_2](\text{C}_3\text{H}_7\text{OH})$ (**4**) were obtained under solvothermal condition with water; butanol-water, ethanol-water and 1-propanol-water as solvents respectively (Scheme 4.1). Systematic solvent variation produced distinct MOFs which did not show any tendency to inter-convert in a *Single Crystal to Single Crystal* fashion. Importantly the phases were also prepared by using a single solvent (Synthesis solvent: H_2O (**2**), EtOH (**3**), n-PrOH (**4**) and n-BuOH (**2***)), instead of solvent mixtures. It was observed from the crystal quality, that although these phases could be formed pure using the single solvent reactions, solvent mixture with water resulted in dramatic improvement in crystal quality without any change in phase.

4.3.2 Crystal structures

Structures of all the phases were determined from single crystal X-ray diffraction. Typically, the frameworks have Zn^{2+} with distorted trigonal bi-pyramidal geometry. Their co-ordinations are from μ -3 bridging aminotriazolate units and bidentately bis-chelating oxalate units, resulting in highly rigid frameworks. Notably, in all the phases $-\text{NH}_2$ of the aminotriazole remains free. The 3-dimensional structure can be viewed as the ZnAtz layers pillared by oxalate units (Figure 4.1).

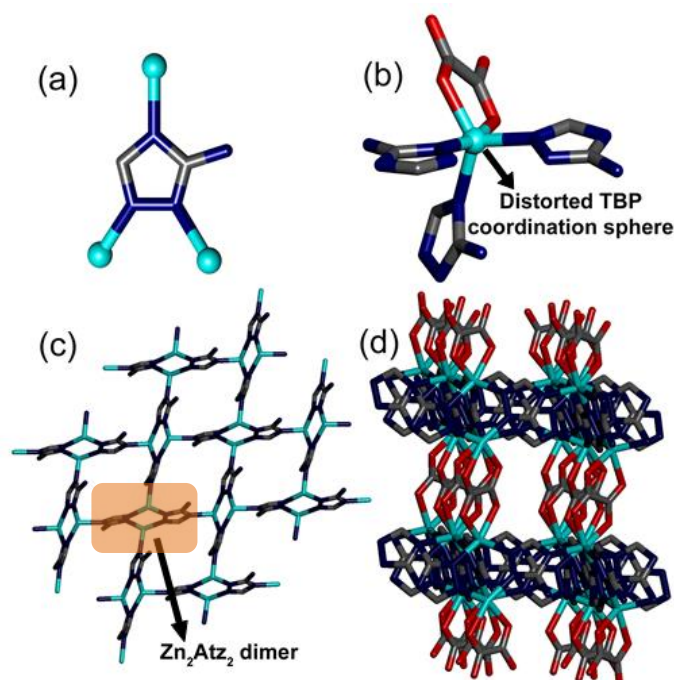


Figure 4.1 (a) μ -3 bridging mode of Atz linker, (b) distorted trigonal bi-pyramidal (TBP) coordination environment for Zn^{2+} , (c) layer formed of Zn_2Atz_2 dimers, and (d) crystallographic view of the 3-dimensional framework formed by oxalate pillaring of ZnAtz layers.

Topologically, the ZnAtz layers formed by linking of dimeric Zn_2Atz_2 units are pillared in an out-of-plane fashion by the oxalate units. Now if these Zn_2Atz_2 dimers are reduced to nodes and the Atz and oxalate units to linkers, the resultant topology in all the cases is a simple six-connected cubic net (*Figure 4.2*). The differences between the structures originate from the extent and mode of puckering of the layers (defined by the angle between the adjacent Zn_2Atz_2 dimers discussed later in the chapter). The Atz and oxalate units together determine the shape and size of the pores.

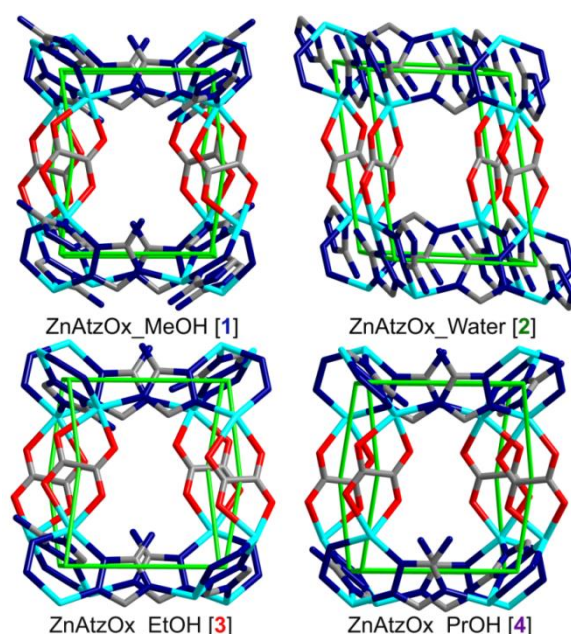


Figure 4.2 The cavities in **1**, **2/2***, **3** and **4** have been shown and the overlaying 6-connected topology represents the cavities as distorted cubes (green). As can be seen the shape of the cubes is determined by tilt of the oxalate pillars and the puckering of the Atz layers.

4.3.3 Bulk characterizations

All samples could be made as pure phases in bulk. It was further confirmed by powder X-ray analysis that the phase **2** and **2*** are same (*Appendix A4. 11*) and here onwards for their bulk phase studies they will be considered as same. Purity of these MOFs was confirmed by the comparison of simulated and bulk phase PXRD patterns (*Figure 4.3a*). The TGA analysis indicated exceptional thermal stability of the compounds in which **2** shows stability up to 310°C (583 K) and **3** and **4** shows thermal stability up to 300°C (573 K) and 290°C (563 K) respectively, which can be attributed to their rigid μ -3 bridging Atz and the bidentately pillaring oxalate units (*Figure 4.3*). Further, high crystallinity were observed in the temperature range of

room temperature-300°C (573 K) from variable temperature PXRD experiment for all the phases and hence found to be consistent with the obtained TGA results (Appendix A4.12- A4.14).

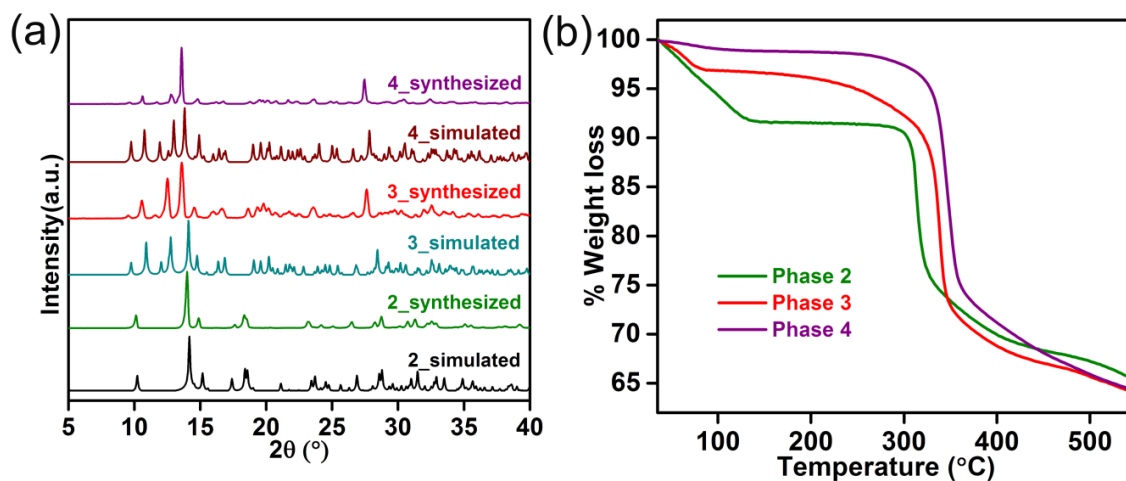


Figure 4.3 (a) Comparison of the simulated with the as-synthesized PXRD patterns for the various phases of ZnAtzOx. (b) TGA graph for the various phases of ZnAtzOx showing thermal stability up to 300°C (573 K).

The IR spectra contain the characteristic peaks due to the carboxylate and aminotriazolate units (Appendix A4.15). Peaks corresponding to CO₂ could be observed in the IR spectra of phase 2 that was exposed to air showing its high affinity for CO₂ (Appendix A4.15). PLATON analyses showed 3, 4 and 2* phase to have an effective solvent accessible volume of 32%, 33%, and 28% respectively. Which was comparable to the parent phase, 1 (31%). As explained earlier, one of the major aim of this study was to improve the capacity of the ZnAtzOx_MeOH (1) phase without losing its inherent selectivity arising from the ultra-microporous character. Thus to evaluate the porosity experimentally, CO₂ adsorption was carried out on these different phases.

4.3.4 Gas adsorption studies

The adsorption measurements were carried out on the activated samples of 2, 3, 4 and 2*. For activation, each of the samples were evacuated at 150°C (423 K) and at (10⁻³ torr vacuum) at the degassing unit of Quantachrome instrument. Then these evacuated samples were subjected directly to the pure CO₂ stream. The CO₂ uptake of 2 and 2* were similar (Appendix A4.16) and were considerably higher than the rest of the phases, including, the parent phase 1 (Figure 4.4a). Phase 3 showed

lower porosity compared to **1** and **2**, while **4** was found to be practically non-porous (*Figure 4.4a*). From here onwards phases **2** and **2*** has not been differentiated, unless required. The relatively higher CO₂ uptake of **2** is achieved by a process of CO₂ assisted gate-opening phenomena (*Figure 4.4a*).

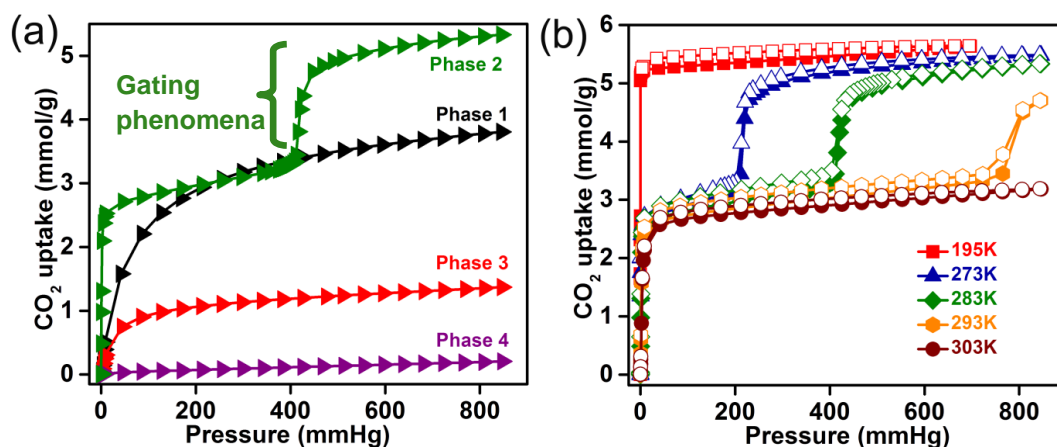


Figure 4.4 (a) CO₂ adsorption comparison for various phases of ZnAtzOx, all measured at 283 K, Colour code: green: ZnAtzOx_Water (**2**), black: ZnAtzOx_MeOH (**1**), red: ZnAtzOx_EtOH (**3**), purple: ZnAtzOx_PrOH (**4**), (b) CO₂ adsorption curve at different temperatures for ZnAtzOx_Water (**2**), please note: solid symbols shows the adsorption branch and the open symbols shows the desorption branch.

Also the profile, particularly in terms of the abruptness of the isotherms at low pressures (0-0.03bar), agrees well between the isotherms of phases **1** and **2** (*Figure 4.4a*). Thus, the gate opening is characterized by a sharp increase in CO₂ uptake at a P/P_0 of 0.2 at 273 K, but lacks any noticeable hysteresis.³⁹ The CO₂ gating in **2** shows temperature dependence, the gating occurs at a CO₂ pressure of 200 mbar at 273 K and shifts to as high as 765 mbar at 293 K (*Figure 4.4b*). This 565 mbar difference in gate opening pressures for a mere 20 K increase in temperature is quite unusual and is reflective of the ultra-microporous character of **2**. This means that a subtle difference in orientation of the organic linkers causes massive difference in the pore accessibilities. Now due to the stepped nature of the 273 K isotherm, surface areas or pore volume determinations from routine DFT models were not feasible. However, taking a logical approach, the 195 K isotherm seems to represent the saturation capacity of the material, while the 303 K isotherm without the gate-opening seemed to represent the capacity due to only one of the adsorption sites or say one type of pore. Thus from 195 K isotherm a BET surface area of 540 m²/g (correlation coefficient, $r = 0.9989$) was calculated, and by separately fitting the low

pressure and high pressure regions of the 273 K data using the standard BET model, 301 m²/g (correlation coefficient, $r = 0.9997$) and 206 m²/g (correlation coefficient, $r = 0.9956$) were obtained, respectively (*Appendix A4.17*). Thus the sum of the surface areas from the low pressure and high pressure regions would yield a surface area comparable to the one from 195 K CO₂ isotherm. This can be explained by considering a dual site model for the CO₂'s filling up the pores in **2**. In fact, the abrupt increase in CO₂ capacity at the gate opening is accompanied likely by an increase in pore volume and this opens up a second adsorption site. To provide further support to this hypothesis, a dual site Langmuir-Freundlich model was employed to calculate the energetics associated with the CO₂-framework interactions for both these sites (*Figure 4.5 and Appendix A4.19*). It turns out that a site I has a HOA of 46 kJ/mol, while the site II has a value of 32 kJ/mol (*Figure 4.5 and Appendix A4.19*). Comparison of these values against the HOA's observed for **1** brings some excellent observations.^{36,37} Phase **1** (ZnAtzOx_MeOH) also had a dual site CO₂ filling, one site with relatively higher HOA (40 kJ/mol) dominated by amine-CO₂ interactions, and the other site with HOA of 32 kJ/mol dominated by CO₂-CO₂ interactions, which were well partitioned in energy contributions via simulations.^{36,37}

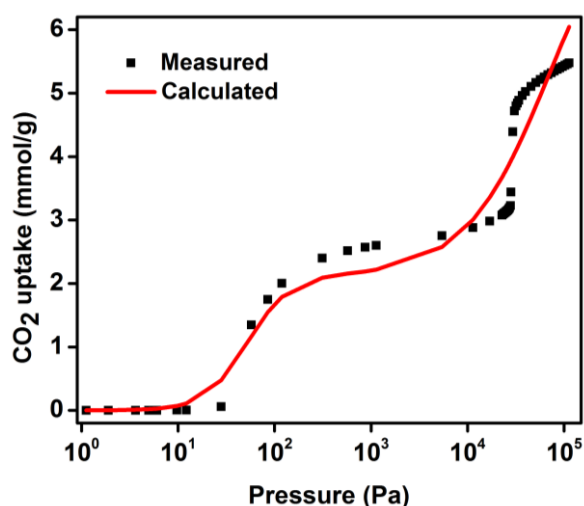


Figure 4.5 Log plot of the Dual site Langmuir-Freundlich model fitted for the 273K CO₂ adsorption branch.

Now, comparing the 195 K or 273 K CO₂ isotherms of **2** with **1**'s, it can be seen that **2** has even more abruptness or steepness at low CO₂ pressures (*Figure 4.4a*), which indicates stronger interactions between the framework and CO₂. This is consistent with the higher HOA obtained for the site I of **2** (46 kJ/mol vs 40 kJ/mol for

1). Meanwhile, the HOA corresponding to the site II of **2** has a value comparable to the one obtained for the second site in **1**, which is mostly due to CO₂-CO₂ interactions. In addition, in **2**, the gate opening significantly enhances the pore volume (from 0.13 cc/g to 0.18 cc/g). Considering that the increase in CO₂ capacity is associated with increase in pore volume resulting from gate opening, it is possible that the second CO₂ site is generated only via this gate opening. Based on the uptakes it can be calculated that the site I holds 1.3 moles of CO₂/FU (formula unit), while the site II would accommodate 0.95 moles/FU. Thus the saturated CO₂ uptake results in **2**.(CO₂)_{2.25}, which is almost one CO₂/FU higher than what was observed for **1**. A good CO₂/N₂ apparent selectivity can be realized by comparing the initial slope of the room temperature isotherms of **2** (*Figure 4.6 and Appendix A4.22*). This room temperature selectivity realized at low pressure of CO₂, is among some of the best performing ultra-microporous MOFs (*Appendix A4.21 and Appendix A4.22*).^{2,38}

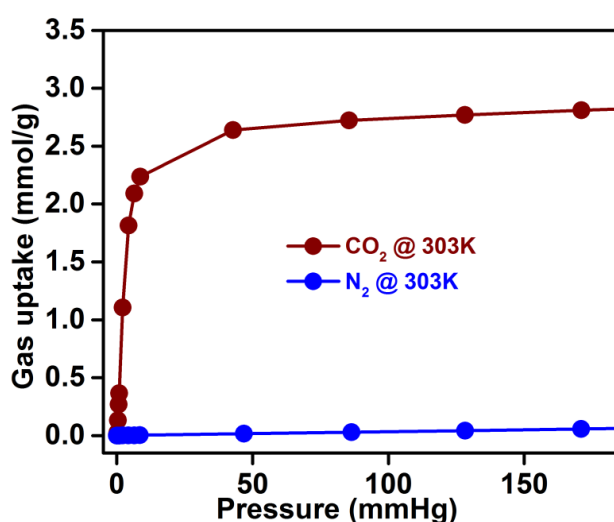


Figure 4.6 An initial slope comparison of the CO₂ and N₂ uptakes in **2** showing the high apparent selectivity for CO₂.

Now to provide a plausible explanation for the origin of gate opening in **2**, possible molecular motion associated with both Atz and oxalate units needed to be considered. Given the rigid μ -3 linking mode of the Atz units and the typically strong Zn-N covalent bonds, it is unlikely that they would go through any significant rotation about the Zn-N bond, particularly under this low CO₂ pressures. On the other hand, an examination of the bond distances reveals that the Zn-O distances are not all symmetrical; in fact, there are shorter (2.0Å) and longer (2.2Å) distances in **2** (*Figure 4.7*). Such relatively longer Zn-O bonds are found also in **3** and **4** (*Appendix A4.23*),

but they are non-porous to CO₂ and no gating phenomena are observed for these phases. This is explained by the symmetrical positioning of the longer Zn-O bonds in **2**. The longer Zn-O bonds (2.2 Å) from Zn and oxalate are positioned diagonally about the oxalate C-C bond; this could facilitate a spindle like rotation or 'swivelling' of the oxalates (*Figure 4.7*). Whereas, in case of **1**, where even weaker Zn-O bond (2.4 Å) are present yet no gate opening is observed, which indirectly suggests that the symmetric arrangement of relatively weaker bonds (*Figure 4.7*) is crucial for the spindle like rotation of the oxalate units.

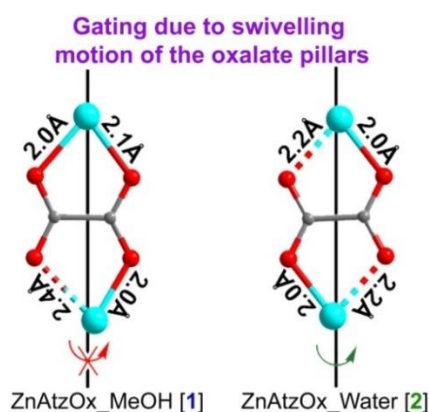


Figure 4.7 Comparison of the Zinc-oxalate units in **1** and **2/2***. Despite the presence of relatively longer Zn-O bond, **1**, does not show any gate opening (flexibility), while the symmetrically positioned weaker Zn-O bonds (2.2 Å) in **2** could be key to favoring the spindle like rotation motion of the oxalate units giving rise to gate opening. [Note: Other phases, **3** (ZnAtzOx_EtOH) and **4** (ZnAtzOx_ProH) do have Zn-O bonds longer than 2.2 Å, again they are not symmetrically (diagonally) positioned (see Appendix A4. 23)].

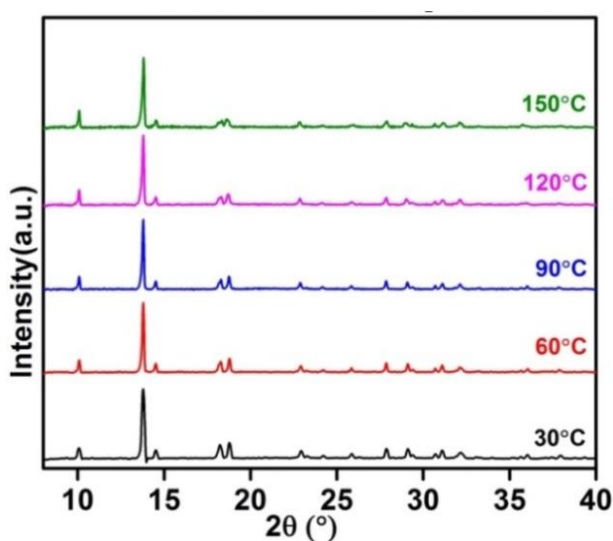


Figure 4.8 PXRD of a ZnAtzOx_Water phase [2] maintained under 900 mbar pressure of CO₂ in a capillary.

However, if they spin by larger angles (for example, >90) it would result in considerable structural rearrangement, which would be expected to show changes in the PXRD pattern. Lack of any major structural change during gate opening, except for the mere volume expansion was confirmed using a PXRD of **2** that was sealed under 900 mbar of CO_2 pressure in a capillary (*Figure 4.8 and Appendix A4.2.4*). Thus a subtle molecular motion could be opening up an additional site for CO_2 to fill up. Pre-gate opening CO_2 uptake (0-200mbar) in **2** is also higher than all the other phases, particularly the **1**.^{36,37} Now this is not due to any structural rearrangements under CO_2 , but is inherent to the as-synthesized framework's structure, which can be explained considering the pillar orientations.

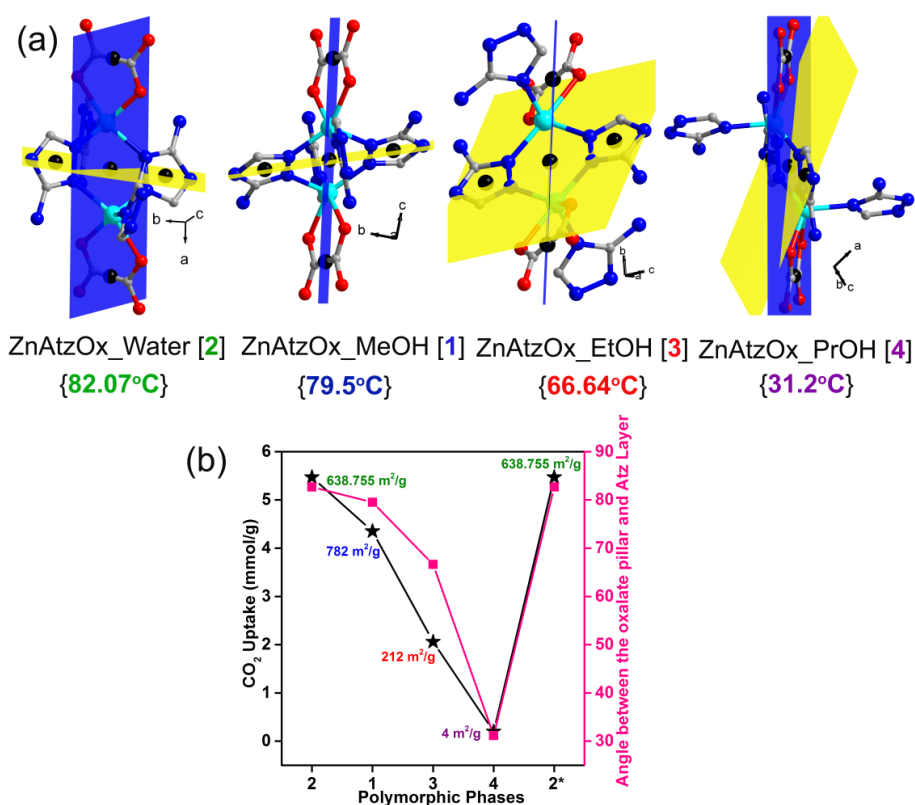


Figure 4.9 (a) Comparison of the angle between the oxalate pillar and the aminotriazolate layer: for the different polymorphic phases of ZnAtzOx framework. Colour code: yellow: ZnAtz layer and blue: oxalate pillar. (b) A plot showing the role of solvents in controlling the porosity of the ultra-microporous ZnAtzOx MOF phases.

The pillaring oxalates are aligned all along the *ab*-plane, thus controlling the accessibility from two orthogonal directions. Given this, their orientation with respect to the Atz layer can also have significant impact in determining the free space volumes (*Figure 4.9*). A comparison of the angles between the mean planes defined

by aminotriazolate layer and the oxalate pillars shows that the porous phases, **1** and **2**, have these values close to 80° , while for the non-porous **3** and **4** they are much lower than this (*Figure 4.9*).

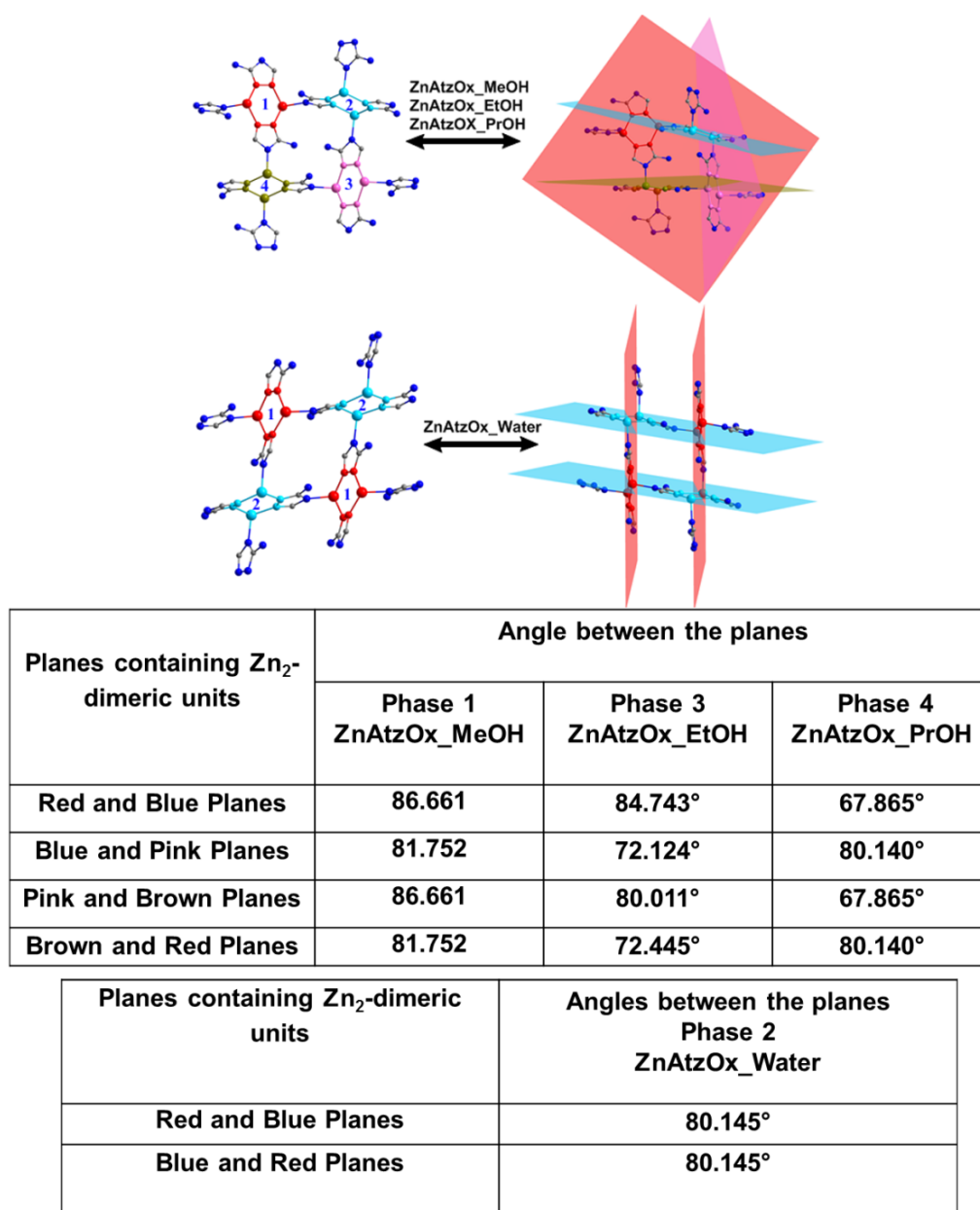


Figure 4.10 Planes containing Zn₂Atz₂-dimeric units of the ZnAtzOx Phases. Right: Figure represents the planes containing these dimers and the graphical representation of the angle between them. Table list the angles between the dimers containing planes for the different phases. Note, each different dimer and the plane have been colour coded.

Further, if virtual planes are drawn passing through the adjacent Zn₂Atz₂ dimers, it can be seen that in case of **1**, **3**, and **4** these planes are converging where as in case of **2** these planes are parallel giving rise to a perfect cube shaped

opening. This perfect positioning of the adjacent Zn_2Atz_2 dimers also contributes to the maximum openness in case of **2** as compared to the other phases (*Figure 4.10*).

Some strong solvent dependent behaviour was observed in for the framework structure of the ZnAtzOx polymorphs. There are two key roles of the solvents: solvents as '*structure directing agent (SDA)*' or as '*template*'. Wherein, (i) solvents with high hydrogen bonding abilities would interact strongly with the polar walls of the framework directing the final structure of the framework and (ii) solvents which are bulkier are generally good as templates allowing the framework to grow around it. Now among the solvents employed in this work, water and methanol are the most polar and hydrogen bonding, while butanol is the bulkiest. It can be rationalized that only the polar solvents acting as SDA or the bulky solvents acting as a template, assist the ZnAtz layer and the oxalate pillars to take a more symmetrical arrangement (angle close to 90°) giving rise to a near-cubic pores with maximum accessibility. At the same time, the inherent molecular-sieving assisted selectivity is not compromised. Thus, an appropriate choice of solvent can aid in rational synthesis of ultra-microporous solids for gas storage and separation.

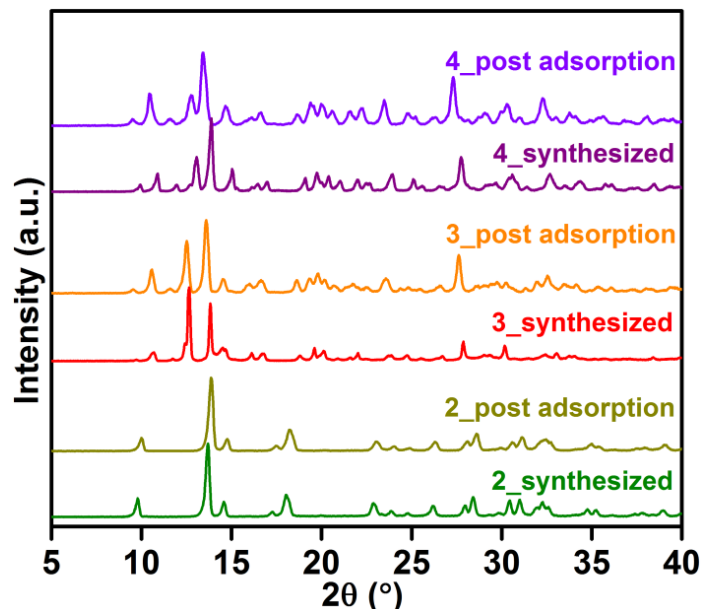


Figure 4.11 Post adsorption PXRD comparisons for the polymorphic phases of ZnAtzOx after 16-adsorption-desorption cycles.

From the performance point of view, the increase in CO_2 uptake due to gate opening from 3.2 mmol/g (700 mbar) to 4.7 mmol/g (1.1 bar) at 293 K, in fact translates to a 65% increase (0.7 to 2 mmol/g) in working capacity for a 1-0.15

vacuum swing at 293 K, considering the pure component isotherms. This truly represents the exceptional tunability of the capacity and selectivity seen in ultra-microporous materials. The exceptional stability of **2** is reflected in the complete maintaining of crystallinity even after 16 adsorption-desorption cycles (room temperature-150°C heating-cooling) (Figure 4.11) Phase **2** also possesses high hydrolytic stability towards both steam and boiling water, which is evident from the comparison of the PXRD patterns and the CO₂ uptake for the steam treated and the water boiled samples with that of the as made sample (Figure 4.12, Appendix A4.25 to Appendix A4.27).

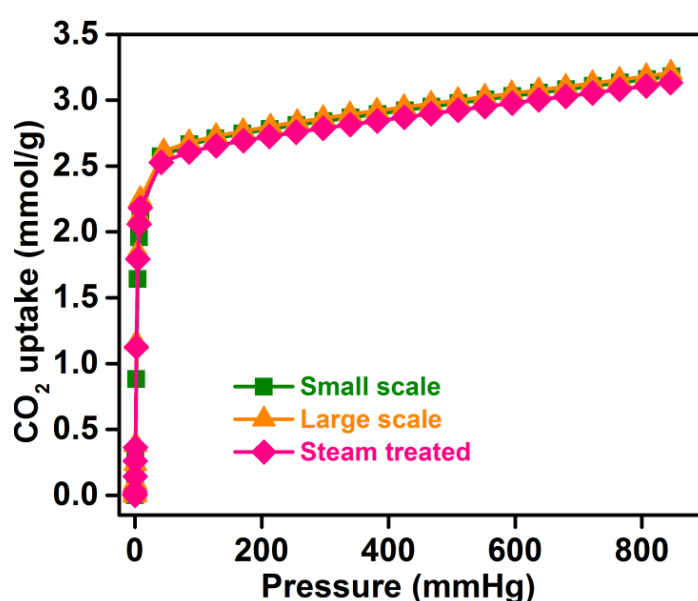


Figure 4.12 CO₂ adsorption comparisons for **2** under various conditions at 303 K.

4.4 Conclusion

In conclusion, the present study demonstrates the synthesis, characterization and adsorption characteristics of a family of ZnAtzOx polymorphs obtained by systematic solvent variation. The compound **2*1/2** obtained by employing butanol-water or only water as the solvent system, was found to be most porous among all. Effectively, it shows a 42% enhancement of CO₂ capacity compared to the most porous rigid ultra-microporous MOF reported in the literature. This enhancement happens via a gate opening phenomenon, which is unprecedented for the rigid ZnAtzOx frameworks. A systematic crystallographic investigation has been carried out from which the gate opening has been attributed to the swivelling motion of the oxalate pillars favoured by the presence symmetrically positioned weak Zn-O bonds from the Zn-Oxalate

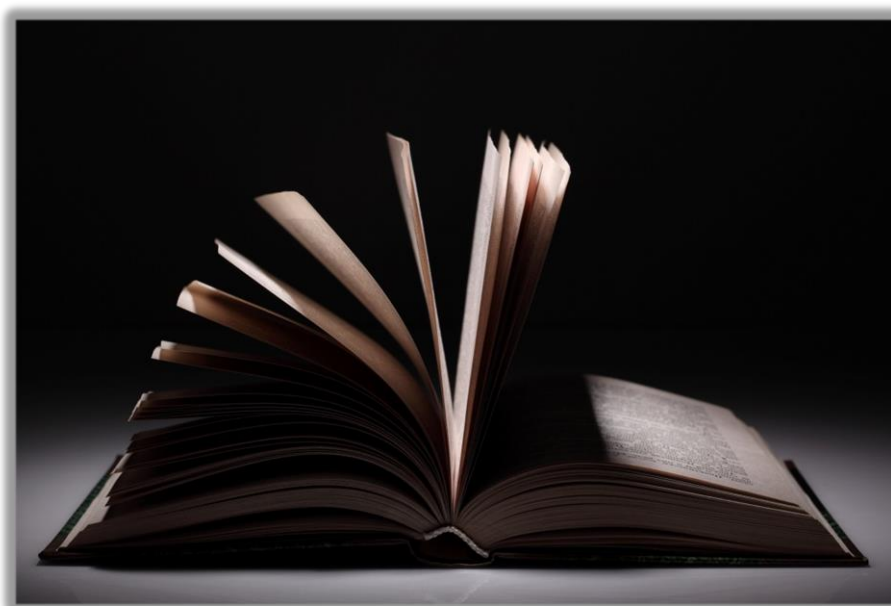
units. A dual site model has been proposed to explain the opening up of a CO₂ site via this gate opening and thus the openness of the ZnAtzOx 3D framework has been tuned by choosing solvents with right polarity or bulkiness. Noticeably, the CO₂ uptake registered by this compound, to the best of our knowledge, is the highest among all triazolato-oxalate frameworks.

4.5 References

1. Zhou, H.-C.; Long, J. R.; Yaghi, O. M. *Chem. Rev.* **2012**, *112*, 673.
2. Zhang, Z.; Yao, Z.-Z.; Xiang, S.; Chen, B. *Energy Environ. Sci.* **2014**, *7*, 2868.
3. Cui, Y.; Yue, Y.; Qian, G.; Chen, B. *Chem. Rev.* **2012**, *112*, 1126.
4. Li, J.-R.; Sculley, J.; Zhou, H.-C. *Chem. Rev.* **2012**, *112*, 869.
5. Yoon, M.; Srirambalaji, R.; Kim, K.; *Chem. Rev.* **2012**, *112*, 1196.
6. Zhu, Q.-L.; Xu, Q. *Chem. Soc. Rev.* **2014**, *43*, 5468.
7. Perry, J.; Perman, J. A.; Zaworotko, M. J. *Chem. Soc. Rev.* **2009**, *38*, 1400.
8. Ma, L. Q.; Abney, C.; Lin, W. B. *Chem. Soc. Rev.* **2009**, *38*, 1248.
9. Li, J.-R.; Kuppler, R. J.; Zhou, H.-C. *Chem. Soc. Rev.* **2009**, *38*, 1477.
10. Lin, R.-B.; Chen, D.; Lin, Y.-Y.; Zhang, J.-P.; Chen, X.-M. *Inorg. Chem.* **2012**, *51*, 9950.
11. Kitagawa, S.; Kitaura, R.; Noro, S.-i. *Angew. Chem. Int. Ed.* **2004**, *43*, 2334.
12. Kitaura, R.; Seki, K.; Akiyama, G.; Kitagawa, S. *Angew. Chem. Int. Ed.* **2003**, *42*, 428.
13. Schneemann, A.; Bon, V.; Schwedler, I.; Senkovska, I.; Kaskel, S.; Fischer, R. A. *Chem. Soc. Rev.* **2014**, *43*, 6062.
14. Li, L.; Wang, Y.; Yang, J.; Wang, X.; Li, J. *J. Mater. Chem. A* **2015**, *3*, 22574.
15. Horike, S.; Shimomura, S.; Kitagawa, S. *Nat. Chem.* **2009**, *1*, 695.
16. Thomas, A. *Angew. Chem. Int. Ed.* **2010**, *49*, 8328.
17. Serre, C.; Millange, F.; Thouvenot, C.; Nogues, M.; Marsolier, G.; Louer, D.; Ferey, G. *J. Am. Chem. Soc.* **2002**, *124*, 13519.
18. Tan, N. Y.; Ruggiero, M. T.; Orellana-Tavra, C.; Tian, T.; Bond, A. D.; Korter, T. M.; Fairen-Jimenez, D.; Axel Zeitler, J. *Chem Commun.* **2015**, *51*, 16037.
19. Yang, W.; Davies, A. J.; Lin, X.; Suyetin, M.; Matsuda, R.; Blake, A. J.; Wilson, C.; Lewis, W.; Parker, J. E.; Tang, C. C.; George, M. W.; Hubberstey, P.; Kitagawa, S.; Sakamoto, H.; Bichoutskaia, E.; Champness, N. R.; Yang, S.; Schröder, M. *Chem. Sci.* **2012**, *3*, 2993.
20. Alhamami, M.; Doan H.; Cheng, C.-H. *Materials* **2014**, *7*, 3198.
21. Zheng, B.; Pan, Y.; Lai, Z.; Huang, K.-W. *Langmuir* **2013**, *29*, 8865.
22. Fairen-Jimenez, D.; Moggach, S. A.; Wharmby, M. T.; Wright, P. A.; Parsons, S.; Duren, T. *J. Am. Chem. Soc.* **2011**, *133*, 8900.
23. Banerjee, A.; Chakraborty, D.; Vaidhyanathan, R. *Eur. J. Inorg. Chem.* **2017**, 2464 (EJIC Just Accepted; DOI: 10.1002/ejic.201700107).
24. Farha, O. K.; Hupp, J. T. *Acc. Chem. Res.* **2010**, *43*, 1166.
25. Burrows, A. D.; Cassar, K.; Friend, R. M. W.; Mahon, M. F.; Rigby S. P.; Warren, J. E. *CrystEngComm* **2005**, *7*, 548.
26. Yangand, X.; Clark, A. E. *Inorg. Chem.* **2014**, *53*, 8930.
27. Lan, Y.-Q.; Jiang, H.-L.; Li, S.-L.; Xu, Q. *Inorg. Chem.* **2012**, *51*, 7484.
28. Dey, C.; Kundu, T.; Biswal, B. P.; Mallick, A.; Banerjee, R. *Acta Cryst.* **2014**, *B70*, 3.
29. Fan, J.; Shu, M.-H.; Okamura, T.; Li, Y.-Z.; Sun, W.-Y.; Tang, W.-X.; Ueyama, N. *New J. Chem.* **2003**, *27*, 1307.

30. Yu, J. H., and Xu, R. R. *Acc. Chem. Res.* **2010**, *43*, 1195.
31. Senkovska, I.; Kaskel, S. *Eur. J. Inorg. Chem.* **2006**, 4564 (DOI: 10.1002/ejic.200600635).
32. Hao, X.-R.; Wang, X.-L.; Shao, K.-Z.; Yang, G.-S.; Su, Z.-M.; Yuan, G. *CrystEngComm* **2012**, *14*, 5596.
33. Peng, L.; Zhang, J.; Xue, Z.; Han, B.; Sang, X.; Liu, C.; Yang, G. *Nat. Commun.* **2014**, *5*, 4465.
34. Ding, R.; Huang, C.; Lu, J.; Wang, J.; Song, C.; Wu, J.; Hou, H.; Fan, Y. *Inorg. Chem.* **2015**, *54*, 1405.
35. Lin, Y.-Y.; Zhang, Y.-B.; Zhang, J.-P.; Chen, X.-M. *Cryst. Growth Des.* **2008**, *8*, 3673.
36. Vaidhyanathan, R.; Iremonger, S. S.; Dawson, K. W.; Shimizu, G. K. H. *Chem. Commun.* **2009**, 5230.
37. Vaidhyanathan, R.; Iremonger, S. S.; Shimizu, G. K. H.; Boyd, P. G.; Alavi, S.; Woo, T. K. *Science* **2010**, *330*, 650.
38. Nugent, P.; Belmabkhout, Y.; Burd, S. D.; Cairns, A. J.; Luebke, R.; Forrest, K.; Pham, T.; Ma, S.; Space, B.; Wojtas, L.; Eddaoudi, M.; Zaworotko, M. J. *Nature* **2013**, *495*, 80.
39. Wu, H.; Reali, R. S.; Smith, D. A.; Trachtenberg, M. C.; Li, J. *Chem. Eur. J.* **2010**, *16*, 13951.
40. Xiang, S.; He, Y.; Zhang, Z.; Wu, H.; Zhou, W.; Krishna, R.; Chen, B. *Nat. Commun.* **2012**, *3*, 954.
41. Shekhah, O.; Belmabkhout, Y.; Chen, Z.; Guillerm, V.; Cairns, A.; Adil, K.; Eddaoudi, M. *Nat. Commun.* **2014**, *5*, 4228.
42. Burd, S. D.; Ma, S.; Perman, J. A.; Sikora, B. J.; Snurr, R. Q.; Thallapally, P. K.; Tian, J.; Wojtas, L.; Zaworotko, M. J. *J. Am. Chem. Soc.* **2012**, *134*, 3663.
43. Prasad, T. K.; Hong, D. H.; Suh, M. P. *Chem. Eur. J.* **2010**, *16*, 14043.
44. Nandi, S.; Collins, S.; Chakraborty, D.; Banerjee, D.; Thallapally, P. K.; Woo, T. K.; Vaidhyanathan, R. *J. Am. Chem. Soc.* **2017**, *139*, 1734.
45. Nandi, S.; Haldar, S.; Chakraborty, D.; Vaidhyanathan, R. *J. Mater. Chem. A* **2017**, *5*, 535.
46. Myers, A. L.; Prausnitz, J. M. *AIChE J.* **1965**, *11*, 121.
47. Kemmer, G.; Keller, S. *Nat. Protoc.* **2010**, *5*, 267.

Chapter 5



Stabilization of an unstable Zinc-aminotriazolate framework via in-situ Schiff bond formation: transformation from 1st generation to 2nd generation MOF

5.1 Introduction

Metal organic frameworks, an important class of porous materials, are used as one of the potential candidates for CO₂ sequestration.¹⁻⁵ Their periodic structures provide opportunity for tuning of the pore openings and make these materials more applicable for practical purposes.³⁻⁸ Retaining their permanent porosity upon activation of a framework is of utmost importance.^{4,9,10} Many porous MOFs with open metal sites are known to show instability towards moisture.¹¹⁻¹⁴ In some cases, frameworks may even collapse after guest removal and this limits their practical utility to a large extent.^{10,15} To increase the gas uptake capacity of the MOFs, pore windows should be increased, which is typically achieved by increasing the length of the linkers.⁶⁻⁸ But long linkers, owing to high void/framework ratio, generally tend to produce interpenetrated structures.¹⁶⁻¹⁸ Another approach is to use small chelating linkers with bulky templating solvents, which can also produce large pore frameworks.¹⁹⁻²³ Though such control over the strategic design of the pore size of the MOFs is possible, still it is hard to predict the stability of the MOFs to solvent removal. The framework frailty upon guest removal or upon undergoing desolvation is still a major concern for significant number of MOFs.^{10,15,24,25} The robustness of a MOF principally depends upon the binding modes of the linkers with the metal ions/clusters and the free space available in framework.²⁴⁻²⁶ The MOFs which show irreversible structural collapse and therefore no permanent porosity are the **1st generation MOFs**.²⁷ However, in the presence of the solvent molecules they may be stable.^{24,25,28} Solvent molecules acting as space fillers, provide sufficient interaction and strength keeping the framework intact.^{24,25,28} Hence, one can attribute the major reason of the framework collapse to the lack of sufficient strength in the solvent-free framework to support the generated void space. Further, the solvents can be subdivided under two major categories i.e. polar and non-polar.^{23,29-33} Former category shows strong interaction with the polar components of the framework, thereby acts as a structure directing agent.^{22,23,28,34} The structure directing role of solvents influence the formation of different framework topologies.^{22,23,28,34-36} Whereas, the ones belonging to the latter category act as templating agents.¹⁹ The bulky non-polar aromatic solvents, act as large template by allowing the framework to grow around it forming large pores.¹⁹ Typically, the activation of MOFs comprises of the exchange

of the high boiling solvents with low boiling solvent by prolonged soaking and then removal of it under vacuum and elevated temperatures.^{10,24,25} However, this results in liquid-to-gas phase transition and thus creating a lot of surface tension and capillary forces which can mediate partial or full collapse of the framework.¹⁰ Due to which in many of the framework, the experimentally observed pore accessibility is significantly lower than those predicted for the solvent free framework structure.^{10,24,25} Additionally, in case of removal of such large templating solvents from the framework generates enormous void space initiating the framework collapse. Some of the other used techniques for activation comprises of CO₂ supercritical drying after solvent exchange, and freeze-drying.¹⁰ In the former one, the MOF is first exchanged with ethanol, followed by which it's exchanged with liquid CO₂ at high pressure over several hours. After this the temperature of the sample is increased above the supercritical temperature of CO₂ (31°C) and then the scCO₂ is slowly released by maintaining the temperature above the critical point.^{10,37-39} In freeze-drying, the MOF is first exchanged with benzene.^{10,40} Then for several times the sample is freeze-dried at 0°C and brought back to room temperature. During the final freeze cycle, the sample is kept under vacuum with the pressure and temperature maintained below the solvent's triple point.¹⁰ Followed by this, the sample is held under reduced pressure which facilitates the escape of benzene molecules from the pores of the framework.^{10,40} The major advantage of these techniques is due to the fact that they allow a supercritical-to-gas phase transformation for scCO₂ drying process and solid-to-gas phase transition for benzene-freeze drying process; thereby significantly reduce the chance of increased surface tension and the related capillary forces responsible for the collapse of the framework.¹⁰ However, apart from these benefits, the activation processes mentioned above are time consuming and many of the times are not practically feasible, which still makes the conventional solvent exchange and vacuum treatment to be one of the most accessible methods for MOFs activation.^{24,25}

Now, to address this concern and to make the large pore MOFs stable after solvent removal, some of the recent report shows the use of pore filling agents or struts, which could be incorporated into the structure.⁴¹⁻⁴⁵ These struts would form strong covalent bond within the framework and provide sufficient organic strength to make it stable upon solvent removal and at the same time leave enough pore

windows for gas adsorption.⁴¹⁻⁴⁵ They also segment (creating small compartments) the available large space into small domains and enhance the molecular sieving effect of the framework.⁴² By this way one can boost the robustness of the framework and thus a permanent porosity could be achieved.^{41,42,43,45}

The present work, demonstrates the synthesis and characterization of a benzene templated Zinc-aminotriazolate 3D framework [1]. The benzene molecules template the formation of a non-interpenetrated diamondoid framework consists of large pores, which irreversibly collapses upon solvent removal, thus becoming a true representative of a **1st generation MOF**. Here, a deliberate by-design approach has been adopted to stabilize the framework 1. The free amines protruding into the pores have been exploited in an attempt to introduce structure stabilizing strut via in-situ Schiff bond formation. Though it partitions the pores into smaller compartments, still leaves sufficient gas accessible permanent porosity in the framework. The Schiff-bond stabilized MOF representing the class of **2nd generation framework** showed a doubling of the CO₂ uptake as compared to the parent MOF. Here, a strategy for stabilizing fragile MOFs, via a pore modulation approach has been adopted to transform a **1st generation MOF to a 2nd generation MOF** with improved gas adsorbing capacity.

5.2 Experimental section

5.2.1 Materials: All chemicals were used from the commercially available sources without any further purification.

5.2.2 Physical measurements:

5.2.2.1 Powder X-ray diffraction: PXRD were carried out using a Rigaku Miniflex-600 instrument and processed using PDXL software.

5.2.2.2 Variable temperature powder X-ray diffraction: VT-PXRD patterns were measured on Bruker D8 Advanced X-Ray diffractometer at different temperatures using Cu-K α radiation ($\lambda = 1.5406 \text{ \AA}$) with a scan speed of $0.5^\circ \text{ min}^{-1}$ and a step size of 0.01° in 2 theta.

5.2.2.3 Thermo-gravimetric analysis: Thermo-gravimetric analysis was carried out on NETSZCH TGA-DSC system. The routine TGAs were done under N₂ gas flow (50 ml/min) and samples were heated from RT to 550°C at 2°C/min.

5.2.2.4 Single crystal X-ray diffraction: Single-crystal data was collected on a Bruker SMART APEX four-circle diffractometer equipped with a CMOS photon 100 detector (Bruker Systems Inc.) and with a Cu K α radiation (1.5418 Å). Single Crystal data was collected using Bruker Single crystal X-ray diffractometer, at wavelength of 1.5418 Å. The incident X-ray beam was focused and monochromated using Microfocus (I μ S). Crystal of **1** was mounted on nylon Cryo loops with Paratone-N oil. Data were collected at 100 K and integrated using Bruker SAINT Software and corrected for absorption using SADABS. Structures were solved by Intrinsic Phasing module of the direct methods and refined using the SHELXTL 2014 software suite. All non-hydrogen atoms were located from iterative examination of difference F-maps following which the structure was refined using least-squares method. Hydrogen atoms were placed geometrically and placed in a riding model.

5.2.2.5 Infra-red spectrophotometry: IR was recorded in attenuated total reflectance (ATR) mode on neat samples on a Bruker Alpha spectrophotometer.

5.2.2.6 UV-Vis spectrophotometry: UV-Vis spectra were recorded for neat samples on SHIMADZU UV-3600 Plus Spectrophotometer.

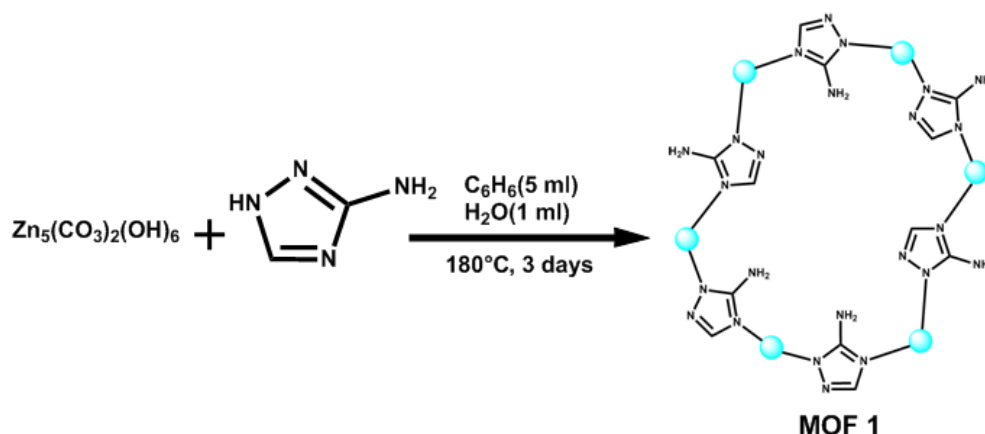
5.2.2.7 Adsorption: Adsorption studies were done on Quantachrome IQ adsorption analyser. All of the gases used were of 99.999% purity. For fitting the isotherms BET and Langmuir methods were employed. For pore size distribution calculation NLDFT was used.

5.2.2.8 Elemental analysis: Elemental analyses were performed on a Vario-EL cube elemental analyser.

5.2.3 Synthesis

5.2.3.1 Synthesis of [Zn(C₂N₄H₃)₂](C₆H₆) (1**):** In a typical synthesis for compound **1**, 0.1 g of Zn₅(CO₃)₂(OH)₆ and 0.3824 g of 3-aminotriazole (Hatz) were made to react under solvothermal conditions in a benzene (5 ml) + water (1 ml) solvent mixture at 180°C for 3 days (*Scheme 5.1*). Colourless single crystals suitable for single crystal

X-ray diffraction studies were obtained. During filtration, the bulk product was thoroughly washed with copious amount of methanol to remove any unreacted organics present and then dried in air, FT-IR (cm^{-1}): 3424, 3145, 2888, 2312, 1640, 1544, 1507, 1209, 1054, 984, 872, 760, 681, 647. Analytical data observed (%): C (38.42), H (3.65), N (36.6); calculated (%): C (38.79), H (3.91), N (36.19).

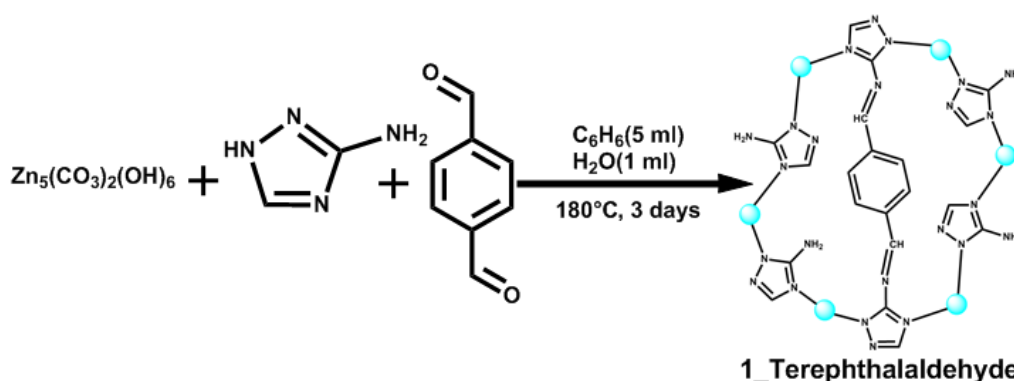


Scheme 5.1 Synthesis scheme for **1**, the cyan spheres represents the Zn^{2+} ions.

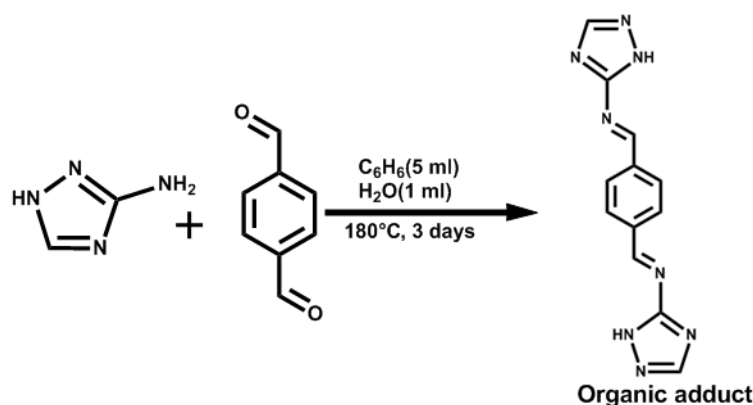
5.2.3.2 Synthesis of 1_Terephthalaldehyde MOF: In a typical synthesis for compound **1_Terephthalaldehyde**, 0.1 g of $\text{Zn}_5(\text{CO}_3)_2(\text{OH})_6$, 0.3824 g of 3-aminotriazole (Hatz) and 0.3050 g of terephthalaldehyde were made to react under solvothermal conditions in a benzene (5 ml) + water (1 ml) solvent mixture at 180°C for 3 days (*Scheme 5.2*). A bright yellow coloured microcrystalline product was obtained (please see for *Figure 5.9*). During filtration, the bulk product was thoroughly washed with copious amount of methanol and acetonitrile to remove any unreacted organics present and then dried in air. Followed by this, it was stirred in methanol-acetonitrile solvent mixture for a period of 12 hour, FT-IR (cm^{-1}): 3926, 3865, 3717, 3649, 3580, 3425, 3362, 3311, 3197, 3153, 2978, 2949, 2887, 2836, 2308, 2220, 2109, 1789, 1643, 1541, 1506, 1207, 1051, 993, 865, 762, 684, 647. Analytical data observed for **1_Terephthalaldehyde** (%): C (38.14); H (3.59) N (37.17); analytical data calculated for $[\text{Zn}(\text{C}_2\text{N}_4\text{H}_3)(\text{C}_2\text{N}_4\text{H})(\text{C}_8\text{H}_6)_{0.5}(\text{CH}_3\text{CN})_{1.5}(\text{CH}_3\text{OH})_{0.5}]^*$ (%): C (38.56); H (3.80) N (37.15). [*The formula has been derived from the CHN analysis]

5.2.3.3 Synthesis of organic adduct: In a typical synthesis, 0.3824 g of 3-aminotriazole (Hatz) was made to react with 0.3050 g of terephthalaldehyde under solvothermal conditions with benzene (5 ml) + water (1 ml) solvent mixture at 180°C

for 3 days (Scheme 5.3). A yellow coloured product was obtained, which has been thoroughly washed with copious amount of methanol to remove any unreacted organics and then dried in air. Followed by this, it was stirred in methanol-acetonitrile solvent mixture for a period of 12 hour and was filtered and dried prior to characterization and other studies. FT-IR (cm^{-1}): 3926, 3866, 3724, 3587, 3530, 3520, 3413, 3362, 3295, 3141, 2973, 2877, 2836, 2662, 2435, 2387, 2305, 2096, 1999, 1924, 1773, 1691, 1635, 1610, 1530, 1391, 1280, 1245, 1201, 1055, 986, 847, 773, 706. Analytical data observed (%): C (54.09); H (3.31) N (42.53), calculated (%): C (54.13%); H (3.79); N (42.08).



Scheme 5.2 Synthesis scheme for **1_Terephthalaldehyde**, the cyan spheres represents the Zn^{2+} ions.



Scheme 5.3 Synthesis scheme for organic adduct.

5.3 Results and discussions

5.3.1 Synthesis

Compound **1** was synthesized solvothermally by reacting $\text{Zn}_5(\text{CO}_3)_2(\text{OH})_6$ and 3-aminotriazole (Hatz), in a molar ratio of 1:5, in a mixture of benzene-water at 180°C

for 3 days (*Scheme 5.1*). The organic diimine struts were introduced into the amine-MOF via an in-situ solvothermal reaction under similar solvothermal conditions with an addition of 2.5 mmol of terephthalaldehyde. The obtained diimine stabilized product was homogeneous yellow colored microcrystalline powder (*Scheme 5.2*). In addition to this, a metal-free organic Schiff adduct was also synthesized under the similar solvothermal reaction conditions by retaining the same 3-aminotriazole to aldehyde ratio (2:1).

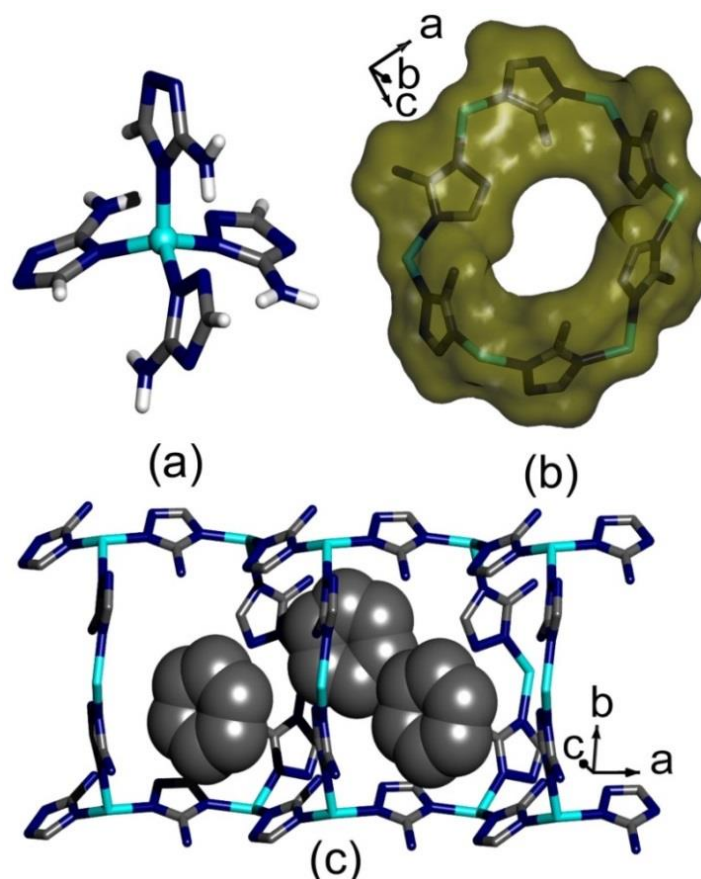


Figure 5.1 (a) Tetrahedral coordination geometry of Zn^{2+} , (b) Connolly surface representation for one pore showing the effective solvent accessible void volume present in the framework, and (c) Presence of the benzene solvent molecule in the framework channel along the a-axis; colour code: Zn: cyan, N: blue, C: grey (hydrogens have been removed for clarity).

5.3.2 Crystal structure

Compound **1** crystallizes in orthorhombic crystal system with $P2_12_12_1$ chiral space group (*Appendix A5.1*). Asymmetric unit of **1** consists of one Zn^{2+} ion and two μ -2 bridging aminotriazolate (Atz) units and one benzene solvent molecule (*Appendix A5.2*). All the atoms of the asymmetric unit have fully occupancy. The co-

ordination environment around Zn^{2+} is tetrahedral (*Figure 5.1*). The framework has pores along all three a-, b- and c-axis and also along [111] direction (*Figure 5.1 and Appendix A5.3-A5.5*). Benzene solvent molecules are packed in an array along porous channel running through the a-axis (*Figure 5.1c*).

The metal centre here acts as a 4-connected node, when the Atz ligands are reduced to linear linkers (*Figure 5.2a*). This 4-connected node forms an adamantane type of secondary building unit, which propagates to give a Diamondoid (*Dia*) network. This has been validated by a topological analysis by TOPOS software which revealed that it forms a uni-nodal 4-c net with point symbol and Vertex symbol as 6^6 and $6_2.6_2.6_2.6_2.6_2.6_2$ respectively (*Figure 5.2*).

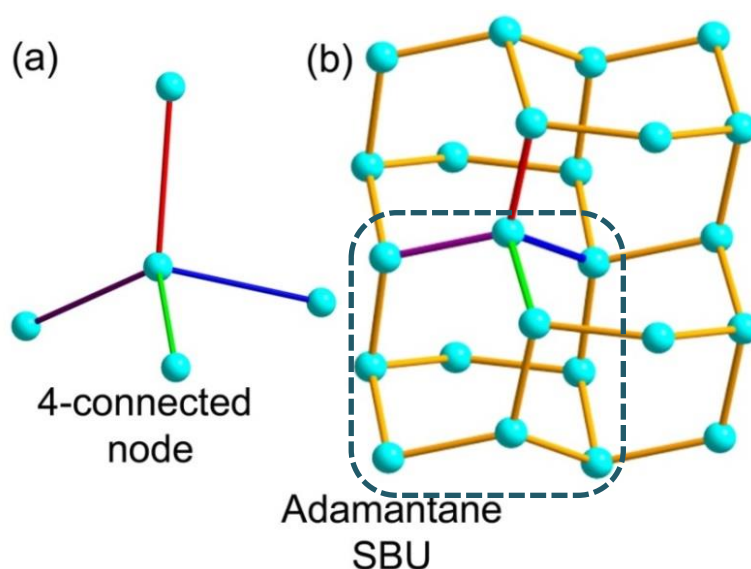


Figure 5.2 (a) 4-connected node, and (b) 6-membered ring having Diamondoid (*Dia*) topology (Dotted lines show the adamantane secondary building unit (SBU), which propagates to form *Dia* topology).

5.3.3 Bulk characterizations

In continuation to the previous chapter, to understand the effect of hydrophobic aromatic solvents, $\text{Zn}_5(\text{CO}_3)_2(\text{OH})_6$, oxalic acid and 3-aminotriazole were made to react at 180°C for 3 days using a benzene-water solvent mixture. The obtained phase was **1**, where it was observed, that oxalic acid does not participate in the framework formation. **1** built from only aminotriazolate ligand, makes the overall framework more basic in character. Another interesting feature observed here was the open diamondoid network with no interpenetration (*Figure 5.2*). In general, MOFs

with diamondoid topology are known to form highly interpenetrated nets,⁴⁶⁻⁵¹ however non-interpenetrated diamondoid frameworks are also rarely known.^{52,53}

In the present framework along with the openness, the free primary amine groups protrude into the pores. From prior reports,^{53,54} it can be anticipated that these MOFs would show high CO₂ uptake capacities. This has been further affirmed by PLATON squeeze, which suggested a presence of 52% solvent accessible void volume in the framework of **1**.

Bulk phase purity of compound **1** was verified by the PXRD comparisons of the simulated and as-synthesized phases, which showed good match (*Figure 5.3a*). TGA analysis of compound **1**, showed a weight loss of 25% (calc. 25.3%) up to 180°C (453 K), which corresponds to loss of lattice benzene solvent molecule (*Figure 5.3b*).

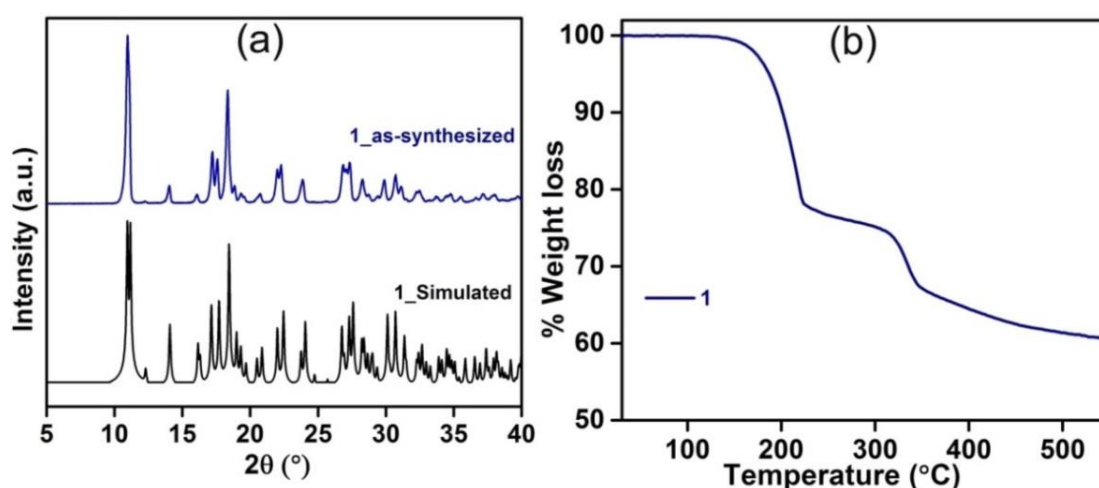


Figure 5.3 (a) Comparison of the simulated and the as-synthesized PXRD patterns of **1** and (b) TGA plot for **1**.

Use of toluene/xylene instead of benzene, also resulted in the formation of framework **1**, as evident from their respective PXRD and TGA profiles (*Appendix A5.6 and Appendix A5.7*). This suggested that the aromatic solvents here act as templating agent rather than as structure directing. They fill up the pores and allow the framework to emerge around it. Intrigued by all these results, gas adsorption studies were carried out on Compound **1**. For this, **1** was activated by soaking in CH₃CN for 3 days with regular replenishments after every 12 hours.

It was observed from the PXRD pattern of the solvent exchanged **1**_CH₃CN sample that no substantial loss in the crystallinity occurred after undergoing this treatment (*Figure 5.4a*). TGA for **1**_CH₃CN indicated that the solvent loss taking place at a much lower temperature as compared to the as-synthesized phase, confirming the successful solvent exchange of **1** (*Figure 5.4b*). Followed by this **1**_CH₃CN sample was evacuated at 60°C (333 K) and at 10⁻³ torr vacuum for 6 hours. From the PXRD of this activated sample it was observed that the solvent removal from framework caused a significant loss in the crystallinity of the sample, or it can be said that the loss of solvent causes partial amorphisation of the sample (*Appendix A5.8*).

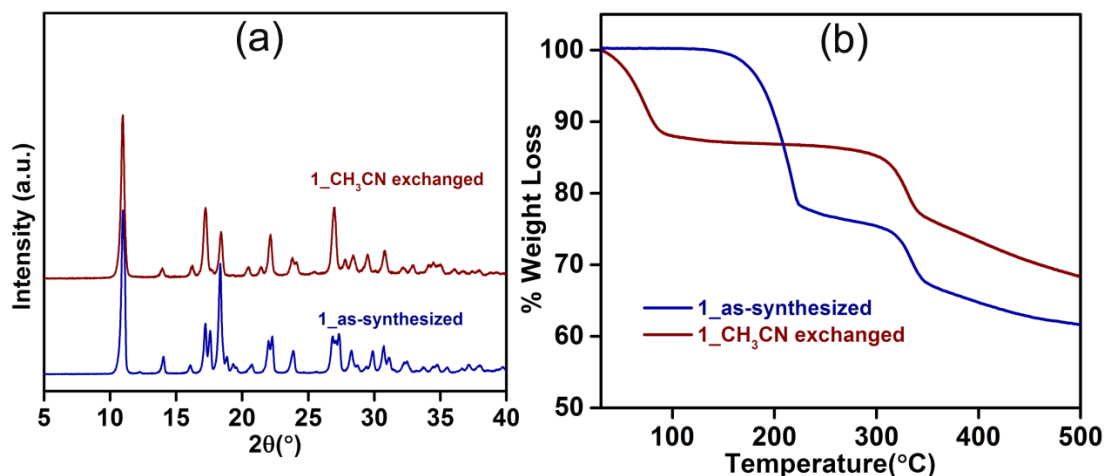


Figure 5.4 (a) PXRD comparisons between the as-synthesized and the CH₃CN exchanged samples of **1**, and (b) TGA comparisons for the as-synthesized and the CH₃CN exchanged sample of **1**.

To prevent the abrupt loss of the solvent from the framework, modifications in the activation procedure were tried and softer methods were used. Typically, the as-synthesized sample of **1** was exchanged with CH₃OH (*Appendix A5.9 and Appendix A5.10*) and then evacuated at room temperature or heated at 100°C (373 K) under N₂. But mere leaving of the solvent from the framework by ambient evaporation over longer time caused a marked reduction in the crystallinity of the sample, as evidenced from their powder pattern (*Figure 5.5*).

It was realized that the reason for this collapse is the strong interaction of the solvent with the framework. This partially collapsed framework was tested for solvent dependent structural transformation by soaking it into benzene for 2-3 days, but the

parent crystalline framework could not be regenerated even after prolonged soaking. This suggested that the framework **1**, behaved as a **1st generation MOF**. Although it was observed that the as-synthesized MOF (having benzene molecules in framework pores) has a very good shelf-life for about 6 months, which is evident from its PXRD pattern, suggesting the strong templating role of the benzene solvent molecules (*Appendix 5.11*).

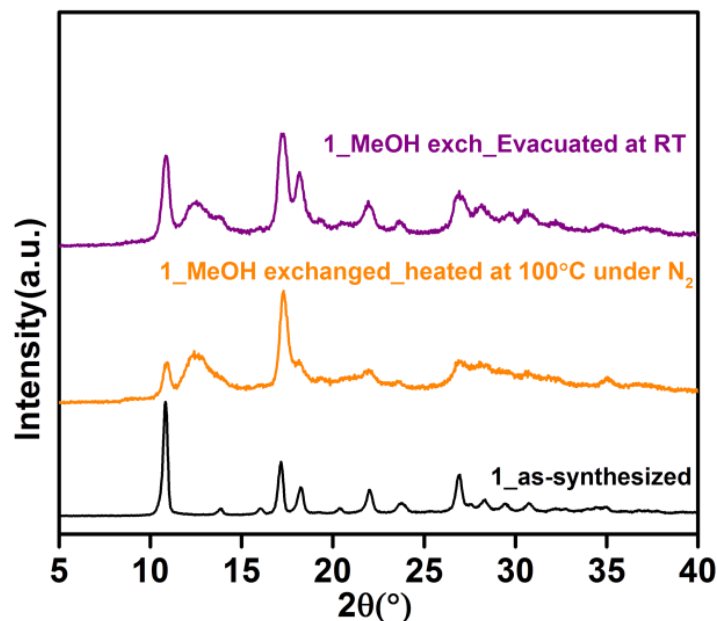


Figure 5.5 PXRD comparisons of the activated samples obtained after softer activation protocols, it could be seen that the mere leaving of the solvent from the framework initiates a significant loss in the crystallinity of the sample.

Now one of the possible ways to make the framework stable to solvent loss would be to incorporate more covalent links into the framework. In some of the recent literature, it has been demonstrated that introduction of size matching ligands/struts into the framework pores as braces, makes the framework stable.⁴¹⁻⁴⁵ Wang et. al.,⁴² have stabilized an unstable Cobalt-dicarboxylate based MOF by bridging the two trigonal prismatic clusters of $\text{Co}_3(\mu_3\text{-O})(\text{COO})_6$ with 4,4'-bipyridine ligand (*Figure 5.6*). It has been showed that the framework obtained after incorporation of the stabilizing struts was stable after solvent removal, as compared to the parent structure, where it was apparent that the structure collapsed after solvent removal. This resulted into an unprecedented ~60% increase in the CO_2 uptake capacity at 195 K and 1 bar pressure for the stabilized framework as compared to its unstable parent structure.⁴²

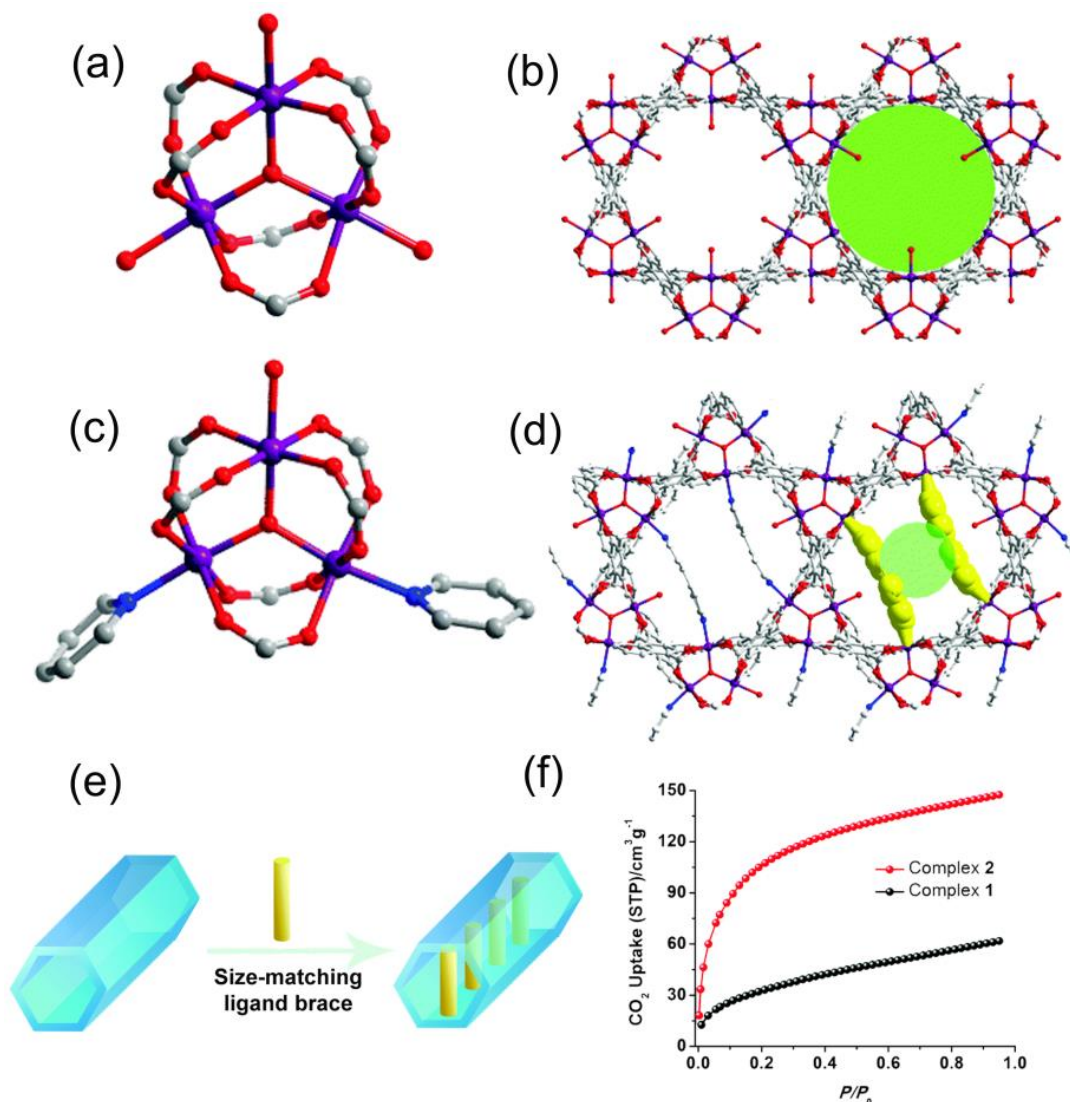


Figure 5.6 (a) The cobalt trigonal prismatic SBU of complex 1 and (b) the view of the packing framework of complex 1. (c) The cobalt trigonal prismatic SBU of complex 2 (the indicated pyridine units are from 4,4'-bpy molecules) and (d) the view of the packing framework of complex 2 (part of the inserted 4,4'-bpy molecules highlighted with yellow colour). (e) Schematic representation of the strategy to boost the robustness of MOFs via introduction of size-matching ligand braces into the open channels, and (f) CO₂ adsorption isotherms of complexes 1 and 2 at 195 K. (Adapted with permission from “Wang et al. *Chem. Commun.* **2016**, 52, 1971” © The Royal Society of Chemistry 2016.)

In a recent report by Gao et al.,⁴³ a fragile Cobalt based MOF has been stabilized by combining another ligand during synthesis procedure. Interestingly, the tripodal ligand “*tpt*” [tpt: 2,4,6-tri(4-pyridyl)-1,3,5-triazine] incorporated in this case has the same trigonal symmetry as that of the pore confinements of the parent MOF (Figure 5.7), and this N-donor tripodal ligand binds with the metal centres resulting in to improved stability and gas uptake.⁴³

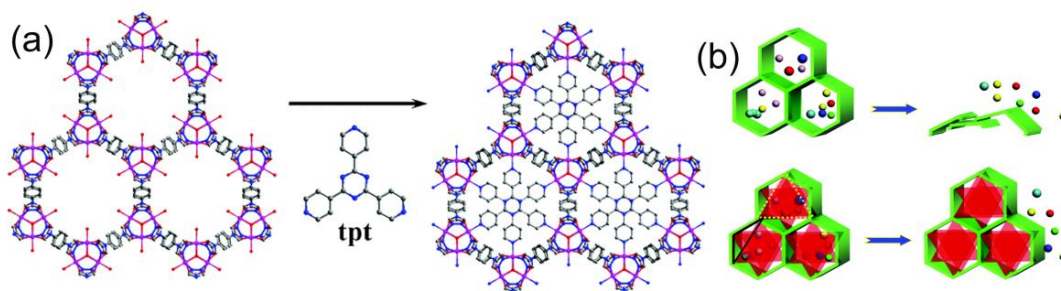


Figure 5.7 The structures of MOFs: (a) framework of Co-MOF1 and framework of the reformed Co-MOF1-tpt, and (b) Schematic representation of the loss of porosity of MOFs due to the deformation/collapse of framework (top) and the stabilization of MOFs (bottom). (Adapted with permission from “Gao et al. *Dalton Trans.* **2016**, *45*, 6830” © The Royal Society of Chemistry 2016.)

Similarly, Chen et al.,¹⁵ have stabilized a Co (II)- 4-(1H-tetrazol-5-yl)benzoate MOF by incorporation of size matching molecular building blocks. This resulted into partition of a hexagonal large porous channel into several numbers of smaller sections. This not only improved the stability of the MOF upon solvent removal but also accounted for an enormous increase in the CO₂ uptake capacity. The same group reported the pore modulation approach to stabilize the same prototype MIL-88 MOF by applying two different molecular braces,⁴⁵ i.e. [Co₂(ina)₃(H₂O)₂]⁺ (ina: isonictinate) and 2,4,6-tri(4-pyridyl)-1,3,5-triazine “tpt”. Noticeably, the MOF stabilised by “tpt” ligand showed comparatively more stability and increased uptake as compared to the framework stabilised by [Co₂(ina)₃(H₂O)₂]⁺ molecular building unit.⁴⁵ Apart from this, in few other examples it has been observed that applying similar techniques, stability have been imparted to the rather unstable frameworks.⁴⁴ One important thing to be noted from all of these reports is that the framework stabilization struts are added in an in-situ manner at the start of the reaction rather than taking a post-synthetic approach.⁴¹⁻⁴⁵

Now, in the present case, it was realized that the free primary amines protruding in the pores of **1** are in fact oriented/ facing towards each other, and are almost at correct distances to incorporate diimine struts as pillars, via formation of Schiff bonds (*Figure 5.8*) between the free primary amines and terephthalaldehyde. Also, from the observation in the previous chapters, it was perceived that for this type of triazolate based frameworks, the triazolates could show slight flexibility during

the process of framework formation and hence could accommodate guest aldehyde-derived moieties, which are almost equal or slightly larger than the space available.

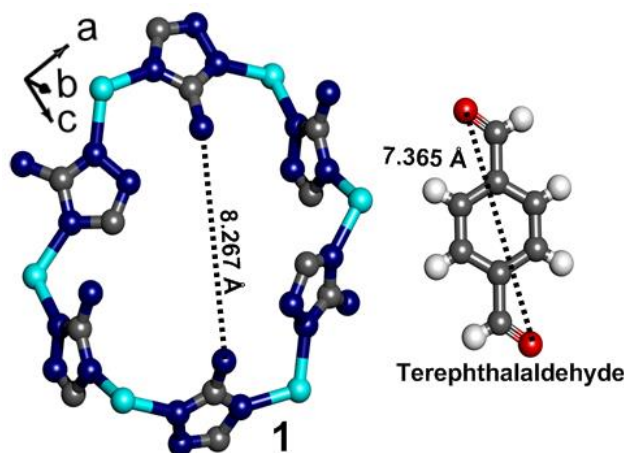


Figure 5.8 Distance between the protruding free primary amines shown in a pore of framework **1**, compared to the dimensions of the terephthalaldehyde; colour code: Zn: cyan, N: blue, C: grey, O: red and H: white.

Considering the rigidity of this aromatic dialdehyde and the strong covalent Schiff links it can form, a much more rigid framework can be envisaged, which will be stable upon solvent loss. With all these thoughts of framework stabilization via in-situ Schiff bonds formation, the Schiff-bond stabilized MOF (**1_Terephthalaldehyde**) was synthesized as mentioned in the above section (*Scheme 5.2*). The **1_Terephthalaldehyde** MOF obtained by in-situ loading under solvothermal conditions was microcrystalline and bright yellow in colour, which indicated the successful formation of the Schiff bonds within the framework (*Figure 5.9*). Repeated attempts were made to grow large single crystals of the Schiff-bond stabilized MOF suited for SCXRD, but our attempts were unsuccessful.

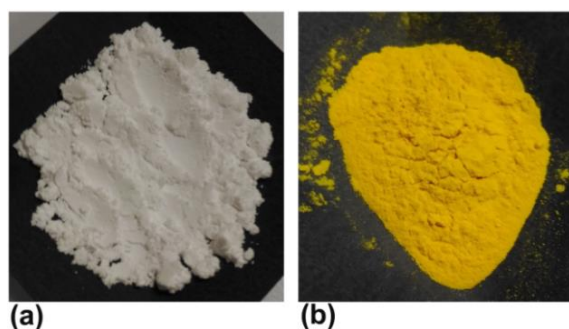


Figure 5.9 Pictures of the as-synthesized MOFs: (a) compound **1** and (b) **1_Terephthalaldehyde**.

The bulk phase purity and crystallinity of the Schiff-bond stabilized MOF could be witnessed from the PXRD comparison between the as-synthesized samples of **1**, and **1_Terephthalaldehyde** (Figure 5.10). The good match between the PXRD profiles suggests the formation of Schiff bonds within the framework **1** doesn't alter the overall structural integrity or the framework topology. In addition to this, a control experiment was also performed in which only the organic parts were made to react under the similar solvothermal conditions (Scheme 5.3). The organic adduct formed was also yellow in colour. However, it was observed from the PXRD, that the organic adduct was amorphous in nature and shows a big hump between the 2θ region of 15° - 30° (Figure 5.10).

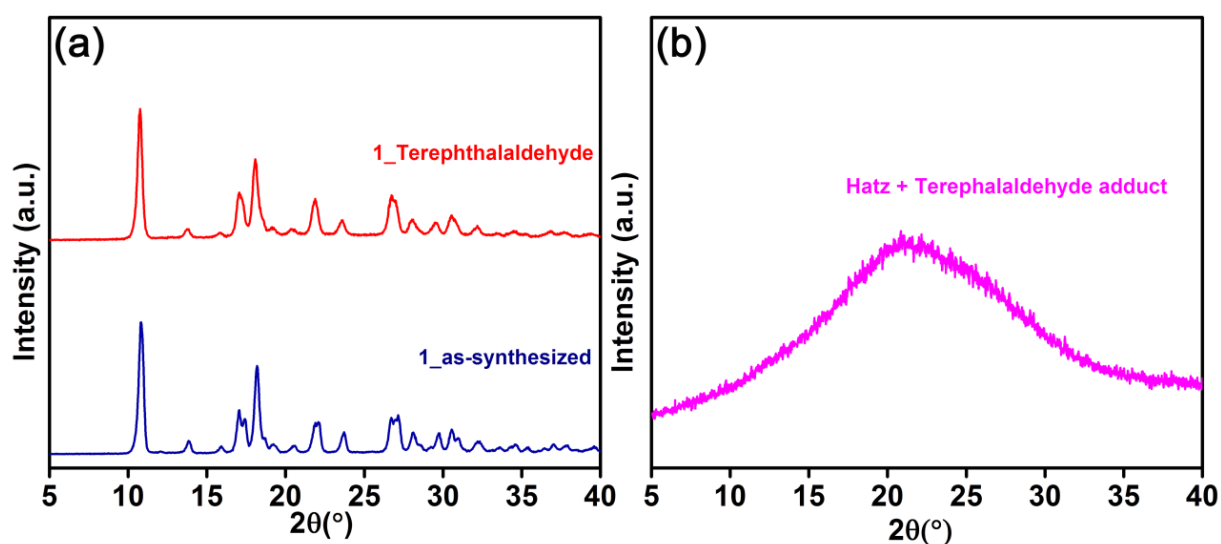


Figure 5.10 (a) PXRD comparison between the as-synthesized sample of **1** and **1_Terephthalaldehyde**, the good match between them confirms the phase purity of the Schiff bond stabilized MOF. (b) The PXRD pattern for the amorphous organic adduct. Non-appearance of any such amorphous hump in PXRD of the Schiff-bond stabilized MOF (**1_Terephthalaldehyde**) suggests the absence of any sort of impurity or competing phases.

Now, absence of any such hump in the PXRD of the Schiff-bond stabilized MOF points to the absence of any sort of impurity or competing phases. It should be noted that a mere mechanical mixture of MOF **1** with the organic adduct yields a powder with relatively mild yellow colour. To impart a strong yellow colour, a lot of impurity should be present and in such a case the hump in PXDR profile would have been prominent, which is not the case. Further, to affirm these observations IR and UV spectra were recorded for all these samples.

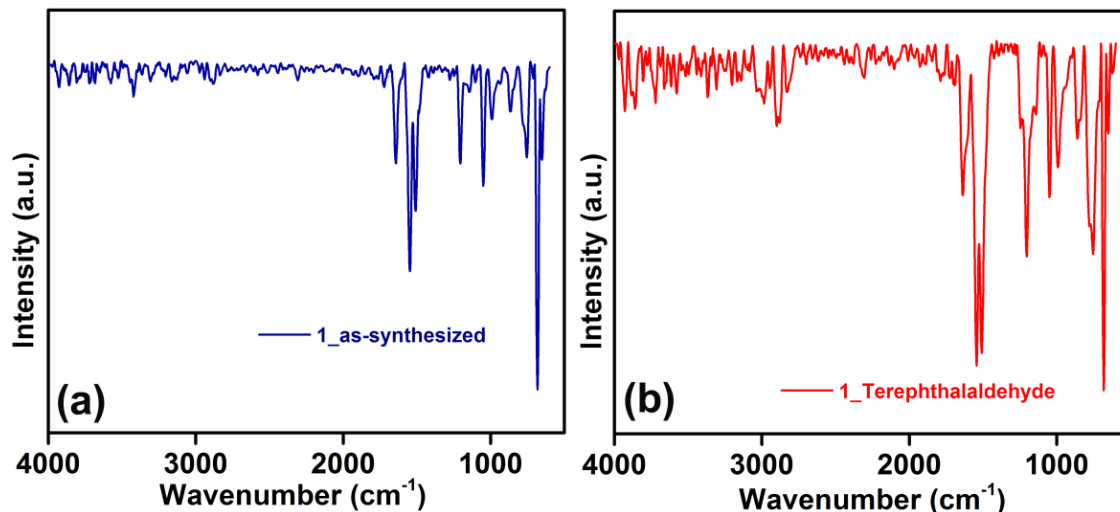


Figure 5.11 (a) IR spectra plots of (a) **1** and (b) **1_Terephthalaldehyde**.

The good match between the IR spectrums of **1** and **1_Terephthalaldehyde** suggested that the overall morphology of the framework is retained even after the insertion of the diimine struts (*Figure 5.11*).

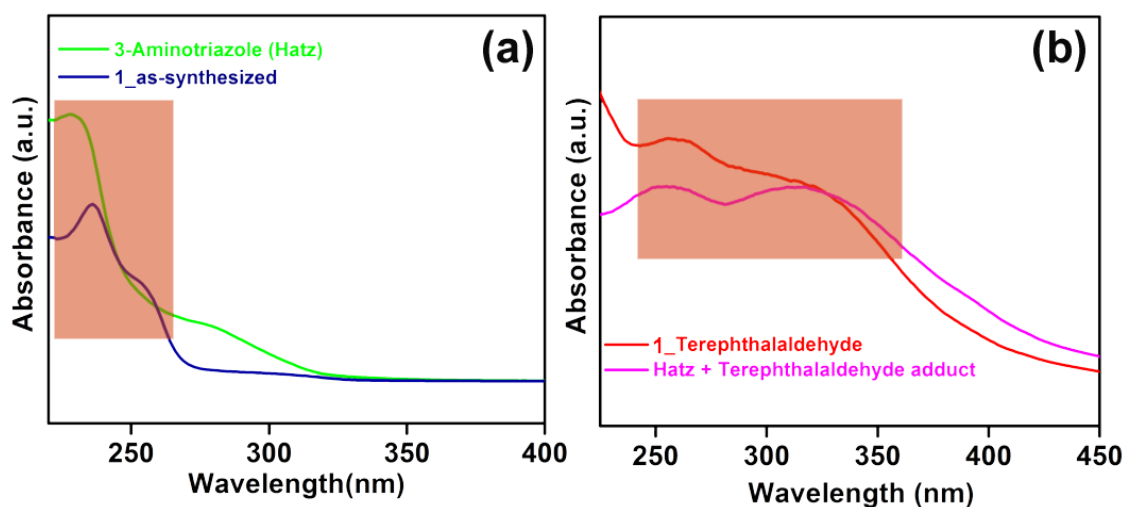


Figure 5.12 (a) UV spectra of **1** in comparison to neat 3-aminotriazole ligand and (b) UV spectra of **1_Terephthalaldehyde** in comparison to the organic adduct.

Also, UV-absorption bands for the as-synthesized samples of **1** and the Schiff-bond stabilized MOF coordinated fine with the UV-absorption bands of their respective ligands, affirming the successful formation of the Schiff-bond stabilized MOF (*Figure 5.12*).

TGA experiments were performed for the Schiff-bond stabilized **1_Terephthalaldehyde** MOF. An initial weight loss ~15% occurs till 80°C (353 K),

followed by an small plateau and weight loss of ~2% till 200°C (473 K), before the final structural degradation which initiates above 280°C (553 K) (*Figure 5.13*). Now, this initial low temperature weight loss of ~15% suggests the presence of low-boiling solvents in the frameworks pores, which was not observed for the benzene templated MOF 1. This could be attributed to the prolonged stirring of the Schiff-bond stabilized MOF in methanol: acetonitrile mixture as part of their filtration procedure (please refer to the synthesis section). Structural stability of **1_Terephthalaldehyde** MOF has been further verified by performing VT-PXRD experiments, which was in agreement with the results obtained by TGA and suggests complete retention of the framework integrity up to 280°C (553 K) (*Appendix A5.13*).

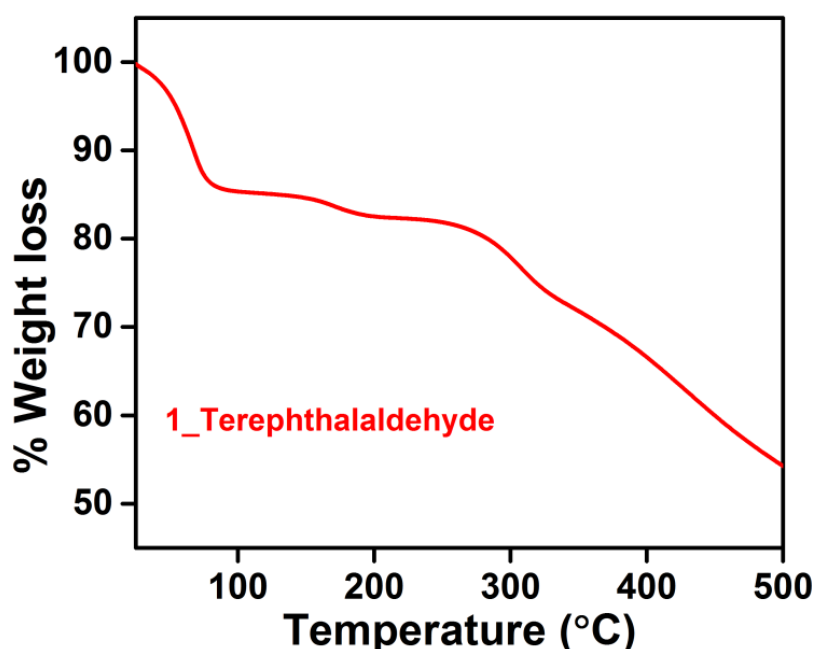


Figure 5.13 TGA plot for the Schiff-bond stabilized MOF **1_Terephthalaldehyde**.

Followed by these initial characterizations, confirming the successful construction of the Schiff-bond stabilized MOF and its improved stability, the CO₂ adsorption analysis has been performed.

5.3.4 Gas adsorption studies

For gas adsorption experiment, since the Schiff-bond stabilized MOF (**1_Terephthalaldehyde**) was already treated with copious amount CH₃CN/CH₃OH, no further solvent exchange was carried out. The sample was activated at 60°C (333

K), 10^{-3} torr vacuum on the degas unit of Quantachrome adsorption analyser and was subjected to the pure CO_2 stream at 273 K.

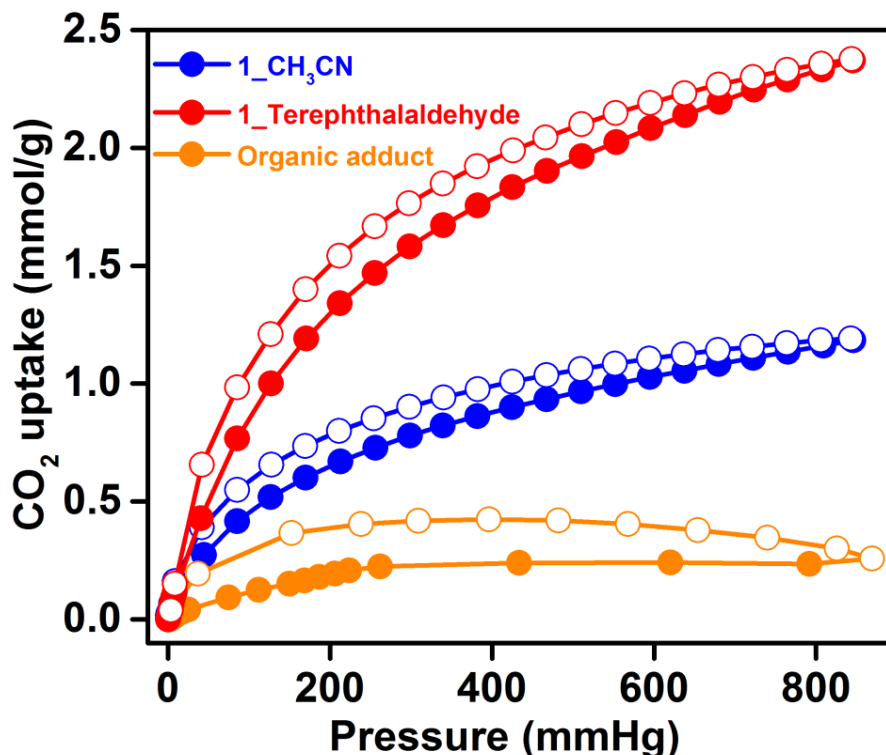


Figure 5.14 CO_2 adsorption graphs for Schiff-bond stabilized MOF and CH_3CN exchanged MOF **1**, it can be seen that for **1_Terephthalaldehyde** MOF the CO_2 uptake is doubled as compared to **1**. Please note that the filled symbols shows the adsorption branch whereas the open symbols shows the desorption branch at a particular temperature.

It was observed that **1_Terephthalaldehyde** had a CO_2 uptake of 2.36 mmol/g at 1.1 bar pressure (*Figure 5.14*). The CO_2 adsorption isotherms were recorded for **1_CH₃CN**, and organic adduct as well. Both the samples were evacuated at 60°C (333 K) and at 10^{-3} torr vacuum before exposing to pure CO_2 stream. The CO_2 uptake for **1_CH₃CN** was 1.18 mmol/g at 273 K (*Figure 5.14*), which was very less as anticipated from the solvent accessible void volume of 52%, calculated by PLATON-squeeze analysis for **1**. On the other hand the organic adduct proved to be almost non-porous to CO_2 under similar conditions. Importantly, by relating the amount of gas uptakes for the **1_CH₃CN** and the Schiff-bond stabilized MOF, one can see that **1_Terephthalaldehyde** showed a two times increase in the CO_2 uptake as compared to **1_CH₃CN**. Further, it can be said that the adsorption amounts for the Schiff-bond stabilized MOF is not due to the presence of any sort of

organic impurity, as the organic adduct is practically non-porous to CO₂ (Figure 5.14).

Surface area and pore size calculations were performed for both **1** and **1_Terephthalaldehyde**. **1** showed a BET surface area of 155 m²/g and Langmuir surface area of 170 m²/g (Appendix A5.14 and Appendix A5.15). However, the BET and Langmuir surface area for **1_Terephthalaldehyde** were estimated to be 350 m²/g and 365 m²/g, respectively which is almost two times that of **1** (Appendix A5.18 and Appendix A5.19). The DFT-pore size distribution on **1_Terephthalaldehyde** suggested that it has a half pore width of 2.5 Å which falls under the ultra-microporous regime (Appendix A5.20 and Appendix A5.21).

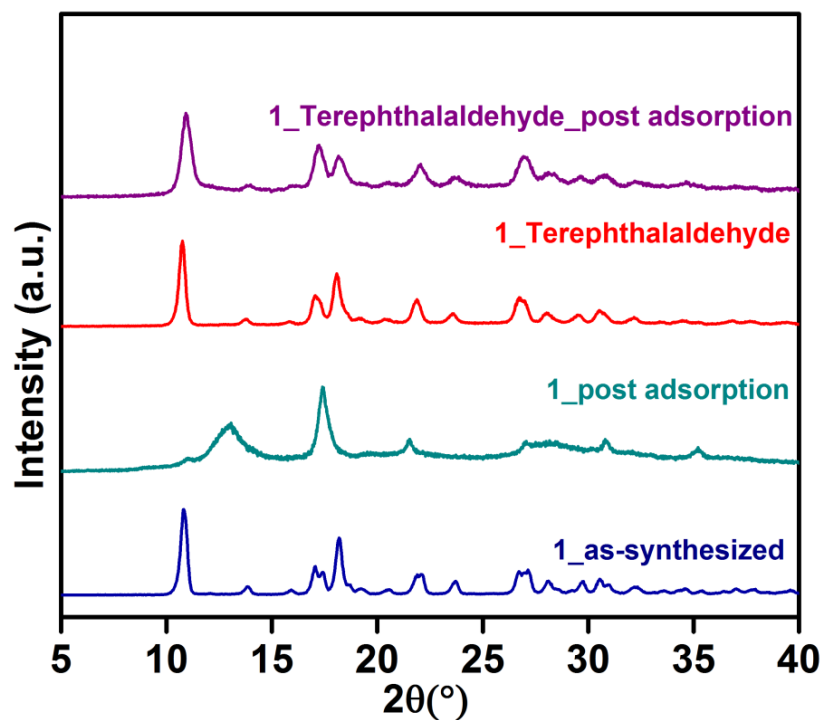


Figure 5.15 Post adsorption PXRD comparisons for **1**, and **1_Terephthalaldehyde** with their respective as-synthesized samples. The Post adsorption PXRD of the Schiff-bond stabilized MOF shows that the sample is stable to multiple adsorption-desorption cycles and thus signifies the framework stability incorporated via formation of Schiff bonds.

Finally, to show the permanent porosity incorporated into these Schiff-bond stabilized MOFs, the post adsorption PXRD pattern for each sample was recorded. It could be witnessed that for the Schiff-bond stabilized MOF, there is no significant loss in crystallinity after multiple adsorption-desorption cycles, and the post adsorption PXRD matches well with the as-synthesized PXRD pattern (Figure 5.15).

On the other hand, the post adsorption PXRD for the 1-CH₃CN sample showed a partial collapse of the framework upon undergoing the activation procedure, which explains its lower CO₂ uptake. Hence, the in-situ Schiff bond formation imparts stability to the framework and transforms a **1st generation MOF to a 2nd generation MOF**.

5.4 Conclusion

In summary, the present chapter demonstrates an effective and novel strategy to stabilize a rather unstable amine-functionalized MOF via in-situ Schiff bond formation. In this pore modulation approach, the relatively larger pores responsible for framework collapse have been stabilized by aromatic diimine strut. This created smaller compartments which still provide access to the CO₂ molecules. The stability of the framework to the activation and adsorption-desorption cycling is evident from the complete retention of crystallinity in the post-adsorption sample and the increased CO₂ uptake. The successful insertion of the diimine pillars has been further confirmed by various analytical techniques such as PXRD, TGA, IR, UV and gas adsorption. It is observed that the framework stabilization leads to an increase in the CO₂ uptake capacity of the Schiff-bond stabilized MOF by two times as compared to its unstable parent framework. This approach would be beneficial in stabilization of amine functionalized 1st generation MOFs.

5.5 References

1. Liu, J.; Thallapally, P. K.; Peter Mc Grail, B.; R. Brown, D.; Liu, J. *Chem. Soc. Rev.* **2012**, *41*, 2308.
2. Sumida, K.; L. Rogow, D.; A. Mason, J.; M. McDonald, T.; D. Bloch, E.; R. Herm, Z.; Bae, T.-H.; R. Long, J. *Chem. Rev.* **2012**, *112*, 724.
3. Caskey, S. R.; Wong-Foy, A. G.; Matzger, A. J. *J. Am. Chem. Soc.* **2008**, *130*, 10870.
4. Nandi, S.; Collins, S. P.; Chakraborty, D.; Banerjee, D.; Thallapally, P. K.; Woo, T. K.; Vaidhyanathan, R. *J. Am. Chem. Soc.* **2017**, *139*, 1734.
5. Nandi, S.; Luna, P. D.; Daff, T. D.; Rother, J.; Liu, M.; Buchanan, W.; Hawari, A. I.; Woo, T. K.; Vaidhyanathan, R. *Sci. Adv.* **2015**, *1*:e1500421.
6. Eddaoudi, M.; Kim, J.; Rosi, N.; Vodak, D.; Wachter, J.; O'Keeffe, M.; Yaghi O. M. *Science* **2002**, *295*, 469.
7. Yaghi, O. M.; O'Keeffe, M.; Ockwig, N. W.; Chae, H. K.; Eddaoudi, M.; Kim, J. *Nature* **2003**, *423*, 705.
8. O'Keeffe, M. *Chem. Soc. Rev.* **2009**, *38*, 1215.
9. Bosch, M.; Zhang, M.; Zhou, H.-C. *Advances in Chemistry* **2014**, [doi.org/10.1155/2014/182327].
10. Mondloch, J. E.; Karagiari, O.; Farha O. K.; Hupp, J. T. *CrystEngComm* **2013**, *15*, 9258.
11. Liu, J.; Benin, A. I.; Furtado, A. M. B.; Jakubczak, P.; Willis, R. R.; LeVan, M. D. *Langmuir* **2011**, *27*, 11451.
12. Schoenecker, P. M.; Carson, C. G.; Jasuja, H.; Flemming, C. J. J.; Walton, K. S. *Ind. Eng. Chem. Res.* **2012**, *51*, 6513.
13. Liu, J.; Wang, Y.; Benin, A. I.; Jakubczak, P.; Willis, R. R.; LeVan, M. D. *Langmuir* **2010**, *26*, 14301.
14. Bellarosa, L.; Castillo, J. M.; Vlugt, T.; Calero, S.; López, N. *Chem. Eur. J.* **2012**, *18*, 12260.
15. Chen, D.-M.; Tian, J.-Y.; Liu, C.-S.; Du, M. *Chem. Commun.* **2016**, *52*, 8413.
16. Ma, S.; Sun, D.; Ambrogio, M.; Fillinger, J. A.; Parkin, S.; Zhou, H.-C. *J. Am. Chem. Soc.* **2007**, *129*, 1858.
17. Reineke, T. M.; Eddaoudi, M.; Moler, D.; O'Keeffe, M.; Yaghi, O. M. *J. Am. Chem. Soc.* **2000**, *122*, 4843.
18. Liu, X.; Park, M.; Hong, S.; Oh, M.; Yoon, J. W.; Chang, J.-S.; Lah, M. S. *Inorg. Chem.* **2009**, *48*, 11507.
19. Choi, E.-Y.; Park, K.; Yang, C.-M.; Kim, H.; Son, J.-H.; Lee, S. W.; Lee, Y. H.; Min, D.; Kwon, Y.-U. *Chem. Eur. J.* **2004**, *10*, 5535.
20. Dey, C.; Kundu, T.; Biswal, B. P.; Mallick, A.; Banerjee, R. *Acta Cryst.* **2014**, *B70*, 3.
21. Senkovska, I.; Kaskel, S. *Eur. J. Inorg. Chem.* **2006**, 4564 (DOI: 10.1002/ejic.200600635).
22. Hao, X.-R.; Wang, X.-L.; Shao, K.-Z.; Yang, G.-S.; Su, Z.-M.; Yuan, G. *CrystEngComm* **2012**, *14*, 5596.

23. Burrows, A. D.; Cassar, K.; Friend, R. M. W.; Mahon, M. F.; Rigby, S. P.; Warren, J. E. *CrystEngComm* **2005**, *7*, 548.
24. Howarth, A. J.; Peters, A. W.; Vermeulen, N. A.; Wang, T. C.; Hupp, J. T.; Farha, O. K. *Chem. Mater.* **2017**, *29*, 26.
25. Farha, O. K.; Hupp, J. T. *Acc. Chem. Res.* **2010**, *43*, 1166.
26. Burtch, N. C.; Jasuja, H.; Walton, K. S. *Chem. Rev.* **2014**, *114*, 10575.
27. Horike, S.; Shimomura, S.; Kitagawa, S. *Nat. Chem.* **2009**, *1*, 695.
28. Stock, N.; Biswas, S. *Chem. Rev.* **2012**, *112*, 933.
29. Sanil, E. S.; Ho Cho, K.; Lee, S.-K.; Lee, U.-H.; Ryu, S. G.; Lee, H. W.; Chang, J.-S.; Hwang, Y. K. *J. Porous Mater.* **2015**, *22*, 171.
30. Wu, Z.-P.; Wang, M.-X.; Zhou, L.-J.; Yin, Z.-L.; Tan, J.; Zhang, J.-L.; Chen, Q.-Y. *Trans. Nonferrous Met. Soc.* **2014**, *24*, 3722.
31. Guasch, J.; Dietzel, P. D. C.; Collier, P.; Acerbi, N. *Microporous Mesoporous Mater.* **2015**, *203*, 238.
32. Goesten, M. G.; Kapteijn, F.; Gascon, J. *CrystEngComm* **2013**, *15*, 9249.
33. Israr, F.; Kimb, D. K.; Kim, Y.; Chun, W. *Quim. Nova* **2016**, *39*, 669.
34. Wu, Y.; Yang, G.-P.; Zhao, Y.; Wu, W.-P.; Liu, B.; Wang, Y.-Y. *Dalton Trans.* **2015**, *44*, 3271.
35. Ding, R.; Huang, C.; Lu, J.; Wang, J.; Song, C.; Wu, J.; Hou, H.; Fan, Y. *Inorg. Chem.* **2015**, *54*, 1405.
36. Zhou, X.; Liu, P.; Huang, W.-H.; Kang, M.; Wang, Y.-Y.; Shi, Q.-Z. *CrystEngComm.* **2013**, *15*, 8125.
37. Nelson, A. P.; Farha, O. K.; Mulfort, K. L.; Hupp, J. T. *J. Am. Chem. Soc.* **2009**, *131*, 458.
38. Farha, O. K.; Yazaydin, A. Ö.; Eryazici, I.; Malliakas, C. D.; Hauser, B. G.; Kanatzidis, M. G.; Nguyen, S. T.; Snurr, R. Q.; Hupp, J. T.; *Nat. Chem.* **2010**, *2*, 944.
39. Xiang, Z.; Cao, D.; Shao, X.; Wang, W.; Zhang, J.; Wu, W. *Chem. Eng. Sci.* **2010**, *65*, 3140.
40. Ma, L.; Jin, A.; Xie, Z.; Lin, W. *Angew. Chem. Int. Ed.* **2009**, *48*, 9905.
41. Zhao, D.; Yuan, D.; Sun, D.; Zhou, H.-C. *J. Am. Chem. Soc.* **2009**, *131*, 9186.
42. Wang, X.; Gao, W.-Y.; Luan, J.; Wojtas, L.; Ma, S. *Chem. Commun.* **2016**, *52*, 1971.
43. Gao, Q.; Zhao, X.-L.; Chang, Z.; Xu, J.; Bu, X.-H. *Dalton Trans.* **2016**, *45*, 6830.
44. Zhao, M.; Ou, S.; Wu, C.-D. *Cryst. Growth Des.* **2017**, *17*, 2688
45. Chen, D.-M.; Zhang, N.-N.; Tian, J.-Y.; Liu, C.-S.; Du, M. *J. Mater. Chem. A*, **2017**, *5*, 4861.
46. Aggarwal, H.; Das, R. K.; Engel, E. R.; Barbour, L. J. *Chem. Commun.* **2017**, *53*, 861.
47. Ju, P.; Jiang, L.; Lu, T.-B. *Inorg. Chem.* **2015**, *54*, 6291.
48. Mehlana, G.; Ramon, G.; Bourne, S. A. *Microporous Mesoporous Mater.* **2016**, *231*, 21.

49. Carrington, E. J.; McAnally, C. A.; Fletcher, A. J.; Thompson, S. P.; Warren, M.; Brammer, L. *Nat. Chem.* **2017**, DOI: 10.1038/NCHEM.2747.
50. Kim, H.; Suh, M. P. *Inorg. Chem.* **2005**, 44, 810.
51. Cheon, Y. E.; Suh, M. P. *Chem. Eur. J.* **2008**, 14, 3961.
52. Udayakumar, D.; Rao, C. N. R. *J. Mater. Chem.* **2003**, 13, 1635.
53. Lin, R.-B.; Chen, D.; Lin, Y.-Y.; Zhang, J.-P.; Chen, X.-M. *Inorg. Chem.* **2012**, 51, 9950.
54. Panda, T.; Pachfule, P.; Chen, Y.; Jiang, J.; Banerjee, R. *Chem. Commun.* **2011**, 47, 2011.

Thesis Summary

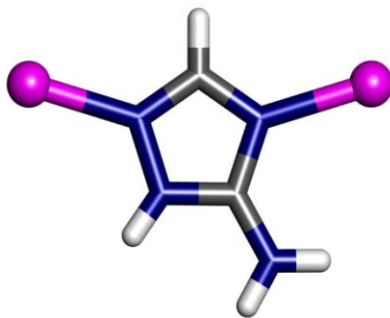
My doctoral research work focuses on understanding and demonstrating the role of some of the fundamental parameters (like change of solvent, temperature and metal cation) in the regulation of the structural features of a series of aminotriazole-oxalate based UMMOFs, and thereby in tuning their CO₂ adsorption capacities. It has been perceived that escalation of the CO₂ level in the atmosphere, resulting from the industrial effluents is a major contributor to global greenhouse effect. UMMOFs have been identified as an important class of material for CO₂ sequestration from flue gas (post-combustive CO₂ capture), which subsequently point towards the need for breakthrough discovery of these materials. This could be attained by a comprehensive investigation of these materials and this is the foremost drive behind the present thesis. The main aim is to enhance the CO₂ uptake capacity and CO₂/N₂ selectivity of these UMMOFs via alterations in the above mentioned parameters. In this attempt we have obtained a series of UMMOFs. Considering the CO₂-interactive design, aminotriazole and oxalic acid were decisively chosen as the ligands, which led to the formation of the UMMOFs with pores lined by polarizing oxalates and basic free amine groups. Further, the need for hydrolytic stability in these materials was realised and examined to make them pertinent candidates for CO₂ sequestration under low CO₂ partial pressures and relative humidity. The first three working chapters represent a steady improvement in the CO₂ uptake capacity and hydrolytic stability shown by the UMMOFs, which have been obtained by variations in the synthetic parameters. While, the last chapter demonstrates the framework stabilization of an unstable Zn-aminotriazolate MOF by in-situ Schiff base formation. It is believed that the work reported in this thesis will help attain a better understanding of the design of UMMOFs and tune their performance as an apt post-combustive CO₂-sequestration material.

This thesis is just a step towards improving the performance of the UMMOFs for their utility in CO₂ capture from industrial effluents. However, this does not claim that it entirely unravels the wholesome problem of selective CO₂ capture from flue gas, thus still leaves a lot of room for improvement in the future.

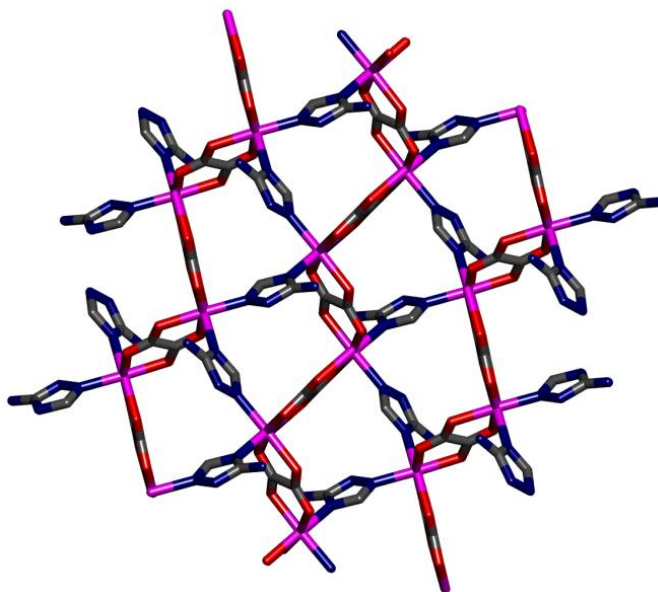
Appendix for Chapter 2

Appendix A2.1 Crystal data table for **1**, **1*** and **2**.

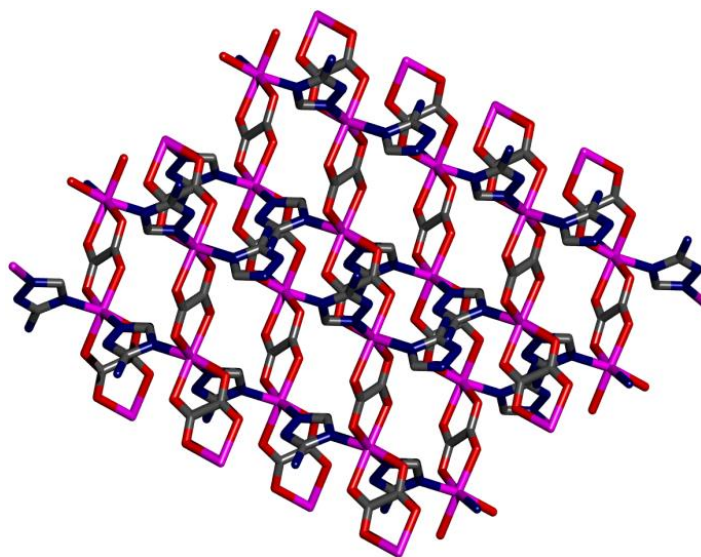
| | 1 | 1* | 2 |
|--|--|---|---|
| Formula | [Co(C ₂ O ₄)(C ₂ N ₄ H ₄)](H ₂ O) ₄ | [Co(C ₂ O ₄)(C ₂ N ₄ H ₄)] | [Co ₂ (C ₂ O ₄) ₂ (C ₂ N ₄ H ₄) ₃](CH ₃ OH) |
| FW | 295.04 g/mol | 231.04 | 578.22 |
| <i>T</i> , K | 100(2) | 100(2) | 100(2) |
| Crystal system, space group | Monoclinic, <i>P</i> 2 ₁ / <i>c</i> | Monoclinic, <i>P</i> 2 ₁ / <i>c</i> | Monoclinic, <i>P</i> 2 ₁ / <i>n</i> |
| <i>a</i> , Å | 9.1332(9) | 7.9846(6) | 8.6554(5) |
| <i>b</i> , Å | 13.8397(12) | 14.4227(11) | 13.7545(8) |
| <i>c</i> , Å | 9.0847(8) | 7.9589(6) | 17.7033(11) |
| β , deg | 117.392(5) | 111.622(4) | 93.073(2) |
| <i>V</i> , Å ³ | 1019.56(17) | 852.05(11) | 2104.6(2) |
| <i>Z</i> , Calculated density | 4, 1.922 g/cm ³ | 4, 1.801 g/cm ³ | 4, 1.825 g/cm ³ |
| μ , mm ⁻¹ | 13.687 | 15.807 | 13.041 |
| <i>F</i> (000) | 588 | 460 | 1168 |
| <i>R</i> _{int} | 0.1039 | 0.0705 | 0.0506 |
| Data/ restraints/para meters | 2015 / 0 / 154 | 1439/0/118 | 4110/9/310 |
| Goodness-of-fit on <i>F</i> ² | 1.060 | 1.072 | 1.067 |
| Final <i>R</i> indices [<i>I</i> > 2 σ (<i>I</i>)] | <i>R</i> 1 = 0.0880 <i>wR</i> 2 = 0.2298 | <i>R</i> 1 = 0.0750, <i>wR</i> 2 = 0.1602 | <i>R</i> 1 = 0.0454, <i>wR</i> 2 = 0.1217 |
| Final <i>R</i> indices [all data] | <i>R</i> 1 = 0.1185, <i>wR</i> 2 = 0.2513 | <i>R</i> 1 = 0.1138, <i>wR</i> 2 = 0.1801 | <i>R</i> 1 = 0.0503, <i>wR</i> 2 = 0.1259 |



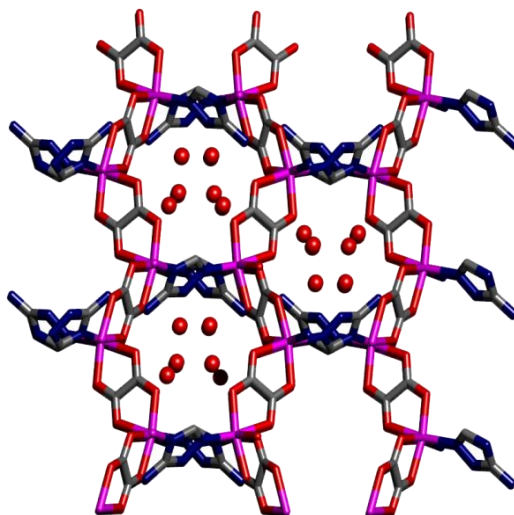
Appendix A2.2 The μ -2 bridging aminotriazole (Hatz) ligand (colour code: Cobalt: magenta; Oxygen: red; Nitrogen: blue; Carbon: grey).



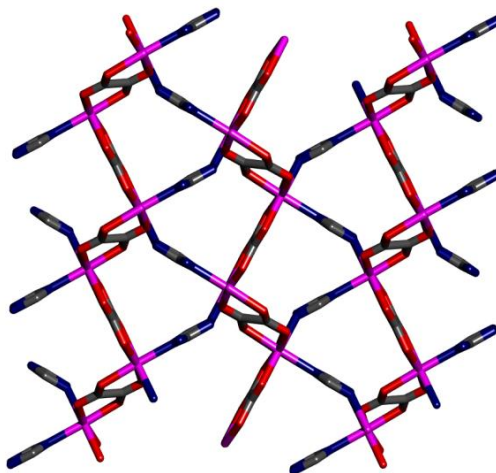
Appendix A2.3 Crystal structure view along a-axis for 1.



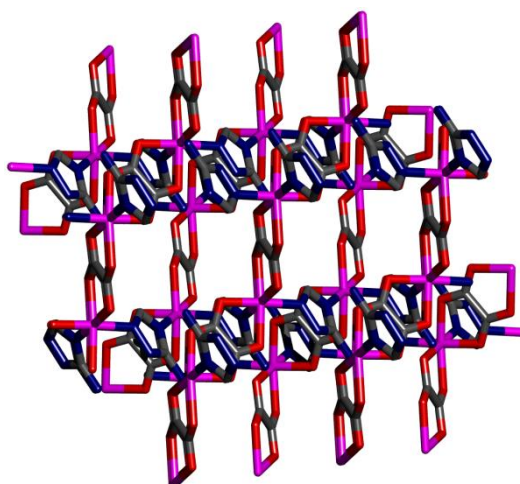
Appendix A2.4 Crystal structure view along b-axis for 1.



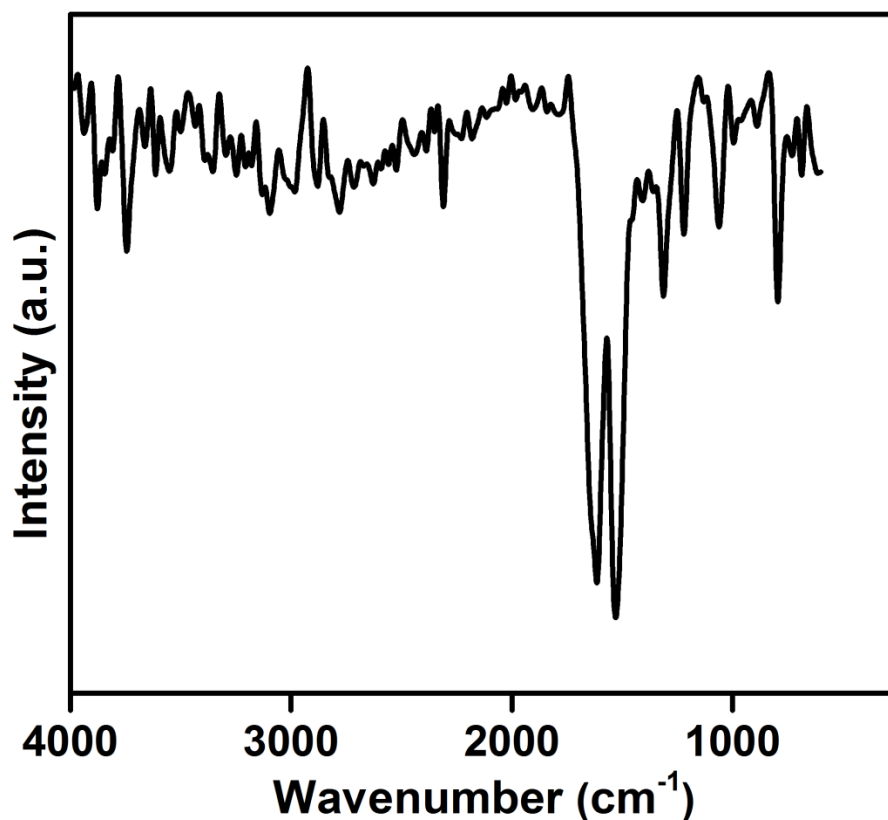
Appendix A2.5 Orthographic projection view of **1** along c-axis; shows the presence of solvent water molecules present throughout the porous channels, hydrogens have been removed for clarity.



Appendix A2.6 Crystal structure view along a-axis for **1***.



Appendix A2.7 Crystal structure view along b-axis for **1***.



Appendix A2.8 Infra-red spectra of 1.

Appendix A2.9 Table showing the unit cell parameters at different temperature for 1.

| Temperature (K) | a(Å) | b(Å) | c(Å) | β | Volume (Å ³) | Crystal system | Score |
|-------------------|--------------------|---------------------|--------------------|---------------------|--------------------------|----------------|-------|
| 300K (26.85°C) | 8.412 (± 0.014) | 14.193 (± 0.02) | 8.701 (± 0.010) | 117.072 (± 0.10) | 924 (± 2.0) | Mono. P | 3.6 |
| 313K (40°C) | 8.014 (± 0.003) | 14.364 (± 0.006) | 8.133 (± 0.004) | 112.705 (± 0.03) | 863 (± 0.6) | Mono. P | 4.1 |
| 323K (50°C) | 8.002 (± 0.007) | 14.384 (± 0.013) | 8.113 (± 0.009) | 112.326 (± 0.06) | 863 (± 1.3) | Mono. P | 3.3 |
| 333K (60°C) | 8.011 (± 0.008) | 14.351 (± 0.014) | 8.082 (± 0.009) | 111.881 (± 0.07) | 861 (± 1.3) | Mono. P | 4.7 |
| 353K (80°C) | 8.022 (± 0.006) | 14.342 (± 0.011) | 8.096 (± 0.008) | 111.763 (± 0.06) | 863 (± 1.1) | Mono. P | 4.9 |
| 373K (100°C) | 8.051 (± 0.008) | 14.318 (± 0.014) | 8.075 (± 0.010) | 111.566 (± 0.08) | 864 (± 1.5) | Mono. P | 4.5 |

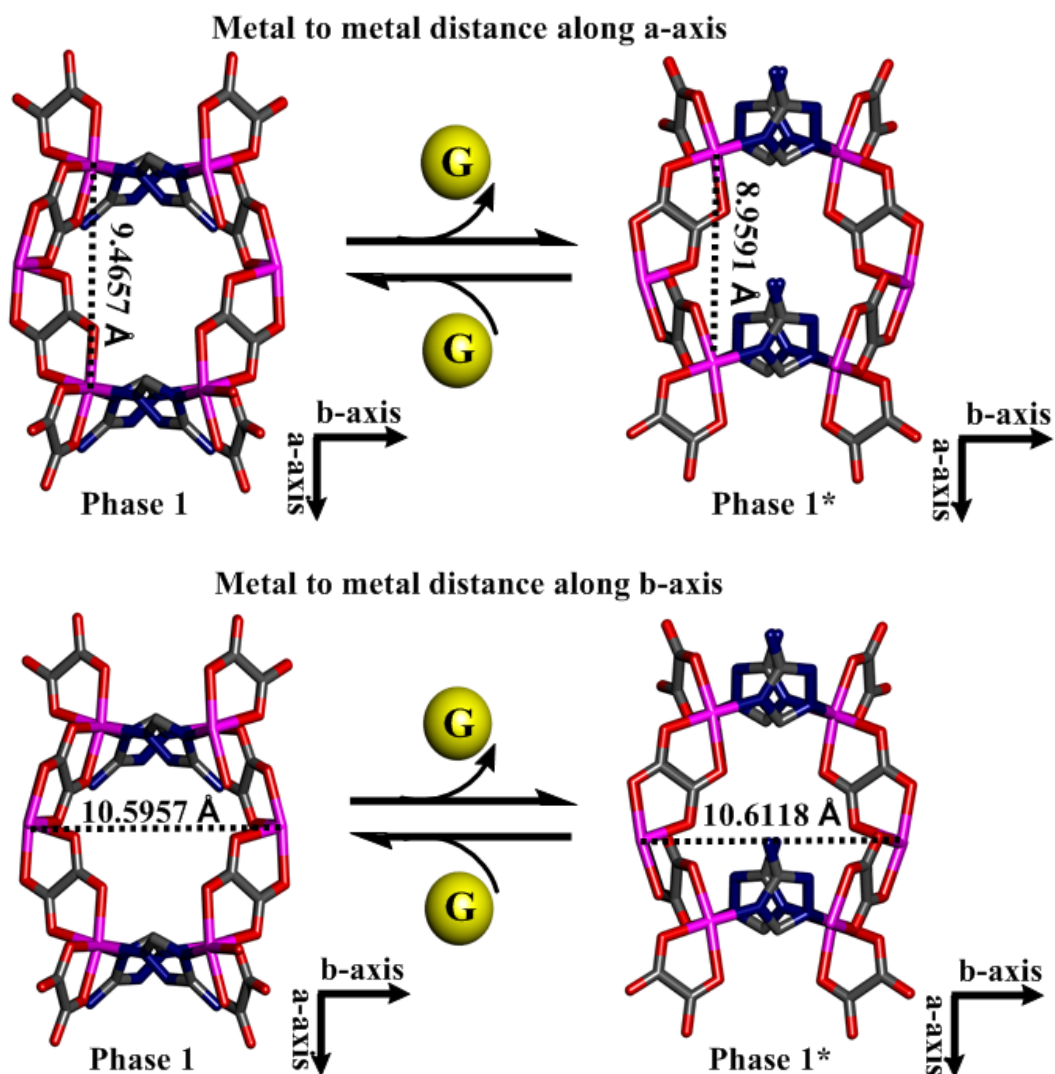
Appendix for Chapter 2

Appendix A2.10 Table showing the hkl listing for phase **1** and **1*** displaying the asymmetric shifts of the reflection peaks upon desolvation.

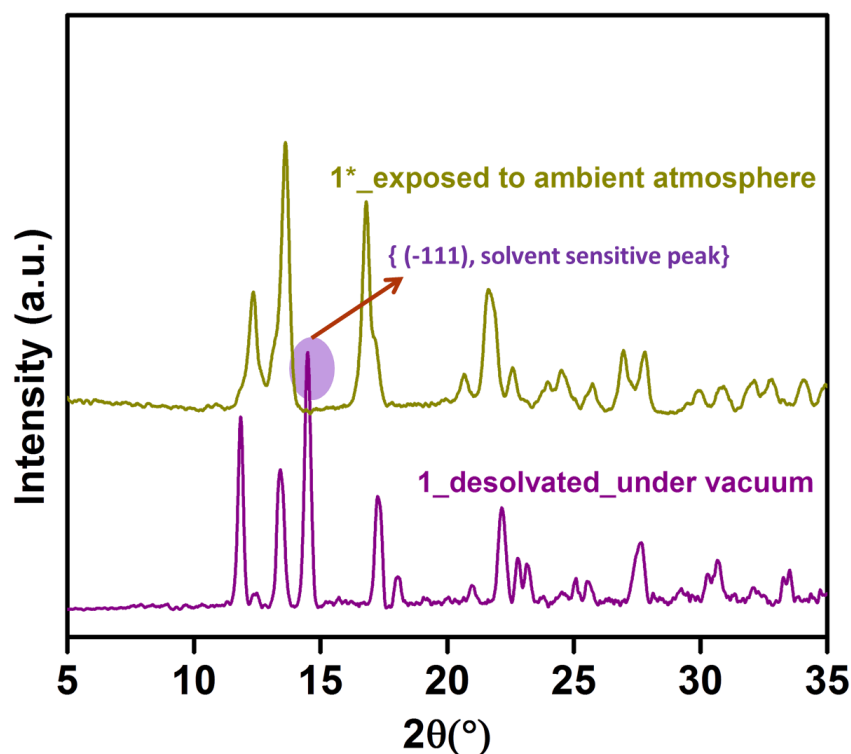
| 2θ(°) for 1 | hkl | 2θ(°) for 1* | hkl |
|--------------------------------------|------------|---------------------------------------|------------|
| 10.902 | 100 | 11.913 | 100 |
| 12.642 | 110 | 12.264 | 020 |
| 12.692 | 011 | 13.405 | 110 |
| 12.783 | 020 | 13.439 | 011 |
| 13.040 | -111 | 14.760 | -111 |
| 16.830 | 120 | 17.130 | 120 |
| 16.868 | 021 | 17.157 | 021 |
| 17.133 | -121 | 18.215 | -121 |
| 19.544 | -102 | 20.747 | 111 |
| 19.810 | 111 | 22.010 | 130 |
| 20.485 | -2-11 | 22.032 | 031 |
| 20.579 | -112 | 22.542 | -102 |
| 21.902 | 200 | 22.874 | -131 |
| 22.022 | 002 | 23.320 | -2-11 |
| 22.151 | 130 | 23.359 | 121 |
| 22.181 | 031 | 23.380 | -112 |
| 22.385 | -131 | 23.958 | 200 |
| 22.745 | 121 | 24.036 | 002 |
| 22.834 | -202 | 24.671 | 040 |
| 22.836 | 210 | 24.750 | 210 |
| 22.950 | 012 | 24.827 | 012 |
| 23.339 | -2-21 | 25.684 | -2-21 |
| 23.422 | -122 | 25.739 | -122 |
| 23.732 | -212 | 27.733 | -212 |

Appendix A2.11 Selected bond lengths in **1** and **1***.

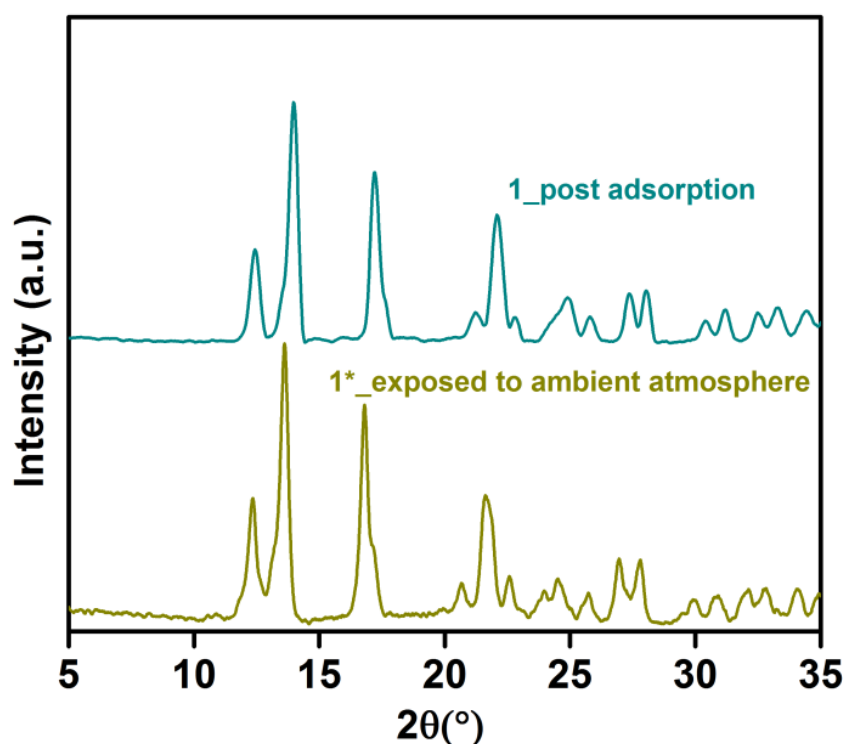
| 1 | | 1* | |
|--------------------------------|----------------------|--------------------------------|-------------------|
| Co1-----O1 | 2.090 Å (± 0.006) | Co1-----O1 | 2.090 Å (± 0.006) |
| Co1-----O2 | 2.136 Å (± 0.005) | Co1-----O2 | 2.102 Å (± 0.006) |
| Co1-----O3 | 2.091 Å (± 0.006) | Co1-----O3 | 2.069 Å (± 0.006) |
| Co1-----O4 | 2.135 Å (± 0.005) | Co1-----O4 | 2.063 Å (± 0.006) |
| Co1-----N1(from bridging Hatz) | 2.095 Å (± 0.007) | Co1-----N1(from bridging Hatz) | 2.103 Å (± 0.007) |
| Co1-----N3(from bridging Hatz) | 2.105 Å (± 0.007) | Co1-----N2(from bridging Hatz) | 2.115 Å (± 0.007) |



Appendix A2.12 Visualization of the significant dimensional changes along **a** and **b**-axes upon desolvation.



Appendix A2.13 PXRD comparison showing the solvent dependence of the (-111) reflection suggesting strong solvent-framework interactions. Even exposure for few seconds to the ambient atmosphere shows the disappearance of this reflection.



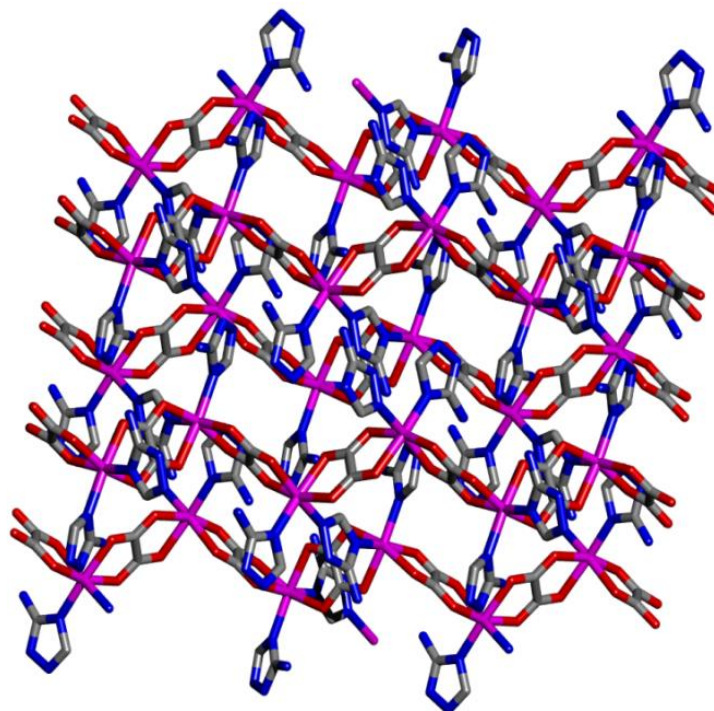
Appendix A2.14 Comparison of the PXRD pattern of the post-adsorption sample with the desolvated sample that was exposed to air. Note: The desolvated phase hydrates immediately upon exposure to air and this causes some changes in the powder pattern (Figure A2.13).

Appendix for Chapter 2

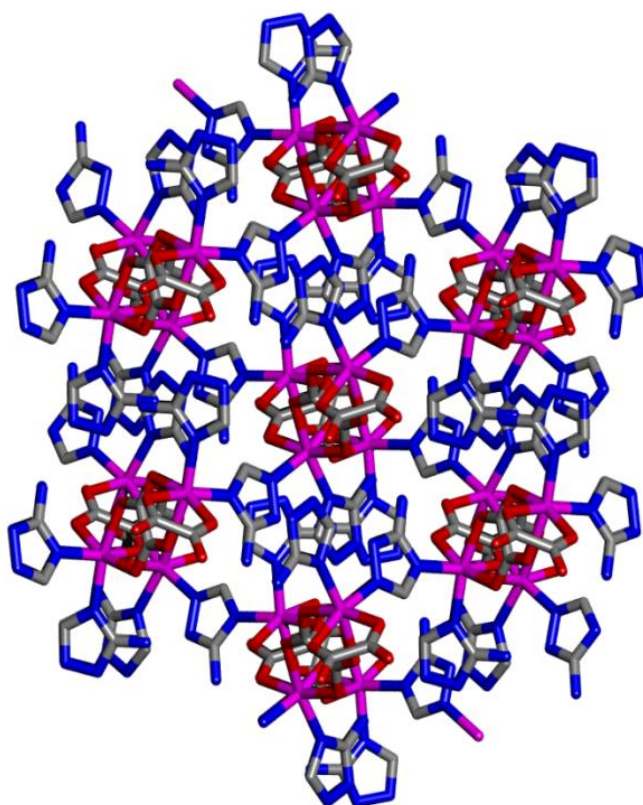
Appendix A2.15 Comparison of the structural changes (unit-cell volume) in the void volume upon desolvation in selected MOFs.

| Parent MOF (Unit cell volume) | Desolvated MOF (Unit cell volume) | change in unit cell volume [%] | change in void volume [%] | Ref. |
|--|---|---|------------------------------------|------------------|
| $[\text{Zn}_2(\text{tp})_2(\text{L}^2)].2.5\text{DMF}.0.5\text{H}_2\text{O}$ (2a) $V = 2069.6(7) \text{ \AA}^3$ | $[\text{Zn}_2(\text{tp})_2(\text{L}^2)]_n$ (2d) $V = 1492.2 \text{ \AA}^3$ | 28% ↓ | 56% ↓ | 45 |
| $[\text{Cd}(\text{pzdc})(\text{azpy})].2\text{H}_2\text{O}$ (1) $V = 3817(14) \text{ \AA}^3$ | $[\text{Cd}(\text{pzdc})(\text{azpy})].2\text{H}_2\text{O}$ (1a) $V = 3861(5) \text{ \AA}^3$ | 1.2% ↑ | 4% ↑ | 46 |
| $[\text{Zn}_3(\text{OH})_2(\text{btca})_2].\text{DMF}.4\text{H}_2\text{O}$ (1) $V = 2535.25(11) \text{ \AA}^3$ | $[\text{Zn}_3(\text{OH})_2(\text{btca})_2].\text{DMF}.0.5\text{H}_2\text{O}$ (1a) $V = 2195.5(6) \text{ \AA}^3$ | 13.4% ↓ | 24.5% ↓ | 47 |
| $[\text{Zn}_3(\text{OH})_2(\text{btca})_2].\text{DMF}.4\text{H}_2\text{O}$ (1) $V = 2535.25(11) \text{ \AA}^3$ | $[\text{Zn}_3(\text{OH})_2(\text{btca})_2].2\text{H}_2\text{O}$ (1b) $V = 2012.4(5) \text{ \AA}^3$ | 20.6% ↓ | 43% ↓ | 47 |
| $[\text{Fe}(\text{pydc})(4,4'\text{-bipy})].\text{H}_2\text{O}$ (1·H₂O) $V = 879.13(9) \text{ \AA}^3$ | $[\text{Fe}(\text{pydc})(4,4'\text{-bipy})]$ (1h) $V = 807.2(5) \text{ \AA}^3$ | 8.2% ↓ | 65% ↓ | 48 |
| $[\text{Fe}(\text{pydc})(4,4'\text{-bipy})].\text{H}_2\text{O}$ (1·H₂O) $V = 879.13(9) \text{ \AA}^3$ | $[\text{Fe}(\text{pydc})(4,4'\text{-bipy})]$ (1v) $V = 821.2(9) \text{ \AA}^3$ | 6.6% ↓ | 56% ↓ | 48 |
| NOTT-202* $V = 13,100(9) \text{ \AA}^3$ | NOTT-202a $V = 14,580(9) \text{ \AA}^3$ | 11% ↑ | 16.6% ↑ | 49 |
| $\{[\text{Co}(\text{C}_2\text{O}_4)(\text{C}_2\text{N}_4\text{H}_4)](\text{H}_2\text{O})_4\}$ $V = 1019.56 \text{ \AA}^3$ | $[\text{Co}(\text{C}_2\text{O}_4)(\text{C}_2\text{N}_4\text{H}_4)]$ $V = 852.05 \text{ \AA}^3$ | 16% ↓ | 78% ↓ | This work |

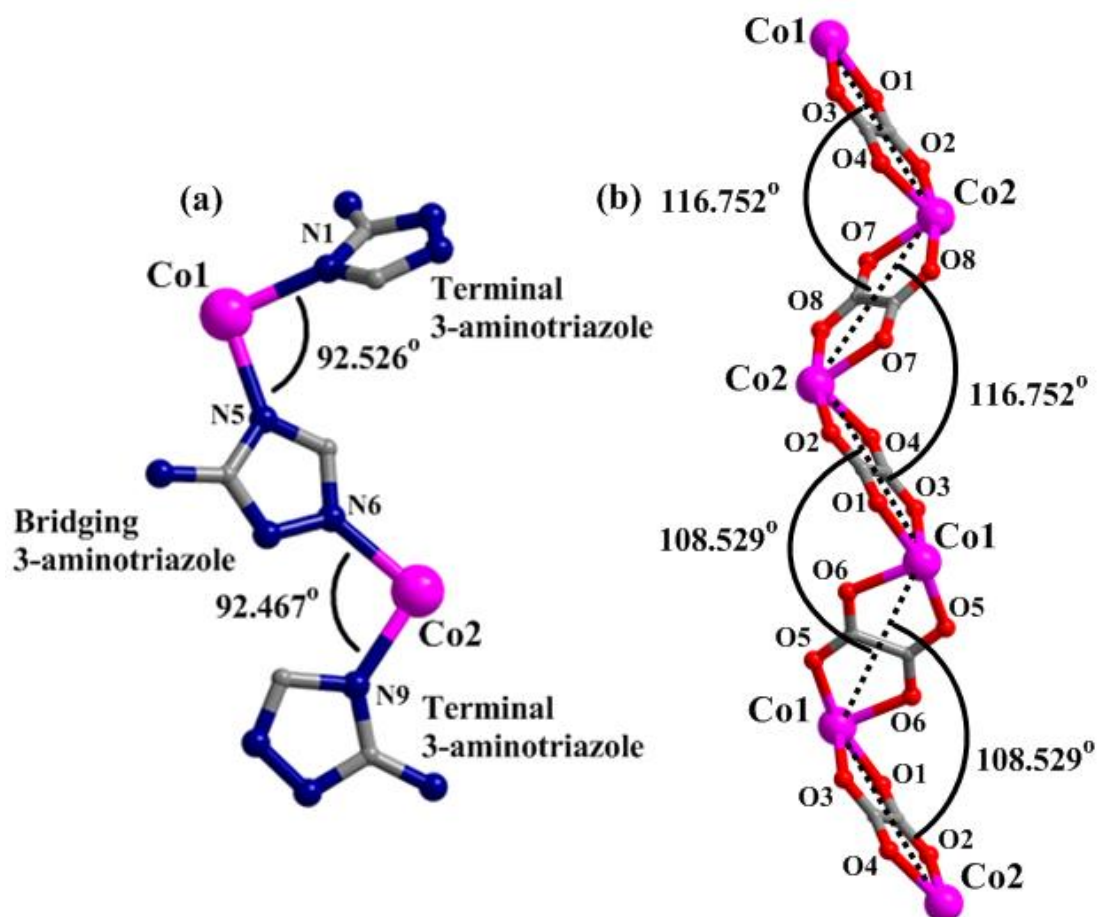
[Note: Ligand abbreviations: H_2tp = Terephthalic acid; L^2 = 2,3-difluoro-1,4-bis(4-pyridyl)benzene; H_2pzdc = pyrazine-2,3-dicarboxylic acid; azpy = 4,4'-azopyridine; H_2btca = benzotriazole-5-carboxylic acid; 4,4'-bipy = 4,4'-bipyridyl; H_2pydc = pyridine-2,5-dicarboxylic acid. Unit cell and void volumes changes upon desolvation; up and down arrows indicate percent decrease and increase; compound numbers from original papers are indicated in brackets.]



Appendix A2.16 Crystal structure view along b-axis for **2**.



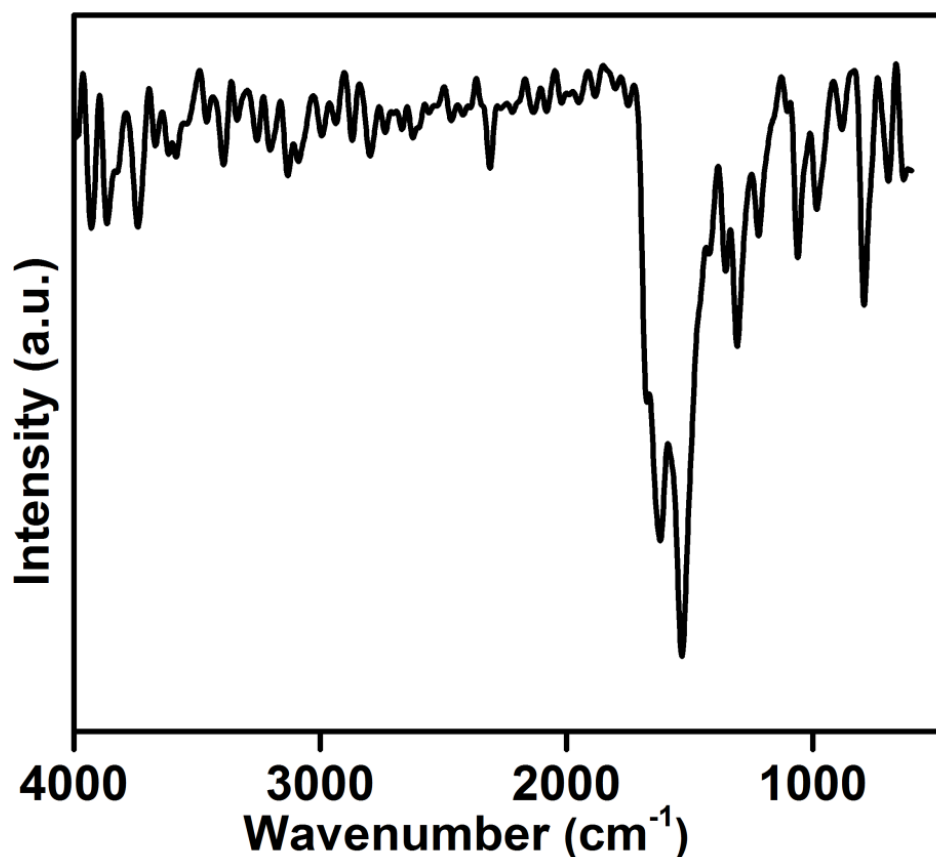
Appendix A2.17 Crystal structure view along c-axis for **2**.



Appendix A2.18 Co-Hatz fragment and Co-Ox chain for MOF 2.

Appendix A2.19 Bond distance table for MOF 2.

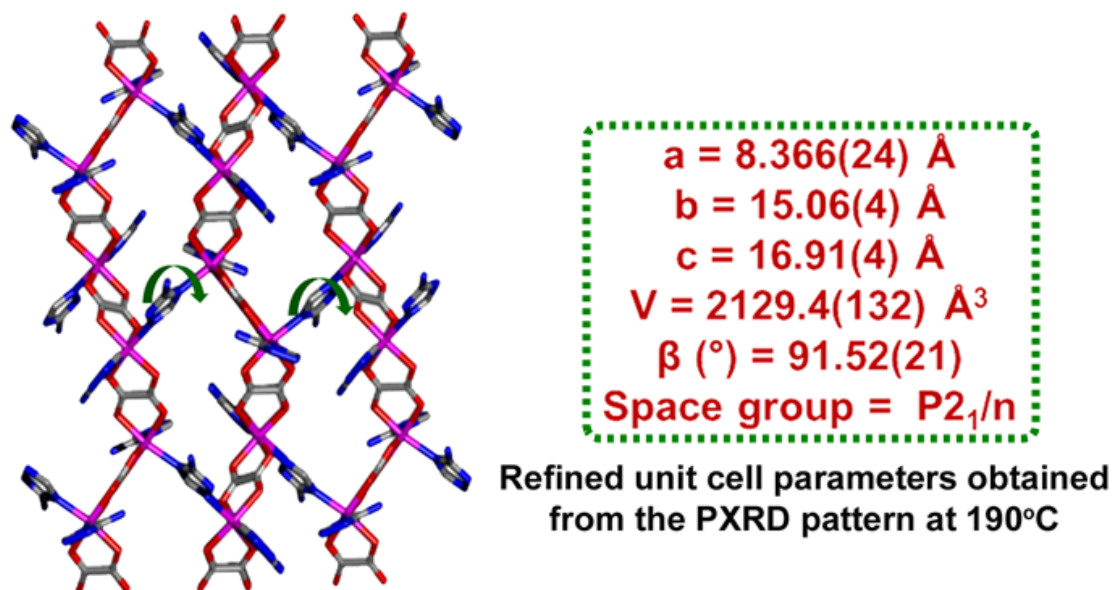
| Bond lengths from the atoms binding to the metal centre | |
|---|-------------------------|
| Co1-----O1 | 2.084 Å (± 0.002) |
| Co2-----O2 | 2.071 Å (± 0.002) |
| Co1-----O3 | 2.128 Å (± 0.002) |
| Co2-----O4 | 2.153 Å (± 0.002) |
| Co1-----O5 | 2.121 Å (± 0.002) |
| Co1-----O6 | 2.148 Å (± 0.002) |
| Co2-----O7 | 2.154 Å (± 0.002) |
| Co2-----O8 | 2.096 Å (± 0.002) |
| Co1-----N1(from terminal Hatz) | 2.081 Å (± 0.002) |
| Co2-----N9(from terminal Hatz) | 2.112 Å (± 0.002) |
| Co1-----N5(from bridging Hatz) | 2.088 Å (± 0.002) |
| Co2-----N6(from bridging Hatz) | 2.114 Å (± 0.002) |



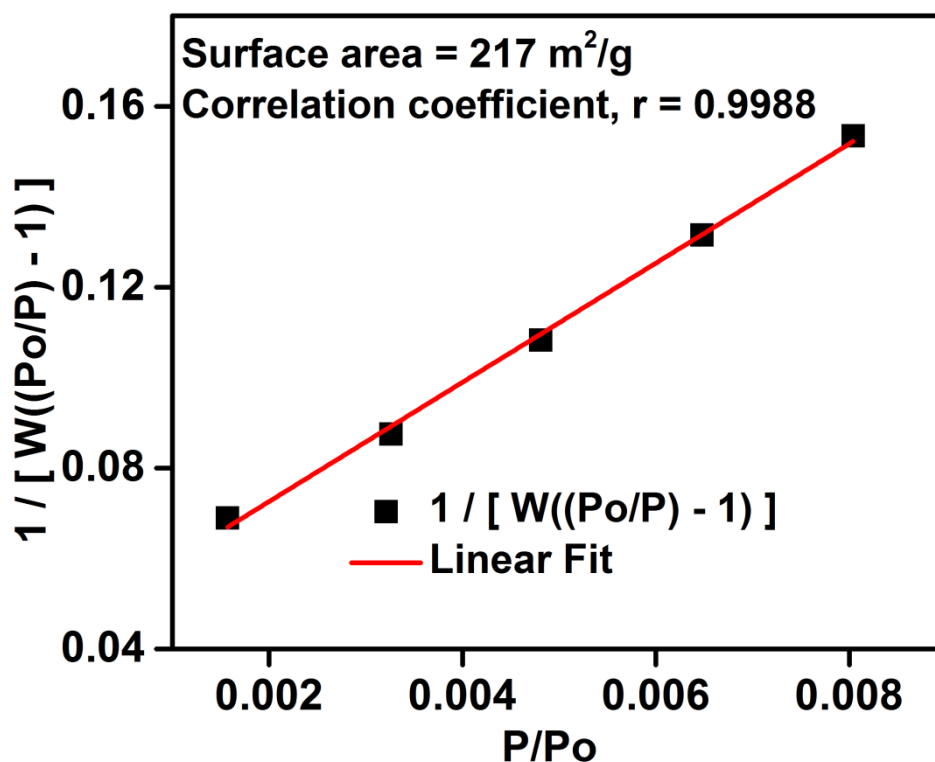
Appendix A2.20 Infra-red spectra of 2.

Appendix A2.21 Table for variable temperature SC-Unit cell data for 2.

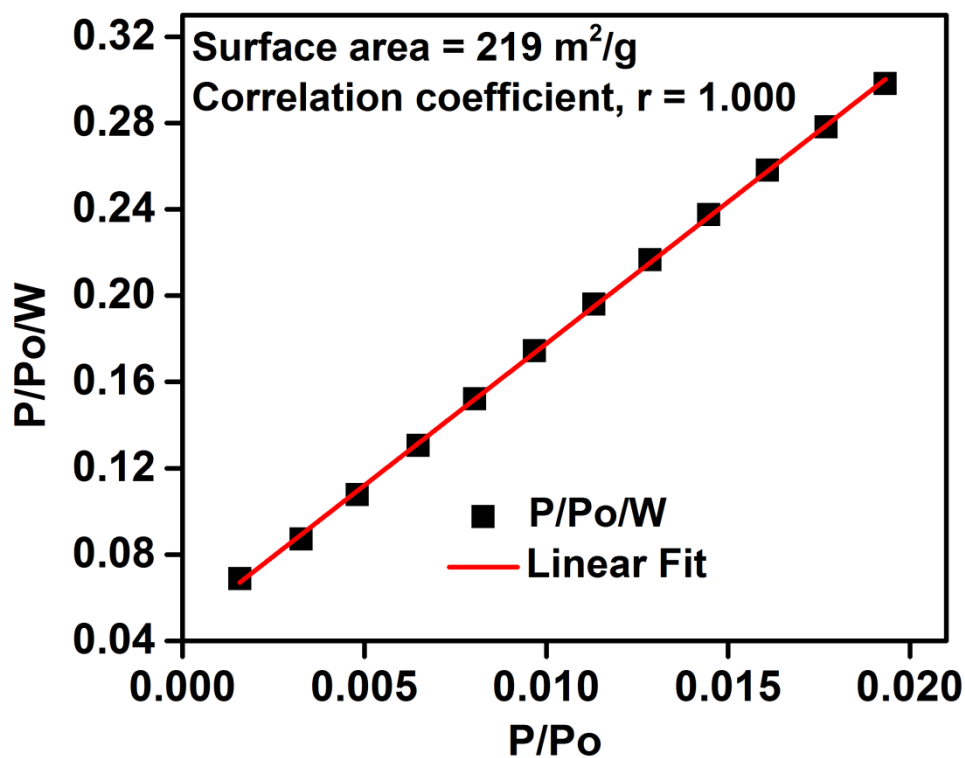
| Temperature (K) | a(Å) | b(Å) | c(Å) | β | Volume (Å ³) | Crystal system | Score |
|---------------------|--------------------------|---------------------------|---------------------------|-------------------------|--------------------------|----------------|-------|
| 100K (-173.15°C) | 8.673 (± 0.011) | 13.755 (± 0.002) | 17.701 (± 0.013) | 93.10 (± 0.10) | 2107 (± 2.0) | Mono. P | 4.0 |
| 300K (26.85°C) | 8.671 (± 0.013) | 13.896 (± 0.004) | 17.704 (± 0.012) | 93.21 (± 0.05) | 2128 (± 0.3) | Mono. P | 3.7 |
| 373K (100°C) | 8.682 (± 0.005) | 13.901 (± 0.006) | 17.722 (± 0.016) | 93.34 (± 0.03) | 2133 (± 1.3) | Mono. P | 3.3 |
| 423K (150°C) | 8.669 (± 0.005) | 13.944 (± 0.012) | 17.681 (± 0.009) | 93.26 (± 0.02) | 2132 (± 1.6) | Mono. P | 3.7 |
| 443K (170°C) | 8.674 (± 0.008) | 14.020 (± 0.003) | 17.759 (± 0.006) | 93.52 (± 0.07) | 2150 (± 2.4) | Mono. P | 4.1 |
| 463K (190°C) | 8.362 (± 0.006) | 15.086 (± 0.004) | 16.923 (± 0.013) | 91.46 (± 0.08) | 2132 (± 1.8) | Mono. P | 3.5 |



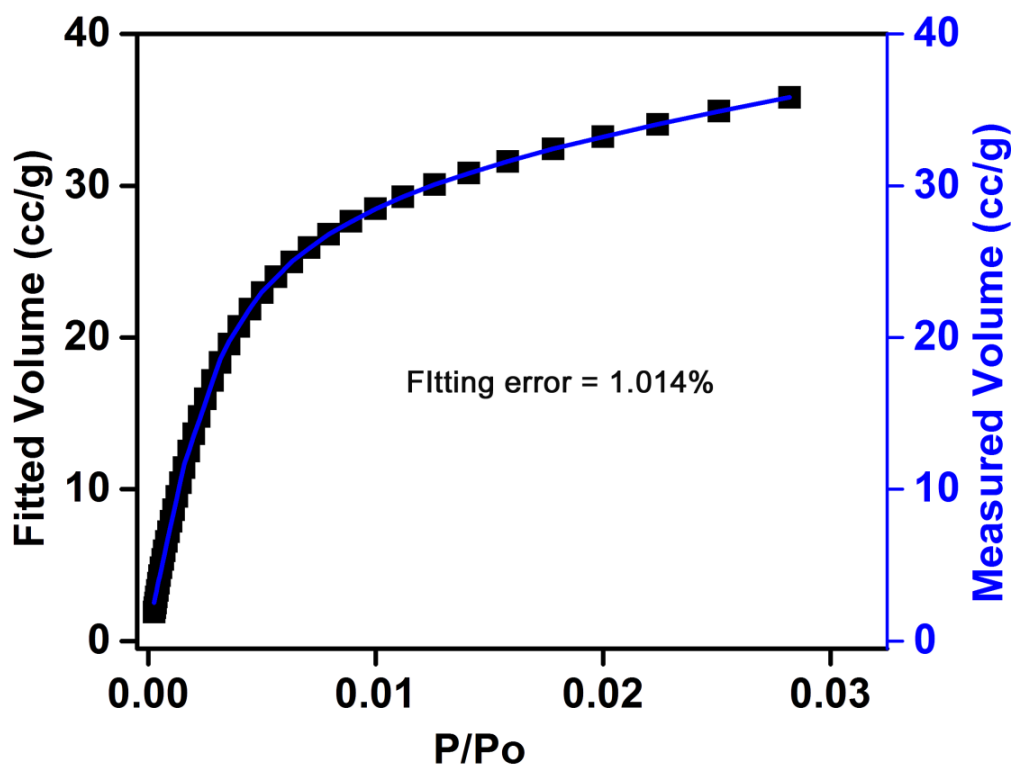
Appendix A2.22 Showing the possible temperature dependent rotation of the μ -2 bridging Hatz units, causing the sliding of the Co-Ox chains; given below is the unit cell parameters obtained by indexing the PXRD pattern at 190°C (463 K); (please see the Figure 2.13 and Appendix A2.21).



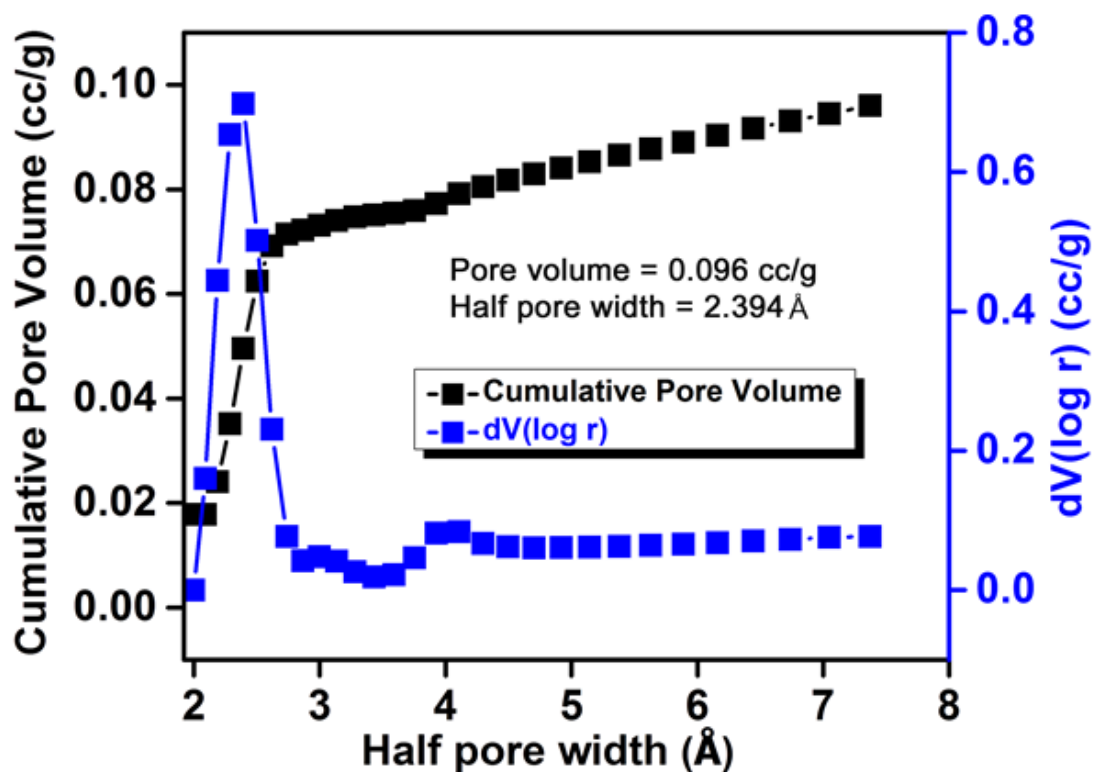
Appendix A2.23 BET surface area fit for 2.



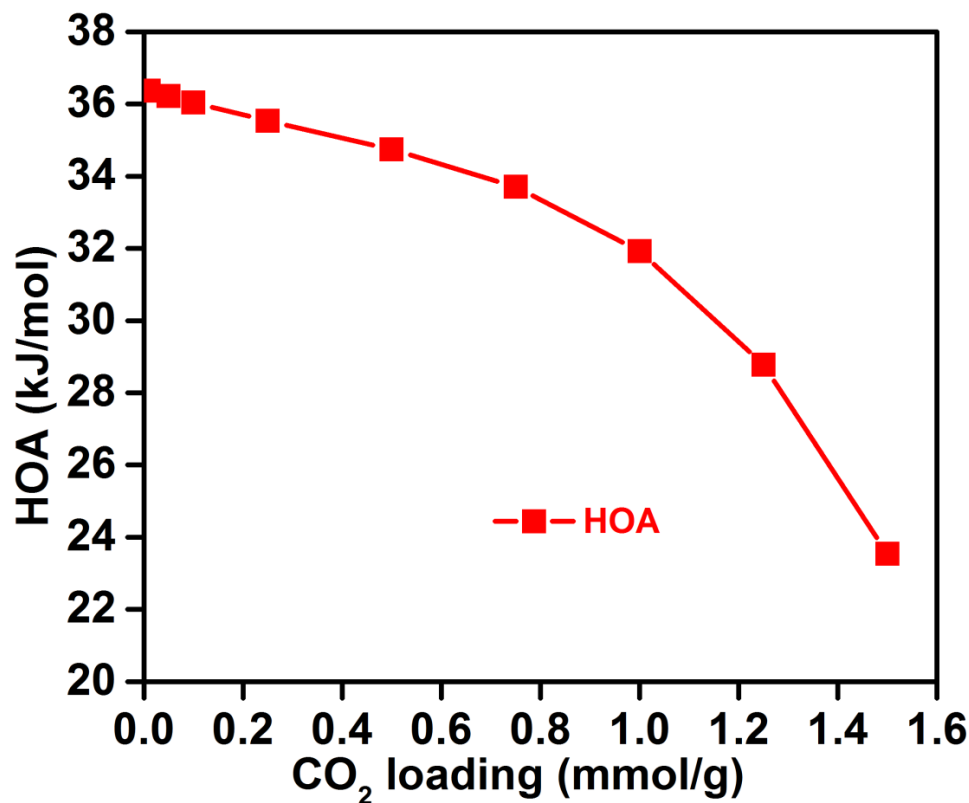
Appendix A2.24 Langmuir surface area fit for 2.



Appendix A2.25 DFT isotherm fitting for 2.



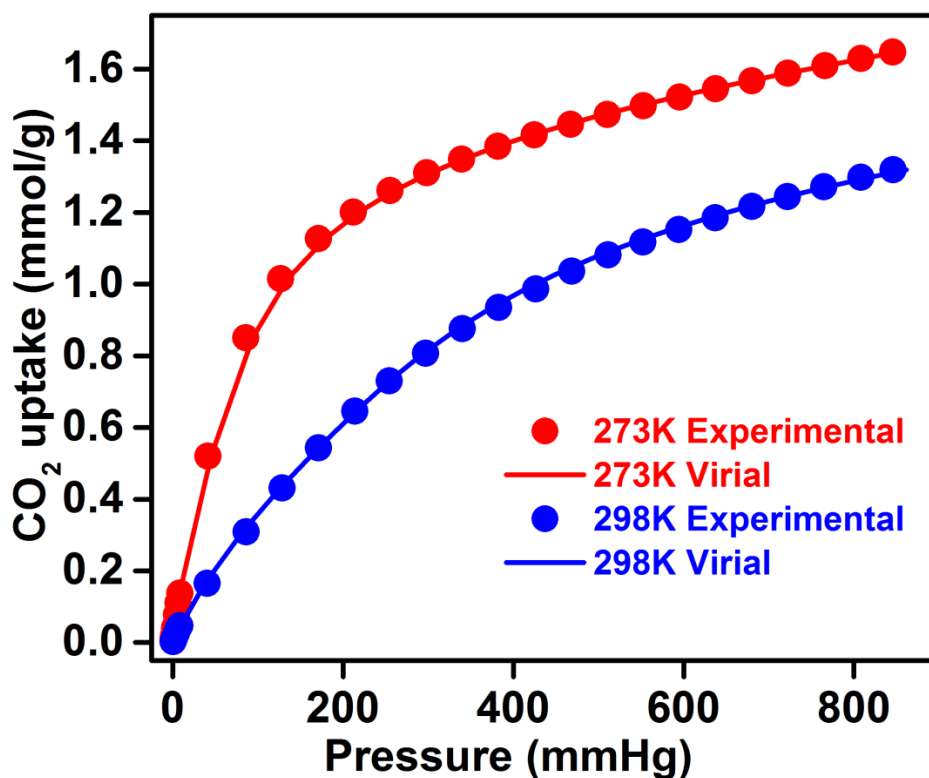
Appendix A2.26 DFT cumulative pore volume and pore size distribution plots for 2.



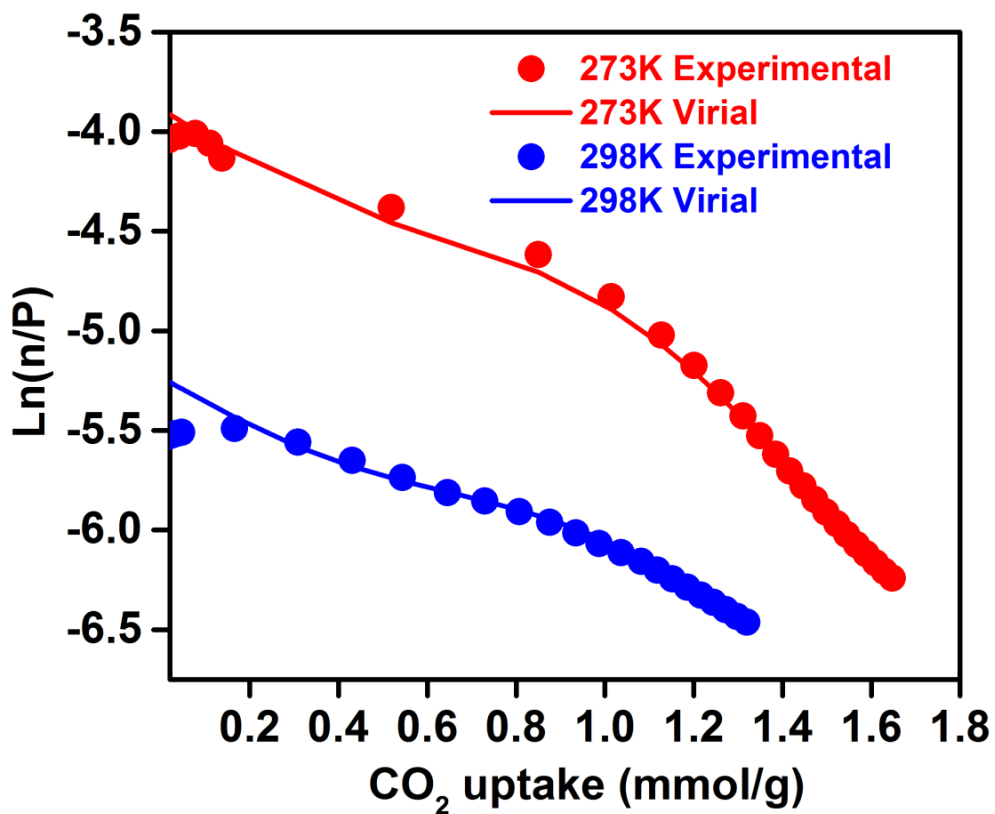
Appendix. A2.27 HOA obtained from virial fitting at temperatures 273 K and 298 K for 2.

Appendix. A2.28 Virial coefficients for 2.

| | | | |
|----|--------------|----|--------------|
| A0 | -4379.377491 | B0 | 19.92851715 |
| A1 | 477.3574325 | B1 | -0.379394243 |
| A2 | -259.04862 | B2 | 1.21595259 |
| A3 | 93.29080202 | B3 | -3.274874541 |
| A4 | 251.4468989 | B4 | 2.268199058 |
| A5 | -22.77939425 | B5 | -0.822817821 |

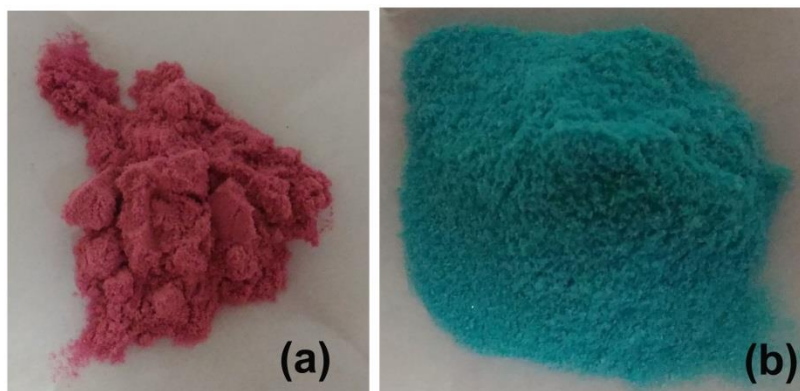


Appendix A2.29 Comparison of the experimental isotherms with isotherms obtained via Virial model for 2 at 273 K and 298 K.



Appendix A.30 Virial plots carried out using CO_2 isotherms collected at 273 K and 298 K for 2.

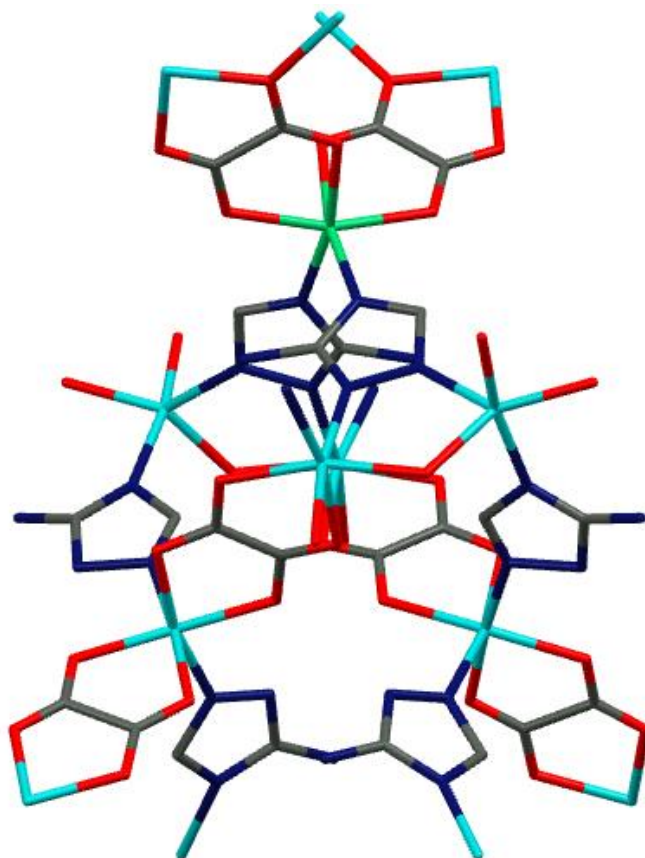
Appendix



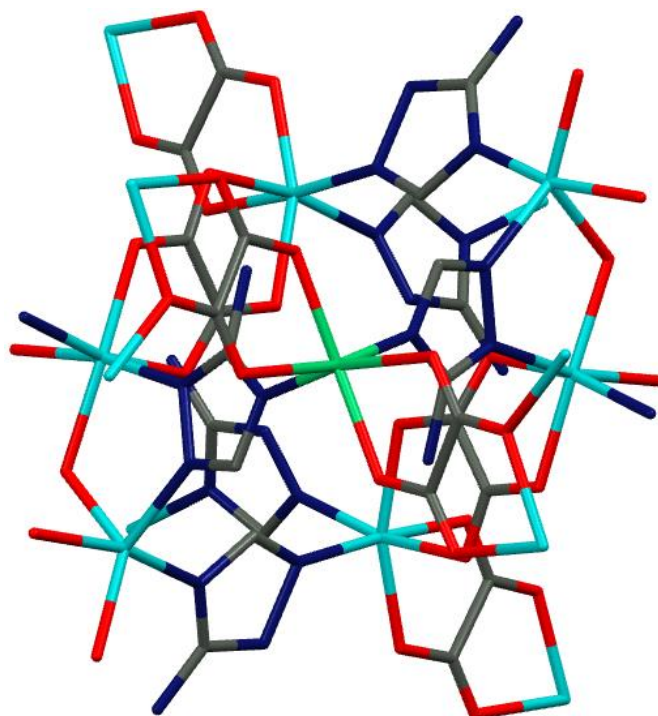
Appendix A3.1 Picture of the bulk samples of (a) compound 1 and (b) compound 2.

Appendix A3.2 Crystal data table for 2_squeezed.

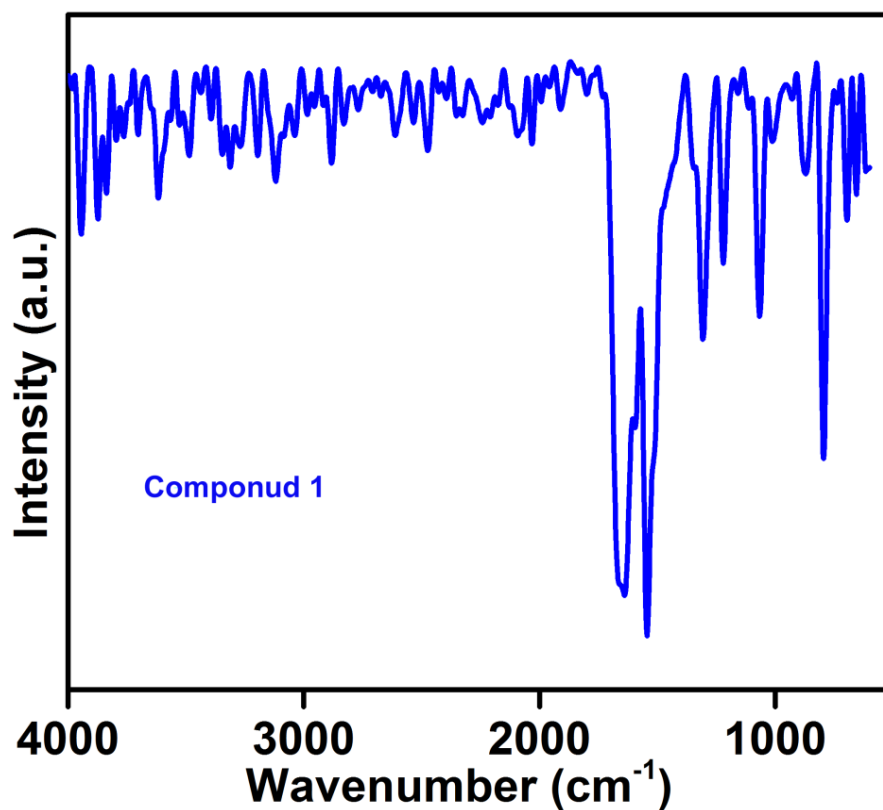
| | 2_squeezed |
|-----------------------------------|--|
| Formula | [Zn ₆ Ni ₁ (C ₂ O ₄) ₆ (C ₂ H ₄ N ₄) ₄ (C ₂ H ₃ N ₄) ₂] |
| FW | 740.79 g/mol |
| T, K | 100(2) |
| Crystal system, space group | Orthorhombic, F d d 2 |
| a, Å | 30.644(4) Å |
| b, Å | 12.0074(13) Å |
| c, Å | 30.182(4) Å |
| V, Å ³ | 11106.(2) Å ³ |
| Z, Calculated density | 16, 1.772 g/cm ³ |
| μ, mm ⁻¹ | 4.043 mm ⁻¹ |
| F(000) | 5872 |
| R _{int} | 0.1763 |
| Data/restraints/parameters | 4572 / 403 / 358 |
| Goodness-of-fit on F ² | 1.072 |
| Final R indices [I>2 sigma(I)] | R1 = 0.1076, wR2 = 0.2636 |
| Final R indices [all data] | R1 = 0.1436, wR2 = 0.2912 |



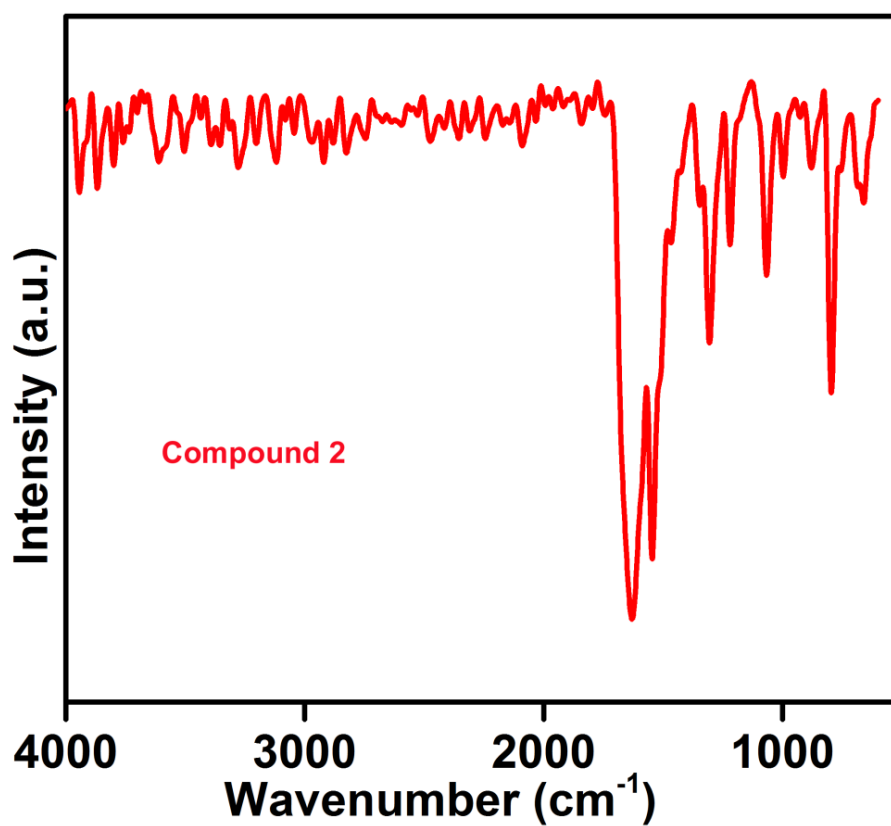
Appendix A3.3 View of the molecular building unit of framework 2 along a-axis.



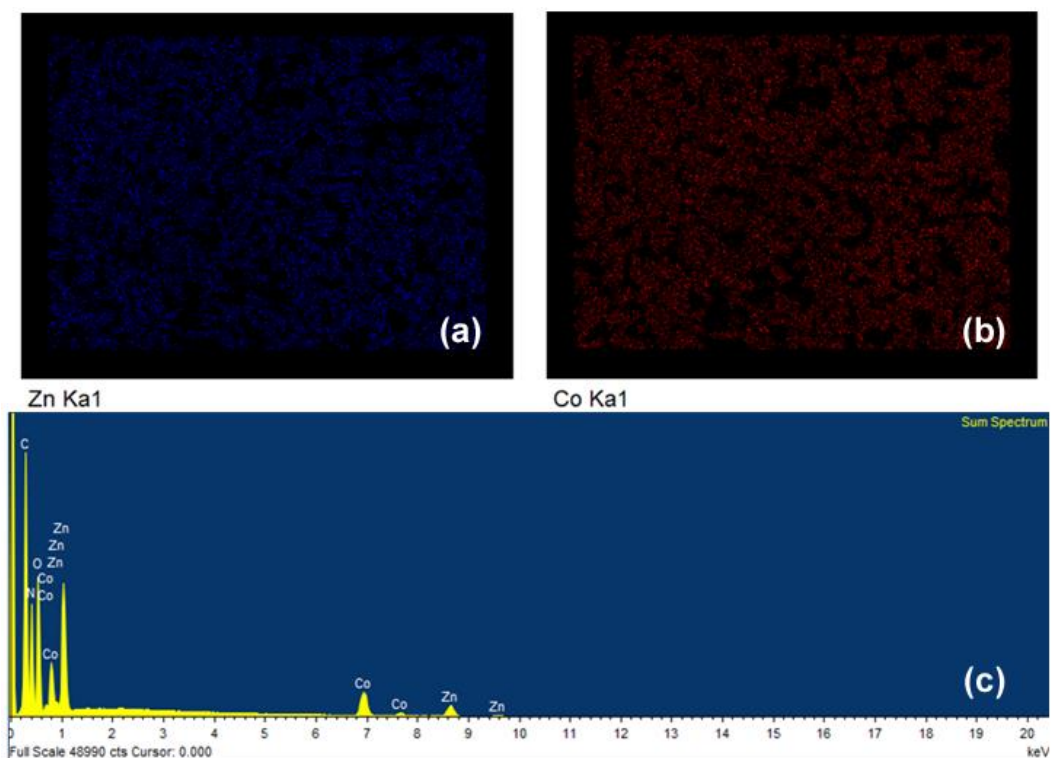
Appendix A3.4 View of the molecular building unit of framework 2 along c-axis.



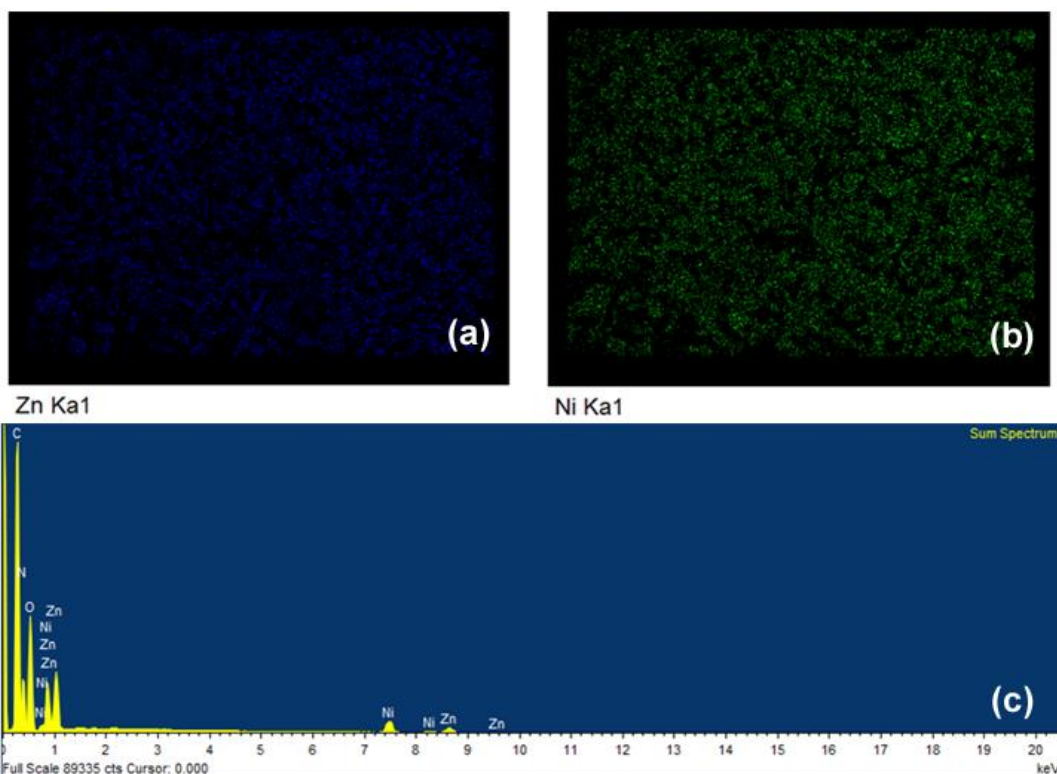
Appendix A3.5 FT-IR spectrum of compound 1.



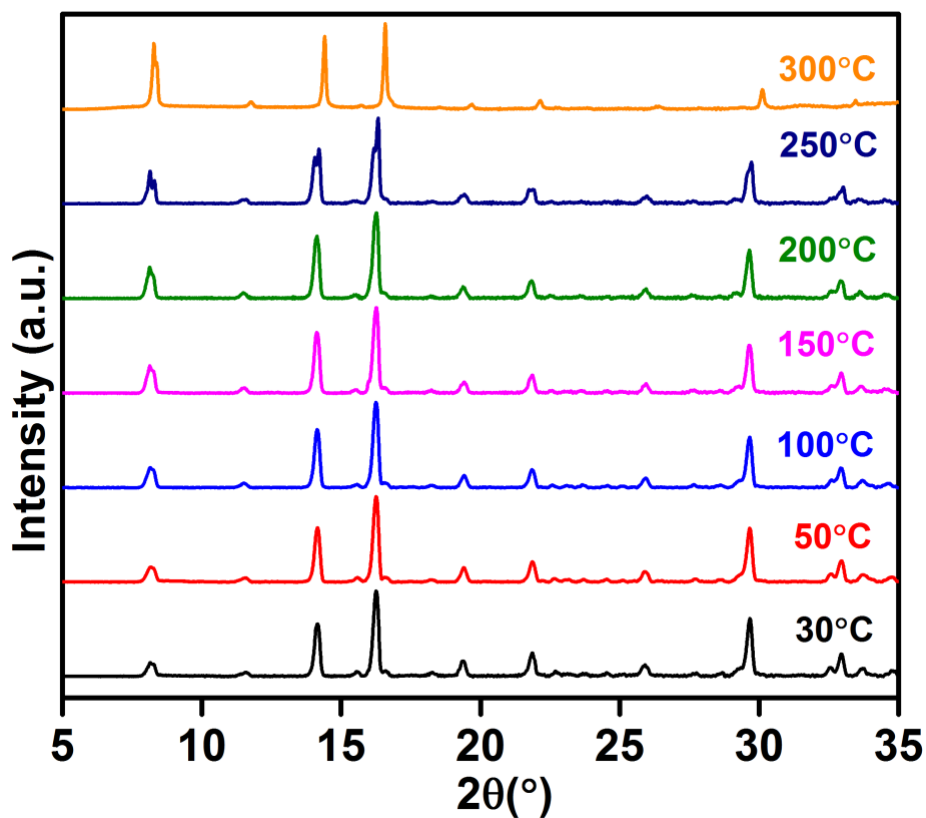
Appendix A3.6 FT-IR spectrum of compound 2.



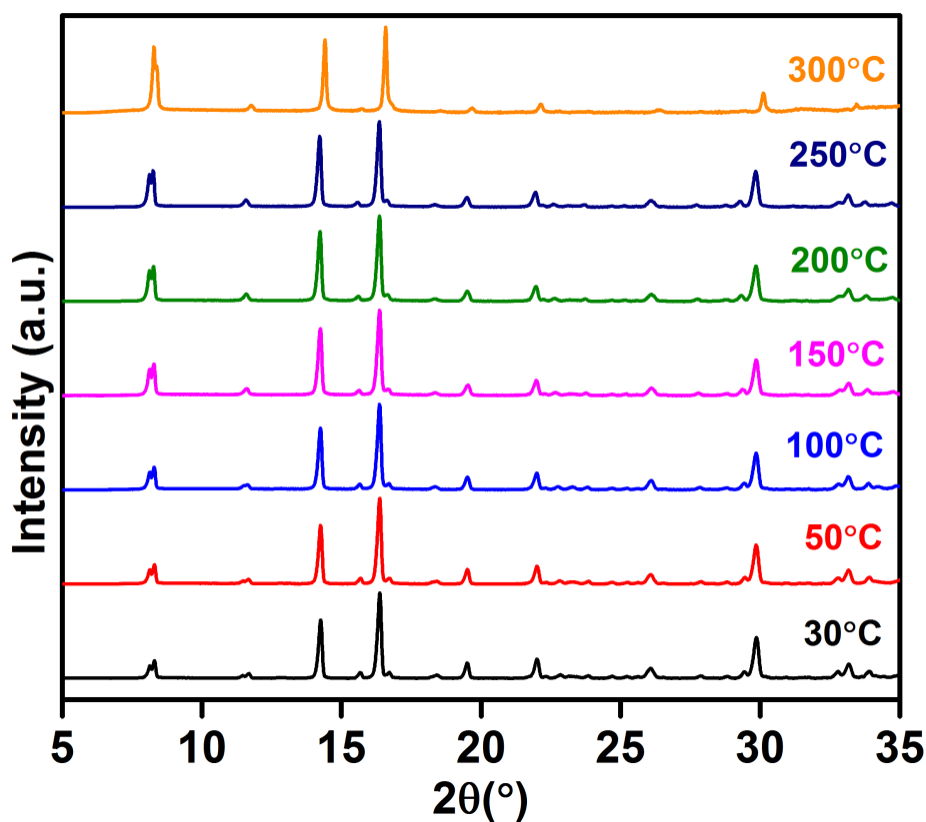
Appendix A3.7 Elemental mapping of compound 1 showing the presence of (a) Zn(II) and (b) Co(II) in the sample. (c) EDAX analysis plot for compound 1.



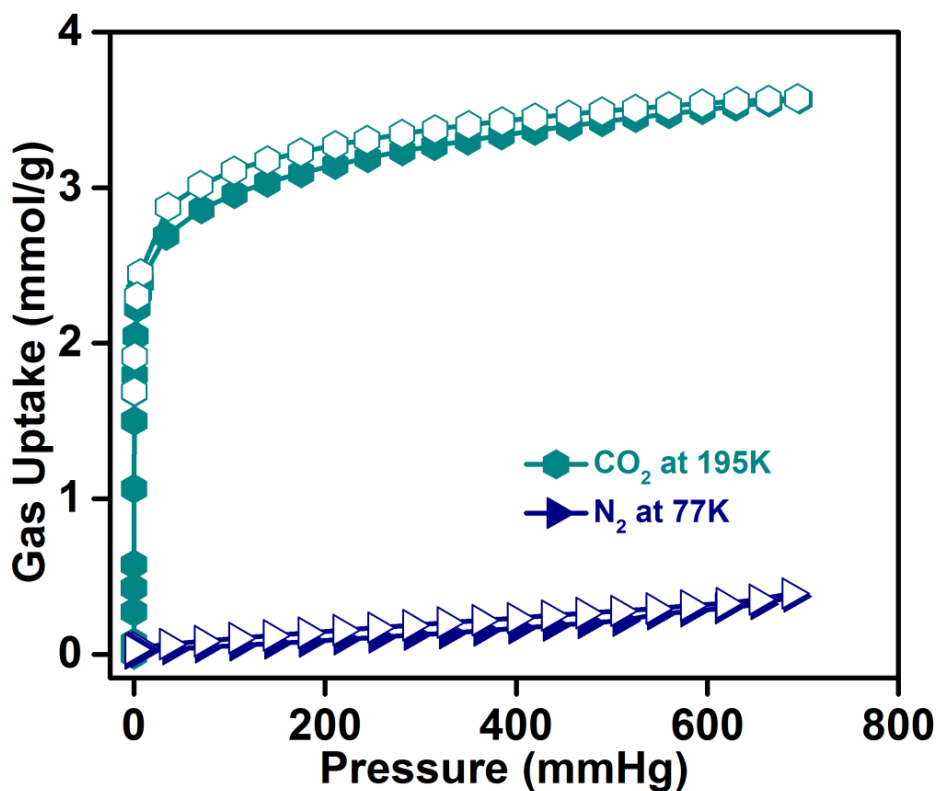
Appendix A3.8 Elemental mapping of compound 2 showing the presence of (a) Zn(II) and (b) Ni(II) in the sample. (c) EDAX analysis plot for compound 2



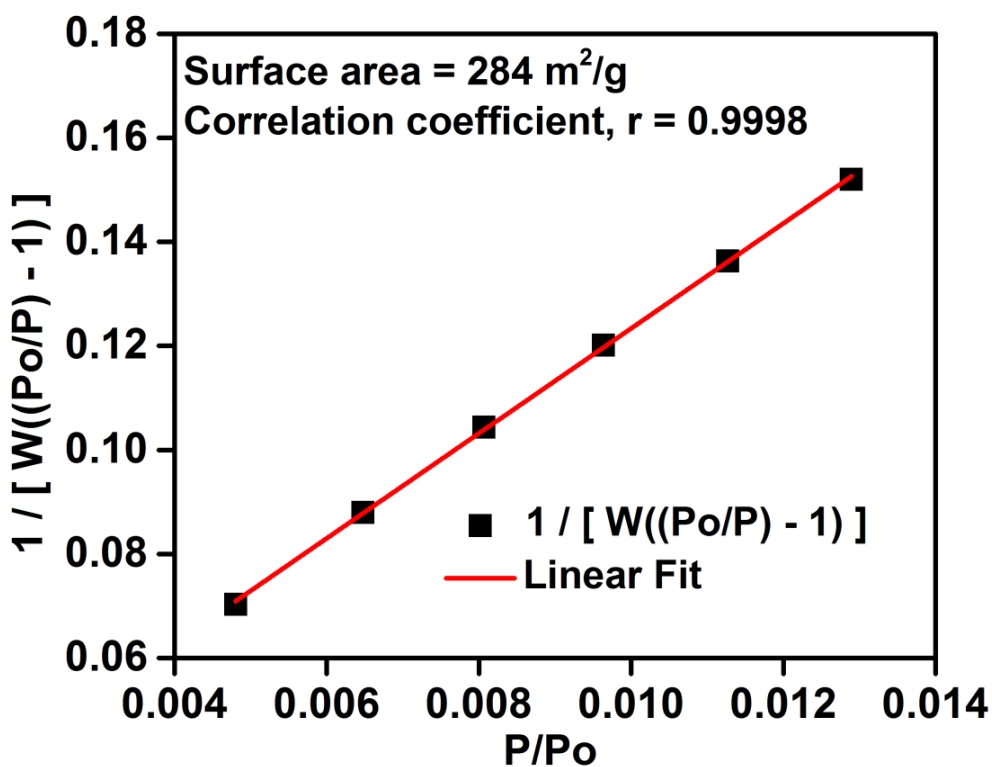
Appendix A3.9 Variable temperature PXRD plots for compound 1.



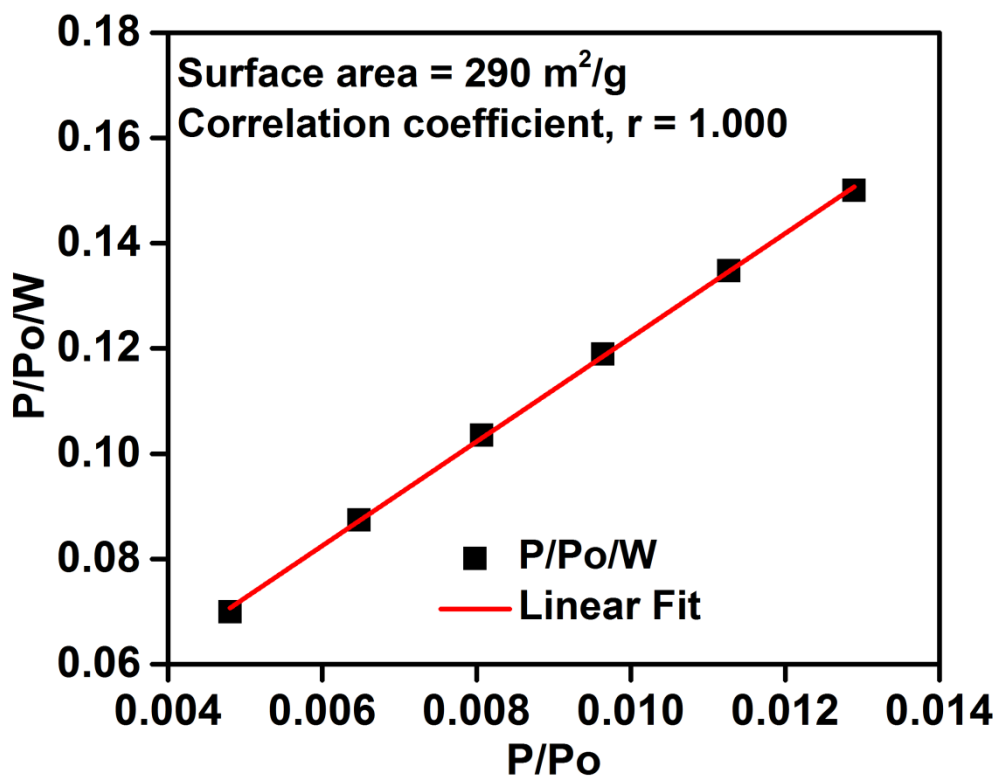
Appendix A3.10 Variable temperature PXRD plots for compound 2.



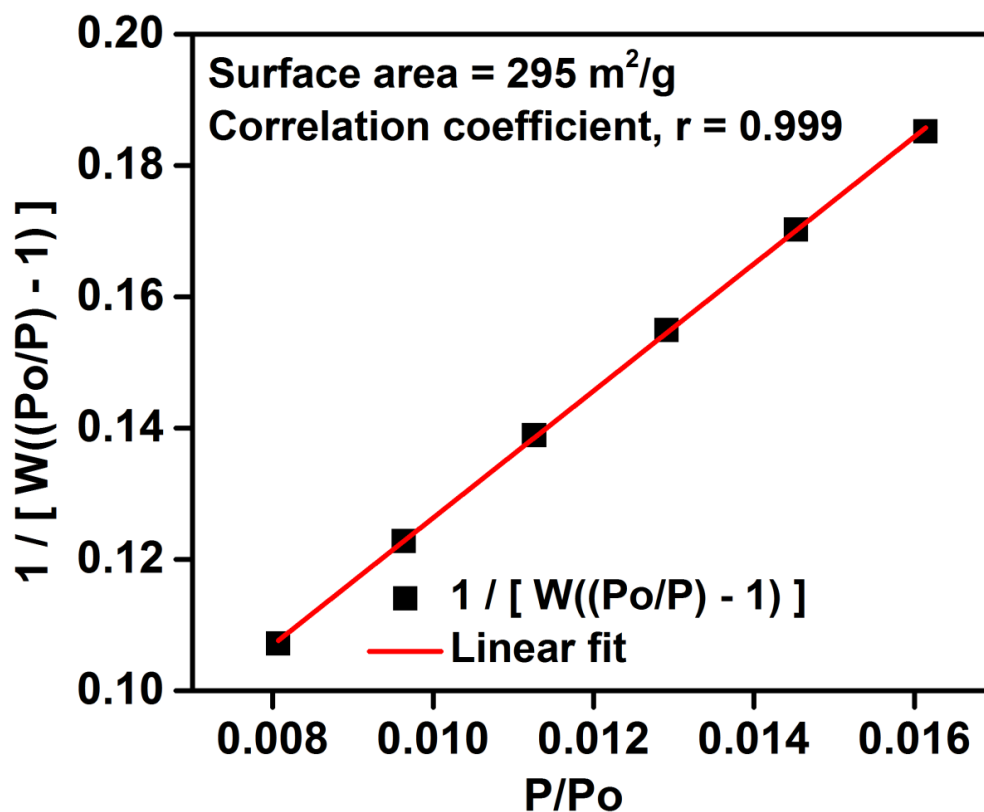
Appendix A3.11 Comparison of the CO₂ adsorption Isotherm (at 195 K) with the N₂ adsorption isotherm (at 77 K) for compound 1. Please note that the filled symbols shows the adsorption branch whereas the open symbols shows the desorption branch at a particular temperature.



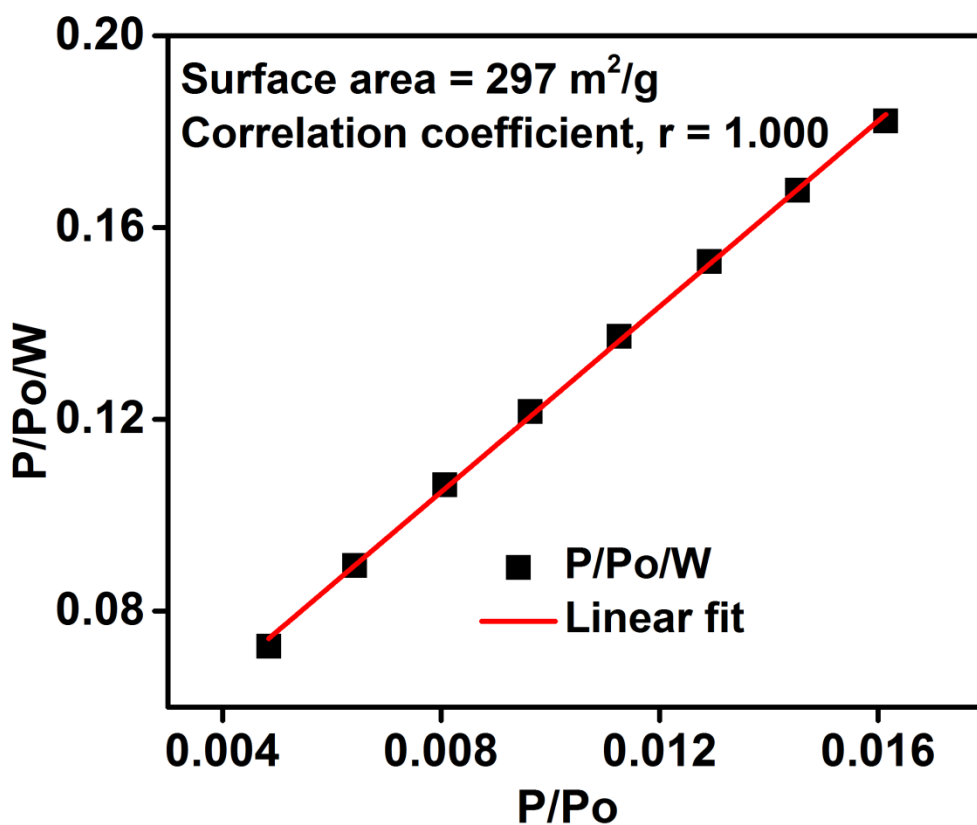
Appendix A3.12 BET surface area fit for compound 1.



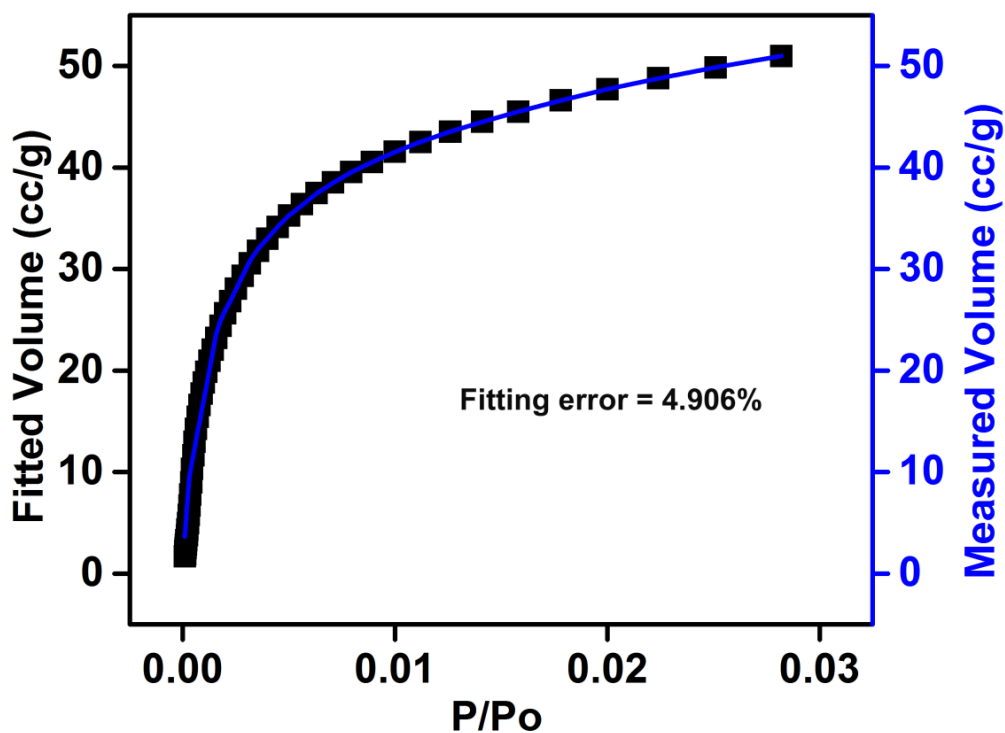
Appendix A3.13 Langmuir surface area fit for compound 1.



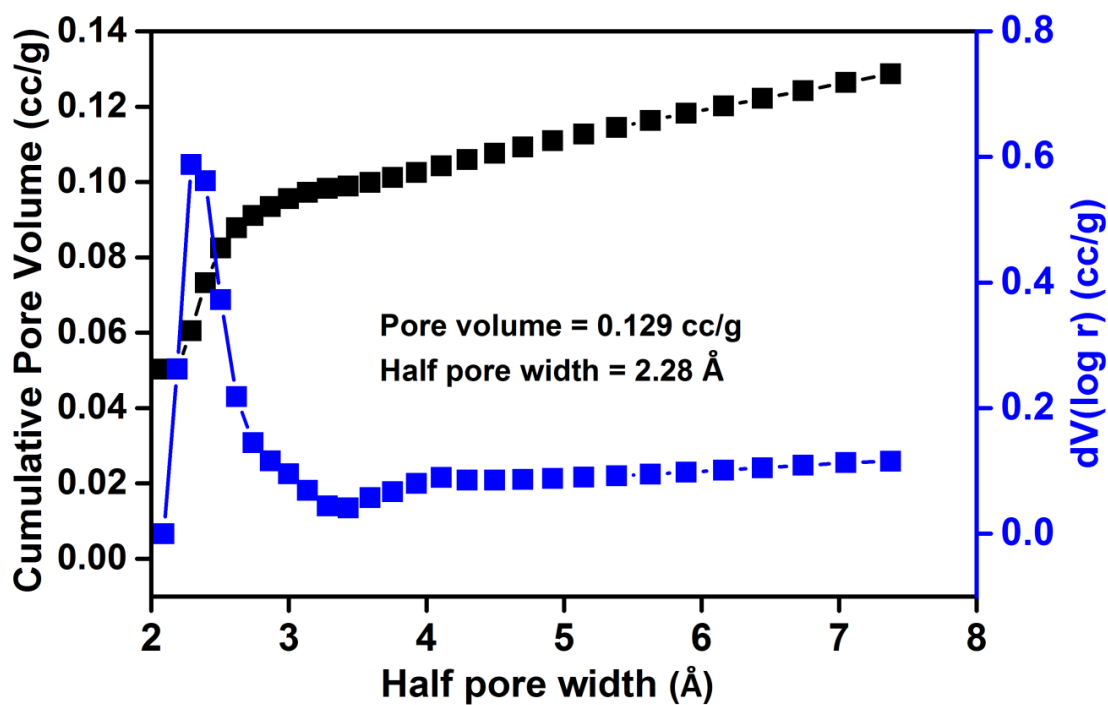
Appendix A3.14 BET surface area fit for compound 2.



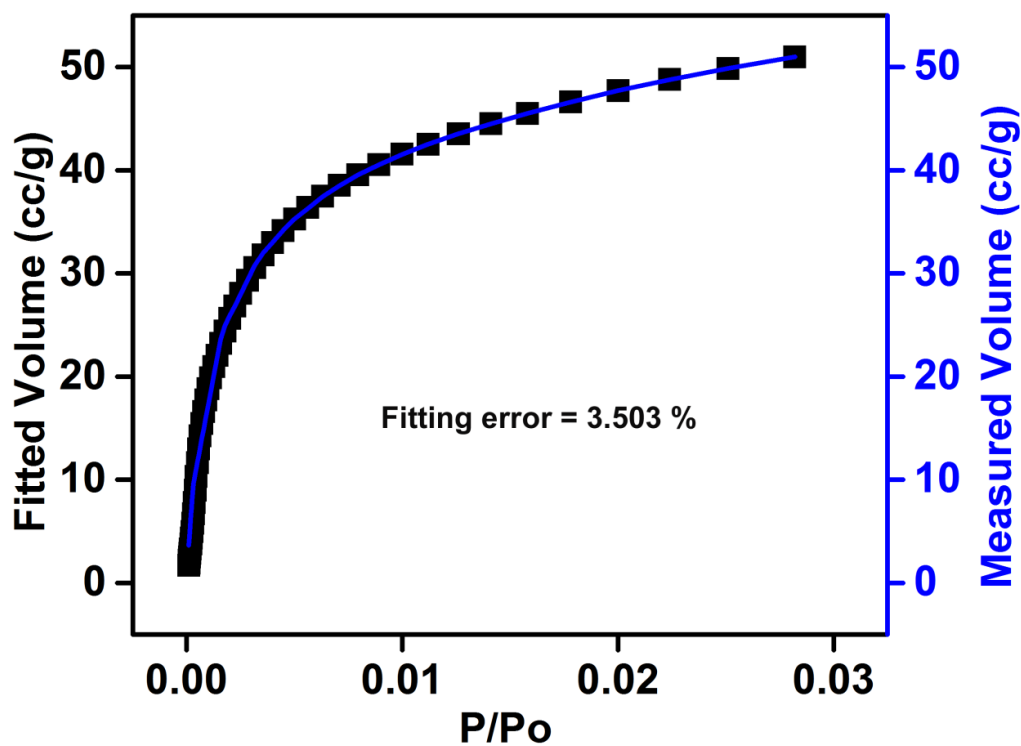
Appendix A3.15 Langmuir surface area fit for compound 2.



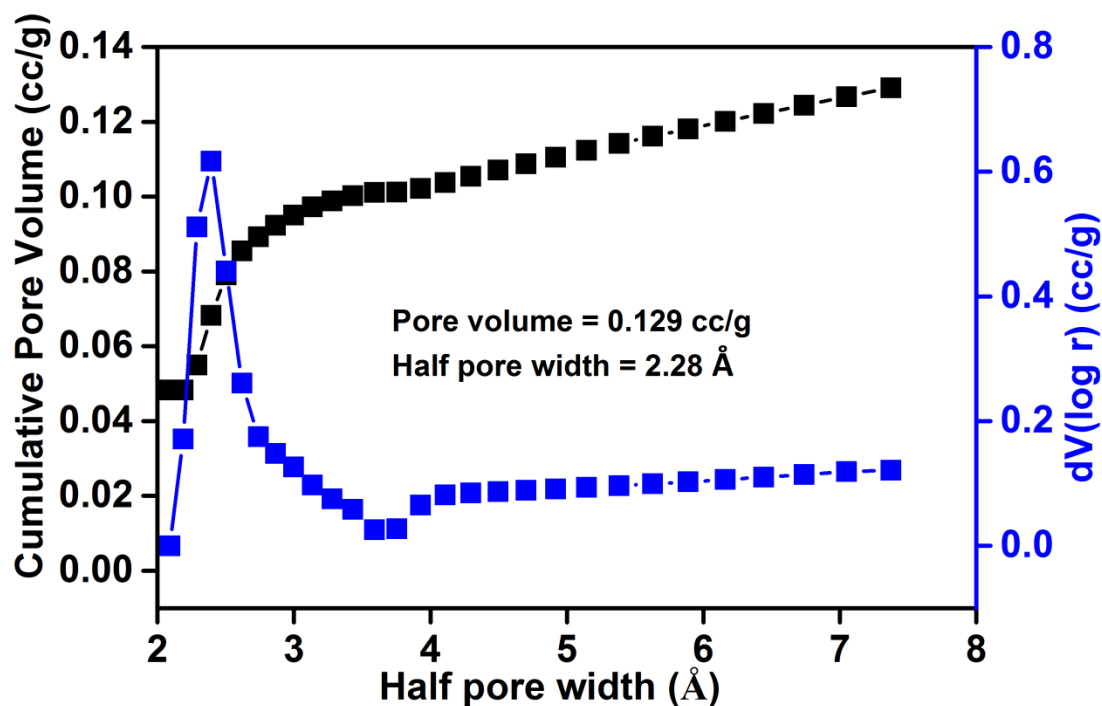
Appendix A3.16 DFT isotherm fitting for compound 1.



Appendix A3.17 DFT cumulative pore volume and pore size distribution for compound 1.



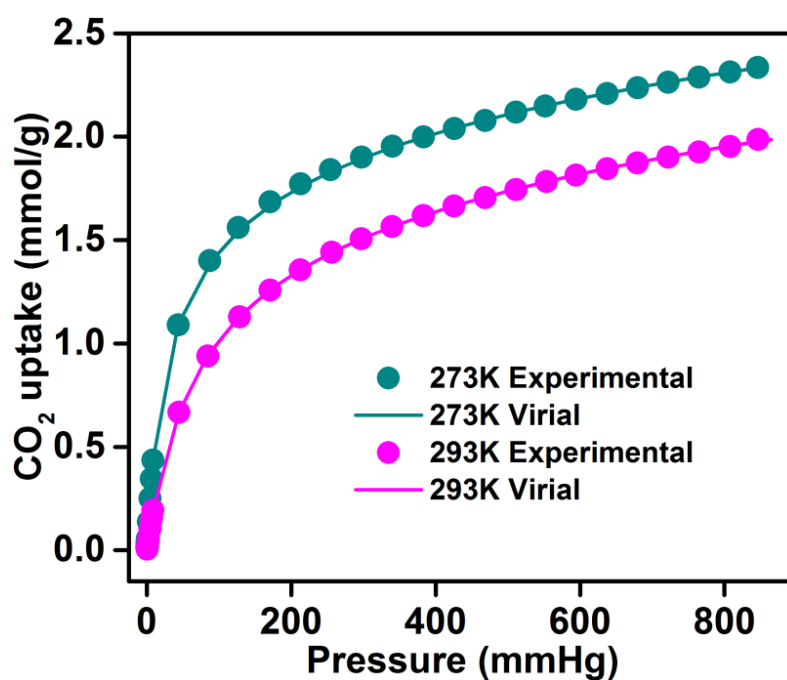
Appendix A3.18 DFT isotherm fitting for compound 2.



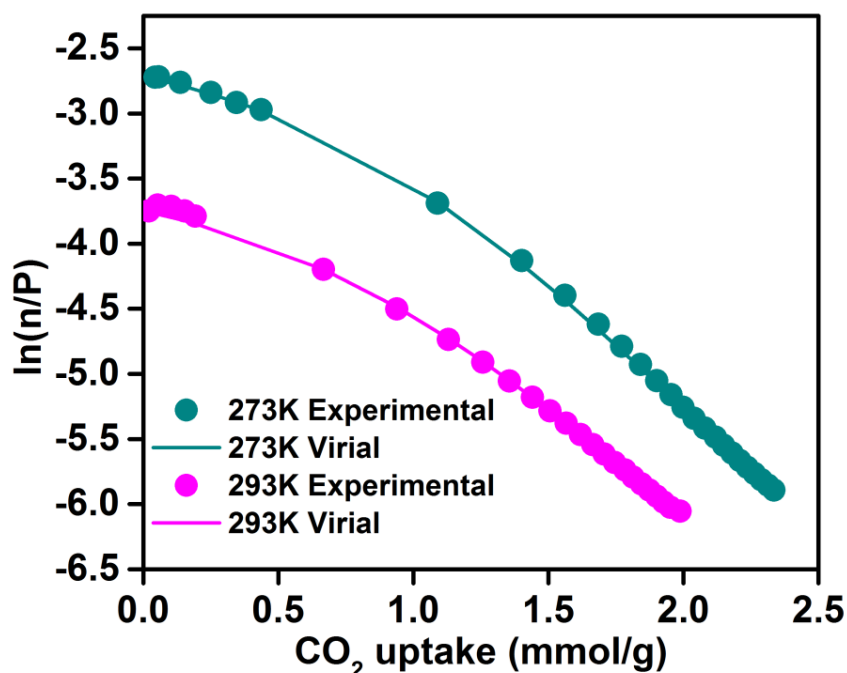
Appendix A3.19 DFT cumulative pore volume and pore size distribution for compound 2.

Appendix. A3.20 Virial coefficients for compound 1.

| | | | |
|----|--------------|----|--------------|
| A0 | -4139.008826 | B0 | 17.87642792 |
| A1 | 136.5179168 | B1 | -0.026355287 |
| A2 | -127.6615581 | B2 | 0.678335614 |
| A3 | 123.6486517 | B3 | -0.228202742 |
| A4 | 3.051418279 | B4 | -0.076304524 |



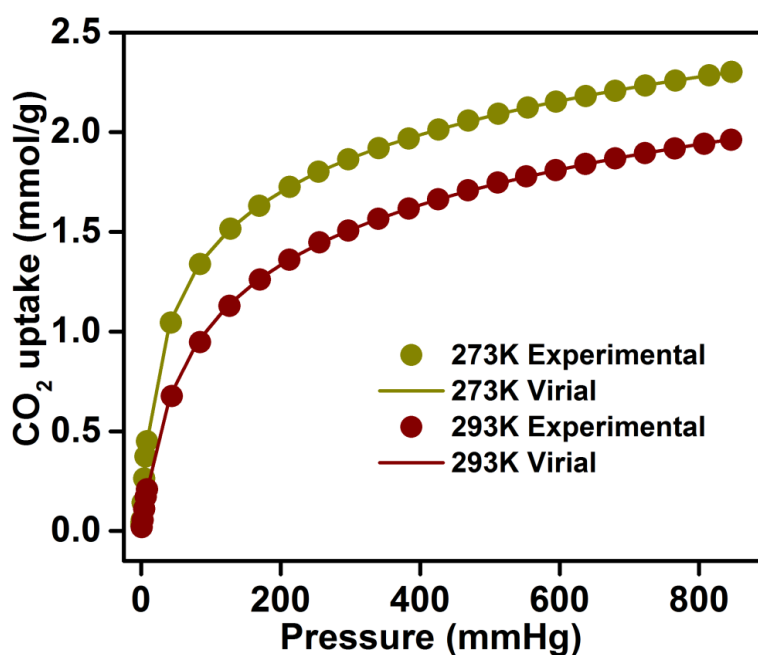
Appendix A3.21 Comparison of the experimental isotherms with isotherms obtained via virial model for compound 1 at 273 K and 298 K.



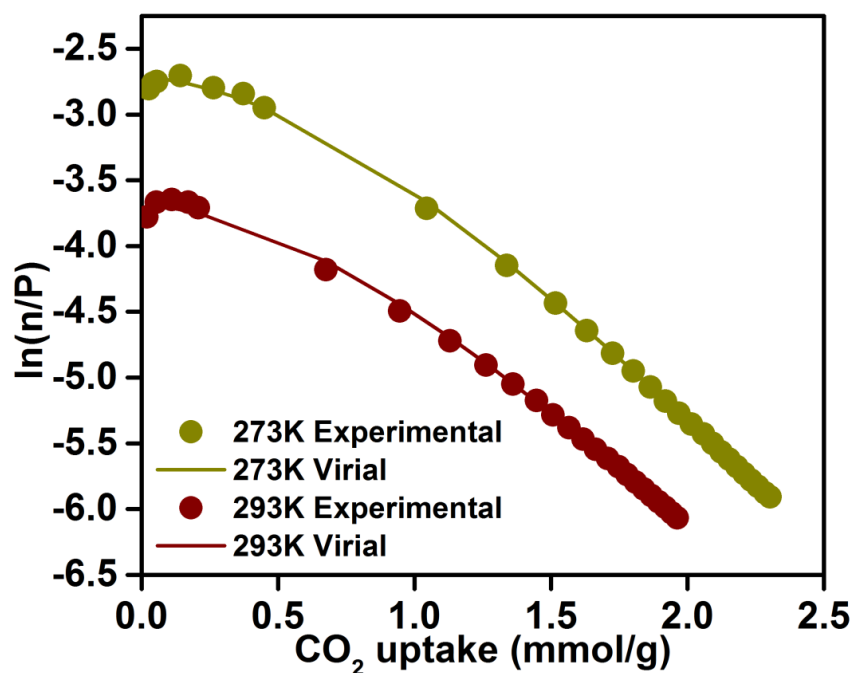
Appendix A3.22 Virial plots carried out using CO_2 isotherms collected at 273 K and 298 K for compound 1.

Appendix. A3.23 Virial coefficients for compound 2.

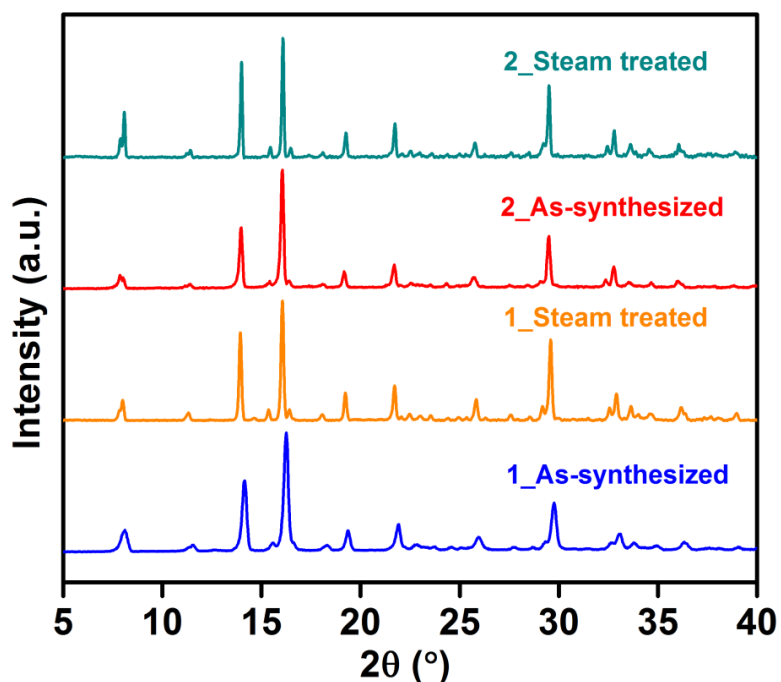
| | | | |
|----|--------------|----|--------------|
| A0 | -3916.379353 | B0 | 17.05345528 |
| A1 | 264.5168371 | B1 | -0.781912351 |
| A2 | -61.48719472 | B2 | 1.09344372 |
| A3 | 54.17410552 | B3 | -0.374909628 |
| A4 | 0.06185793 | B4 | 0.011311792 |



Appendix A3.24 Comparison of the experimental isotherms with isotherms obtained via virial model for compound 2 at 273 K and 298 K.



Appendix A3.25 Virial plots carried out using CO_2 isotherms collected at 273 K and 298 K for compound 2.

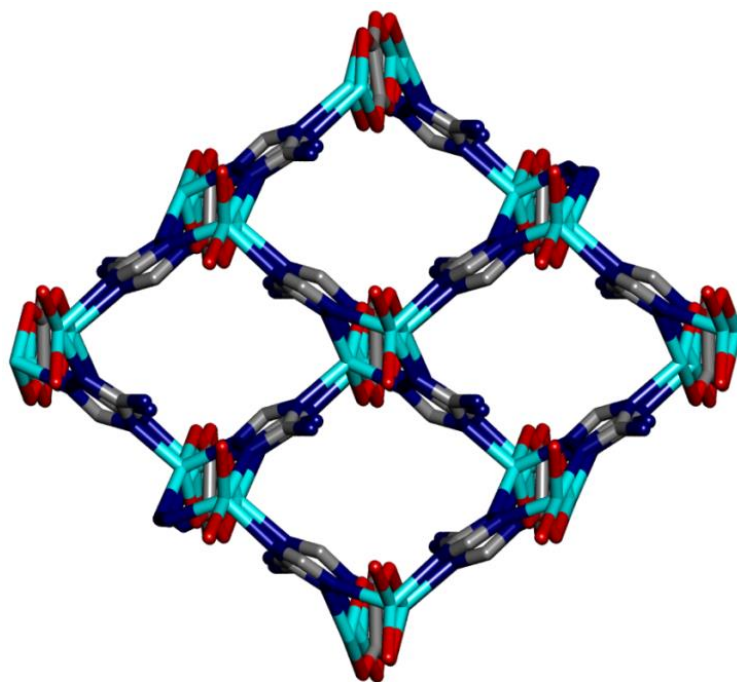


Appendix A3.26 PXRD patterns of the steam treated samples of compound 1 and compound 2, showing no substantial loss in the crystallinity after undergoing stream treatment for three days.

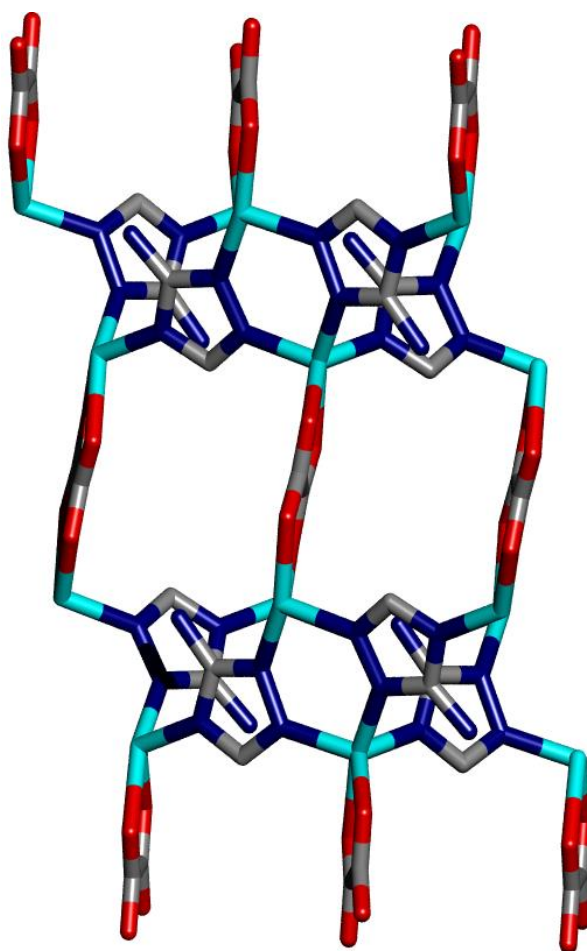
Appendix for Chapter 4

Appendix A4.1. Crystal data table for **2*/2**, **3** and **4**.

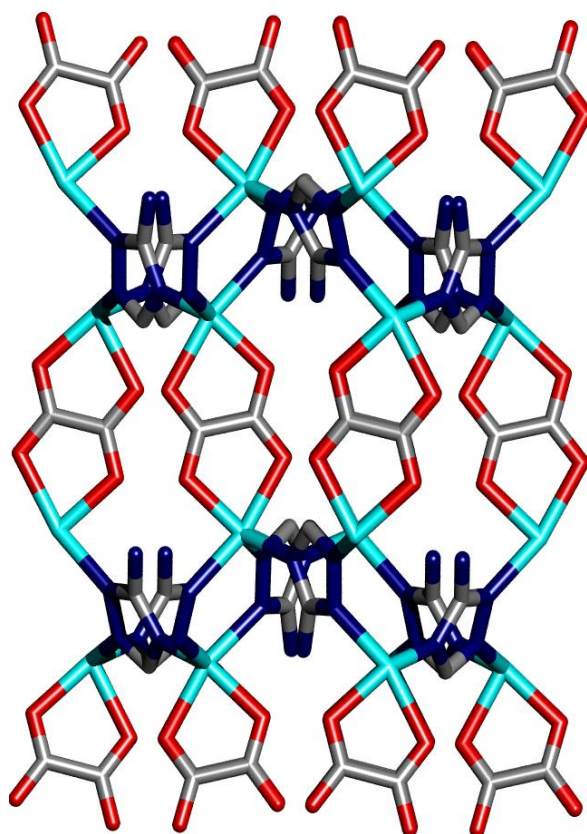
| | 2*/2 | 3 | 4 |
|--|---|--|--|
| Formula | $[\text{Zn}_2(\text{C}_2\text{O}_4)(\text{C}_2\text{N}_4\text{H}_3)_2](\text{H}_2\text{O})_x$ | $[\text{Zn}_2(\text{C}_2\text{O}_4)(\text{C}_2\text{N}_4\text{H}_3)_2](\text{C}_2\text{H}_5\text{OH})$ | $[\text{Zn}_2(\text{C}_2\text{O}_4)(\text{C}_2\text{N}_4\text{H}_3)_2](\text{C}_3\text{H}_7\text{OH})$ |
| FW | 400.93 g/mol | 429.99 | 445.02 |
| T , K | 100(2) | 100(2) | 200(2) |
| Crystal system, space group | Monoclinic, $P 2_1/c$ | Monoclinic, $P 2_1/n$ | Monoclinic, $P 2_1/n$ |
| a , Å | 17.576(4) | 8.9818(10) | 9.1877(4) |
| b , Å | 7.9026(16) | 13.8656(13) | 13.6108(6) |
| c , Å | 10.347(2) | 12.4104(12) | 12.5305(5) |
| β , deg | 100.213(7) | 105.360 | 104.6290(10) |
| V , Å ³ | 1414.4(5) | 1490.4(3) | 1516.16(11) |
| Z , Calculated density | 4, 1.883 g/cm ³ | 4, 1.916 g/cm ³ | 4, 1.950 g/cm ³ |
| μ , mm ⁻¹ | 4.533 | 4.351 | 4.301 |
| $F(000)$ | 792 | 860 | 896 |
| R_{int} | 0.0625 | 0.0925 | 0.0240 |
| Data/restraints/parameters | 2517 / 0 / 199 | 2952/ 13/ 208 | 2975/ 22/ 216 |
| Goodness-of-fit on F^2 | 1.047 | 1.188 | 1.055 |
| Final R indices [$I > 2\sigma(I)$] | $R1 = 0.1084$ $wR2 = 0.3081$ | $R1 = 0.0999$, $wR2 = 0.2087$ | $R1 = 0.0271$, $wR2 = 0.0712$ |
| Final R indices [all data] | $R1 = 0.1141$, $wR2 = 0.3127$ | $R1 = 0.1082$, $wR2 = 0.2127$ | $R1 = 0.0280$, $wR2 = 0.0719$ |



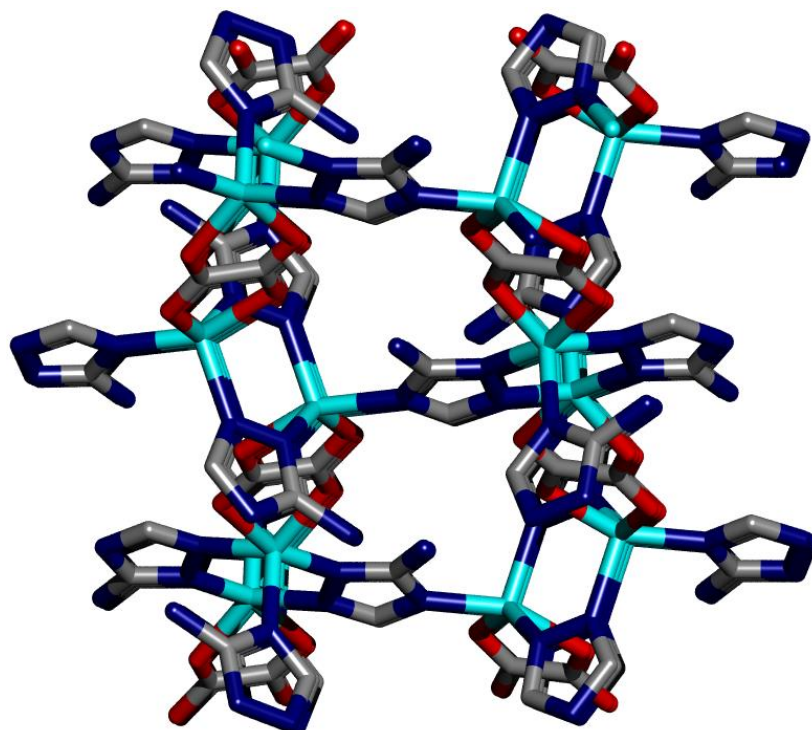
Appendix A4.2 Crystal structure view along a-axis for phase $2/2^*$.



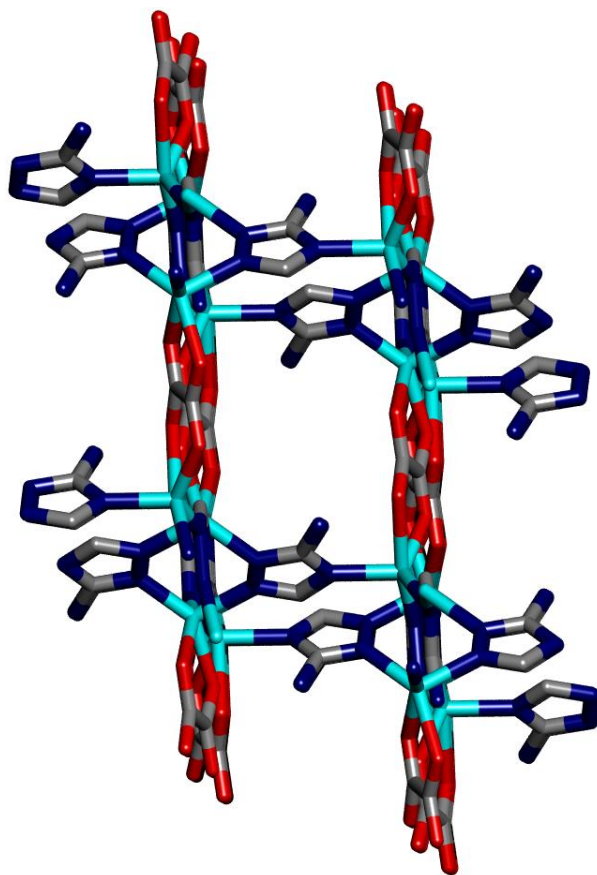
Appendix A4.3 Crystal structure view along b-axis for phase $2/2^*$.



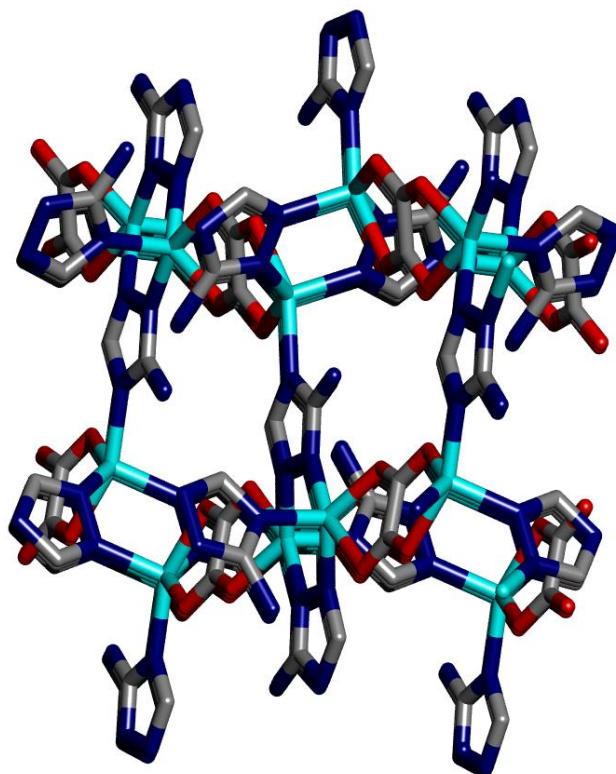
Appendix A4.4 Crystal structure view along c-axis for phase 2/2*.



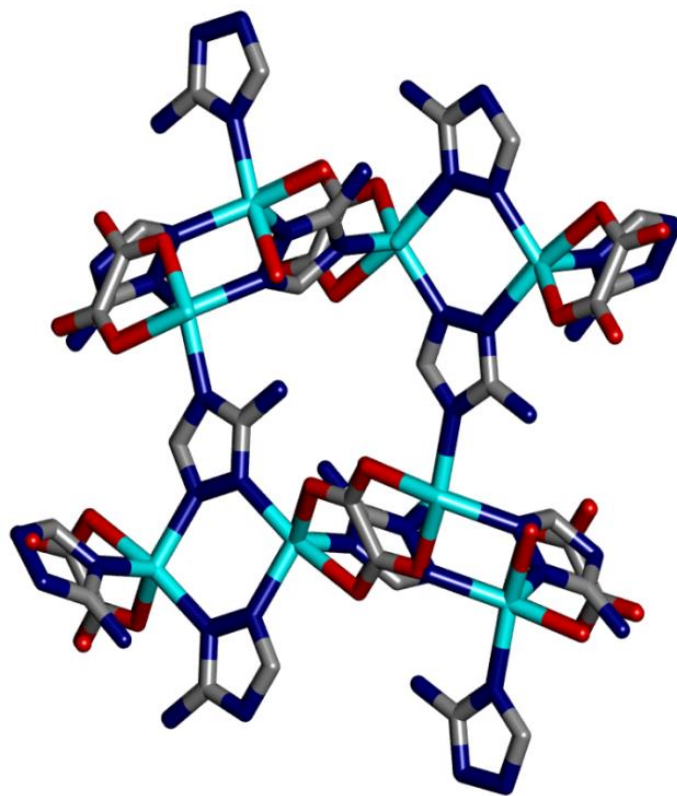
Appendix A4.5 Crystal structure view along a-axis for phase 3.



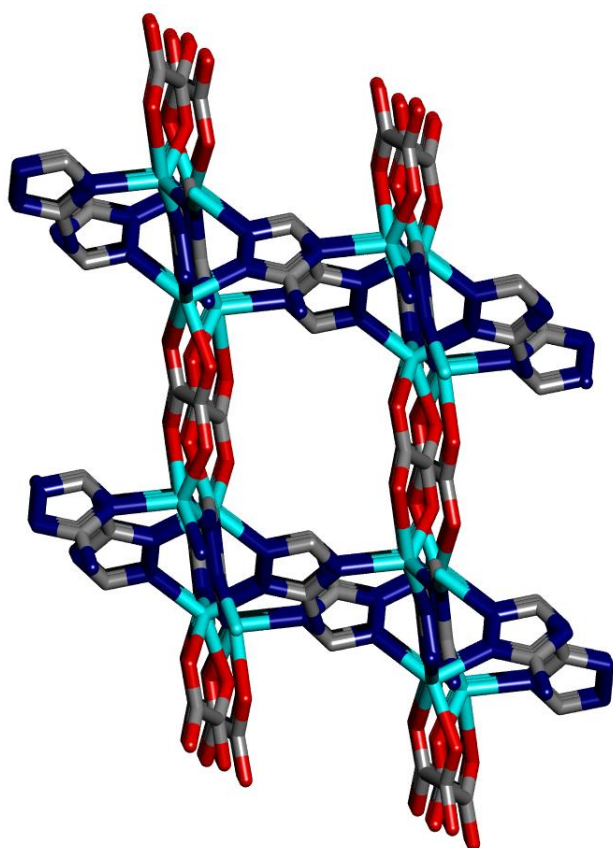
Appendix A4.6 Crystal structure view along b-axis for phase 3.



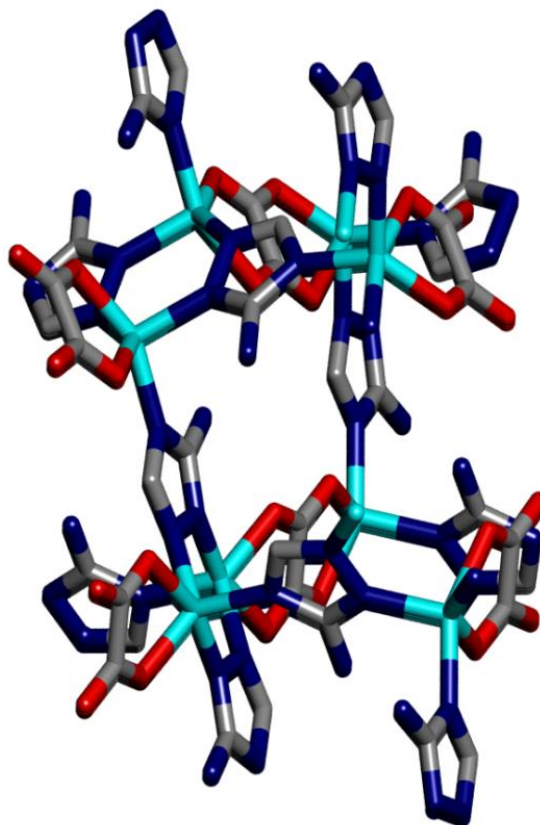
Appendix A4.7 Crystal structure view along c-axis for phase 3.



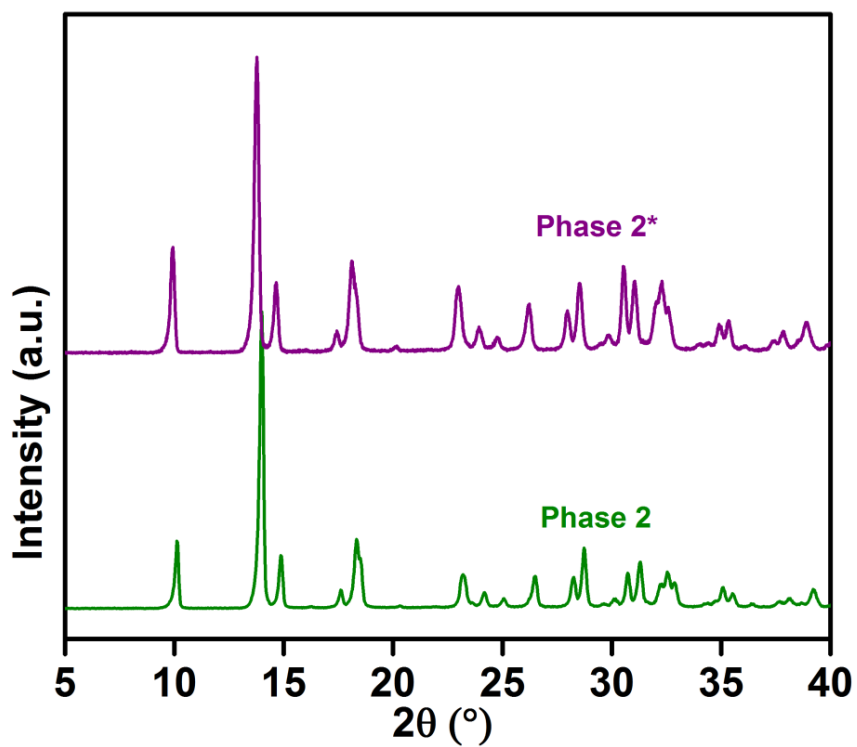
Appendix A4.8 Crystal structure view along a-axis for phase 4.



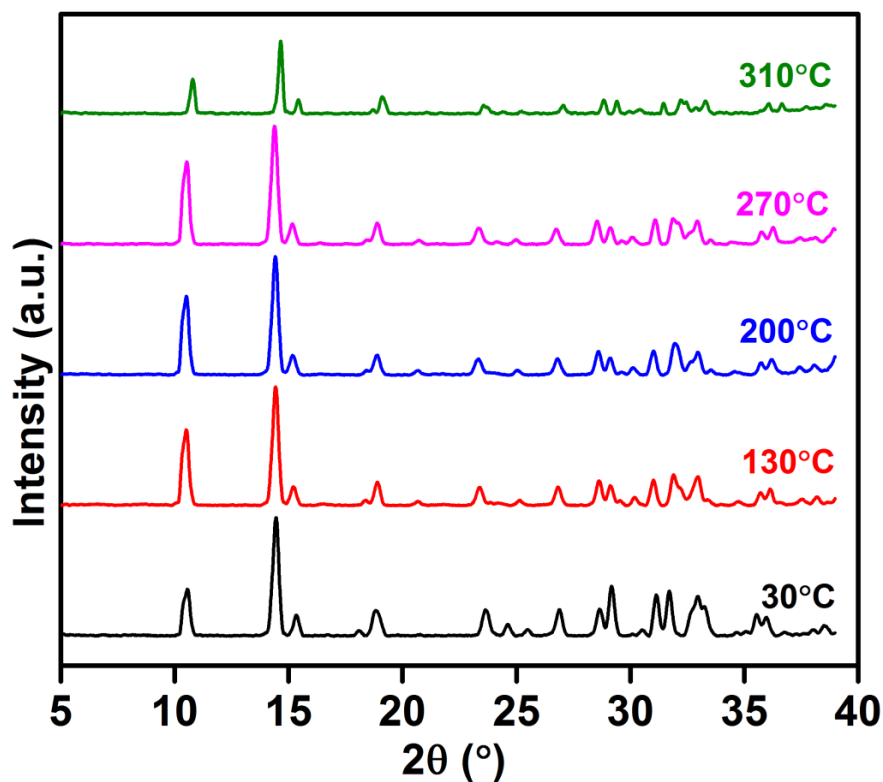
Appendix A4.9 Crystal structure view along b-axis for phase 4.



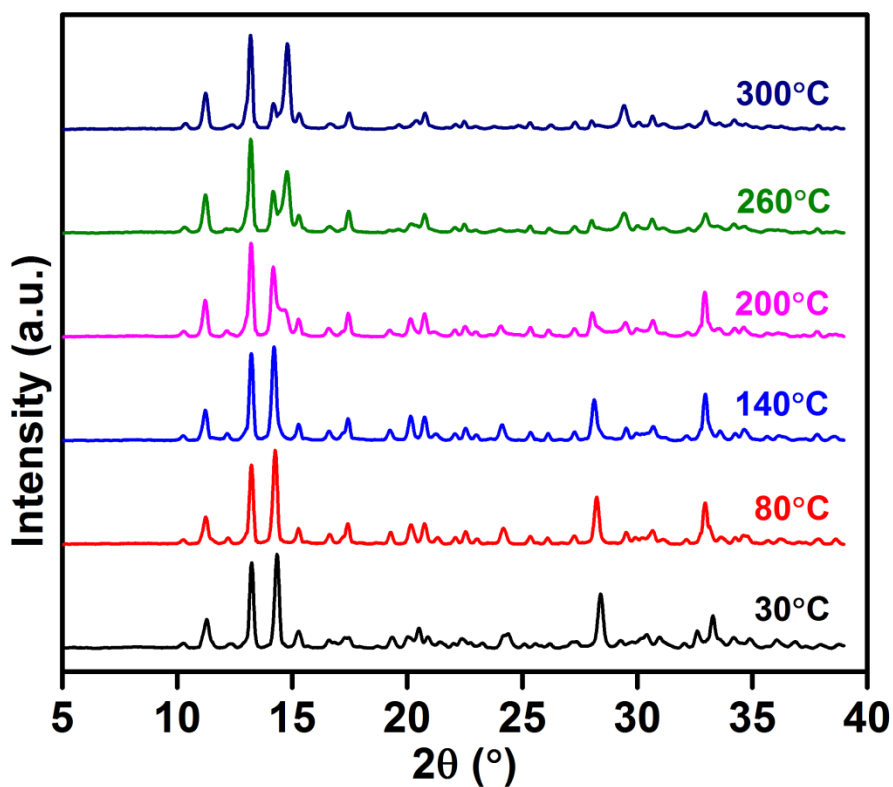
Appendix A4.10 Crystal structure view along c-axis for phase 4.



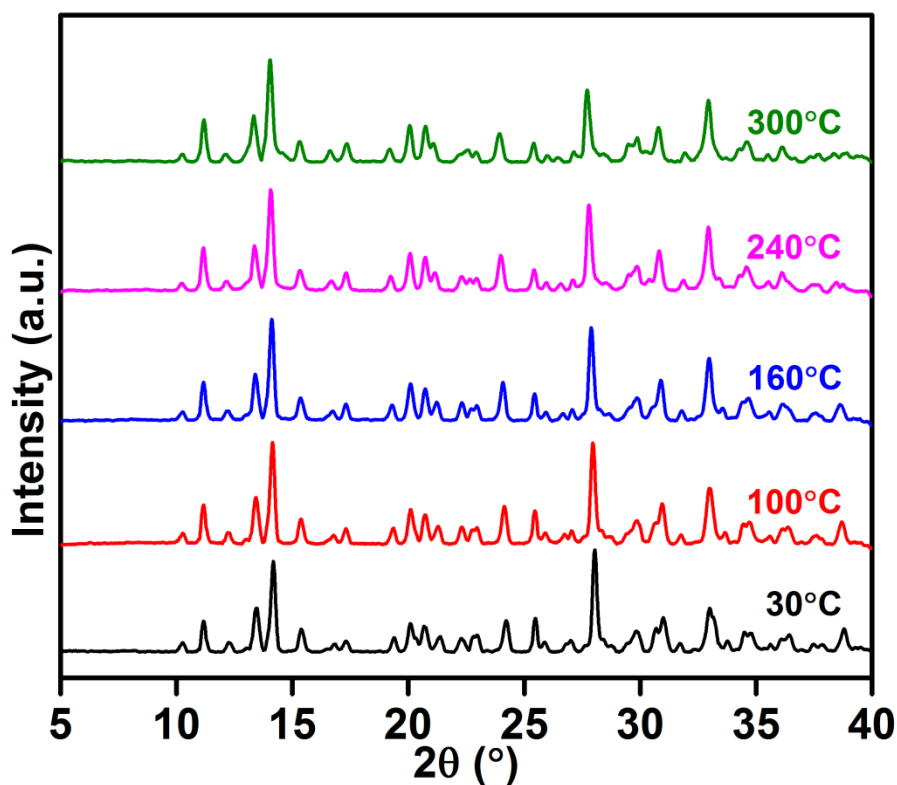
Appendix A4.11 PXRD comparison for MOFs 2 and 2*.



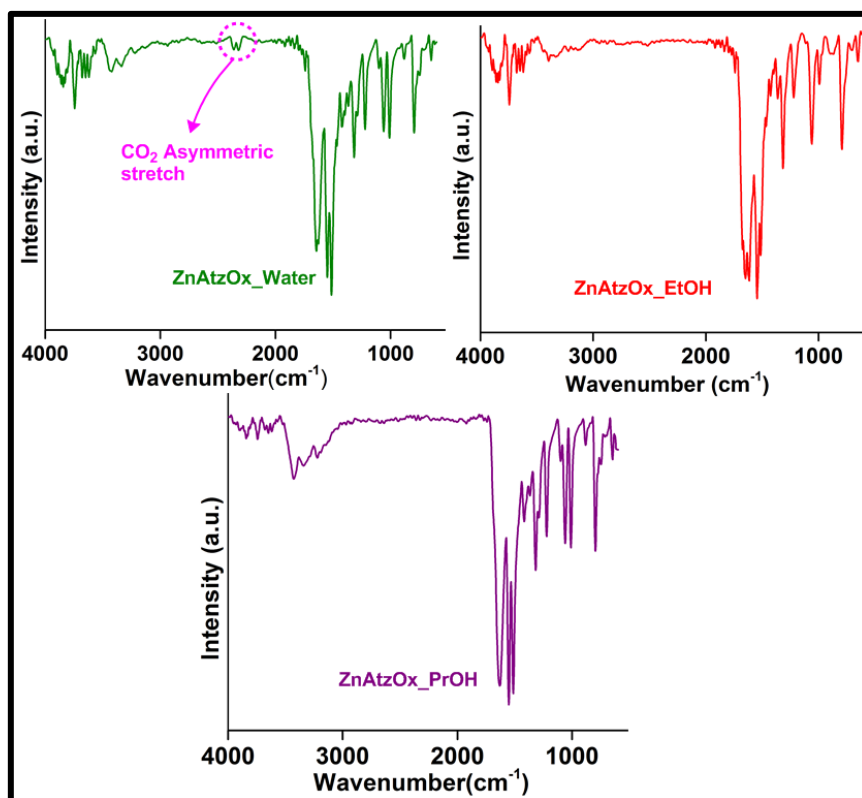
Appendix A4.12 Variable temperature PXRD plots for phase 2.



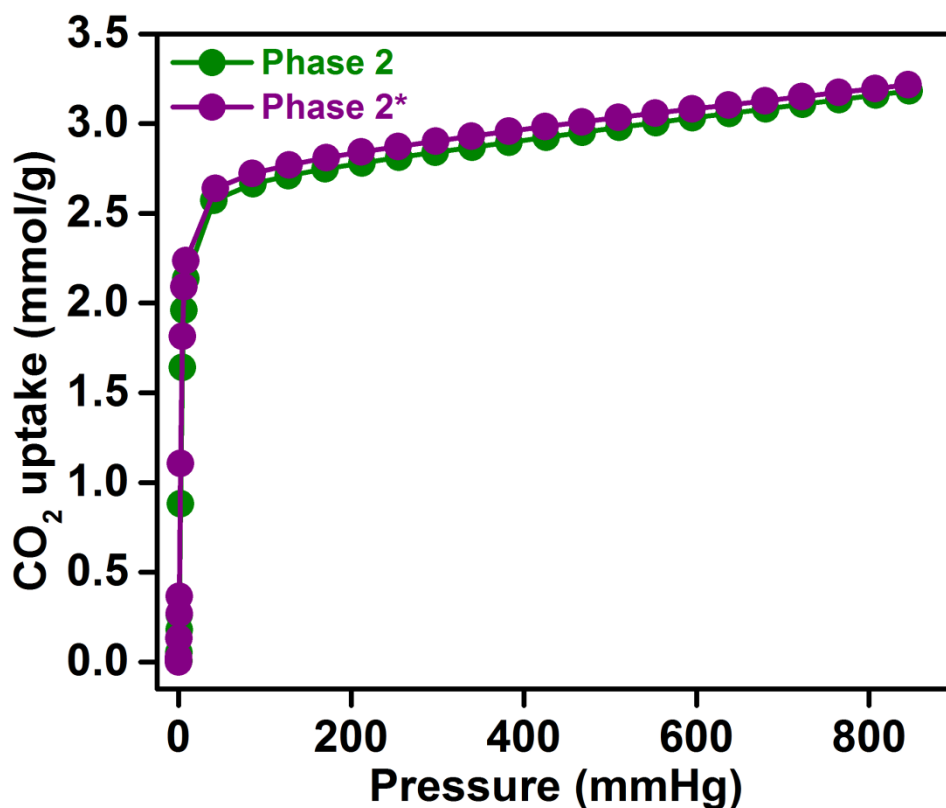
Appendix A4.13 Variable temperature PXRD plots for phase 3.



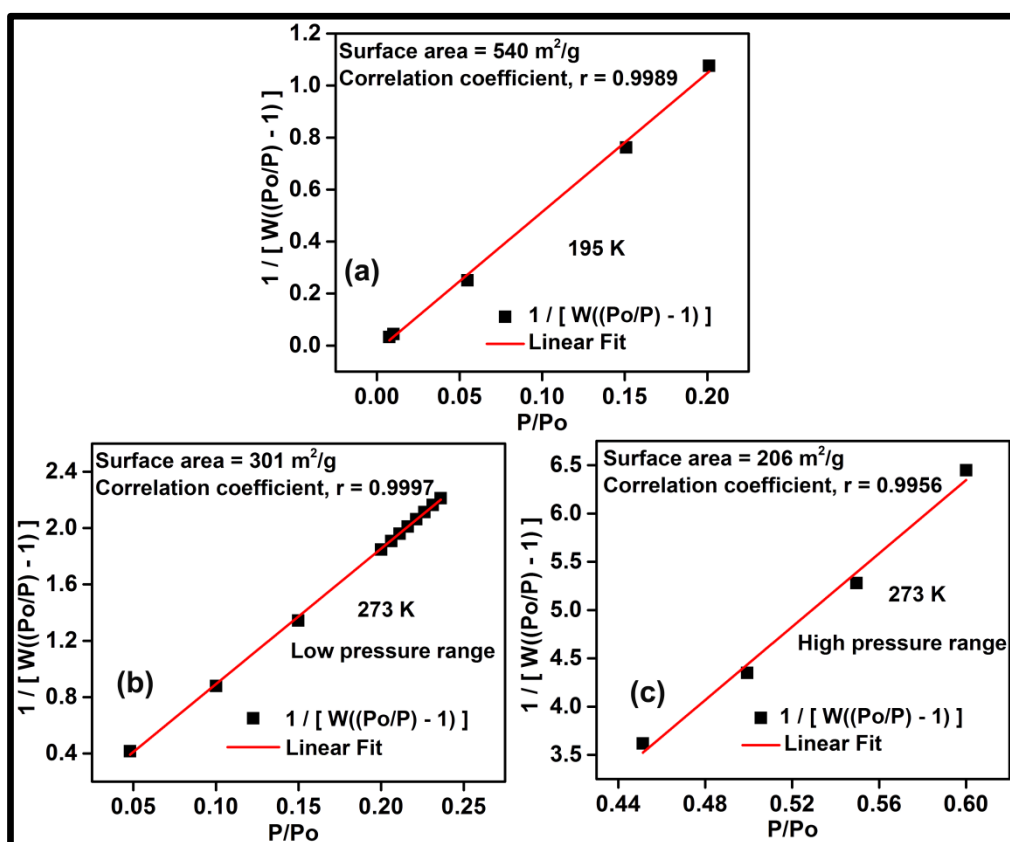
Appendix A4.14 Variable temperature PXRD plots for phase 4.



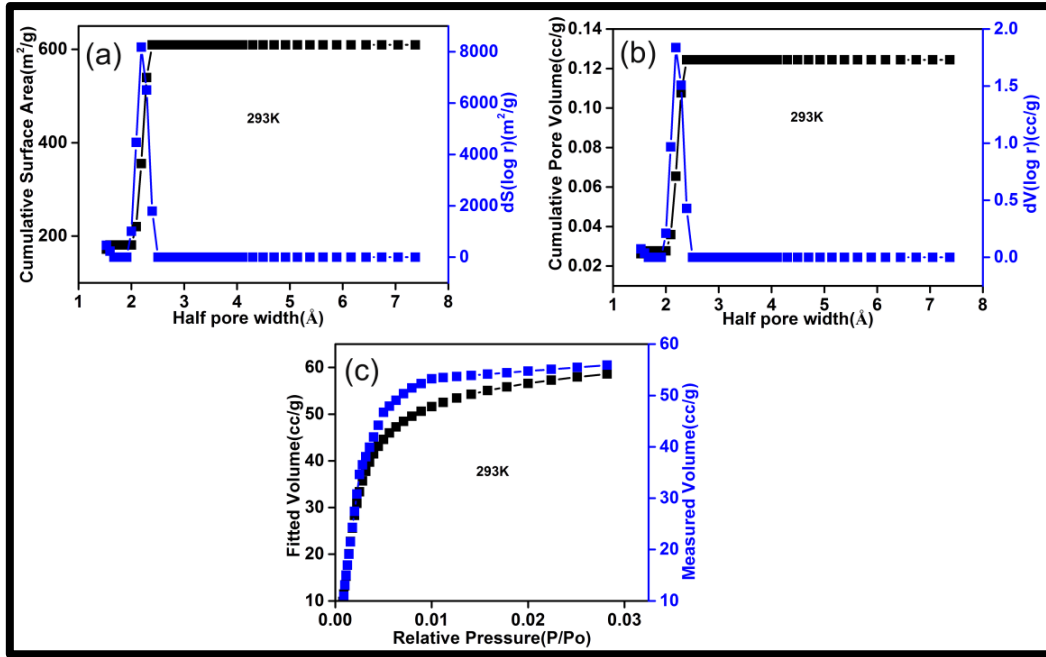
Appendix A4.15 Infra-red spectra of 2, 3 and 4 showing the characteristic bands corresponding to oxalate and Atz units. Infra-red spectra of 2 showing in addition the bands due to CO_2 are being adsorbed from air. The sample was not treated with any pure CO_2 .



Appendix A4.16 CO₂ adsorption isotherms for 2 and 2* at 303 K.



Appendix A4.17 BET surface area fits for 2 (top) from 195 K CO₂ isotherm and (bottom) 273 K CO₂ isotherm.



Appendix A4.18 DFT pore size evaluations and fit comparisons for **2**. Note: Due to the stepped nature of the 273 K isotherm DFT (273 K, Carbon) model could not be fitted to it. The 195 K data without steps is too far away from the 273 K model; hence the model has been fitted to 293 K data.

Dual site Langmuir-Freundlich parameters and calculations

Dual site Langmuir-Freundlich modeling of CO₂ isotherms of **2**:

The dual site model was carried out using the 273 K adsorption branch.

Fit parameters:

$$q \equiv q_A + q_B = \frac{q_{sat,A} b_A P^2}{1 + b_A P^2} + \frac{q_{sat,B} b_B P}{1 + b_B P}$$

$$b_A = b_{A0} \exp\left(\frac{E_A}{RT}\right); \quad b_B = b_{B0} \exp\left(\frac{E_B}{RT}\right);$$

$$b_{A0} = 4.78 \times 10^{-13} \text{ Pa}^{-2}$$

$$b_{B0} = 8.09 \times 10^{-12} \text{ Pa}^{-2}$$

$$E_A = 46.46 \text{ kJ/mol}$$

$$E_B = 32.65 \text{ kJ/mol}$$

$$q_{sat,A} = 2.12 \text{ mol/kg}$$

$$q_{sat,B} = 6.39 \text{ mol/kg}$$

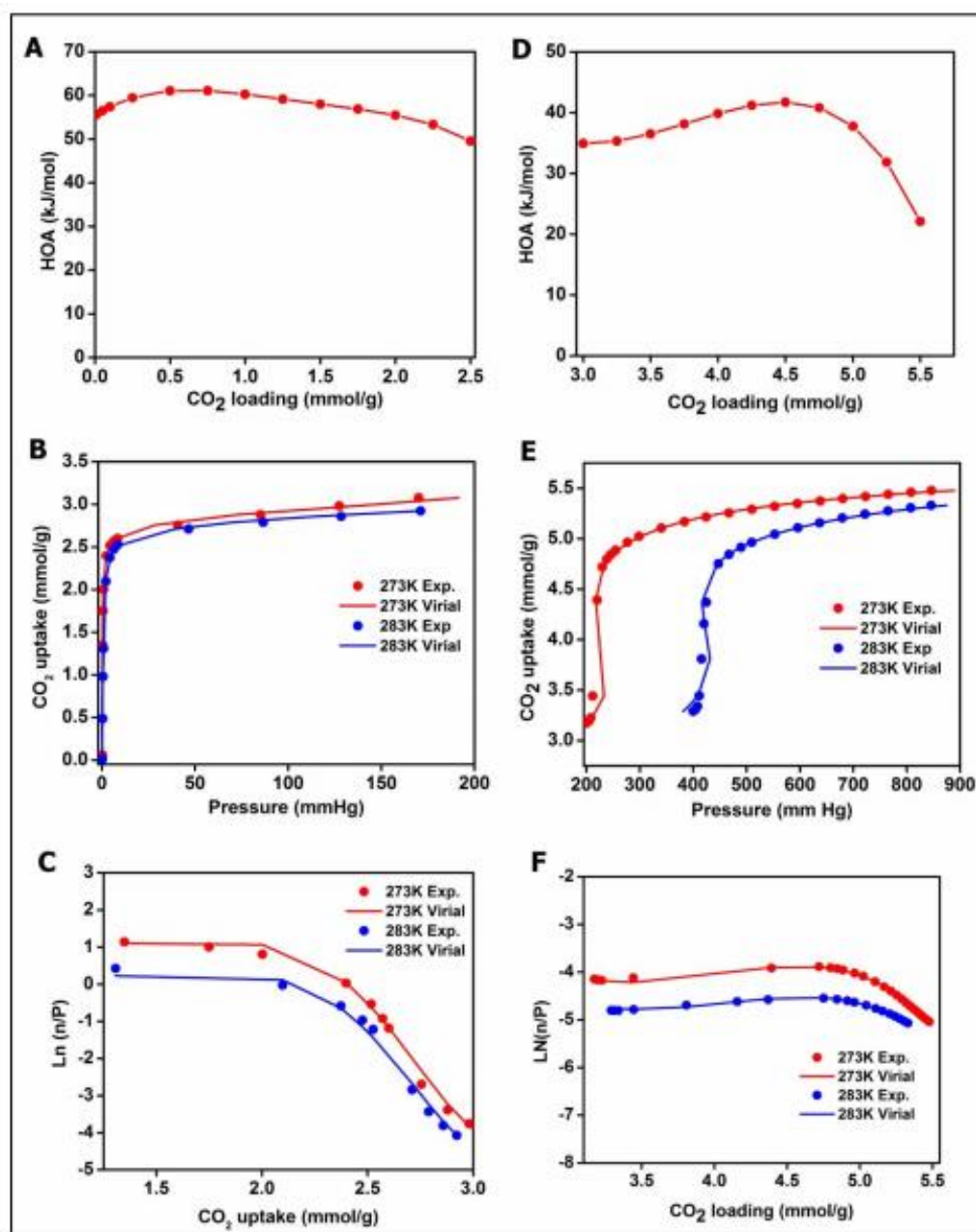
Appendix for Chapter 4

Appendix A4.19 CO₂ adsorption isotherm at 273 K showing measured and calculated uptakes from a dual site Langmuir-Freundlich model

| Pressure (Pascal) | Amount adsorbed (mmol/g) | Calculated Amount adsorbed | Pressure (Pascal) | Amount adsorbed (mmol/g) | Calculated Amount adsorbed | Pressure (Pascal) | Amount adsorbed (mmol/g) | Calculated Amount adsorbed |
|-------------------|--------------------------|----------------------------|-------------------|--------------------------|----------------------------|-------------------|--------------------------|----------------------------|
| 1.11972 | 0.000232 | 0.00032323 | 25626.57 | 3.144192 | 3.81814238 | 102027 | 5.439214 | 5.89181804 |
| 1.89286 | 0.000388 | 0.00293759 | 26197.66 | 3.158746 | 3.8457536 | 107728.4 | 5.459737 | 5.9754255 |
| 3.63909 | 0.001138 | 0.01051918 | 26745.27 | 3.174661 | 3.8719258 | 112801.5 | 5.478045 | 6.0454546 |
| 4.95876 | 0.001777 | 0.0192921 | 27289.63 | 3.193929 | 3.89765309 | | | |
| 6.02516 | 0.002286 | 0.02824791 | 27789.74 | 3.224946 | 3.92103915 | | | |
| 9.70424 | 0.004379 | 0.07127763 | 28238.63 | 3.441951 | 3.94182874 | | | |
| 12.21028 | 0.005451 | 0.11044401 | 29364.32 | 4.392018 | 3.99314446 | | | |
| 28.03299 | 0.061107 | 0.47487415 | 30642.98 | 4.719813 | 4.05005236 | | | |
| 57.59893 | 1.349134 | 1.16629683 | 31790.53 | 4.798821 | 4.09991834 | | | |
| 85.312 | 1.749272 | 1.54820701 | 32806.13 | 4.844228 | 4.14312949 | | | |
| 118.8769 | 2.002335 | 1.78703956 | 33971.56 | 4.885201 | 4.19168385 | | | |
| 311.0689 | 2.398433 | 2.09059692 | 36905.26 | 4.964237 | 4.30925951 | | | |
| 571.8303 | 2.517281 | 2.15464673 | 39813.83 | 5.024152 | 4.41967423 | | | |
| 865.7169 | 2.571411 | 2.19052754 | 45398.78 | 5.105884 | 4.6162006 | | | |
| 1131.49 | 2.600661 | 2.21703078 | 51135.2 | 5.167951 | 4.7993246 | | | |
| 5439.466 | 2.755094 | 2.57645091 | 56580.44 | 5.214911 | 4.95790172 | | | |
| 11345.24 | 2.879379 | 3.00290301 | 62270.4 | 5.255844 | 5.10974633 | | | |
| 16978.3 | 2.981254 | 3.35613001 | 67986.75 | 5.290705 | 5.24976323 | | | |
| 22667.29 | 3.077513 | 3.66966756 | 73657.78 | 5.320063 | 5.37772526 | | | |
| 23351.49 | 3.092728 | 3.70482487 | 79341.08 | 5.347433 | 5.49627008 | | | |
| 23931.03 | 3.105879 | 3.7342069 | 85043.16 | 5.373357 | 5.60652104 | | | |
| 24492.24 | 3.118643 | 3.76231926 | 90690.04 | 5.39667 | 5.70803465 | | | |
| 25073.78 | 3.131161 | 3.79110356 | 96360.24 | 5.418129 | 5.80306892 | | | |

Virial Analysis for evaluation of Heat of Adsorption (HOA) for CO₂ in 2:

HOA calculations employing virial model proved extremely difficult owing to the stepped nature of the isotherm. However, a two site fit could be carried out and it yielded an HOA of 60 kJ/mol for the low zero-loading adsorption sites, while it presented a value of 46 kJ/mol for the second site. This is much higher than the values obtained from the dual site model discussed earlier. We remark, for this unusual gate opening case in an ultra-microporous rigid framework, the dual site model seemed to be more realistic. This is because comparing the abruptness of the low pressure CO₂ uptake between **1**(ZnAtzOx_MeOH) and **2**(ZnAtzOx_Water), it can be expected that **2** would have relatively higher interactions, but is unlikely to be possessing an interaction that is 20 kJ/mol higher for **2**. Or in other words, the initial slope of CO₂ adsorption isotherm would have been expected to be much steeper for **2** if it had to have an HOA as high as 60 kJ/mol.



Appendix A4.20 HOA plots and associated Virial analysis for 2.

Appendix A4.21 Chart showing the CO₂ and N₂ uptakes of different ultra-microporous MOFs at pressures relevant to vacuum swing adsorption based CO₂/N₂ separation from flue gas (85N₂:15CO₂) compositions.

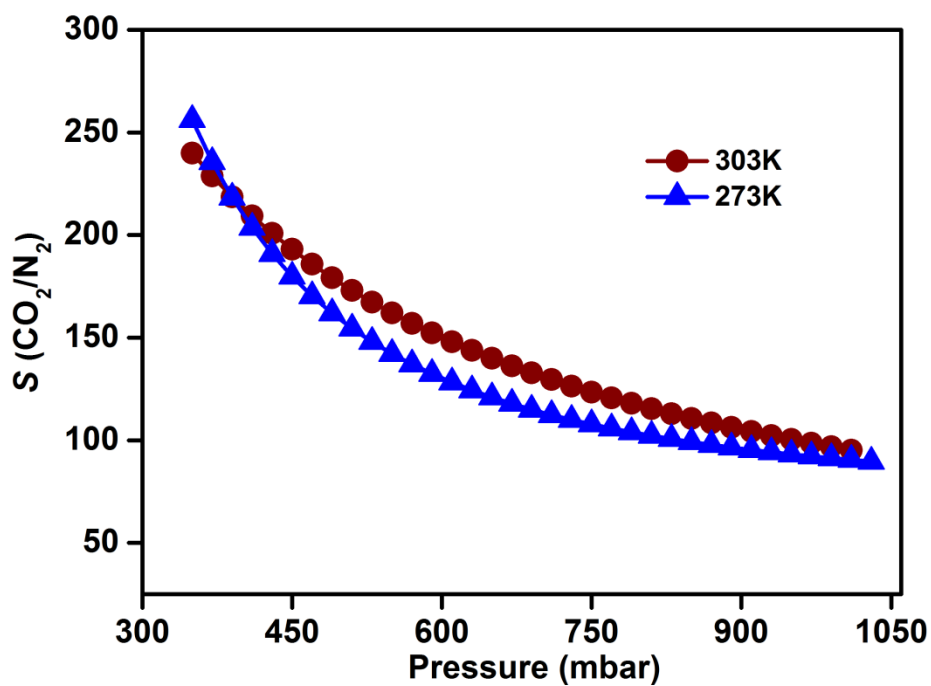
| Metal Organic framework | CO ₂ Uptakes (mmol/g) (0.15 bar) | N ₂ Uptakes (mmol/g) (0.85 bar) | Temperature | References |
|---|---|--|-------------|------------------|
| UTSA-16 | 2.64 | 0.05 | 296 | 40 |
| SIFSIX-3-Zn | 2.43 | 0.14 | 298 | 38 |
| SIFSIX-3-Cu-i | 2.38 | 0.16 | 298 | 38 |
| Zn ₂ (atz) ₂ (ox) | 2.05 | -- | 298 | 36,37 |
| MAF-66 | 1.25 | 0.030 | 298 | 10 |
| SIFSIX-3-Cu | 0.31 | 0.10 | 298 | 41 |
| [Cu(bpy-1)2(SiF6)] | 0.69 | 0.15 | 298 | 42 |
| SNU-50 | 0.68 | -- | 298 | 43 |
| IISERP-MOF2 | 1.62 | 0.008 | 303 | 44 |
| IISERP-MOF4 | 0.64 | 0.008 | 303 | 45 |
| IISERP-MOF5 | 0.61 | 0.009 | 303 | 45 |
| IISERP-MOF6 | 0.63 | 0.008 | 303 | 45 |
| IISERP-MOF7 | 0.52 | 0.007 | 303 | 45 |
| IISERP-MOF8 | 0.56 | 0.007 | 303 | 45 |
| IISERP-MOF9 | 0.59 | 0.009 | 303 | 45 |
| CoHatzOx_MeOH | 0.43 | 0.03 | 298 | Chapter 2 |
| ZnCo-BMMOF | 0.92 | 0.10 | 303 | Chapter 3 |
| ZnNi-BMMOF | 0.96 | 0.08 | 303 | Chapter 3 |
| ZnATzOx_Water, 2, (This work) | 2.70 | 0.1 | 303 | Chapter 4 |

Ideal Adsorbed Solution Theory (IAST):

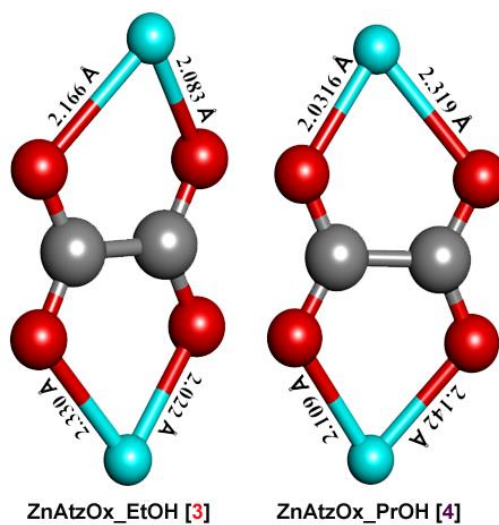
IAST calculations were undertaken as described by Prausnitz et al.⁴⁶ The isotherms were fitted using Dual site Langmuir or modified Dual site Langmuir model by solving the Langmuir equation using the solver function in Microsoft Excel following a similar protocol to Keller et al.⁴⁷ The selectivity equation is provided below.

Selectivity:

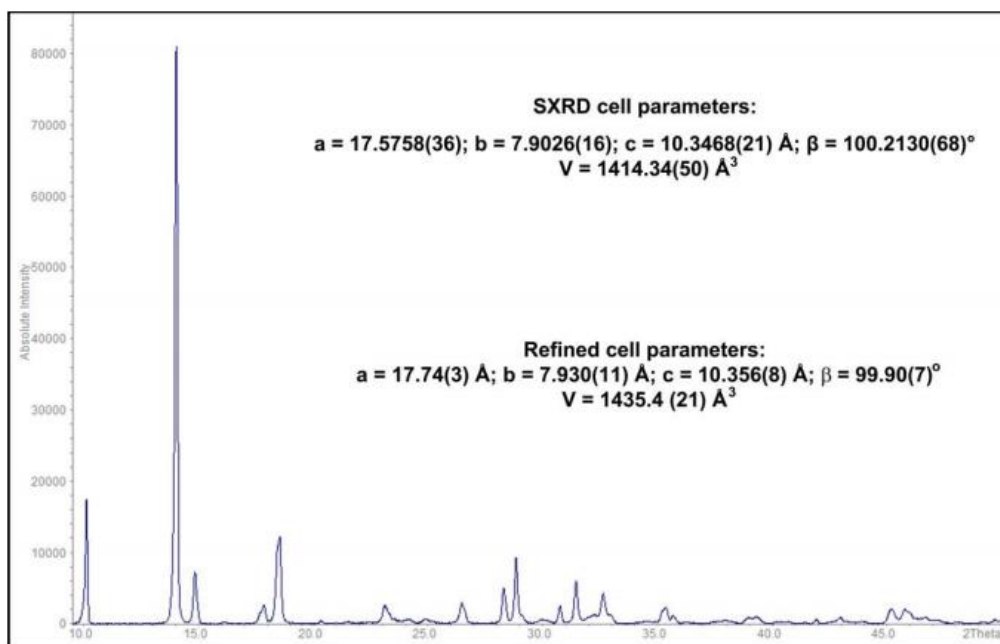
$$S_{1,2} = \frac{q_1/q_2}{P_1/P_2}$$



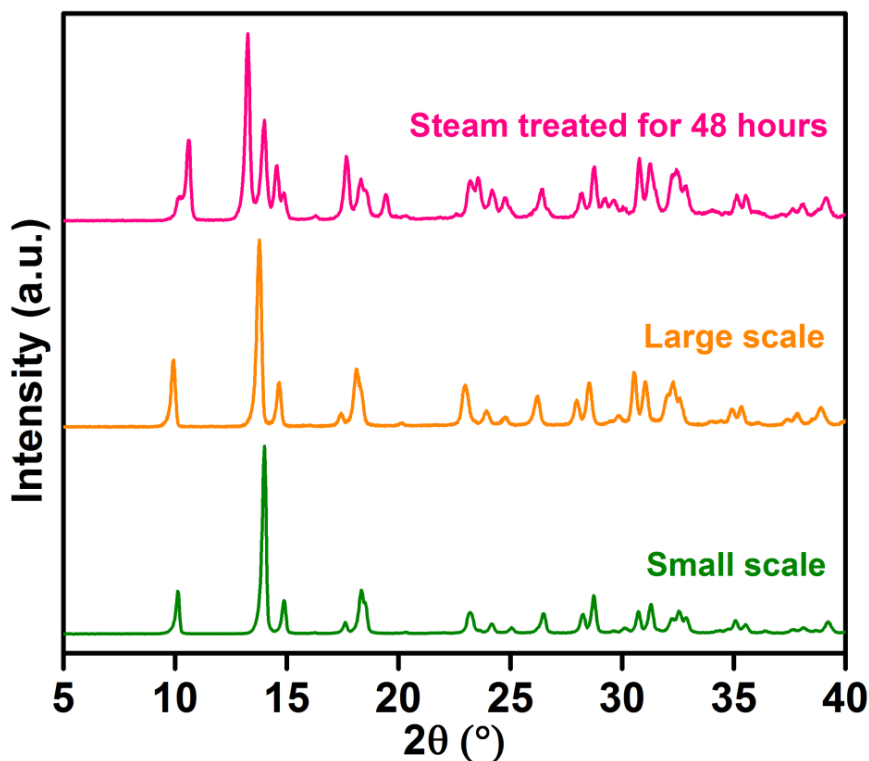
Appendix A4.22: CO₂/N₂ selectivities calculated using IAST methods.



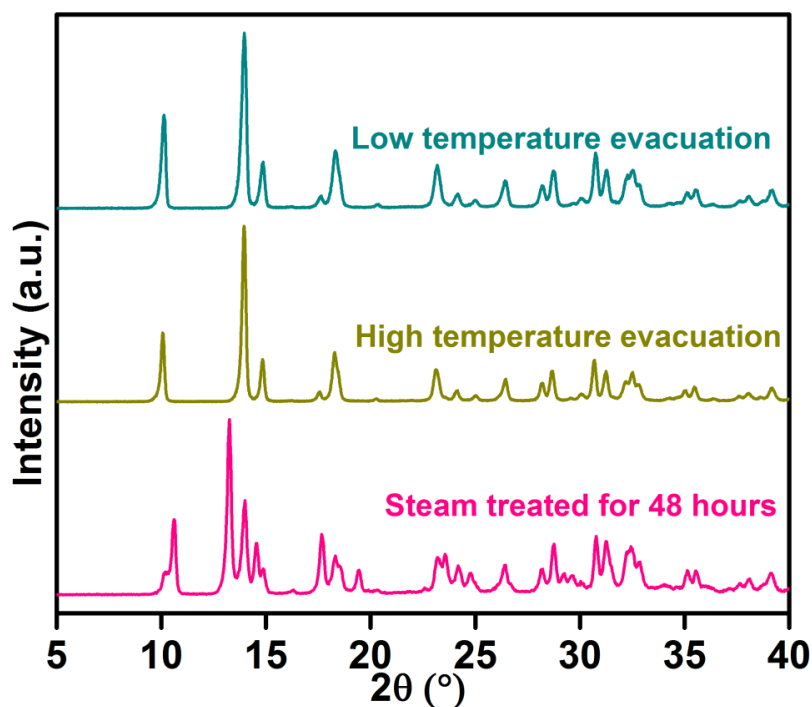
Appendix A4.23: Zinc-oxalate units in **3** and **4**, showing the as-symmetrical positioning of relatively longer Zn -O bond.



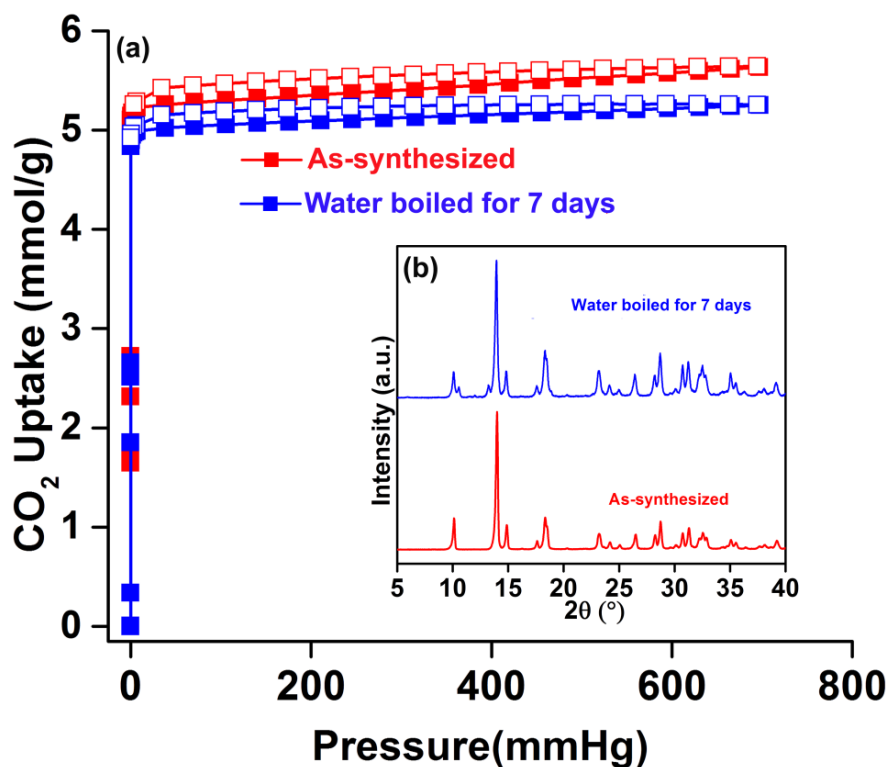
Appendix A4.24 Unit cell refinement performed on the PXRD data of a sample of **2** that was maintained at 900 mbar pressure of CO₂ in a capillary.



Appendix A4.25 Comparisons of the PXRD patterns of phase **2** synthesized in mg and gm scales and also the steam treated sample. Note: The changes in the relative intensities are strongly dependent on extent of solvent inclusion.



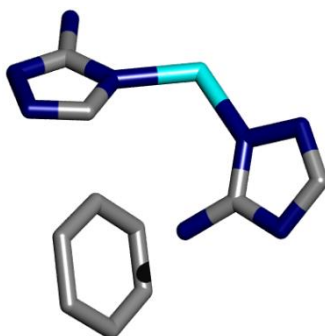
Appendix A4.26 Comparison of the PXRD patterns of phase 2 exposed to moisture, high temperature (HT) evacuated (150°C), low temperature (LT) evacuated. Note: The changes in relative intensities are strongly dependent on extent of solvent inclusion.



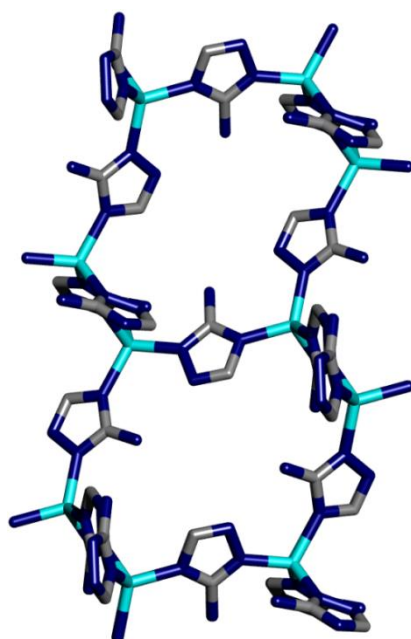
Appendix A4.27 (a) CO₂ adsorption for water boiled phase 2 at 195 K. About 6% of loss is observed. However, when this same sample was again subjected to water boiling (24 hours) no further loss of uptake was observed. Inset: (b) Comparison of the PXRD patterns of the as-synthesized and the water boiled samples of phase 2.

Appendix A5.1 Crystallographic data table

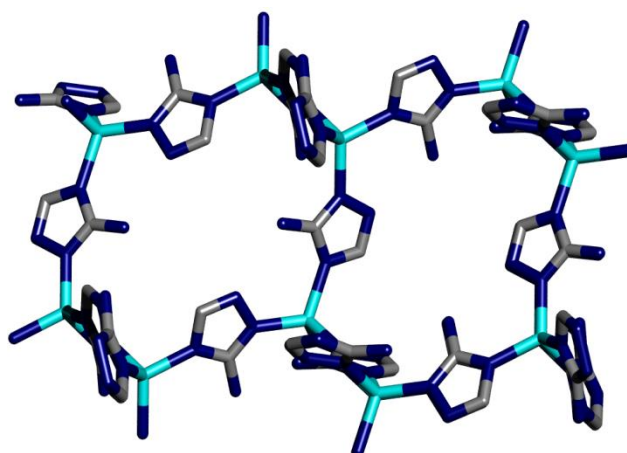
| | 1 |
|---------------------------------------|---|
| Formula | [Zn(C ₂ N ₄ H ₃) ₂](C ₆ H ₆) |
| FW | 309.65 g/mol |
| T, K | 100(2) |
| Crystal system, space group | Orthorhombic, <i>P</i> 2 ₁ 2 ₁ 2 ₁ |
| a, Å | 10.0084(3) |
| b, Å | 10.3360(3) |
| c, Å | 12.9252(4) |
| V, Å ³ | 1337.07(7) |
| Z, Calculated density | 4, 1.538 g/cm ³ |
| μ, mm ⁻¹ | 2.567 |
| F(000) | 632 |
| R _{int} | 0.0248 |
| Data/ restraints/para meters | 2179 / 0 / 172 |
| Goodness-of-fit on F ² | 1.120 |
| Final R indices [I > 2 sigma(I)] | R1 = 0.0220 wR2 = 0.0575 |
| Final R indices [all data] | R1 = 0.0224, wR2 = 0.0578 |



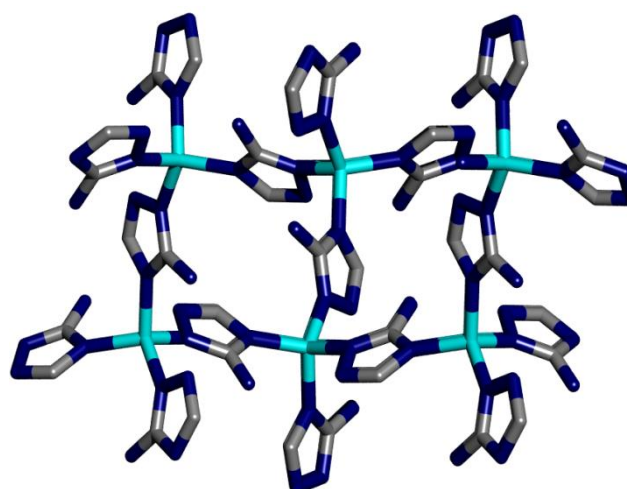
Appendix A5.2 Asymmetric unit of 1 (Zn: cyan, N: blue, C: grey; Hydrogens have been removed for clarity).



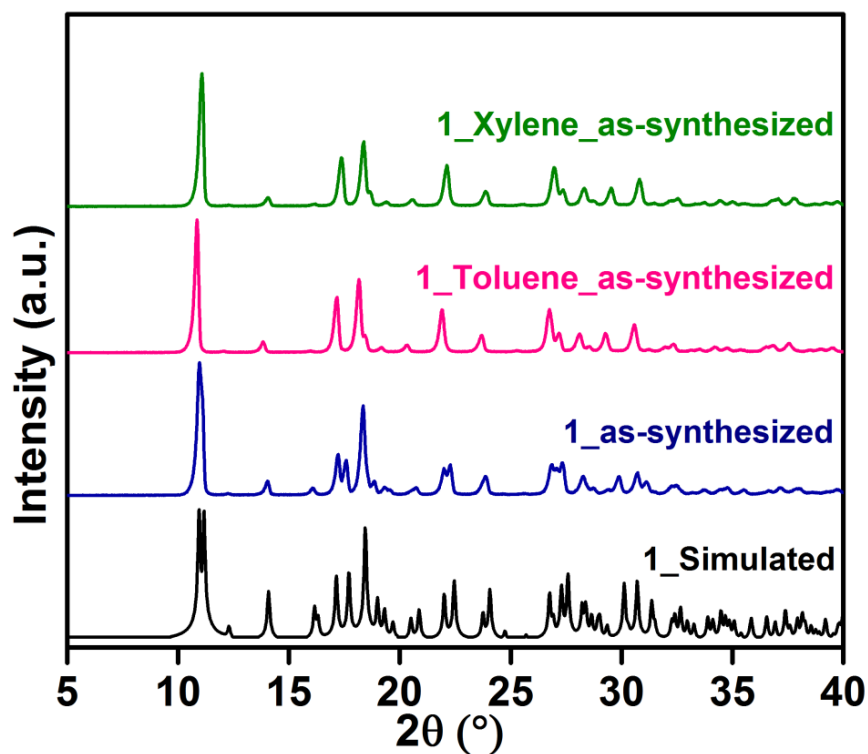
Appendix A5.3. View along crystallographic a-axis of 1.



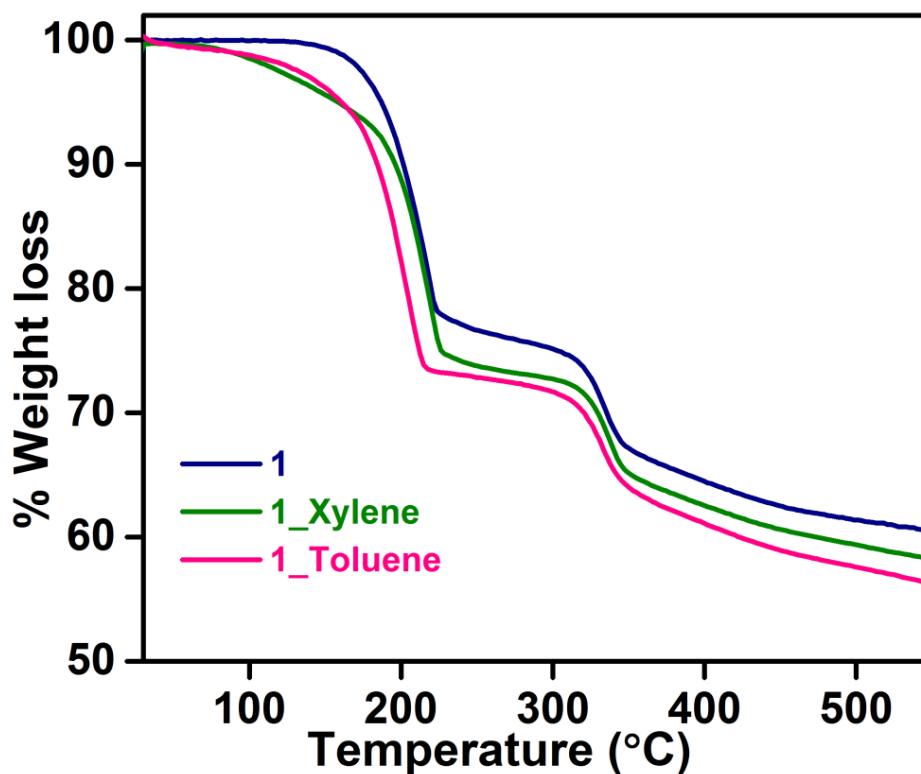
Appendix A5.4 View along crystallographic b-axis of 1.



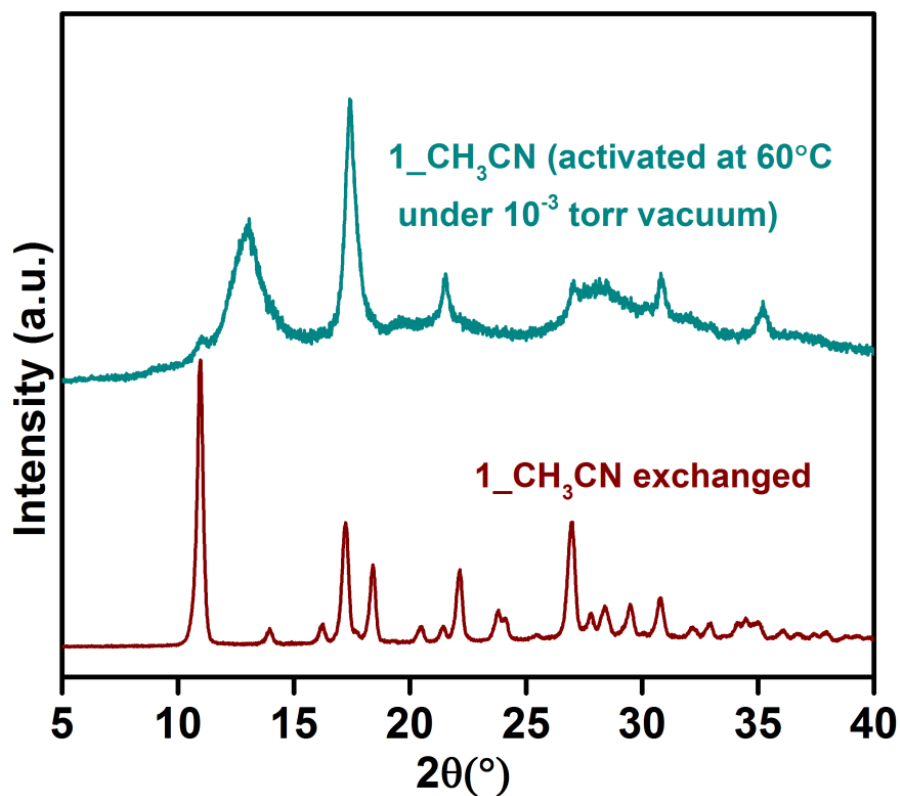
Appendix A5.5 View along crystallographic c-axis of 1.



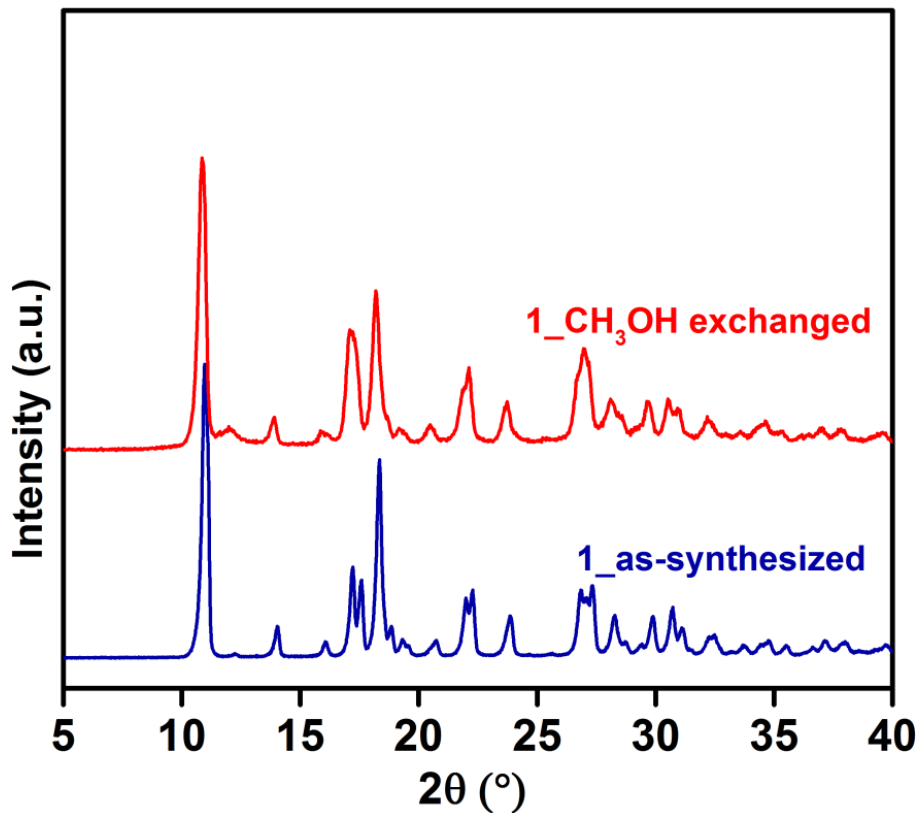
Appendix A5.6 Comparison between the simulated PXRD pattern of **1** with that of the bulk phases of **1**, **1_toluene**, and **1_xylene**; it could be seen that toluene and xylene also form the same phase, indication the templating role of these aromatic solvent.



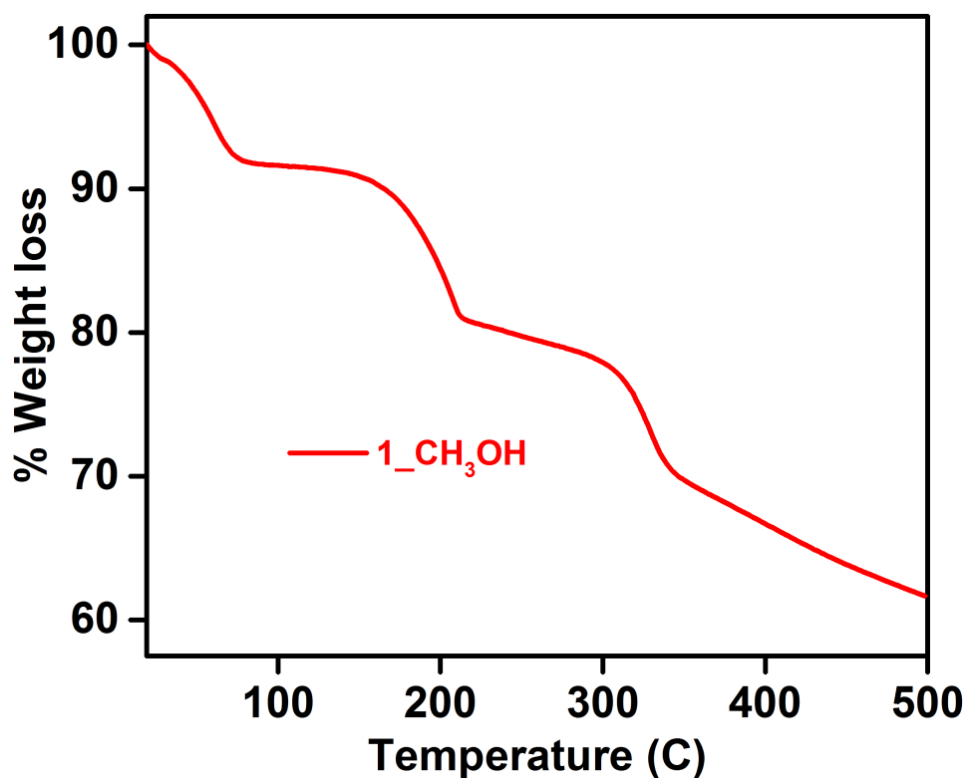
Appendix A5.7 Similar TGA profile obtained for **1**, **1_Toluene** and **1_Xylene**, signifying templating role of the aromatic solvents.



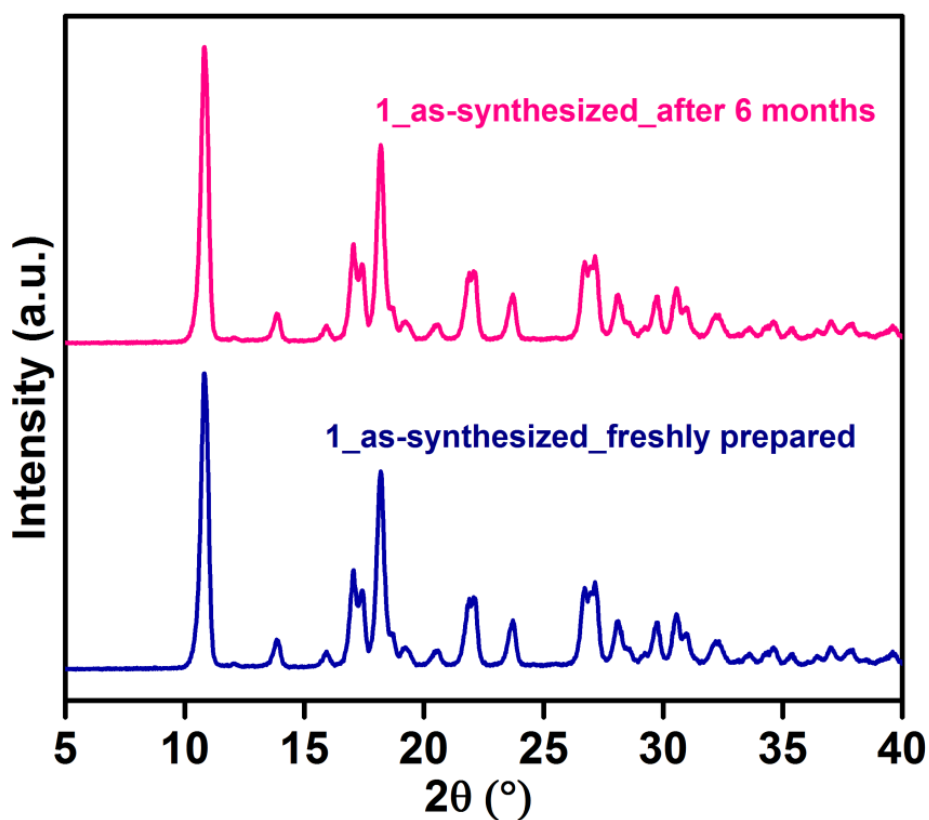
Appendix A5.8 PXR D for the 60°C (10⁻³ torr vacuum) activated 1-CH₃CN sample showing that significant loss in the crystallinity of the sample upon solvent removal.



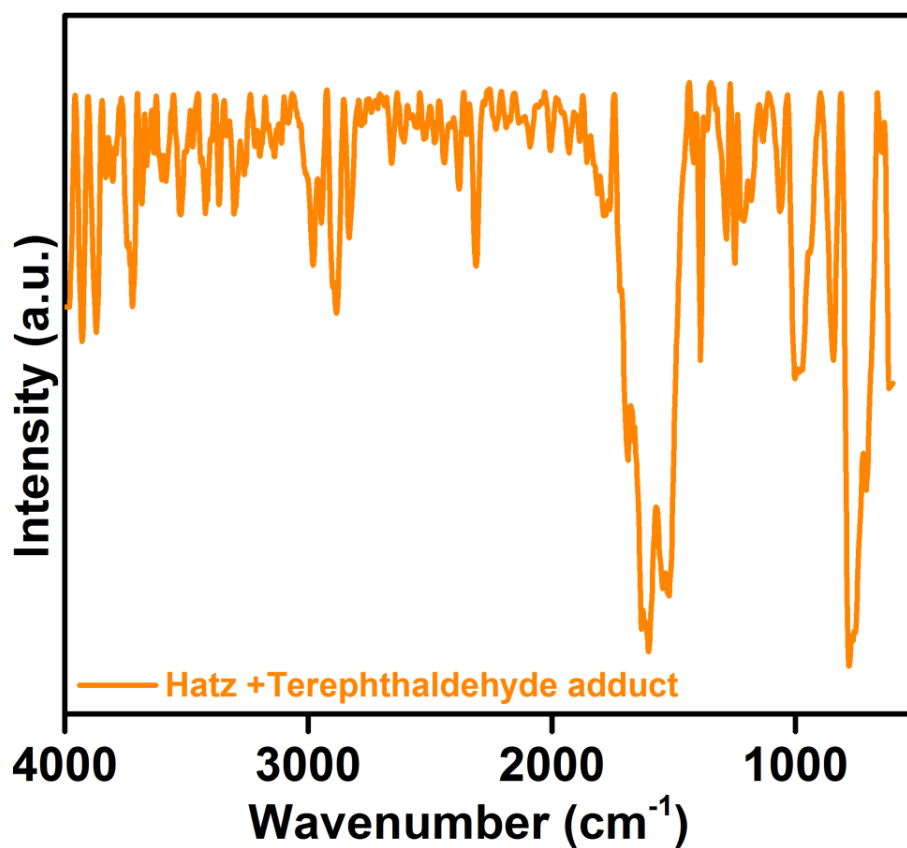
Appendix A5.9 PXR D of 1-CH₃OH sample.



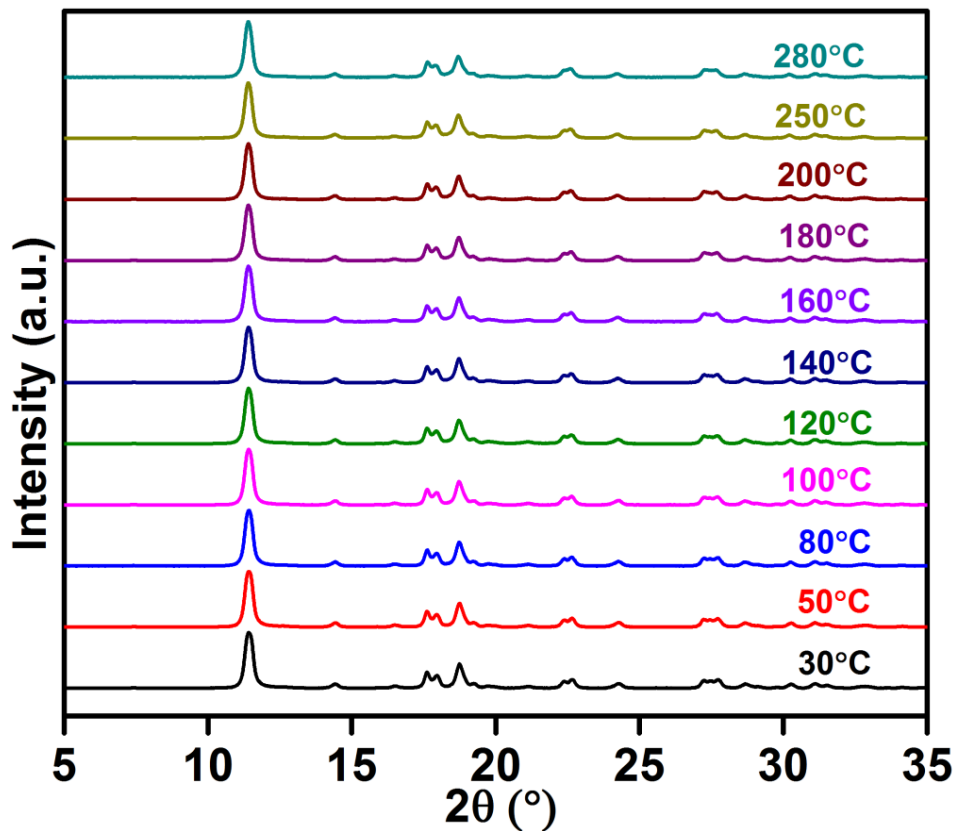
Appendix A5.10 TGA of 1_CH₃OH sample showing the low temperature solvent loss, which is confirming the solvent exchange.



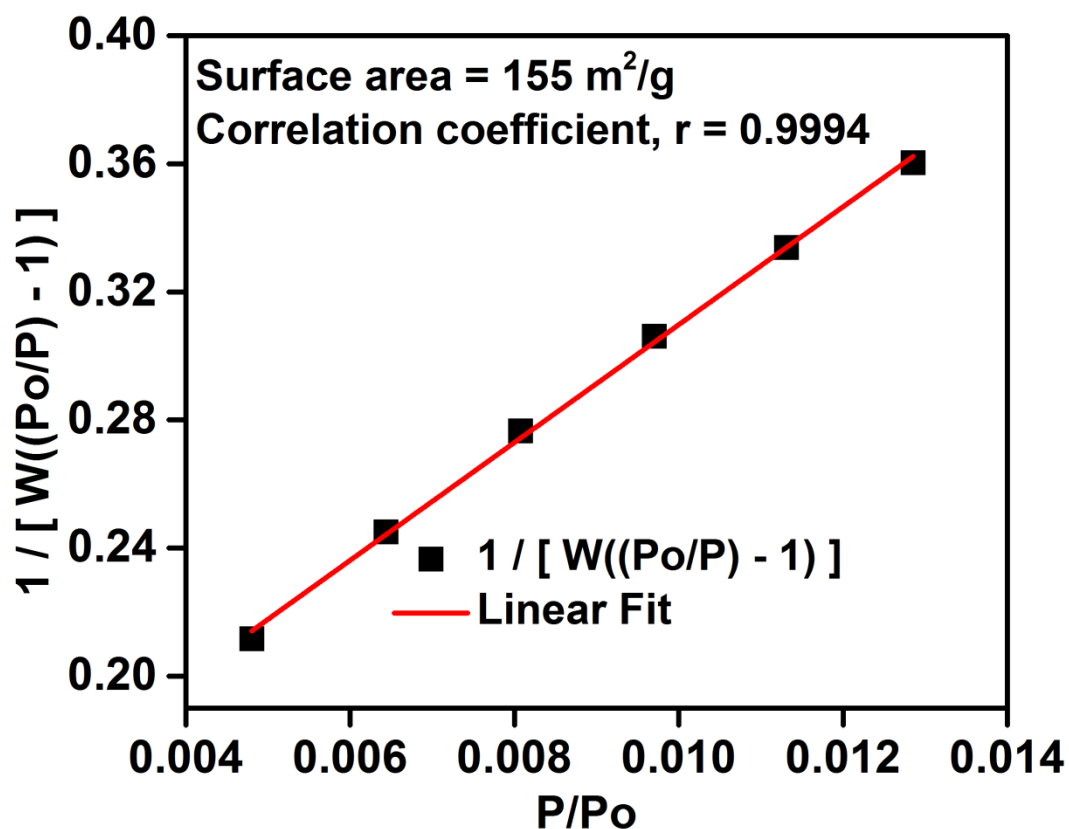
Appendix A5.11 Showing the strong templating role of benzene solvent molecules, as it can be seen the sample 1_as-synthesized is completely stable even after 6 months.



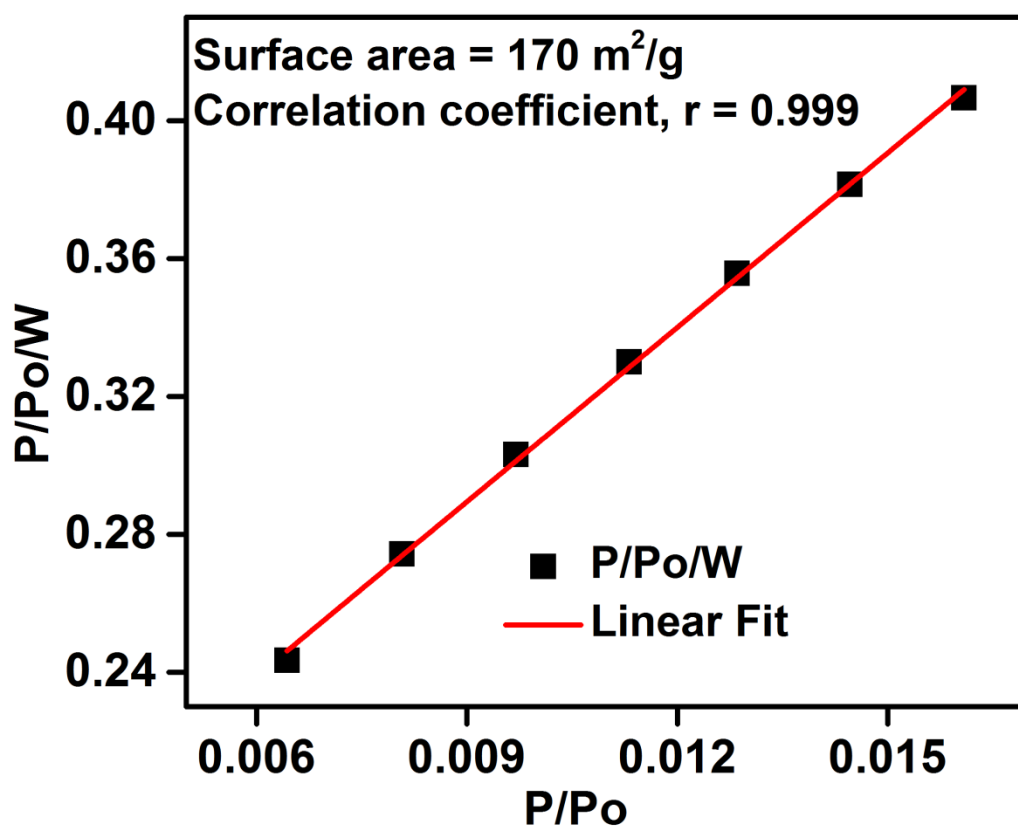
Appendix A5.12 IR spectra of the Organic adduct.



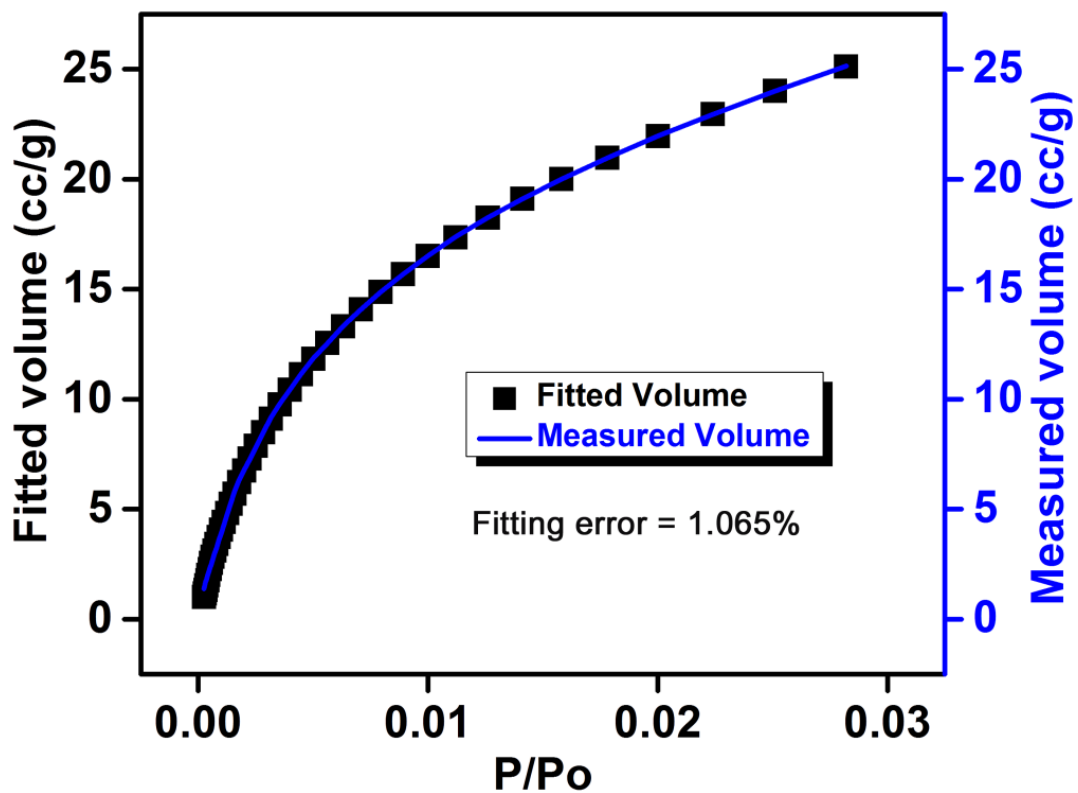
Appendix A5.13 VT-PXRD plot of 1-Terephthaldehyde.



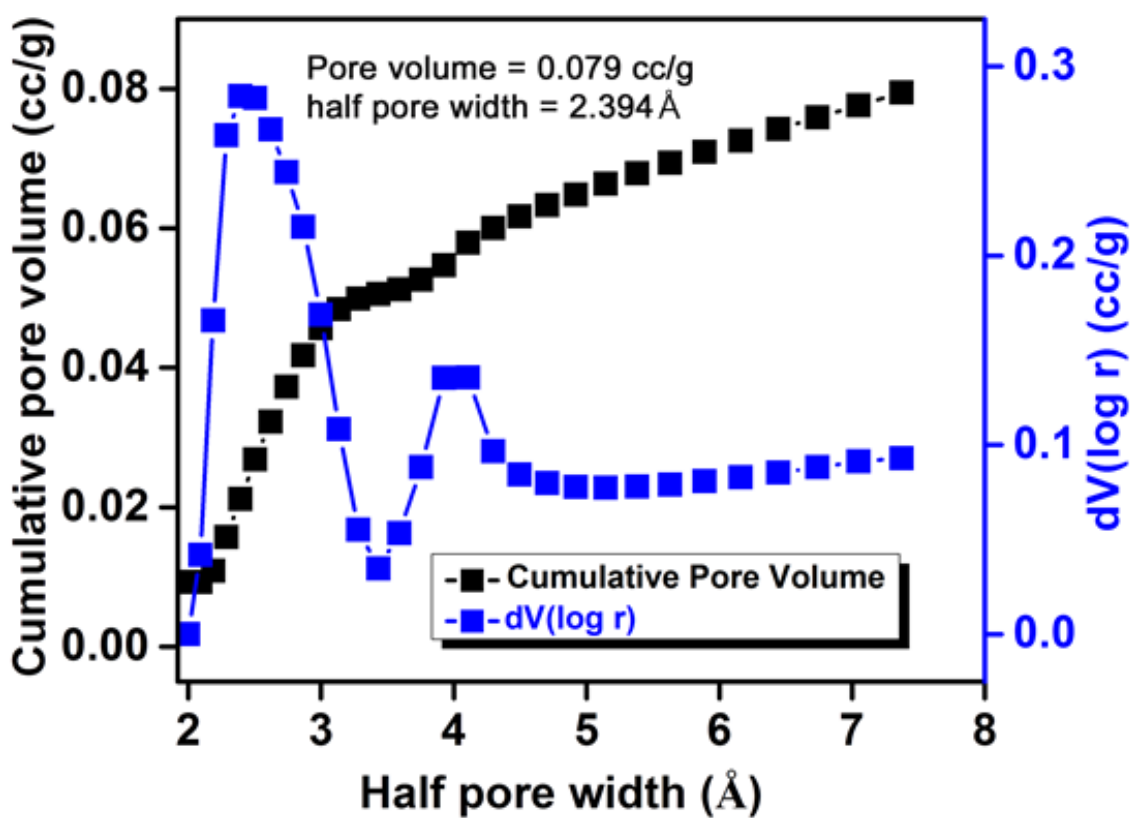
Appendix A5.14 BET surface area fit for 1.



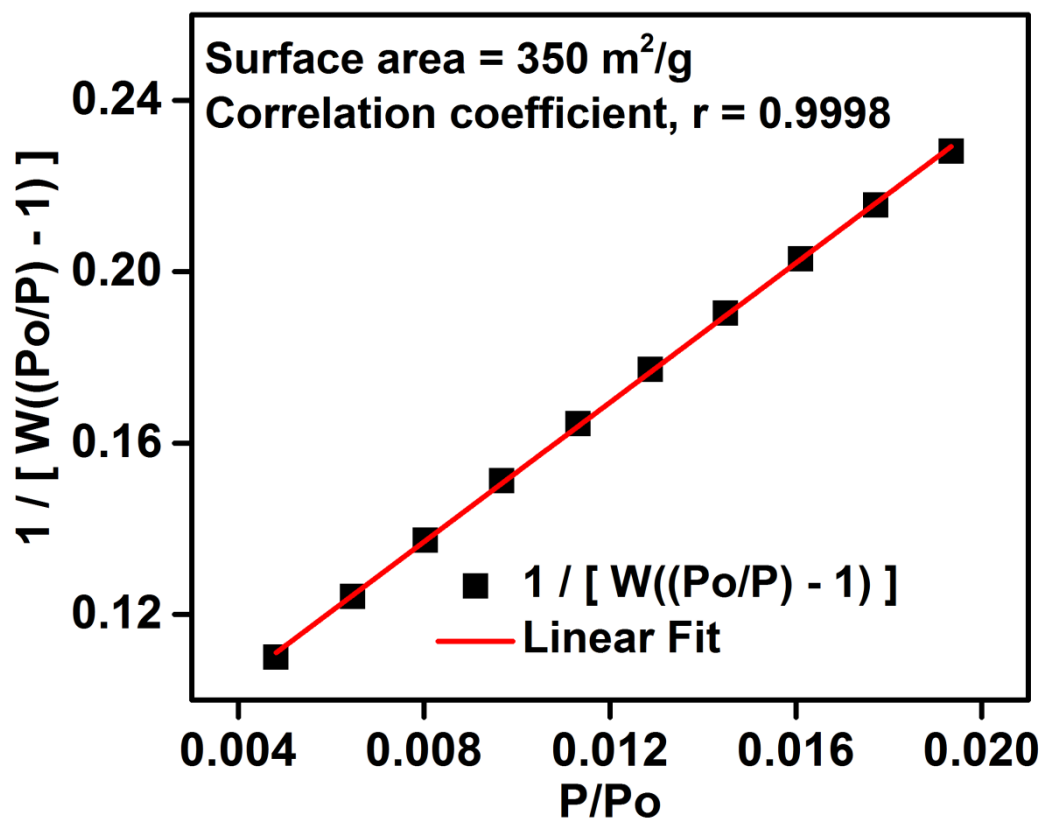
Appendix A5.15 Langmuir surface area fit for 1.



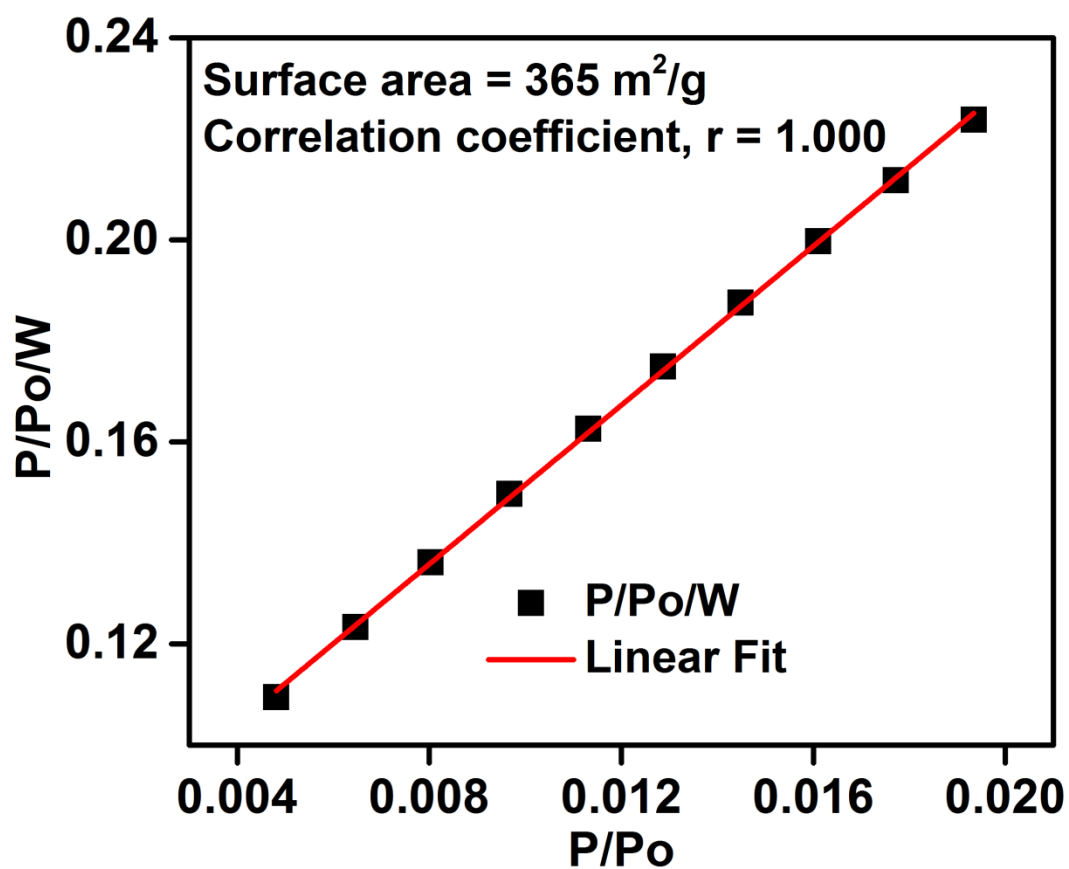
Appendix A5.16 DFT isotherm fitting comparison for 1.



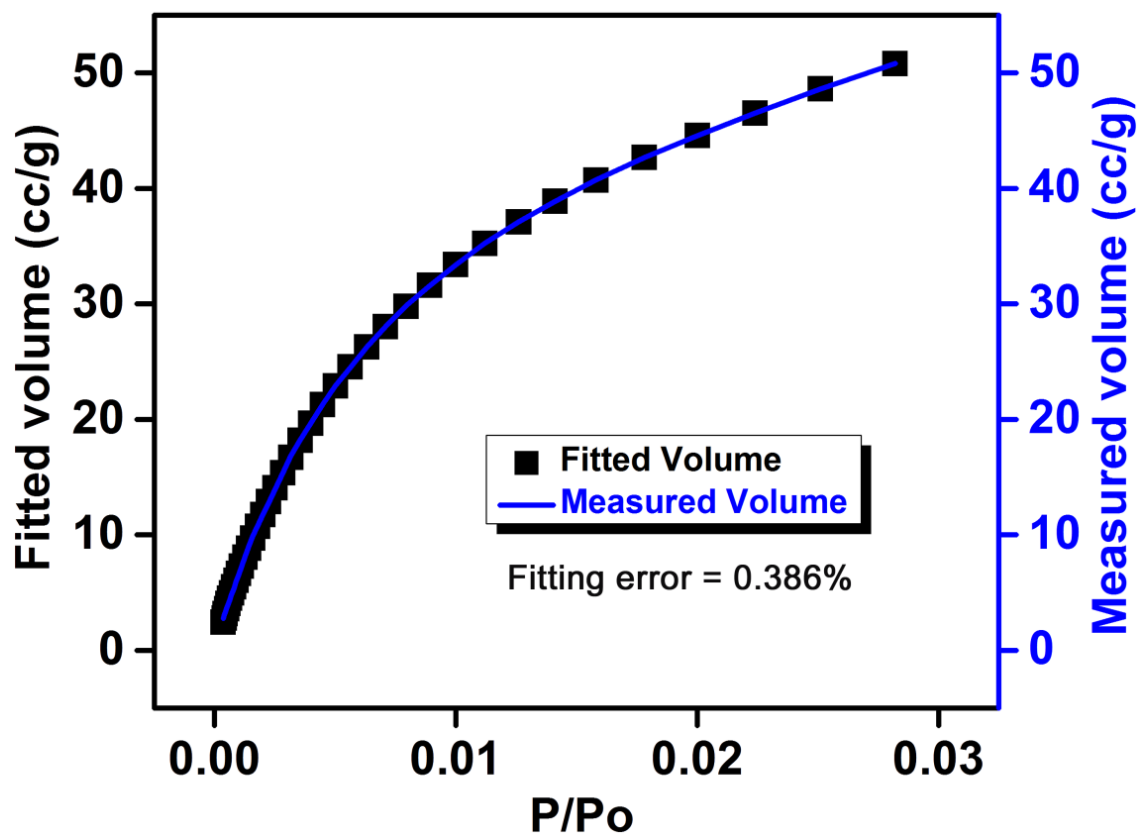
Appendix A5.17 DFT pore volume and pore size distribution plot for 1.



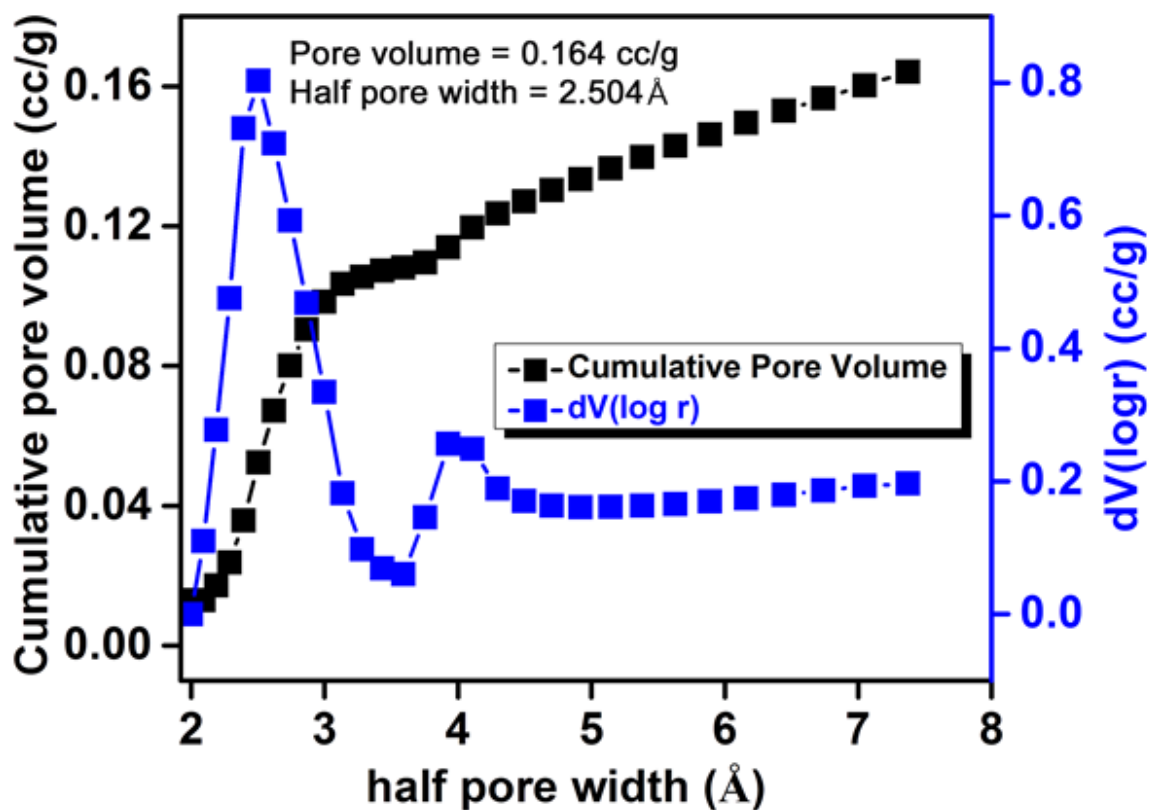
Appendix A5.18 BET surface area fit for 1_Terephthalaldehyde.



Appendix A5.19 Langmuir surface area fit for 1_Terephthalaldehyde.



Appendix A5.20 DFT isotherm fitting comparison for 1_Terephthalaldehyde.



Appendix A5.21 DFT pore volume and pore size distribution plot for 1_Terephthalaldehyde.